

*On the search for the
synchrotron cosmic web*

School of Electrical Engineering,
Computing and Mathematical Sciences

*On the Search for the
Synchrotron Cosmic Web*

Torrance Hodgson

Orcid ID 0000-0003-3443-7123

This thesis is presented for the degree of
Doctor of Philosophy of Curtin University

September 2022

Declaration

To the best of my knowledge, this thesis contains no material previously published by any other person except where due acknowledgement has been made.

This thesis contains no material which has been accepted for the award of any other degree or diploma in any university.

Copyright

© Torrance Hodgson 2022

This work is licensed under Creative Commons Attribution 4.0 International (CC-By 4.0). This license does not extend to materials contained within that are reproduced with permission from the respective copyright holder. The full text of this license is available at:

<https://creativecommons.org/licenses/by/4.0/legalcode>

Permission has been obtained to reproduce papers for the purposes of this thesis. *Publications of the Astronomical Society of Australia* and *The Astrophysical Journal* have allowed for full reproduction of authored papers for non-commercial use in a thesis.

The idea is like grass. It craves light, likes crowds, thrives on crossbreeding, grows better for being stepped on.

— Ursula Le Guin, *The Dispossessed*

Contents

Acknowledgements	i
Abstract	iii
1 Introduction	1
1.1 The cosmic web and its radio signature	1
1.2 Prior detection attempts	8
1.2.1 Direct detection	9
1.2.2 Cross-correlation	10
1.2.3 Stacking	11
1.3 Continuing the search	12
1.3.1 An opportune moment	12
1.3.2 Murchison Widefield Array	13
1.3.3 An outline of this thesis	15
2 Following up on direct detection candidates	17
2.1 Background	17
2.2 Method	18
2.3 Key results	19
3 The USS Jellyfish	21
3.1 Background	21
3.2 Method	22
3.3 Key results	24
4 The FIGARO simulation	27
4.1 Background	27
4.2 Method	28

4.3	Key results	31
5	Detecting the synchrotron cosmic web twice?	33
5.1	Background	33
5.2	Method	35
5.3	Key results	36
6	Simulated stacking with FIGARO	39
6.1	Background	39
6.2	Method	39
6.3	Key results	40
7	Conclusion	45
7.1	Summary	45
7.2	Final remarks	48
A	Statement of contribution	53
B	Published papers	55
B.1	Hodgson et al. (2020)	56
B.2	Hodgson et al. (2021b)	75
B.3	Hodgson et al. (2021a)	86
B.4	Hodgson et al. (2022b)	105
B.5	Hodgson et al. (2022a)	130

Acknowledgements

Foremost, I wish to acknowledge and thank my supervisors Melanie and Ben here in Perth, and Franco in Bologna. It was Melanie who encouraged me to come to Perth to do my PhD in the first place, and both her and Ben have worked incredibly hard on my behalf, providing direction, discussion, and encouragement at the times I needed it most. (Not to mention also fighting battles for me on more than one occasion.) And Franco, though I never had the opportunity to meet in person due to the pandemic, went to exceptional lengths to provide all things simulation-related, as well as to help me understand the fine technical details, which was no small feat when working remotely.

I am very thankful to the contributions made by collaborators and co-authors, whose contributions are detailed in [Appendix A](#). In addition, I want to acknowledge the informal help from a number of others: André Offringa for ongoing development of `wsclean` and willingness to help me understand difficult calibration and imaging problems; Cathryn Trott for letting me schedule a number of impromptu meetings to talk through problems; and Ramesh Bhat for his role as head of my PhD panel and in helping me manage some early teething problems.

A special thanks to my desk-mate and fellow graduate of Victoria University of Wellington, Stefan, who was on the receiving end of constant questions and rants, sanity checks, and who, especially at the start, really helped me find my feet. Thanks also to my colleagues-cum-friends amongst the PhD cohort at ICRAR, especially Steve, Jai, Ronniy, Pikky, Kat, Ben and Jaiden.

I have learnt that a PhD is at least as much an emotional struggle as it is an intellectual one. To lovers and partners, former and present—Ajay, Dhia,

Jake, Zi, Angus, Matthew, Allen—thank you for your constant support and understanding as I battled with this work.

And to my family, but especially Mum, for being that special rock in my life, no matter what.

Abstract

The imagery of the ‘cosmic web’ has been used to describe the Universe on the very largest of scales. It describes the ongoing process of structure formation, starting with primordial perturbations in the mass distribution of the early Universe, and since growing into an ontology of structures: large-scale voids, emptying onto surrounding sheets, collapsing down into filaments, and feeding into galaxy groups and clusters.

As part of this ongoing process, recent cosmological simulations suggest strong accretion shocks (having Mach numbers $\mathcal{M} \sim 10\text{--}100$) should form along the virial boundaries of clusters and filaments and that these are capable of exciting a fraction of the free electrons in the warm-hot intergalactic medium to relativistic energies. In turn, as they interact with weak intra-cluster magnetic fields (predicted to be on the order of $\mathbf{B} \sim \text{nG}$), these high energy electrons radiate this energy as synchrotron emission. The cosmic web is thus predicted to have a radio component that traces out its structure: the *synchrotron cosmic web*.

This thesis aims to continue the search for this faint, tell-tale radio signature of the cosmic web. It does so using a twofold approach, using both empirical observations and radio simulations.

The observational aspect of this work focuses on low-frequency observations, and primarily using the Murchison Widefield Array which we believe to be ideally suited for detecting the steep-spectrum synchrotron cosmic web. We attempt to replicate two important results published concurrently with this PhD, namely by [Vacca et al. \(2018\)](#) which claimed direct detection of numerous candidate sources associated with the cosmic web, and [Vernstrom et al. \(2021\)](#) which claimed statistical detection of filamentary emission by way of a stacking procedure. We follow up on both of these

studies, finding against their key claims in both cases. We also present a promising and highly unusual candidate of our own in the cluster Abell 2877 which we similarly find to be unrelated to the synchrotron cosmic web.

In addition to this observational work, we also develop the Filaments and GALactic RadiO (FIGARO) simulation, the first low-mid frequency radio simulation of the radio sky that combines the synchrotron cosmic web as well as the various subtypes of active galactic nuclei and star forming galaxies. We use FIGARO to investigate the nature, luminosity, and distribution of the synchrotron cosmic web. We develop a picture that differs from previous expectations, instead locating it in the form of long, narrow arcs of emission about cluster peripheries, finding the filaments themselves to host radio emission orders of magnitude fainter. FIGARO has also allowed us to model detection techniques and test their efficacy, especially in the presence of much brighter radio populations. In particular, we test both the radial cross-correlation and cluster-pair stacking techniques, finding both to suffer from important limitations that continue to stymie practical detection.

This work makes important strides towards understanding the nature of the synchrotron cosmic web as well as providing tools towards its detection. Ultimately, however, and despite our best effort, the synchrotron cosmic web continues to prove elusive.

Chapter 1

Introduction

The synchrotron cosmic web is the radio signature of the large-scale structure of the Universe. It is a signature that is the result of the process of gravitational collapse and structure formation, a process that continues through to the current epoch. But it is also only a prediction. The synchrotron cosmic web is found in our most sophisticated cosmological simulations, but in practice it is exceptionally faint, hidden and obscured by much brighter radio populations. Nonetheless, numerous attempts have been made towards detecting its signature, and in doing so it is hoped both to confirm our best cosmological models as well as provide us with one of the first pictures of the magnetised Universe. The work of this PhD continues that search.

1.1 The cosmic web and its radio signature

On the very largest of scales, the Universe is not homogeneous. Primordial density fluctuations in the early Universe have, under gravitational collapse, produced a web-like structure: overdensities have become amplified to produce massive, gravitationally bound clusters and galaxy groups, connected by a network of diffuse thread-like filaments; meanwhile, underdense regions have emptied out to produce cavernous voids. We call this sponge-like structure of the large-scale Universe the ‘cosmic web’.

The cosmic microwave background gives us one of the clearest pictures of the density variations of the early Universe, already present at just 380,000 years after the Big Bang. By this point, quantum fluctuations during inflation had grown under baryon acoustic oscillations, and at the moment of last scattering the large-scale structure of the Universe was allowed to proceed

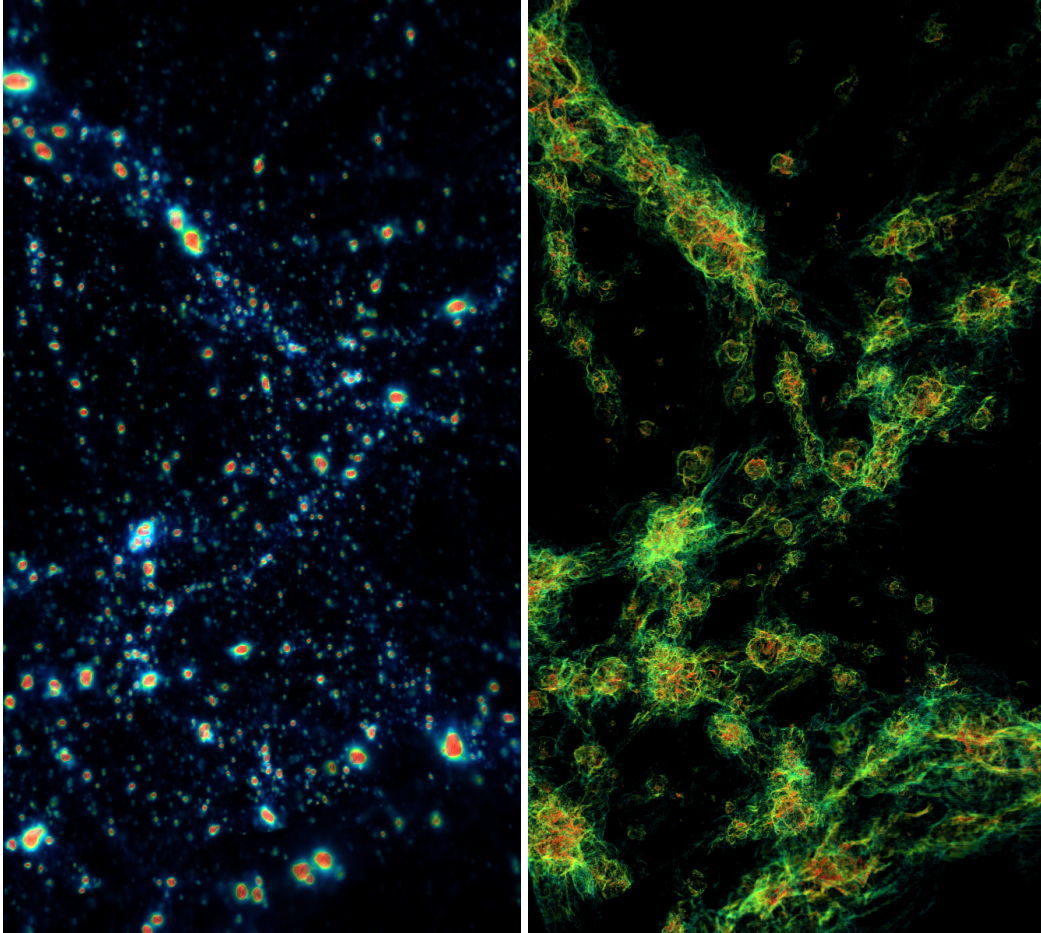
primarily under gravitational collapse. Both theoretical models and N-body simulations have predicted that, under these kinds of early fluctuations, the Universe should proceed to collapse into highly asymmetric forms, with both planar and filamentary structures. Zel'dovich (1970) provided an early formalism which showed how such systems would evolve towards a range of morphologies of voids, sheets, filaments and clusters. Early computer N-body simulations allowed the exploration of this evolution in significantly more depth and validated the models of Zel'dovich by showing a tendency towards precisely this morphology of structures (e.g. Davis et al., 1985; White et al., 1987). Meanwhile, empirical confirmation of this large-scale structure has come in the form of increasingly deep and complete galaxy surveys. Modern-day surveys such as 2dFGRS (Colless et al., 2003), Sloan Digital Sky Survey (Tegmark et al., 2004), and 2MASS (Huchra et al., 2005) have confirmed the structure many times over, showing galaxies that are located together in clusters, that trace out thin intervening filaments, and that skirt around largely empty voids.

N-body simulations, however, have pointed to something that has yet to be rigorously, empirically confirmed. Starting with the work of Cen & Ostriker (1999) and Davé et al. (2001), these simulations pointed to a hitherto hidden population of baryons tracing out these large-scale cosmic web structures, providing a solution to one of the outstanding problems of cosmology, the so-called 'missing baryon problem'. This 'warm-hot intergalactic medium' (WHIM), which is predicted to trace out the length of filaments and the periphery of clusters, is shock-heated to temperatures of 10^5 – 10^7 K by ongoing gravitational collapse, highly ionised as a result, and extremely diffuse. These properties, however, make its detection extremely difficult: its thermal emission is too faint to be detectable with current generation X-ray instruments; its ionised state prohibits probing it via absorption or emission features; and its low density makes detection by other means such as the Sunyaev-Zel'dovich effect extremely difficult. Nonetheless, numerous tentative and increasingly convincing reports have been published in support of the existence of the WHIM as it traces out the cosmic web, and

these have come by way of a range of detection techniques, including: direct detection of extended X-ray emission around a massive cluster (Eckert et al., 2015); weak absorption lines in a distant quasar attributed to trace metals in foreground overdense filaments (Nicastrò et al., 2018); stacking of X-ray data to detect either thermal emission or the thermal Sunyaev-Zel'dovich effect (de Graaff et al., 2019; Tanimura et al., 2019, 2020); and most recently, using the dispersion measure of fast radio bursts to account for the missing baryons (Macquart et al., 2020).

The synchrotron cosmic web is radio emission that we expect to trace out accretion shocks along the edges of the WHIM as part of the ongoing process of large-scale structure formation. After the earliest simulations predicting the existence of a shock-heated WHIM, a number of other authors also pointed to the likely existence of high-energy, relativistic populations of electrons tracing out the filaments and cluster peripheries (e.g. Keshet et al., 2004; Ryu et al., 2008; Skillman et al., 2011). One of the earliest of these was by Keshet et al. (2004). They noted the role of collisionless, non-relativistic shocks around supernova remnants (SNRs) in accelerating electron plasmas to relativistic energies, so called Fermi type I or diffusive shock acceleration (DSA), where the electron acceleration efficiency had been observed as high as $\xi_e = 0.05$. By extension, infall accretion shocks along the outskirts of the low-density WHIM, which have been predicted to have Mach numbers as high as $M = 10^3$ (Pfrommer et al., 2006; Kang et al., 2007), should host similar kinds of relativistic electron populations, and these populations in turn should radiate their energy as synchrotron radio emission as they interact with intracluster magnetic fields. In this way, the cosmic web is expected to have a 'radio signature' tracing out large-scale structure formation processes.

More recent modelling of the synchrotron cosmic web has been provided by Vazza et al. (2015) and Vazza et al. (2019). Both of these involved running magneto-hydrodynamic (MHD) cosmological simulations of the Universe from high redshift until the present epoch. These simulations traced the evolution of a number of observables, allowing the identification



(a) Dark matter distribution

(b) Synchrotron emission

Figure 1.1 An illustration of the 100^3 Mpc^3 volume at redshift $z = 0.025$, from the simulation in [Vazza et al. \(2019\)](#). The comparison shows the distribution of dark matter on the left, with bright points indicating clusters and galaxy groups, whilst on the right we show the associated synchrotron cosmic web emission.

in post-processing of accretion shocks and associated magnetic fields and to ultimately model the radio luminosity. [Figure 1.1](#) shows a side-by-side illustration of the mass distribution and synchrotron cosmic web emission from within a snapshot at redshift $z = 0.025$ from [Vazza et al. \(2019\)](#). On the left, we see bright points representing clusters and galaxy groups. These are clearly not randomly distributed but are clustered and trace filamentary paths throughout the volume. On the right, we show the associated synchrotron emission. This traces out the same paths, surrounding and enveloping the dense cores of the clusters and galaxy groups, and also contains a significant amount of fine structure from individual shock fronts.

The modelling for synchrotron emission at shock boundaries depends on a number of factors. In [Vazza et al. \(2019\)](#), this modelling draws from earlier work by [Hoeft & Brüggen \(2007\)](#) and includes the following terms:

$$P_\nu \propto S \cdot n_d \cdot \xi_e \cdot \nu^{-\alpha} \cdot T_d^{3/2} \cdot \frac{B^{1-\alpha}}{B_{\text{CMB}}^2 + B^2} \quad (1.1)$$

where S is shock surface area, n_d is the downstream electron density, ξ_e is the electron acceleration efficiency, ν is the observing frequency, α is the radio spectral index and is typically around -1 , T_d is the downstream electron temperature, B is the magnetic field at the site of the shock, and B_{CMB} is the equivalent magnetic field strength of the cosmic microwave background, approximately $B_{\text{CMB}} = 3.25(1+z)^2 \mu\text{G}$. Of each of these terms, many are well understood and constrained from the simulation. What are not well understood, however, are the electron acceleration efficiency and the cosmic magnetic field strengths, and these two terms are responsible for the largest uncertainties in our prediction for the luminosity of the synchrotron cosmic web.

The electron acceleration efficiency is a term in this formalism that can be thought of as describing the fraction of electrons accelerated to relativistic speeds. [Hoeft & Brüggen \(2007\)](#) model this term as a function of Mach number and the downstream electron temperature, $\xi(\mathcal{M}, T_d)$, and it has the shape as shown in [Figure 1.2](#). For especially strong shocks, $\mathcal{M} > 5$, this term is largely constant and peaks at 5%, but rapidly declines for weaker

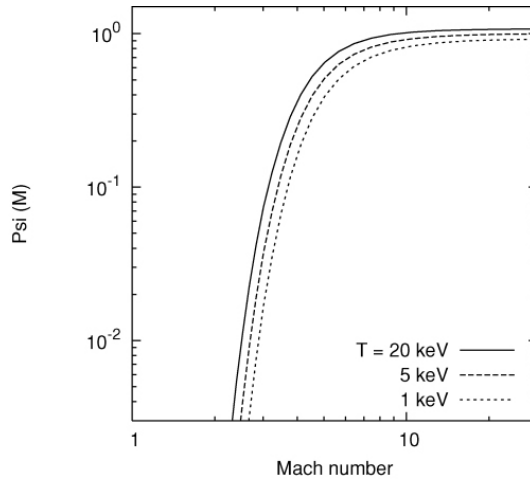


Figure 1.2 The electron acceleration efficiency, as modelled by [Hoeft & Brüggen \(2007\)](#). Note that this plot displays $\Psi(\mathcal{M}, T_d)$, which is related to the electron acceleration efficiency by the parameterisation $\xi(\mathcal{M}, T_d) = \xi_{e,0}\Psi(\mathcal{M}, T_d)$, where $\xi_{e,0} = 10^{-3}$.

shocks. Radio observations, however, suggest that this modelling of the electron acceleration efficiency is not the whole picture. Radio relics, for example, are a class of cluster-scale emission structures that typically form long arcs tracing the periphery of massive clusters, and are believed to be generated by shocks resulting from cluster merger events (e.g. [Ensslin et al., 1998](#); [Miniati et al., 2000](#); [Giovannini & Feretti, 2000](#); [Ryu et al., 2003](#)). [Botteon et al. \(2020\)](#), for example, studied ten such radio relics with known shock strengths measured from X-ray observations—typically in the range of $\mathcal{M} = 2 - 3$ —and found that the shock strengths alone were insufficient to account for the luminosity of the observed relic emission, at least according to standard DSA modelling such as [Hoeft & Brüggen \(2007\)](#). The leading explanation for this discrepancy is to posit significant suprathermal electron populations, so called ‘fossil electrons’, existing in the region of these shocks, which in turn boost the electron acceleration efficiency. The origin of fossil electrons in cluster environments is still the subject of debate but relies on some kind of previous acceleration mechanism such as active galactic nuclei activity or previous shock events. Outside of clusters, the role of fossil electron populations in the sparse, low-density environment of the WHIM, perhaps from previous epochs of accumulated accretion shock activity, is

believed to be much less significant but still unknown. For example, in their detection of a radio ridge spanning the intracluster environment between merging clusters Abell 399 and Abell 401, [Govoni et al. \(2019\)](#) pointed to the mismatch between their detection and simulation, suggesting that a fossil electron population spanning the 3 Mpc ridge at energies $\gamma \geq 1000$ was necessary to account for the luminosity.

The second, poorly understood term is the strength of the intracluster magnetic field. In fact, it is this term that has been one of the principal motivations for detection attempts of the synchrotron cosmic web. The predicted luminosity of synchrotron cosmic web emission in intracluster environments is particularly sensitive to magnetic field strengths: for values $B \ll B_{\text{CMB}}$, the luminosity in [Equation 1.1](#) scales approximately as $P_\nu \propto B^2$. To date, the primary method to measure intracluster magnetic fields has been by probing the rotation measures of distant, polarised radio sources and from this, attempting to measure the contribution from intervening magnetised plasmas. [Pshirkov et al. \(2016\)](#), for example, found the rotation measures of a few thousand extragalactic sources to display no statistically significant redshift dependence, and in this way were able to place an upper limit of 1.7 nG for intracluster magnetic fields coherent on 1 Mpc scales. Similarly, [O’Sullivan et al. \(2019\)](#) used the rotation measure difference across the lobes of a specific radio galaxy, one of whose line-of-sight passed through an overdense region of intersecting filaments, to place an upper limit on the magnetic field of 0.3 μG ; however, they deemed the chance that the rotation measure difference was entirely attributable to the intervening filaments at only 5%, and likely that the intracluster magnetic field strength was much lower still. [Vernstrom et al. \(2019\)](#) performed a similar technique, comparing the rotation measure difference between pairs of sources that appeared nearby on the sky, breaking this population down into those that were physically nearby, and those that were unrelated. By attributing the entirety of the rotation measure difference of these two populations to extragalactic magnetic fields, they found an upper limit magnetic field strength of 37 nG. These few studies, which are all upper limits and, in some cases, clearly

very conservative upper limits, make it clear there is still some way to go in our understanding of cosmic magnetic fields. This makes it difficult to predict the luminosity of synchrotron cosmic web emission with certainty; but simultaneously, making a detection of the synchrotron cosmic web would allow us to provide robust constraints on these large-scale magnetic fields.

1.2 Prior detection attempts

Despite the uncertainties in these key terms, a number of authors have made predictions about both the likelihood of detecting the synchrotron cosmic web with the next generation of radio telescopes, as well as the best methods to do so. [Brown \(2011\)](#), for example, discussed then-current predictions of cosmic web emission at levels of a few $\mu\text{Jy arcmin}^{-2}$ at 1.4 GHz, and the challenges of observing such a faint signal. Under the assumption that the synchrotron cosmic web was extended and smoothly varying on large angular scales, they noted the importance of interferometers needing to sample short baselines, or else risk resolving out the large-scale cosmic web emission. They also noted the danger of unresolved sources, especially ordinary galaxies which are strongly correlated with large-scale structure, obscuring or even creating false signals that we might attribute to the synchrotron cosmic web. Given the faintness of the emission, [Brown \(2011\)](#) pointed to the statistical methods of stacking and cross-correlation, which we discuss shortly, to find the faint signal hidden in amongst the noise of radio surveys.

[Vazza et al. \(2015\)](#) used simulations to forecast the possibility of detecting the synchrotron cosmic web, and specifically with reference to a few current and planned low frequency instruments. They considered two scenarios to factor in uncertainties in cosmic magnetic field strengths—a low and high amplification model—where the magnetic field was renormalised in post-processing in an attempt to provide lower and upper limits on the radio emission. [Vazza et al. \(2015\)](#) drew a number of conclusions related specifically to practical questions of detection with current and upcoming radio telescopes. Specifically: only in the high amplification model was

it possible to directly detect the brightest accretion shocks, whilst in the low amplification scenario the chance of making a detection of any kind was reduced tenfold; in the high amplification model, filaments were \sim Mpc wide and emitting at $\sim\mu\text{Jy arcsec}^{-2}$ at 100 MHz; and low-frequency observations with wide fields of view were best suited to make detections, given the steep spectral index of emission ($\alpha \lesssim -1$) and the large, extended emission structures. In a follow-up study, [Vazza et al. \(2019\)](#) were less bullish in the prospects for detection of the cosmic web. Instead, they emphasised the possibility of detecting synchrotron emission in the disturbed, extreme peripheries of clusters in pre-merger scenarios.

It is in the context of these predictions that we turn to discuss the detection attempts to date.

1.2.1 Direct detection

As noted, we might expect exceptionally bright emission to be found around the periphery of massive clusters, especially along ‘bridges’ between clusters where the emission has been amplified as the result of compression prior to merging. To date, two such intracluster bridges have been detected. [Govoni et al. \(2019\)](#) reported the detection of a radio bridge extended between merging clusters Abell 399 and Abell 401 which was detected at 140 MHz with the Low Frequency Array (LOFAR). The bridge spans the two clusters, which are separated by a projected distance of 3 Mpc, and has a mean surface brightness of $0.38 \mu\text{Jy arcsec}^{-2}$. The bridge is much longer than the maximum distance that relativistic electrons can travel in their lifetime, and necessitates in situ (re)acceleration. The mechanism that has accelerated the electrons along this bridge is not well understood, and comparison to simulations of similar cluster mergers suggests much higher effective electron acceleration efficiencies than we can currently account for. [Botteon et al. \(2020\)](#) also reported the detection of a radio bridge between merging clusters Abell 1758N and Abell 1758S, separated by only 2 Mpc. The emission was detected also with LOFAR, and clearest at 144 MHz, with an integrated flux of 24.2(49) mJy. Once again, the emission is difficult to explain, but the

authors consider Fermi type II emission processes as modelled by [Brunetti & Vazza \(2020\)](#) that result from turbulent dynamics between the merging clusters. The authors also point to the similarity with the ridge in Abell 399-401, and specifically the fact that all individual clusters in these two merging scenarios also host radio halos, showing that these are especially dynamic and energetic systems.

The case of radio bridges between merging clusters represents one extreme of cosmic web emission: radio emission that results from compressed, turbulent regions between massive and dynamically disturbed clusters. It is not, however, the general case of cosmic web emission, which we expect to be caused by more widespread accretion processes. In [Vacca et al. \(2018\)](#), the authors claimed to have made numerous detections of this more general type of emission in an $8^\circ \times 8^\circ$ area of the sky hosting a number of massive nearby galaxy clusters, by combining observations from the Sardinia Radio Telescope and archival NRAO VLA¹ Sky Survey data. They identified 28 large-scale synchrotron sources which had no or weakly associated X-ray emission—implying they were not related to the interior of clusters—and concluded they were therefore candidates for synchrotron cosmic web emission. In this thesis, we follow up on this report and attempt to detect and more fully characterise these candidate sources in [Chapter 2](#).

1.2.2 Cross-correlation

In contrast to direct detection, the cross-correlation method aims to make a statistical detection of the faint synchrotron cosmic web signal at or beneath the noise level of our radio maps. The method involves cross-correlating our radio maps with kernels constructed to map out our ‘best guess’ estimate for the expected distribution of the cosmic web; these two-dimensional cross-correlation maps are then radially averaged to produce a one-dimensional cross-correlation as a function of angular offset. The idea is that the synchrotron cosmic web would impart a positive peak at zero degrees offset, but unfortunately other similarly correlated radio sources may also contribute

1. National Radio Astronomy Observatory Very Large Array

to this signal. This method allows us to essentially integrate across a large area of sky and therefore increase our sensitivity.

Both [Brown et al. \(2017\)](#) and [Vernstrom et al. \(2017\)](#) employed this method, however their ‘best guess’ kernels were constructed by differing means. In [Brown et al. \(2017\)](#), this kernel was constructed by a cosmological simulation that traced magnetic field amplification over time, and which was constrained to reproduce local large-scale structure in the current epoch out to $z = 0.048$. This kernel was then cross-correlated against maps of the sky produced by the Parkes radio telescope at 2.3 GHz, finding no statistically significant peak in the radial cross-correlation at 0° offset. [Vernstrom et al. \(2017\)](#), instead, used galaxy density maps as their kernel, on the assumption that these were tracers for large-scale structures of clusters and filaments, and in turn that the synchrotron cosmic web would be densest in these regions. In fact, the radial cross-correlation results showed a peak at 0° , but [Vernstrom et al. \(2017\)](#) were unable to claim that this correlation was the result of synchrotron cosmic web emission as opposed to other correlated but unrelated emission, and in particular unresolved galactic radio emission.

1.2.3 Stacking

Stacking is another kind of statistical method, whereby a mean image is constructed from many observations of a particular feature. The idea is that, with sufficiently large numbers of observations, the noise in the stacked mean image will average down and so make clearly detectable any shared emission structures. We reported earlier on this technique being used in detecting X-ray emission from the WHIM, for example in [Tanimura et al. \(2019\)](#) where known cluster pairs were stacked, and a faint intracluster signal spanning the cluster pairs became visible as the noise was reduced. Very recently, a similar kind of stacking methodology was employed by [Vernstrom et al. \(2021\)](#) to detect the synchrotron cosmic web, where hundreds of thousands of pairs of close-proximity luminous red galaxies (LRGs)—used as tracers for clusters and galaxy groups—were stacked in low-frequency radio observations. After subtracting out the contribution from the clusters and

LRGs themselves, they found excess intracluster emission persisted along the intracluster bridge at 5σ significance. In fact, they detected this signal across multiple instruments and frequencies, giving a spectral index of $\alpha = -1$, consistent with simulation predictions by [Vazza et al. \(2015\)](#). The result is surprising, given that it suggests magnetic field strengths of at least 30–60 nG, which exceed previous upper limits set by Faraday rotation measurements. This apparently robust result warrants considerable attention, and in this thesis we dedicate both [Chapter 5](#) and [Chapter 6](#) to empirical and simulated replications of its result.

1.3 Continuing the search

1.3.1 An opportune moment

This work seeks to continue on from these earlier detection attempts, and it does so at an opportune moment. As I discuss next, widefield, low-frequency radio telescopes are necessary for deep and expansive searches across a part of the radio spectrum well suited for detecting the synchrotron cosmic web. In particular, the Murchison Widefield Array (MWA, see [subsection 1.3.2](#)) had just finished its reconfiguration to Phase II at the outset of this PhD. In addition, this PhD also began just as new, high-resolution synchrotron cosmic web simulations were being finalised in preparation for [Vazza et al. \(2019\)](#).

This project thus seized upon these developments with dual aims: to develop radio sky models of the cosmic web and verify tests for its detection; and then apply these tests to real-world observational data. When researching at the frontiers of science, however, the best laid plans will always be subject to change. In the course of this PhD, two significant concurrent developments occurred: one was the announcement of the potential direct detection by [Vacca et al. \(2018\)](#), and then, most recently, the stacking result published by [Vernstrom et al. \(2021\)](#). As a result, whilst we have adhered loosely to these original dual aims, our research path has remained flexible

and has adapted to these developments, as can be seen in the production of papers.

1.3.2 Murchison Widefield Array

In most of our observational work in this thesis, the MWA is our preferred radio telescope, and the reasons for this come down to the nature of the synchrotron cosmic web itself.

The MWA is a low-frequency radio interferometer located in the Murchison Shire, in Western Australia. It consists of a number of tiles distributed across the desert floor, each consisting of 4×4 dipole antennae, that are electronically pointed by introducing delays across the tile. The practical observing frequencies for the instrument are from 72–231 MHz, and it has a large frequency-dependent field of view that is approximately 30° – 50° in diameter. The original MWA, assigned the retronym ‘Phase I’ ([Tingay et al., 2013](#)), was a fairly compact array, having 128 tiles distributed out to a maximum baseline length of just under 3 km and with a dense core of sub-100 m baselines. In 2017, the MWA was upgraded to its current ‘Phase II’ operation ([Wayth et al., 2018](#)), which increased the number of tiles to 256 but, due to hardware limitations, only 128 of these could be correlated at any one time.² The Phase II instrument would cycle between two 128-tile configurations from semester to semester, known as the ‘extended’ and ‘compact’ configurations. The ‘extended’ configuration had a maximum baseline of 5.4 km whilst also significantly smoothing out the intermediate baseline coverage compared to the Phase I instrument. Meanwhile, the ‘compact’ configuration had a significantly reduced maximum baseline and made use of tiles arranged in a ‘hex’ configuration with numerous redundant baselines. The compact configuration is poorly suited for continuum imaging and herein we use Phase II as synonymous with its extended configuration. Both Phase I and II were limited to 128 tiles, and so both had identical point-

2. More recent work, which postdates the observations used in this PhD, has upgraded the correlator (see Morrison, et al., submitted) and is soon to increase the number of receivers so as to relax this limitation.

source sensitivity. Instead, their unique characteristics owed principally to their differing uv coverage. The Phase I instrument was ideally suited to observing and detecting emission of large angular extent, thanks to its concentration of short baselines. However, it had a low resolution on the order of multiple arcminutes and its irregular baseline coverage meant its dirty beam suffered from significant sidelobe structures, which in turn made deconvolution more difficult. Phase II nearly doubled the resolution of the array whilst also producing a dirty beam with better behaved sidelobes, sacrificing in the process some of its sensitivity to large-scale emission. In the course of this PhD, we have used both configurations and their respective strengths.

The MWA is well suited to detect the synchrotron cosmic web for a number of reasons. We have already noted that the synchrotron cosmic web is expected to have a relatively steep spectral index of $\alpha \lesssim -1$. This is steeper than the active galactic nuclei and star-forming galaxy populations, whose mean spectral index is about $\alpha \approx -0.8$ (e.g. [Mauch et al., 2003](#); [Lane et al., 2014](#); [Hurley-Walker et al., 2017](#)). This means that at lower radio frequencies, ~ 100 MHz, we expect the synchrotron cosmic web to be more luminous, as a fraction of other radio sources, than at higher \sim GHz frequencies. The MWA, with its 72–231 MHz frequency range, is thus well suited. Secondly, the low resolution of the MWA and its numerous short baselines, especially in Phase I, make it sensitive to large-scale, extended emission. This is a requirement for observing the assumed large-scale, extended emission of the synchrotron cosmic web itself, although this is an assumption that shall be considerably revised in the course of this PhD. Finally, the large field of view of the MWA is crucial to this work. Statistical detection techniques such as the radial cross-correlation technique or stacking require large areas of the sky to be observed, spanning hundreds of square degrees. This requirement can only practically be met using an instrument with an especially wide field of view.

Thus, the MWA has been the primary instrument used in the observational work of this thesis, and additionally, its observing characteristics have been a key consideration when producing radio sky models.

1.3.3 An outline of this thesis

This PhD is a thesis by publication, meaning the science output of this work is produced as a series of published, peer-reviewed papers. I have chosen to structure the thesis as a series of paper summaries that give background context, a high level description of the method and any key findings. The emphasis in these summaries has been to establish the papers as part of a overarching research narrative, which they might otherwise lack as disparate papers. The papers themselves are reproduced with permission in [Appendix B](#).

The paper summaries are arranged chronologically, beginning firstly with follow-up observations in [Chapter 2](#) of the field observed by [Vacca et al. \(2018\)](#) and our attempt to corroborate their 28 candidate synchrotron cosmic web sources. [Chapter 3](#) represents a false lead of our own: the so-called Ultra Steep Spectrum Jellyfish is an astonishing radio source that sheds light on the complexity of plasma physics and long-dormant electron fossil electron populations, but ultimately was not connected to the cosmic web. [Chapter 4](#) presents the Filaments and GALactic RadiO (FIGARO) simulation, the first radio sky simulation incorporating traditional radio sources such as active galactic nuclei and star-forming galaxies, as well as the cosmic web itself. [Chapter 5](#) attempts to reproduce the surprising result of [Vernstrom et al. \(2021\)](#) with independent observations and processing pipelines. This thesis culminates in [Chapter 6](#) where we apply the stacking methodology of [Vernstrom et al. \(2021\)](#) to FIGARO so as to understand the results of such a technique as predicted by our current best models. I conclude by summarising my work to date, and comment on the outlook for the ongoing search for the synchrotron cosmic web.

The work is presented in the order that it was finally published. However, I would note that work on FIGARO began from the outset and ran concurrently alongside the first two papers. And the final two chapters were undertaken in the opposite order, since it was only after initially testing the stacking results with FIGARO—and getting such very different results—that

I then deployed much of this stacking and modelling code towards stacking the empirical observations.

Chapter 2

Following up on direct detection candidates

This chapter summarises the paper *Low(er) frequency follow-up of 28 candidate, large-scale synchrotron sources* (Hodgson et al., 2020). The full paper is republished with permission in [Appendix B.1](#).

2.1 Background

Immediately upon undertaking this research, [Vacca et al. \(2018\)](#) published a report claiming the detection of synchrotron emission associated with the cosmic web. In this chapter, I document our own attempt to follow up on these claims with independent observations in an effort not only to corroborate their results but to also further understand the nature of these candidates.

[Vacca et al. \(2018\)](#) made observations at 1400 MHz with the Sardinia Radio Telescope (SRT; [Prandoni et al., 2017](#)) of an $8^\circ \times 8^\circ$ field known to host a number of massive galaxy clusters. The synchrotron cosmic web was expected to be diffuse and large in angular extent, and the low-resolution, single-dish SRT was believed to be ideal in detecting such emission which might otherwise be resolved out by interferometers. The SRT observations were combined with higher-resolution archival NRAO VLA Sky Survey (NVSS; [Condon et al., 1998](#)) data, and these observations were combined using a weighted sum in Fourier space ('feathered') so as to produce a single combined map of the field at the NVSS resolution of $45''$. Bright, compact

radio sources were subtracted out, and the map was then convolved to a lower resolution of $3.5'$ so as to emphasise the expected extended emission of the synchrotron cosmic web.

What remained in this map were 35 regions of emission, weakly detected at 3σ to as high as 6σ above the noise. The authors suggested that these broad islands of emission represented a new population of faint, diffuse synchrotron sources and that their association with an overdense region of the Universe likely meant that they were emission associated with the cosmic web itself.

2.2 Method

We chose to re-observe this field at lower frequencies than the SRT, as this would not only help us establish spectral information about these candidate sources but also take advantage of the expected brighter emission of the synchrotron cosmic web at these frequencies, as explained in [Chapter 1](#).

We used the Murchison Widefield Array (MWA) in both its Phase I ([Tingay et al., 2013](#)) and Phase II ([Wayth et al., 2018](#)) configurations, observing at 154 MHz. The Phase I instrument, in particular, had a high density of short baselines that were ideal for detecting extended sources. We also made use of the Australian Square Kilometre Array Pathfinder (ASKAP; [Hotan et al., 2014](#)), then under commissioning, observing at 887 MHz.

For this work, I developed calibration, imaging, and mosaicing pipelines for both the MWA and ASKAP observations that would form the basis for future imaging work in this thesis. As ASKAP was still in commissioning with few external tools available, this process also involved special work to accommodate the 36 phased array feed (PAF) pointings and their unique primary beams, and to combine these into a single mosaic.

I performed bright source subtraction on the MWA Phase II data as well as the ASKAP data using a simple modification of the CLEAN procedure, and in particular, the ‘auto-mask’ functionality of `wsclean`. I was able to remove all sources with a peak brightness greater than 8σ of the local map noise,

then perform a multi-scale clean on the faint, sub- 8σ sources, before finally convolving the map to $3.5'$ so as to match the resolution of the combined SRT and NVSS image. This technique proved to be both robust and effective at emphasising extended emission without pollution from embedded bright, compact sources.

2.3 Key results

Of the 35 regions identified in [Vacca et al. \(2018\)](#), we were able to make the following classifications: known radio halos (2 sources); radio galaxy (1 source); Galactic HII emission (7 sources); blended compact sources (3 sources); non-synchrotron but otherwise unknown source (1 source). For the remaining majority of sources, we were not able to make any kind of corroborating detection. None of the candidate sources were confirmed as being associated with the synchrotron cosmic web.

There is a well-founded concern that our use of interferometers, compared to the single-dish SRT, may resolve out emission regions with large angular extent. In the past, understanding an interferometer's angular sensitivity has been addressed by reference to the shortest baseline in an array and the corresponding angular size of its fringe pattern on the sky. However, this technique does not take into account the combined effect of all baselines in an array, the effect of baseline weighting schemes, data flagging, and so on, which may result in resolving out sources earlier than the shortest baseline would suggest. In this paper, I developed an alternative technique for measuring sensitivity to extended sources by way of directly simulating extended sources into the visibility data and imaging with identical weighting parameters. These results showed that the MWA Phase II started to become less sensitive to emission on scales greater than $3'$ in extent. However, assuming a spectral index of $\alpha < -0.7$, I was able to show that MWA Phase I, as well as the convolved Phase II and ASKAP images, were more sensitive than the SRT for angular scales up to $30'$. This angular scale was far larger than any of the regions detected by [Vacca et al. \(2018\)](#) and so our non-detection

for many of the 35 candidate sources was not caused by insufficient angular sensitivity.

We concluded in this paper that the uncorroborated sources were spurious. Many of these sources were only weakly detected, at around 3σ , and could be wholly attributed to noise. Moreover, the feathering and point source subtraction technique used were evidently imperfect, as the combined map contained a number of imaging artifacts or points where sources had been over-subtracted.

Chapter 3

The USS Jellyfish

This chapter summarises the paper *Ultra-steep-spectrum radio “jellyfish” uncovered in A2877* (Hodgson et al., 2021b). The full paper is republished with permission in [Appendix B.2](#).

3.1 Background

The Ultra-Steep-Spectrum (USS) Jellyfish was first detected whilst searching images from the Galactic and Extra-Galactic All-Sky MWA (GLEAM; [Wayth et al., 2015](#); [Hurley-Walker et al., 2017](#)) survey for sources with steep spectral indices. This source had a steep spectral index that was an extreme outlier and manual inspection showed it to be an extended source, unconnected to any particular galactic emission, to the north-west of cluster Abell 2877. This steepness suggested this source was not typical synchrotron emission of the kind formed by radio galaxies, and moreover there was no indication that Abell 2877 was undergoing a merger event that might suggest it was a radio relic.

Its position towards the periphery of Abell 2877 raised the possibility that this emission was driven by weak accretion shocks from large scale structure formation processes, however the images from GLEAM made further analysis difficult. In this chapter, I made a number of additional observations in radio as well as X-ray to attempt to understand the origin of the emission.

3.2 Method

We re-observed the USS Jellyfish using two instruments spanning low to mid radio frequencies.

The first of these was the MWA Phase II instrument. The GLEAM survey—in which we originally detected the USS Jellyfish—was produced using observations made with the MWA Phase I, whilst the MWA Phase II instrument reconfigured the array to include longer baselines with smoother coverage in uv space. These changes meant the Phase II observations would achieve higher resolution and could be deconvolved more deeply to achieve better noise characteristics of the final maps. We used archival Phase II observations across five bands from 72–231 MHz, each observed for a duration of 2.4 hours.

The second instrument was the Australia Telescope Compact Array (ATCA; [Frater et al., 1992](#)), spanning 1325–3123 MHz, which observed for a duration of 14 hours.

The image processing for the MWA was novel and only briefly touched upon in this chapter. Traditional MWA imaging workflows image short, two-minute ‘snapshots’ independently, a requirement necessitated by the rapidly changing primary beam, and then mosaic these cleaned and restored snapshots to achieve the full integration. This mosaicing requires reprojecting each restored snapshot to a common projection, as well as convolving the images to a common resolution, a process that always reduces the resolution. The workflow used here was quite different:

1. All snapshots were imaged using a common projection from the outset and cleaned to a common flux limit.
2. Dirty residual images, CLEAN component maps, and point spread function (PSF) maps were independently stacked; the individual restored images for each snapshot were discarded.

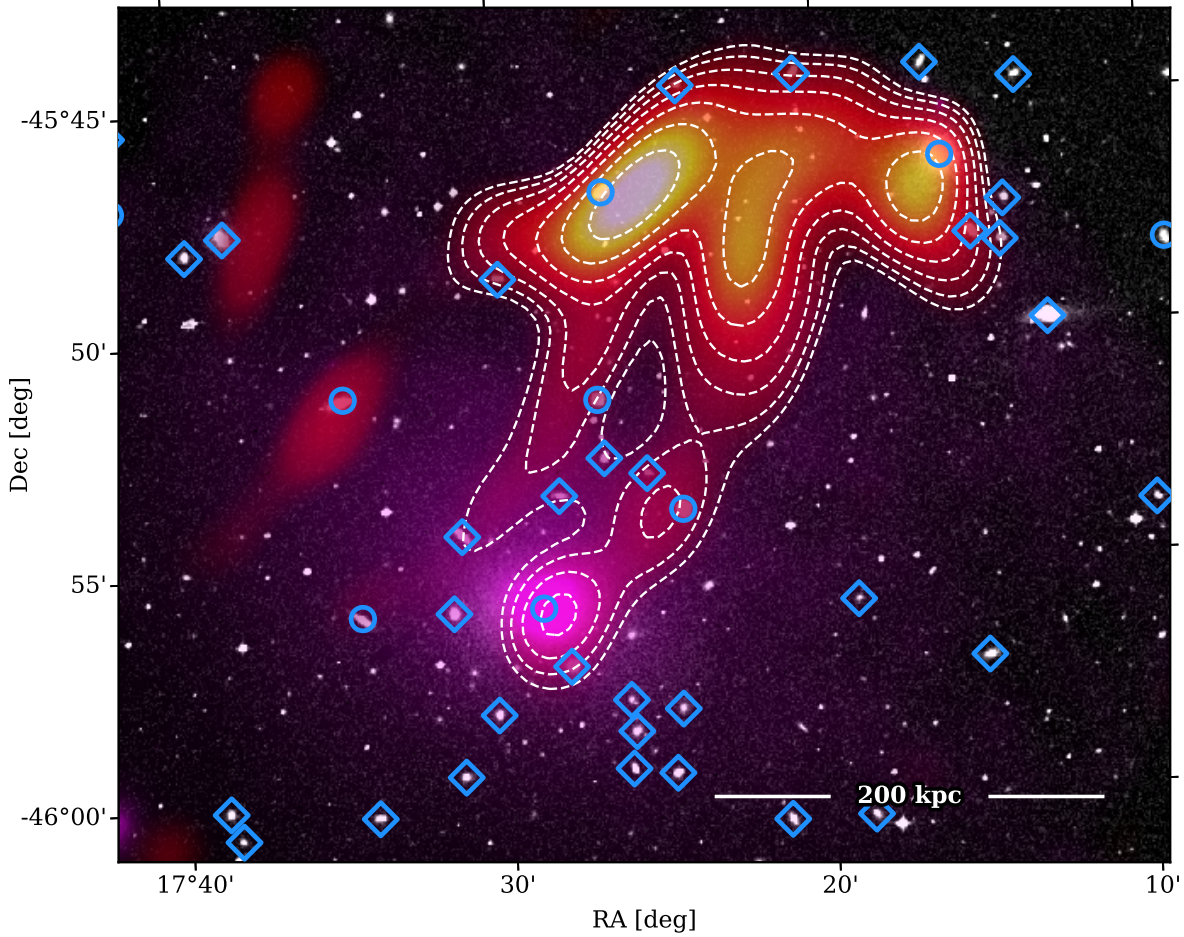


Figure 3.1 Composite image of the USS Jellyfish in Abell 2877 showing the optical Digitized Sky Survey (background) with XMM X-ray data (magenta overlay) and MWA 118.5 MHz radio data (red-yellow overlay). Contours are provided for the MWA overlay ranging from $7.3 \text{ mJy beam}^{-1}$ and increasing by factors of $\sqrt{2}$, but for clarity, are restricted only to the USS Jellyfish proper. Blue circles indicate cluster radio sources from [Hopkins et al. \(2000\)](#), and blue diamonds indicate positions of other probable cluster members based on redshift proximity.

3. A final, additional CLEAN cycle was completed on the stacked residual map using the stacked PSF, allowing for significantly deeper deconvolution.
4. The stacked CLEAN components were convolved with a Gaussian kernel that had been fitted to the stacked PSF, and finally combined with the stacked residuals to produce the restored mosaic of the field.

There were a number of benefits to this workflow. First, we avoided flux errors that, in practice, arise from the reprojection of snapshot maps by using a common projection from the outset. Second, by using the stacked PSF, we accurately fitted the true dirty beam used in the full integration rather than having to convolve the maps to a lower resolution. Third, we performed a kind of final, joint deconvolution step that allowed for deconvolution of faint sources that only become visible with integrations longer than 2 minutes. The result of this process was that we produced images that were deeper, less noisy, more flux correct, and at a higher resolution than if we had followed the traditional MWA workflow. In fact, even at just 2.4 hours integration, the images produced here remain the deepest MWA images published to date.

In addition to the radio data, we also made use of X-ray data from archival XMM-*Newton* observations specifically to search for evidence of cluster-scale shocks that might be responsible for the USS Jellyfish.

3.3 Key results

The MWA Phase II observations showed the USS Jellyfish to have an even steeper spectrum than initially indicated in GLEAM. Across the five bands, the integrated flux decreased rapidly from 1.10(6) Jy at 87.5 MHz to 0.003(7) Jy, consistent with zero, at 215.5 MHz, and a mean spectral index across the three central bands of $\alpha = -5.97^{+0.40}_{-0.48}$. The integrated flux also displayed strong spectral curvature over this range.

The ATCA observations showed no evidence of the diffuse, extended emission of the USS Jellyfish; instead, these observations were useful in

identifying compact emission sources in Abell 2877. Similarly, no diffuse emission was detected from the Rapid ASKAP Continuum Survey (RACS; [McConnell et al., 2020](#)) at 887 MHz.

The XMM data found no evidence of strong shocks in the northwest of Abell 2877, although its poor sensitivity in this region leaves the possibility of a weak shock being present. These data did, however, show that Abell 2877 strongly resembled a cool-core cluster, and confirmed our initial hypothesis that this was a relaxed system that did not have a history of dynamic, cluster-scale shocks.

In [Figure 3.1](#) we show a composite image of the USS Jellyfish, combining MWA Phase II data at 118.5 MHz, the XMM X-ray data, and background optical data from the Digitized Sky Survey.

The final hypothesis for the USS Jellyfish was that of a ‘polyphoenix’: the gentle re-acceleration of multiple, entangled radio galaxy remnants. In this case, these remnants had likely mixed together over a Gyr timescale and were only recently reaccelerated by one or more weak (Mach number $\mathcal{M} < 2$) cluster-scale shocks, whose cause remains unknown. The USS Jellyfish sheds light on the possibilities for plasma acceleration in cluster environments, the role of very ancient fossil electrons, and the poorly understood electron acceleration efficiency. Whilst ultimately the USS Jellyfish was not connected to the synchrotron cosmic web, it shed light on complex shocked acceleration processes that are possible both in cluster environments as well as the more sparse WHIM.

Chapter 4

The FIGARO simulation

This chapter summarises the paper *FIGARO simulation: Filaments and GALactic RadiO Simulation* (Hodgson et al., 2021a). The full paper is republished with permission in [Appendix B.3](#).

4.1 Background

In the introduction, I noted the difficulty encountered in some previous detection attempts. Without accurate models of the synchrotron cosmic web, previous searches such as [Brown et al. \(2017\)](#) and [Vacca et al. \(2018\)](#) were optimised under the assumption that its emission would appear as extended and smoothly varying on large angular scales. These searches thus made use of low resolution instruments that were sensitive to these large angular scales. In the case of [Vernstrom et al. \(2017\)](#), their positive cross-correlation result could not be understood without models that could predict the role of confounding signals from clustering radio or star-forming galaxies.

These factors pointed towards the need to develop an accurate map of the radio sky on which we could test detection techniques. By happy chance, two independent research groups released the ingredients needed for such a radio model. The first of these was by [Vazza et al. \(2019\)](#) who produced a full MHD simulation spanning a 100^3 Mpc^3 volume and evolved from an initial redshift of $z = 45$ until the current epoch. This simulation included a number of observables but, for our purposes, the evolution of mass distribution and, of course, the synchrotron cosmic web emission itself were key. Secondly, [Bonaldi et al. \(2019\)](#) released their Tiered Radio Extragalactic Continuum

Simulation (T-RECS). This simulation allowed the construction of catalogues of active galactic nuclei (AGNs) and star-forming galaxies (SFGs)—the two primary radio populations at low to mid radio frequencies (e.g. 100 MHz to 3 GHz)—and their various subtypes across a range of redshift depths and an arbitrary field of view. The resulting catalogue closely matched empirical models of these sources, such as their respective luminosity functions, as well as factoring in redshift dependence. Crucially, T-RECS had the option to run in a ‘clustering’ mode, where we could feed in the location of dark matter (DM) halos and allow the model to preferentially position its catalogue of radio sources to align with these overdense regions representing the location of galaxies.

This chapter details the construction of the Filaments and GALactic Radio (FIGARO) simulation based on these two foundational simulations, as well as early work exploring the validity and robustness of some detection techniques when applied to it.

4.2 Method

The process to construct FIGARO was twofold. In the first instance, we constructed a light cone with a field of view of $4^\circ \times 4^\circ$ out to a redshift of $z = 0.8$ for each of the MHD simulation observables, including the cosmic web emission and the DM density. This was done by simply stacking the volume in redshift space, selecting the nearest simulation snapshot by redshift, and appending to the light cone in increments of 100 Mpc. For variation, on each iteration the volume was randomly rotated and laterally offset, and this allowed us to construct 10 unique light cones, so-called ‘realisations’, that helped give us some idea of the cosmological variance we would expect, especially at low redshifts. This difference could be significant depending on whether, by chance, the nearest stacked volumes placed a massive galaxy cluster in the foreground or, alternatively, a largely empty void.

Secondly, having constructed this light cone, we then used T-RECS to populate the light cone with AGN and SFG populations. Some minor

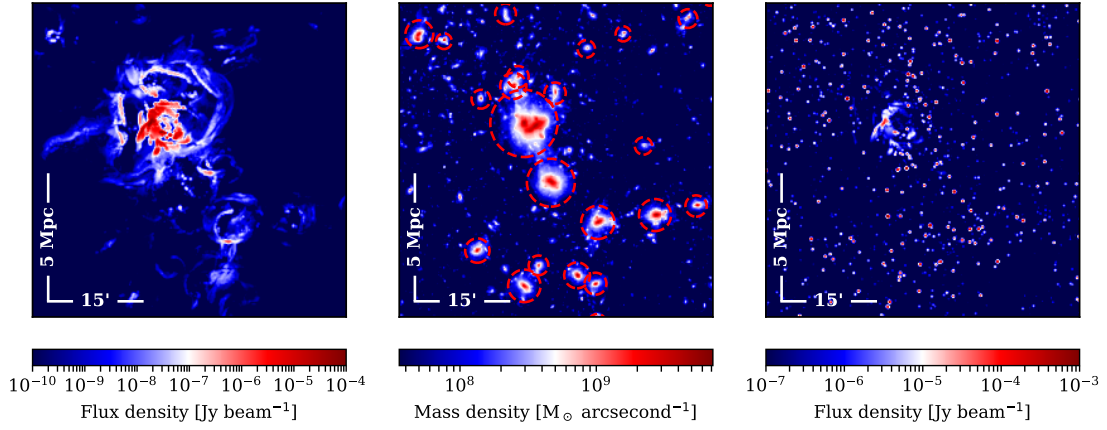


Figure 4.1 A $50' \times 50'$ field of view showing redshift range $0.15 \leq z < 0.2$ extracted from realization 3. This redshift range has a comoving depth of 203 Mpc, and so this extraction incorporates the full simulation volume stacked twice in the radial direction. The 5 Mpc scale has been calculated at the mean redshift $z = 0.175$. *Left:* The synchrotron cosmic web emission at 900 MHz with resolution $20''$. *Middle:* The associated mass distribution, with halos of mass $M > 10^{12.5} M_{\odot}$ indicated by dashed red circles of radii r_{200} . *Right:* The combined cosmic web emission and T-RECS radio population for this redshift range at 900 MHz with resolution $20''$. The T-RECS radio population are modelled as simple point sources.

modifications to the T-RECS codebase allowed us to use our own DM halo catalogue rather than the one T-RECS had been constructed to use. We constructed a simple DM halo finder to extract the location, mass and radii of DM halos in the original MHD simulation, set this as input to T-RECS and thus constructed a full extragalactic radio catalogue for each unique realisation. As an example, [Figure 4.1](#) shows how these different parts come together in the final FIGARO simulation.

Much of this chapter is concerned with testing and verifying our simulation. For example, we compared our DM halo catalogue with those of other simulations and models to ensure correctness, specifically agreement of halo mass functions and two-point correlation functions. We identified radio relic emission from within the simulation and ensured agreement with the current empirical luminosity function for this population. And we checked for agreement of the angular two-point correlation function of the clustered T-RECS radio sources against empirical measurements of this function.

The results of FIGARO are subject to the same limitations of the underlying simulations on which it is built. We note two especially important limitations of the MHD simulation: first, that only diffusive shock acceleration processes are considered in modelling the synchrotron cosmic web, although alternative acceleration mechanisms such as Fermi II processes are not believed to be especially important in low-density environments outside cluster interiors; and second, that these DSA populations were modelled as always acting upon an electron population that was at thermal equilibrium. This latter aspect ignores the role of previous epochs of acceleration activity and of the role of AGN acceleration, both of which would increase the luminosity of DSA processes. The paper notes a number of techniques that we implemented to mitigate this possible under-estimation of the radio power of the synchrotron cosmic web.

4.3 Key results

The distribution of the cosmic web emission differed considerably from what had been earlier assumed. Rather than smoothly tracing out the large scale structure, the emission was primarily localised around the periphery of DM halos and was often morphologically akin to radio relics. That is, the emission tended to trace out long, curved arcs that were situated in spherical shells around DM halos in the region $0.75 \cdot r_{200} < r < 1.5 \cdot r_{200}$, where r_{200} is the virial radius of the respective DM halo. As opposed to radio relics, however, these emission sources were driven by largely stationary accretion shocks occurring at the virial boundary. Moreover, the most massive clusters hosted a majority of the power: the 12 most massive clusters in the simulation hosted 90% of the total power output. Beyond the DM halo periphery, the filaments themselves hosted only very weak emission, orders of magnitude fainter and, for practical purposes, undetectable.

The angular size of the emission also differed from earlier expectations: the shocks were irregular and ‘knotty’, and these brightest of knots were not especially extended. The characteristic angular scale of the emission varied by redshift, ranging from a mean of $105''$ in the redshift slice $0 < z < 0.05$ to $22''$ in the region $0.2 < z < 0.3$.

We performed a radial cross-correlation of the known mass density map with the final FIGARO simulation and found a positive signal at $\theta = 0^\circ$ offset, as also found in [Vernstrom et al. \(2017\)](#). Whilst this positive correlation was in part the result of AGN and SFG populations also similarly clustering, a significant component of this signal was a result of synchrotron cosmic web emission alone, accounting for up to half of the signal at the lowest redshifts. Additional cluster sources such as radio halos, relics, and phoenixes—not modelled here—would reduce this signal. Importantly, we also showed that the cosmic web emission did not cluster in the same way as the AGN and SFG populations and thus was separable with more accurate correlation kernels.

The FIGARO simulation was made publicly available for future work in developing detection techniques.¹

1. FIGARO is available at <http://dx.doi.org/10.26185/6141609552cdd>.

Detecting the synchrotron cosmic web twice?

This chapter summarises the paper *Searching for the synchrotron cosmic web again: A replication attempt* (Hodgson et al., 2022a). The full paper is republished with permission in [Appendix B.4](#).

5.1 Background

At the beginning of 2021, it came as a surprise that [Vernstrom et al. \(2021\)](#), herein V2021, reported detection of the synchrotron cosmic web—specifically, the filaments themselves—by a stacking technique. This forced us to change course on earlier plans for my PhD, resulting in both the current chapter and the next attempting to replicate and simulate their results.

The method used in V2021 began by finding pairs of close-proximity (< 15 Mpc) luminous red galaxies (LRGs). LRGs are a class of galaxy, typically very old, whose locations are known to be strongly correlated with cluster centres. Thus, LRGs can act as a proxy for galaxy clusters, of which we otherwise know only a few thousand from X-ray observations. Next, the method made an important assumption: some proportion of close-proximity pairs of LRGs are connected by a filament. Their method proceeded by taking these LRG pairs, identifying them in extant radio surveys, and ‘stacking’ them. This stacking process involved rotating and rescaling the radio image of the LRG pair such that the positions of each LRG in the pair aligned with all the other pairs, and then finding a combined mean image. In doing this

hundreds of thousands of times, this technique aimed to reduce the noise present in the original radio survey images and allow the detection of any faint radio emission that might span, on average, the LRG pairs.

V2021 used radio data from the GLEAM survey in three frequency bands spanning 72–170 MHz, as well as observations made by the Owens Valley Radio Observatory Long Wavelength Array (OVRO-LWA; [Eastwood et al., 2018](#)) at 73 MHz. Using a catalogue of LRGs from [Lopes \(2007\)](#), V2021 found 390,808 pairs that met the dual constraints that their spatial separation was no more than 15 Mpc and their angular separation was in the range $20' < \theta < 180'$.

Upon stacking these pairs, the mean images contained bright peaks of emission at each of the stacked LRG locations, located on a normalised grid at $x = \{-1, 1\}$ and $y = 0$. These peaks of emission were from LRG emission as well as any correlated cluster emission. The novelty of their method was in the next step: assuming that LRG and cluster emission should be radially symmetric, with the exception of the intracluster bridge, they modelled each peak by constructing a profile that was the radial average of its exterior, 180° sweep. This model profile could then be subtracted from the image, and any asymmetry about the LRG peaks or excess interior intracluster emission would then be visible.

Upon subtraction of this model, V2021 found evidence of significant excess intracluster emission. This emission was broad and extended, peaking at the LRG pair midpoint and extending out in all directions. Their own calculations suggested that this emission was indicative of intracluster magnetic fields in the range $30 \text{ nG} < B < 60 \text{ nG}$. In addition, V2021 also stacked X-ray data from the ROSAT All-Sky Survey ([Voges et al., 1999](#)), similarly finding excess X-ray emission in the intracluster region.

Whilst the excess X-ray signal was approximately in line with simulations, the excess radio emission was surprising for a number of reasons. The magnetic field strength estimates are about an order of magnitude greater than previous upper limits obtained using Faraday rotation measurements. Moreover, their magnetic field estimate is strictly a *lower* limit since: not all

LRG sources map to cluster centres; in turn, not all close-proximity LRG pairs are linked by a filament; and more so, not all filaments link directly in a straight line. Finally, the transverse width (i.e. in the direction perpendicular to the line linking the LRG pair) is much wider than expected, suggesting either that the filaments are wider than simulations suggest or that a significant fraction trace an indirect path between clusters.

The importance of this result led us to attempt to replicate their results, which we document in this chapter.

5.2 Method

Whilst V2021 used archival MWA Phase I and OVRO-LWA observations, we chose here to use more recent MWA Phase II observations observed at 118.5 MHz. These observations had been scheduled as part of the upcoming GLEAM-X survey ([Hurley-Walker et al., 2022](#)) and spanned much of the region of sky containing the LRG pairs, which we arranged into 14 fields centred at declinations $\delta = \{3^\circ, 20^\circ\}$ and in 20° increments of right ascension spanning $120^\circ < \alpha < 240^\circ$. In total, there were 512 observations available, of which 291 were used in the final mosaicing after quality control checks. This chapter spends some time documenting the calibration, imaging, ionospheric corrections, mosaicing and verification of these fields.

The final fields were convolved to a common resolution of $3'$ (measured at zenith), approximating the resolution of the GLEAM observations. However, these fields had noise levels that were a factor of 9 times lower, on average, owing to advancements in calibration and imaging since the GLEAM survey was made, combined with much deeper deconvolution limits allowed for by the Phase II instrument.

To mitigate the effects of bright radio sources, V2021 used a wavelet decomposition technique that identified compact sources and removed these sources down to approximately 5σ of the map noise. In our case, however, this process was significantly simpler: we kept the residual images after cleaning and used these in our stacking instead.

Identically to V2021, we set to construct an LRG-pair catalogue to be used in stacking, also drawn from [Lopes \(2007\)](#). We constructed three catalogues based on varying selection criteria as well as the original catalogue used by V2021. We also wrote our own independent stacking and modelling code, which we verified using synthetic maps with faint, embedded ‘filament’ signals.

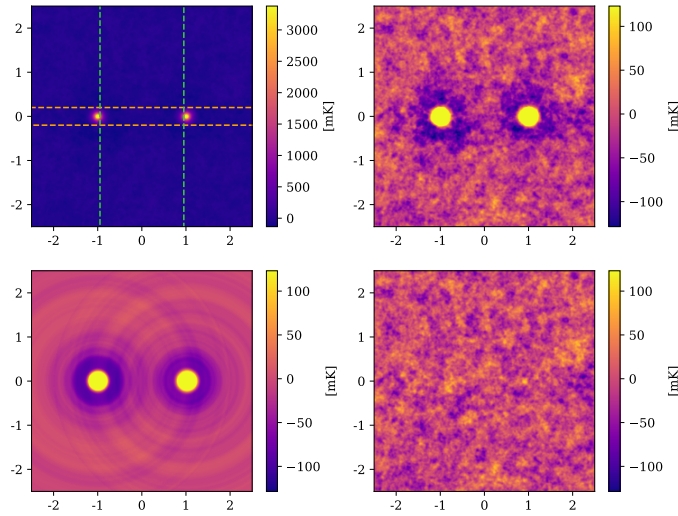
We proceeded to stack, and the final model-subtracted residual images were searched for excess intracluster signals using simple one-dimensional profiles as well as integrated profiles.

5.3 Key results

The stacked residual images we produced had better noise properties than those stated in V2021, by more than double in the best case. And yet, none of the LRG-pair catalogues produced any statistically significant intracluster signal, and certainly not the kind of broad, extended signal visible in V2021. [Figure 5.1](#) gives one such example using the ‘Max 15 Mpc’ LRG pair catalogue showing the stacked, model and residual images, as well as the various one-dimensional and integrated profiles.

In addition to the missing signal, we also noted that the LRG peaks in the stacked images, prior to model subtraction, were markedly narrower than those shown in V2021. We showed that this was a result of the peak emission being primarily due to unresolved emission. In contrast, some significant fraction of those in V2021 must have been resolved at the MWA Phase I resolution to account for their width.

The issue of sensitivity to large angular scales was again a concern, as it was also in [Chapter 1](#). Using the same technique, we showed that MWA Phase II starts to resolve out structures at 50’, but with the additional convolution step used in our maps, we remained more sensitive than the MWA Phase I instrument for angular scales of up to 150’. Moreover, we constructed a LRG-pair catalogue especially to avoid concerns about resolving



(a) *Top left*: The original mean stack image, with overlays indicating the region over which the transverse mean (dashed orange horizontal lines) and longitudinal mean (dashed green vertical lines) are calculated. *Top right*: The mean stacked image with the colour scale reduced to $\pm 5\sigma$ to emphasise the noise. *Bottom left*: The model image, on the same colour scale. *Bottom right*: The residual stack after model subtraction, with the colour scale set to $\pm 5\sigma$.

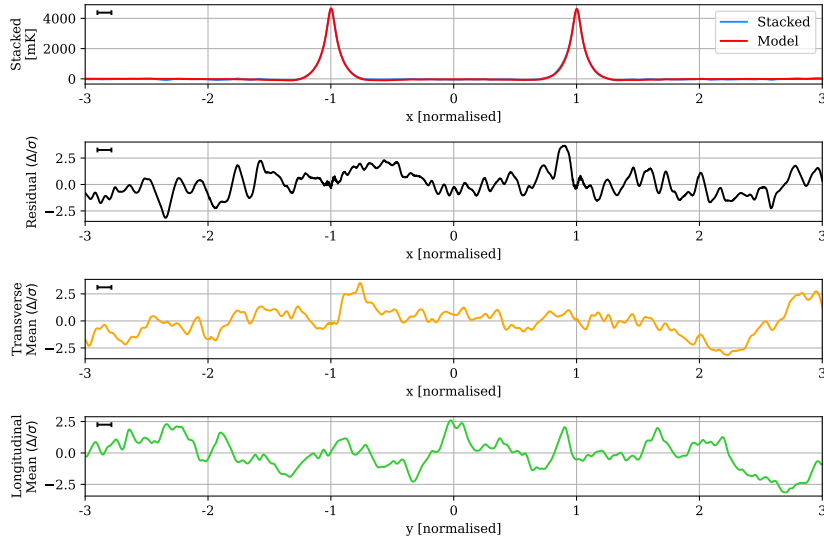
Figure 5.1 The Max 15 Mpc stack, with mean LRG peaks of 4292 mK, residual noise of 25 mK, and effective resolution of 0.11.

out extended emission, with reduced angular constraints of $15' < \theta < 60'$. After stacking, it too showed no evidence of excess intracluster emission.

Given this inability to reproduce the results of V2021 by stacking these MWA Phase II fields, we then turned to stacking both the original GLEAM and the ROSAT maps using our own code. In the case of GLEAM stack, we were again unable to reproduce the excess radio emission; in the case of the ROSAT stack, however, we detected a strong excess intracluster signal at approximately the level detected in V2021.

The reason for this failure to replicate the results of V2021 remains unclear. In the interest of resolving this, as part of this paper we also released the 14 fields, the stacked maps, and the code used in stacking and modelling.¹

1. These data are available at <http://dx.doi.org/10.26185/6295b420b6b91>.



(b) *One:* The one-dimensional profile along $y = 0$ for both the stacked image (blue) and the model (red). *Two:* The one-dimensional profile along $y = 0$ of the residual stack, renormalised to the estimated map noise. *Three:* The transverse mean along the region $-0.2 < y < 0.2$ of the residual stack, renormalised to the estimated map noise. *Four:* The longitudinal mean along the region $-0.95 < x < 0.95$ of the residual stack, renormalised to the estimated map noise. The black rule in the top left shows the full width at half maximum (FWHM) of the effective resolution.

Figure 5.1 (Continued) The Max 15 Mpc stack, with mean LRG peaks of 4292 mK, residual noise of 25 mK, and effective resolution of 0.11.

Simulated stacking with FIGARO

This chapter summarises the paper *Stacking the synchrotron cosmic web with FIGARO* (Hodgson et al., 2022b). The full paper is republished with permission in [Appendix B.5](#).

6.1 Background

One of the key properties of FIGARO, as we noted in [Chapter 4](#), was *where* the bulk of the synchrotron cosmic web emission was located. It was principally located around the periphery of massive clusters, whilst emission along the filaments proper was multiple orders of magnitude fainter. When V2021 published their stacking results, it was therefore surprising to see the excess emission so clearly peaking equidistant to the LRG pairs, apparently associated with the filaments.

Our earlier analysis of FIGARO had focused on the radial cross-correlation detection method rather than stacking, as this had been the leading technique employed to date. In this chapter, however, we returned to FIGARO this time to focus on its predictions for stacking the simulated radio sky.

6.2 Method

As in [Chapter 5](#), we attempted here to stay as close to the methodology of V2021 as possible.

We began first by expanding the field of view of each the 10 FIGARO realisations from $4^\circ \times 4^\circ$ to $15^\circ \times 15^\circ$. This step was necessary to provide us with enough stacks to push down the noise to comparable levels as in

V2021. AGN and SFG populations were modelled as simple point sources and the fields were convolved with the MWA Phase I beam at an observing frequency of 150 MHz. No noise was added and no calibration artefacts introduced; from an observational standpoint, this was an ideal case. As in [Chapter 5](#), point sources were subtracted by a simple cleaning procedure, down to 10 mJy beam^{-1} , to produce residual images that were ultimately used during stacking.

Next, we needed to form a catalogue of LRG pairs. Whilst FIGARO did not have LRGs as part of its catalogue, we did instead have complete knowledge of the location of massive galaxy clusters by way of the DM halo locations. Thus we found all DM halo pairs that met the original selection criteria ($r < 15 \text{ Mpc}$; $20' < \theta < 180'$) and which were above a mass threshold. Given our complete knowledge of the simulation volume, however, this distribution of DM halo pairs differed markedly from that of V2021 or [Chapter 5](#), in particular at high redshift where the [Lopes \(2007\)](#) catalogue became increasingly incomplete. To rectify this, we then sampled from this DM halo pair catalogue in such a way as to closely reproduce the distribution of redshifts, spatial separations and angular separations as found in the ‘Max 15 Mpc’ catalogue of [Chapter 5](#). In this way, we sampled 7000 pairs from each of the 10 realisations.

Stacking and modelling proceeded identically as in [Chapter 5](#) using the same stacking and modelling code with one exception: that not only did we stack the full FIGARO field, but we also stacked the cosmic web emission by itself, giving us a clear idea of its stacked profile in the absence of the much brighter AGN and SFG populations.

6.3 Key results

Our final stacked image matched the twin peaks as found in V2021. This, of course, was by construction since FIGARO had associated AGN and SFG populations with many of the DM halos used in our stacks. As in [Chapter 5](#), the narrow widths of the peaks indicated that the unresolved AGN and SFG

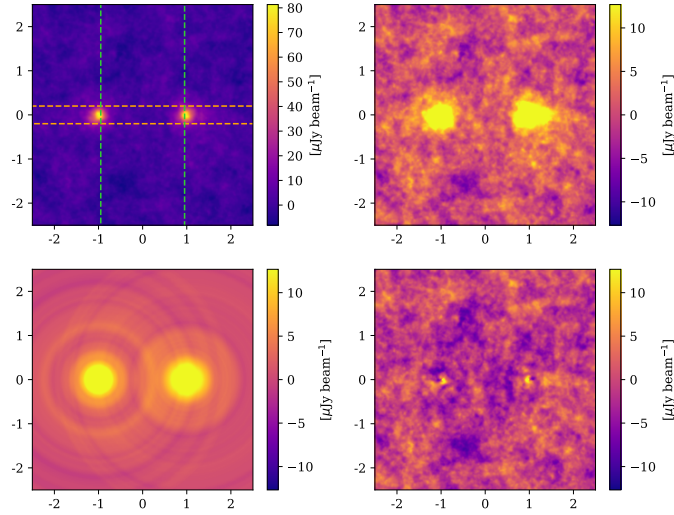
populations dominated any kind of cosmic web emission also present, even after cleaning to 10 mJy beam^{-1} . Crucially, no excess intracluster emission was observed.

If we instead turn to the stacked image of the cosmic web by itself (Figure 6.1), in absence of the dominating AGN and SFG sources, we found similar twin peaks although markedly wider, being a result of the resolved cosmic web emission. This stack had a noise level a factor of 3 lower than the full sky stack, however even here we found no excess emission along the intracluster region.

We did, however, find excess emission on the immediate interiors of the peaks. In fact, the peaks were not symmetric about $x = \{-1, 1\}$ and instead reached their maximum emission slightly inset, at $x \approx \pm 0.95$. We attributed this asymmetry to asymmetric accretion shocks about the clusters. Interior shocks tended to be, on average, more luminous than the exterior shock as a result of the compression of the interior environment, which in turn lead to increased electron density and stronger magnetic fields.

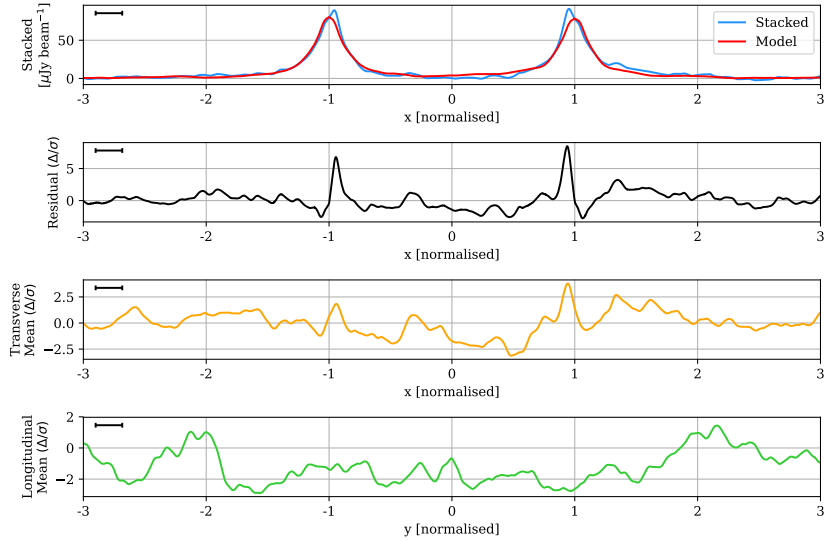
This simulated stacking experiment came with all the limitations of the underlying MHD simulation upon which FIGARO was built. Key amongst these limitations was the absence of AGN feedback and relatedly no modelling of fossil electron populations, both of which might act to boost synchrotron cosmic web emission. Additionally, the MHD simulation was seeded with simple uniform magnetic fields at 0.1 nG , whereas more complex seed magnetic field configurations may have significant effects at later epochs.

Nonetheless, and with these limitations in mind, this stacking experiment suggested a quite different result than that found in V2021.



(a) *Top left:* The original mean stack image, with overlays indicating the region over which the transverse mean (dashed orange horizontal lines) and longitudinal mean (dashed green vertical lines) are calculated. *Top right:* The mean stacked image with the colour scale reduced to $\pm 5\sigma$ to emphasise the noise. *Bottom left:* The model image, on the same colour scale. *Bottom right:* The residual stack after model subtraction, with the colour scale set to $\pm 5\sigma$.

Figure 6.1 The synchrotron cosmic web stack, with estimated noise $2.5 \mu\text{Jy beam}^{-1}$ and effective resolution 0.21. The left peak has a maximum of $89.46 \mu\text{Jy beam}^{-1}$ and a FWHM of 0.27; the right peaks at $91.1 \mu\text{Jy beam}^{-1}$ and has a FWHM of 0.28.



(b) One: The one-dimensional profile along $y = 0$ for both the stacked image (blue) and the model (red). **Two:** The one-dimensional profile along $y = 0$ of the residual stack, renormalised to the estimated map noise. **Three:** The transverse mean along the region $-0.2 < y < 0.2$ of the residual stack, renormalised to the estimated map noise. **Four:** The longitudinal mean along the region $-0.95 < x < 0.95$ of the residual stack, renormalised to the estimated map noise. The black rule in the top left shows the FWHM of the effective resolution.

Figure 6.1 Continued The synchrotron cosmic web stack, with estimated noise $2.5 \mu\text{Jy beam}^{-1}$ and effective resolution 0.21. The left peak has a maximum of $89.46 \mu\text{Jy beam}^{-1}$ and a FWHM of 0.27; the right peaks at $91.1 \mu\text{Jy beam}^{-1}$ and has a FWHM of 0.28.

Conclusion

The synchrotron cosmic web is the predicted radio signature produced as part of the ongoing process of large-scale structure formation of the Universe. Its detection would provide not only a validation of our current best cosmological models as well as an account for the missing baryon population residing in the WHIM but also a unique vantage upon the sparse, intracluster environment, especially its magnetic field configuration and the complex plasma physics that it hosts.

Continuing from earlier work by [Brown et al. \(2017\)](#) and [Vernstrom et al. \(2017\)](#), and concurrent with [Vacca et al. \(2018\)](#) and [Vernstrom et al. \(2021\)](#), the aim of this PhD has been to continue this search and contribute meaningfully to this nascent field.

7.1 Summary

In this search for the synchrotron cosmic web, we have married observational studies with simulation.

Both [Chapter 2](#) and [Chapter 5](#) sought to understand previously published detections of the synchrotron cosmic web. In the first of these, we followed up on a report by [Vacca et al. \(2018\)](#) of numerous, extended synchrotron sources in an area of the sky known to host a number of massive galaxy clusters. These candidate sources were suggested as being the first of a much larger, heretofore undetected population of synchrotron sources associated with the cosmic web. Our own observations with the MWA and ASKAP radio telescopes, however, did not corroborate the detection of the majority of these candidates despite showing we had the sensitivity to do so, and

in the remainder of the cases we showed the emission regions to be due to other, unrelated phenomena.

In [Chapter 5](#) we similarly sought to corroborate and characterise the recent detection by [Vernstrom et al. \(2021\)](#). The authors reported to have detected synchrotron emission associated with cosmic web filaments by stacking close-proximity pairs of LRGs—proxies for connecting filaments—and detecting excess emission present along the stacked bridge. This result, though seemingly robust, was significant and warranted replication, especially since it pointed to higher intracluster magnetic field strengths than previous upper limits. We imaged these fields using the upgraded MWA Phase II, significantly improving upon the noise characteristics of the original study. However, we failed to corroborate their results after stacking both these new observations as well as the original data. To date, the origin of this discrepancy still remains unclear.

Parenthetically, both studies point to the importance of replication work in radio astronomy. Such replication work helps to highlight the numerous, subjective and otherwise arbitrary decisions made during a study, from the seemingly trivial such as the use of radio contours when presenting a final work, to ad hoc choice of priors during error and uncertainty analysis, to technical choices around calibration, imaging and data processing that are rarely discussed in a finished work. But replication also helps catch errors in code and data pipelines that, whilst increasingly important to radio astronomy, are otherwise rarely subject to close examination or to peer review; I uncovered such errors in at least three of the works used heavily in the course of this PhD.

Meanwhile, our own hopeful detection, the USS Jellyfish—an astounding source of radio emission in its own right—proved to be also unrelated to the synchrotron cosmic web. In [Chapter 3](#) we discussed the uniquely steep spectral properties of this source that spanned the north-west of cluster Abell 2877. None of the typical cluster-scale mechanisms were adequate to describe this source, however comparison to similar emission from MHD

simulations led us to hypothesise the ‘polyphoenix’ mechanism coupled with (multiple) weak cluster-scale shocks.

In addition to this observational stream of work, we also undertook a simulation and modelling stream. In developing FIGARO in [Chapter 4](#), our aim was twofold: to understand the distribution and intensity of radio emission associated with the cosmic web, and secondly to provide a basis upon which we could develop and test detection techniques. It became evident that prior expectations of smooth, extended radio emission that broadly traced the underlying mass density of the cosmic web were ill-founded. Instead, we observed radio relic-like shells of emission—forming long, narrow arcs of emission tracing shock fronts—about the periphery of massive galaxy clusters. The intervening filaments, on the other hand, were at least two orders of magnitude less luminous

As this very different picture of the cosmic web emerged, FIGARO also provided a testbed to test detection techniques. FIGARO included not just a light cone of cosmic web emission but, crucially, the embedded population of much brighter AGNs and SFGs. These populations were constructed to cluster realistically with respect to the underlying mass distribution and thus constructed to model the same kind of obscuring, contaminating effects as we encounter in empirical observation. Against this model, we tested the radial cross-correlation technique using a mass-weighted kernel, finding that this method did indeed detect cosmic web emission but that this result was also strongly contaminated by emission from the embedded radio population, accounting for more than half of the signal at the very lowest redshift range and quickly dominating the signal at higher redshifts.

With the release of [Vernstrom et al. \(2021\)](#), it also proved an opportune moment to test their stacking methodology against FIGARO’s simulated radio sky. In [Chapter 6](#) we stacked 70,000 DM halo pairs from ten $15^\circ \times 15^\circ$ FIGARO realisations finding results that were consistent with our empirical replication attempt: similar, narrow-sized peaks where we had stacked the cluster centres, whilst no statistically significant excess emission along the intracluster bridge. After ‘turning off’ the emission from the embed-

ded radio population, we revealed the much fainter stacked signal of the cosmic web alone. Even here we could not discern emission attributable to the filaments. Instead, FIGARO suggested such an exercise would result in asymmetric peaks, shifted slightly interior to the cluster pair, and likely the result of underlying compression of the intracluster environment. Even under the ideal observing conditions of this simulation, the excess filamentary emission—measured to be two orders of magnitude fainter than the cluster peaks—was too faint to reliably detect against foreground and background emission.

7.2 Final remarks

Ultimately, after four years of work, we did not detect the synchrotron cosmic web. But neither did the other work concurrent with our own, at least insofar as our replication work shows.

In starting this work, we focused primarily on low-frequency observations with the MWA. The motivation here was the belief that the steep spectral index of cosmic web emission would be most detectable at these frequencies, whilst the reduced resolution was believed to be an advantage in detecting its extended emission. However, we have shown that slightly higher observations at approximately 800 MHz, such as with ASKAP and newly commissioned MeerKAT, to be similarly effective and that their higher resolution can be an advantage to match the smaller than expected angular extent of the cosmic web. Moreover, certain instrumental characteristics of these arrays—such as their tracking and rotating dishes, as well as their avoidance of the worst of the low-frequency ionospheric effects—make calibration and imaging considerably easier.

Our radio sky models leave open the possibility that a small subset of outlier, cosmic web emission may be detected directly. We noted a small number of luminous knots along otherwise undetectable shock fronts, potentially rising to the level of detection, although prone to being misattributed to other phenomena. Such outlier knots, however, whilst interesting in their own

right, are not especially useful in understanding the magnetic and plasma environments of cluster peripheries or filaments, in general.

Statistical methods such as the radial cross-correlation technique and stacking continue to suffer from numerous difficulties. We have shown that the mass-weighted radial cross-correlation is capable of picking up some of the cosmic web emission around cluster peripheries, however the more luminous AGN and SFG populations pollute and dominate this signal. Moreover, practical attempts at the radial cross-correlation technique only have imperfect knowledge of the underlying mass distribution which further complicates matters. Meanwhile, the stacking technique as implemented in [Vernstrom et al. \(2021\)](#), even under ideal circumstances, requires vastly more close-proximity pairs to robustly detect emission from the filaments proper. Variations on this method such as weighting the stacks by the mass of respective cluster pairs could be more effective and would be worth pursuing in future work as more galaxy clusters (rather than proxy objects such as LRGs) become known.

This is still an active area of research, and both the simulation and detection of the synchrotron cosmic web have much room for improvement. More ambitious MHD simulations, for example, at higher resolution and larger volumes, would be capable of incorporating a more diverse and massive population of clusters, as well as modelling fine-grain processes that might lead to Fermi type II processes. The incorporation of fossil electron populations and AGN ejecta would also surely be an essential ingredient towards more accurate simulations that may yet radically change our current picture of the synchrotron cosmic web. As for the practical task of detection, we look forward to the development of novel detection techniques to take advantage of the latest generation of radio telescopes that might yet hold hope for uncovering the elusive synchrotron cosmic web.

Appendices

Appendix A

Statement of contribution

Low(er) frequency follow-up of 28 candidate, large-scale synchrotron sources (Hodgson et al., 2020) is my own work, with the following exceptions. M. Johnston-Hollitt and B. McKinley provided guidance throughout the study, and discussion and interpretation of results. M. Johnston-Hollitt aided in identifying associated emission in optical data as Galactic H₂ emission. V. Vacca made available the SRT & NVSS images used in their original work. T. Vernstrom requested the 887 MHz ASKAP observation, although data processing and imaging are my own. T. Vernstrom additionally suggested the convolution step used in the production of the ‘ASKAP-subtracted’ image. All co-authors, and especially V. Vacca, provided feedback during the preparation of the manuscript.

Ultra-steep-spectrum radio “jellyfish” uncovered in A2877 (Hodgson et al., 2021b) is my own work, with the following exceptions. M. Johnston-Hollitt suggested searching GLEAM for steep spectrum sources that led to the original discovery. M. Johnston-Hollitt, F. Vazza and B. McKinley provided discussion and interpretation of results. F. Vazza noted the similarity of the USS Jellyfish to magnetohydrodynamic simulation, suggested its inclusion for comparison, and provided detailed analysis of the simulation. D. Wittor contributed work towards passive tracers used in this simulation. I. Bartalucci reduced the XMM-Newton observations and produced the surface brightness profile of the northwest sector of Abell 2877. All co-authors provided feedback during the preparation of the manuscript.

FIGARO simulation: Filaments and GALactic RadiO simulation (Hodgson et al., 2021a) is my own work, with the following exceptions. F. Vazza provided the underlying cosmological simulation data and provided extensive

guidance in their interpretation, as well as providing an understanding of the plasma physics used in their construction. F. Vazza also provided an initial prototype code for the construction of light cones and constant technical support as I wrote the final code. F. Vazza, M. Johnston-Hollitt, and B. McKinley provided guidance throughout the study, discussion of results, and feedback during the preparation of the manuscript.

Searching for the synchrotron cosmic web again: a replication attempt (Hodgson et al., 2022a) is my own work, with the following exceptions. M. Johnston-Hollitt and B. McKinley aided in discussion and interpretation of results. N. Hurley-Walker provided an updated sky model used in the calibration of the MWA Phase II observations. Additionally, N. Hurley-Walker suggested stacking both the ROSAT and original GLEAM data as additional tests, and provided the original data from the latter survey. All co-authors provided feedback during the preparation of the manuscript.

Stacking the synchrotron cosmic web with FIGARO (Hodgson et al., 2022b) is my own work with the following exceptions. M. Johnston-Hollitt, F. Vazza and B. McKinley aided in discussion and interpretation of results, as well as additional feedback during the preparation of the manuscript. Additionally, F. Vazza provided the final paragraph of the Discussion, regarding the limitations in assuming a uniform seed magnetic field.

Appendix B

Published papers

The following papers are reproduced with permission from their respective copyright owners.

B.1 Hodgson et al. (2020)

Low(er) frequency follow-up of 28 candidate, large-scale synchrotron sources

[Hodgson, Johnston-Hollitt, McKinley, Vernstrom & Vacca \(2020\)](#)

© ASA 2020. Reproduced with permission.

Research Paper

Low(er) frequency follow-up of 28 candidate, large-scale synchrotron sources

Torrance Hodgson¹, Melanie Johnston-Hollitt¹, Benjamin McKinley^{1,2}, Tessa Vernstrom³ and Valentina Vacca⁴¹International Centre for Radio Astronomy Research (ICRAR), Curtin University, 1 Turner Ave, Bentley, WA 6102, Australia, ²ARC Centre of Excellence for All Sky Astrophysics in 3 Dimensions (ASTRO3D), Bentley, Australia, ³CSIRO Astronomy and Space Science, PO Box 1130, Bentley WA 6102, Australia and ⁴INAF - Osservatorio Astronomico di Cagliari, Via della Scienza 5, I-09047 Selargius (CA), Italy

Abstract

We follow up on a report by Vacca et al. (2018) of 28 candidate large-scale diffuse synchrotron sources in an $8^\circ \times 8^\circ$ area of the sky (centred at RA $5^{\text{h}}0^{\text{m}}0^{\text{s}}$; Dec $5^\circ 48' 00''$). These sources were originally observed at 1.4 GHz using a combination of the single-dish Sardinia Radio Telescope and archival NRAO VLA Sky Survey data. They are in an area with nine massive galaxy clusters at $z \approx 0.1$ and are candidates for the first detection of filaments of the synchrotron cosmic web. We attempt to verify these candidate sources with lower frequency observations at 154 MHz with the Murchison Widefield Array and at 887 MHz with the Australian Square Kilometre Array Pathfinder (ASKAP). We use a novel technique to calculate the surface brightness sensitivity of these instruments to show that our lower frequency observations, and in particular those by ASKAP, are ideally suited to detect large-scale, extended synchrotron emission. Nonetheless, we are forced to conclude that none of these sources are likely to be synchrotron in origin or associated with the cosmic web.

Keywords: cosmic web – radio continuum emission

(Received 18 June 2020; revised 17 July 2020; accepted 17 July 2020)

1. Introduction

Up to half of the baryons in the present-day Universe are unaccounted for. We know how many baryons were present in the early Universe from fluctuations in the cosmic microwave background (CMB), and some 2 billion years later at redshift 3, the majority of the baryon budget of the Universe could be found in galaxies, proto-clusters and, mostly, in the Lyman- α forest. In the present-day Universe, however, if we take stock of the known baryon populations we come up short, and this has given rise to the ‘missing baryon problem’ (e.g., see Nicastro et al. 2017 for review). Cosmological simulations have long pointed to the likely explanation that these baryons reside in a warm-hot intercluster medium that is distributed in a large-scale filamentary network, the so-called ‘cosmic web’ (e.g., Cen & Ostriker 1999). However, due to its extremely diffuse nature, intermediate temperature range (10^5 – 10^7 K), and highly ionised state, it is very difficult to detect. The low density of this medium and intermediate temperature result in only very weak X-ray emission via thermal free-free radiation; the highly ionised state makes detection via absorption/emission lines difficult; and the low-mass, low-density environment makes detection via the Sunyaev-Zel’dovich effect problematic (with the exception of bridges connecting close pairs of galaxy clusters).

Nonetheless, there have been early attempts to detect the cosmic web by way of some of these mechanisms. For example, Eckert et al. (2015) measured residual X-ray emission as large as 8 Mpc in

scale around galaxy cluster Abell 2744, implying this existence of a large-scale, energetic baryon population. Nicastro et al. (2018) claimed that Oxygen VII absorption features in a distant quasar pointed to the detection of an intervening overdense baryonic region. Tanimura et al. (2019) and de Graaff et al. (2019) have both independently claimed to have made statistical detections of the intercluster medium by way of the Sunyaev-Zel’dovich effect. Most recently, Macquart et al. (2020) have used the dispersion measure of a small number of localised fast radio bursts to measure the electron column density along the line of sight to these events and have measured a value for the baryon count of the Universe that is consistent with those derived from CMB measurements.

Recently, there has been work to understand the radio emission properties of the cosmic web. Infall accretion shocks along the length of filaments and at the edge of clusters should have high Mach numbers ($\mathcal{M} \approx 10$ – 100). These in turn are capable of producing relativistic electrons and—given the presence of background magnetic fields—associated synchrotron emission (e.g., Wilcots 2004). Such emission would provide not only confirmation of the cosmic web but would also provide a probe into intercluster magnetic field strengths, which up till now are largely unknown. Early detection attempts such as Brown et al. (2017) and Vernstrom et al. (2017) have assumed synchrotron cosmic web emission to be spatially smooth and characteristically large in angular scale, in an effort to distinguish it from the more general extra-galactic synchrotron emission produced by radio galaxies. In Vernstrom et al. (2017), for example, low-frequency radio images were cross-correlated with galaxy density maps (as tracers of large-scale structure), with the expectation that the synchrotron cosmic web would appear as excess radio emission with angular scales larger than the embedded radio galaxy population. More

Author for correspondence: Torrance Hodgson, E-mail: torrance@pravic.xyz

Cite this article: Hodgson T, Johnston-Hollitt M, McKinley B, Vernstrom T and Vacca V. (2020) Low(er) frequency follow-up of 28 candidate, large-scale synchrotron sources. *Publications of the Astronomical Society of Australia* 37, e032, 1–18. <https://doi.org/10.1017/pasa.2020.26>

Table 1. List of images used in this work. Resolution and noise values are given for the centre of the field. Resolution values describe the major and minor axes of an elliptical Gaussian fitted to the synthesised beam. The bandwidth of all MWA images is 30.72 MHz and the bandwidth of all ASKAP images is 288.

Image name	Instrument	Duration [hours]	Frequency [MHz]	Briggs' weighting	Resolution [arcsec ²]	Noise [Jy beam ⁻¹]
MWA-1	MWA	2.3	154	0	210 × 210	8.4 × 10 ⁻³
MWA-2	MWA	6.5	154	0	79 × 62	2.3 × 10 ⁻³
MWA-subtracted	MWA	6.5	154	0	210 × 210	5.4 × 10 ⁻³
ASKAP-B+0.5	ASKAP	13	887	0.5	21 × 17	4.3 × 10 ⁻⁵
ASKAP-B-1	ASKAP	13	887	-1	9.6 × 7.6	5.8 × 10 ⁻⁵
ASKAP-subtracted	ASKAP	13	887	0.5	210 × 210	7.5 × 10 ⁻⁴
SRT-NVSS diffuse	SRT & VLA	18 (SRT)	1400	-	210 × 210	3.1 × 10 ⁻³

recent work utilising full magneto-hydrodynamic simulations has attempted to directly model the filamentary accretion shocks and from this derive values for their radio luminosity (Vazza *et al.* 2015, 2019). As is typical of synchrotron shocked emission, these simulations suggest radio emission with steep spectral indices of approximately -1 to -1.5 , as well as peak radio surface brightnesses in the order of 10^{-6} Jy arcsec². Such simulations, however, depend on assumptions about filamentary magnetic field strengths and electron acceleration efficiencies, which are poorly constrained or understood.

To date, these attempts at detecting the synchrotron cosmic web have been unsuccessful with two exceptions. First, a small 'bridge' between two interacting clusters Abell 399 and 401 was recently reported to have been detected by Govoni *et al.* (2019); however, this emission is primarily the result of a pre-merger cluster-cluster interaction rather than the more general infall accretion shocks we expect to find in the cosmic web. Second, by Vacca *et al.* 2018 (henceforth: VA18), is the focus of this current follow-up study.

VA18 reported the detection of 28 candidate, large-scale synchrotron radio sources using the single-dish Sardinia Radio Telescope (SRT; Prandoni *et al.* 2017) and archival interferometric NRAO VLA^a Sky Survey (NVSS; Condon *et al.* 1998) data observed at 1.4 GHz. These sources were observed in an $8^\circ \times 8^\circ$ region of sky centred at RA $5^{\text{h}}0^{\text{m}}0^{\text{s}}$ and Dec $5^\circ 48' 0''$. This region of sky contains 43 galaxy clusters, 13 of which have spectroscopic redshifts, with 9 being in the redshift range $0.08 \leq z \leq 0.15$ (see Tables 1 & 2 in VA18 for full list). Additionally, some of these clusters have been identified as members of superclusters: Einasto *et al.* (2002) have catalogued superclusters SCL 061 and SCL 062 and Chow-Martínez *et al.* (2014) have catalogued MSCC 145 which partially overlaps with SCL 062. However, VA18 exclude the possibility that these sources are associated with galaxy cluster cores due to the lack of associated X-ray emission typical of dense cluster environments; indeed, the sources populate a previously empty region of the X-ray luminosity/radio power space ($L_{X,0.1-2.4 \text{ keV}} - P_{1.4 \text{ GHz}}$). Instead, they have raised the possibility that these new found synchrotron sources are in fact a detection of radio emission from the intercluster medium, that is, the synchrotron cosmic web.

Given the potential significance of these candidate sources and the new population of synchrotron sources they may represent, we here report on lower frequency observations using the Murchison

Widefield Array (MWA; Tingay *et al.* 2013; Wayth *et al.* 2018) at 154 MHz and the Australian Square Kilometre Array Pathfinder (ASKAP; Hotan *et al.* 2014) at 887 MHz to verify the candidate sources and measure their spectral properties.

These lower frequencies are ideal for detecting synchrotron emission. The spectral energy distribution (SED) of synchrotron sources can usually be well approximated by a power law, where the spectral flux density S is a function of frequency ν of the form:

$$S(\nu) \propto \nu^\alpha \quad (1)$$

The coefficient α is known as the spectral index. For astronomical synchrotron sources, this coefficient depends, amongst other things, on the electron injection power coupled with the ageing dynamics of the electron population. Active radio galaxies (AGN) tend to have a shallower SED at around $\alpha \approx -0.7$, whilst as populations of relativistic electrons age, for example in AGN remnants, their SED tends to steepen. Synchrotron shocks tracing the cosmic web should have spectral indices of at least -0.7 , and most likely -1 or steeper (Vazza *et al.* 2015). This typically negative spectral index ensures that synchrotron sources are brightest at lower radio frequencies. Thus, these lower frequency observations take advantage of the expected brighter emission to corroborate the detections in VA18 and additionally provide us with spectral information that can allow us to infer the emission mechanisms of any confirmed candidate sources.

This paper proceeds as follows: in Section 2, we briefly review the observations and data of VA18, before in Section 3 detailing our own observations with both MWA and ASKAP, which also includes our point source subtraction method. We measure our surface brightness sensitivity in Section 4, and in Section 5 we present the results of our observations. Finally, in Section 6, we discuss at length all potential corroborating detections as well as drawing from other extant surveys to help classify these emission sources.

2. SRT+NVSS data

VA18 fully document their observations and data processing methods, which we briefly summarise here. The SRT data consisted of 18 h of observing in the L-band (1.3–1.8 GHz) using the 'on-the-fly' mapping strategy, as well as some additional time on specific subfields. The SRT has a beam size of $13.9' \times 12.4'$ at 1550 MHz and the resulting images had a noise of 20 mJy beam^{-1} . In addition to this low-resolution, single-dish data, VA18 also obtained archival NVSS observations of the field that were in two

^aNational Radio Astronomy Observatory Very Large Array.

Table 2. Diffuse large-scale emission regions identified by VA18. An asterisk by the name indicates that VA18 considered it possible that the region was contaminated by residuals from compact source subtraction.

Source	RA (J2000) h:m:s	Dec (J2000) d:m:s	SRT significance σ	MWA detection	ASKAP detection	HII region	Notes
A1	04:59:08.81	+08:48:52	6	Yes	Yes	No	Radio halo in A523
A2	04:57:43.81	+08:47:03	3	No	No	No	
A3	04:56:23.85	+09:27:59	3	No	No	No	
B1	04:49:29.06	+08:30:16	3	No	No	Yes	
B2	04:53:19.21	+07:48:11	3	No	No	No	
B3	04:51:39.15	+07:15:01	3	No	No	No	Double-lobed radio galaxy immediately south of source
C1*	05:15:39.81	+06:51:47	5	No	No	Partly	Excluding northern zoom
	05:15:31.00	+06:49:40	5	Yes	Yes	No	Northern zoom only
C2	05:12:24.80	+07:25:01	3	No	No	No	
C3	05:10:39.64	+07:06:07	4	No	No	No	
C4	05:12:34.29	+06:49:01	3	No	No	No	
C5	05:11:21.76	+06:49:35	3	No	No	No	
C6*	05:12:26.81	+06:20:31	4	No	Yes*	Partly	North-west contour only but does not overlap
C7	05:07:44.04	+06:26:13	4	No	Yes	Yes	
C8	05:06:57.73	+06:21:59	3	No	No	Yes	
C9*	05:05:57.34	+06:14:45	3	Yes	No	No	
C10	05:06:19.45	+06:04:59	3	No	Yes	Yes	
D1	05:05:00.00	+06:44:00	3	No	No	No	
D2	05:01:52.93	+06:06:57	4	No	No	No	
D3	05:00:19.57	+05:44:24	3	No	No	No	
E1	04:57:26.67	+06:52:01	5	No	Yes	No	
E2*	04:55:05.24	+06:17:21	4	Yes	No	No	
E3	04:57:10.28	+06:04:15	3	No	No	No	
F1	05:11:24.89	+03:46:42	3	Yes	No	No	SRT and MWA contours only partially overlap
G1	05:02:21.28	+05:26:12	3	No	No	No	
G2	04:55:03.01	+05:33:20	3	No	Yes	Yes	
G3	05:00:28.92	+05:03:38	3	No	No	No	
G4	04:59:12.63	+05:01:05	3	No*	No	No	SRT contours sit immediately North of large extended emission system in MWA
G5	04:57:59.36	+04:58:01	3	No	No	No	
G6*	04:58:34.65	+04:42:47	4	Yes	No	No	
H1	04:49:56.16	+04:48:46	3	No	No	No	
H2	04:49:28.39	+04:31:12	3	No	No	No	
I1	04:54:06.90	+02:33:02	5	Yes	Yes	No	Radio halo in A520
I2	04:55:06.23	+02:33:02	3	No	N/a*	No	Source beyond ASKAP primary beam
I3	04:55:06.23	+02:30:33	3	No	N/a*	No	Source beyond ASKAP primary beam
J1	04:48:37.81	+03:00:55	3	No	No	No	

bands centred at 1.4 GHz and which had a resolution of $45''$ and an average noise of $0.45 \text{ mJy beam}^{-1}$. The datasets were combined using SCUBE (Murgia *et al.* 2016), which performs a weighted sum in Fourier space of the power spectra of the single-dish and the NVSS data after correcting for any misalignment of overall power on overlapping angular scales. To perform the combination, the SRT image was produced over the same frequency range as the NVSS image. The combined power spectrum was tapered with the NVSS beam and the data back-transformed to obtain the combined image. The resulting combined image was finally convolved to a resolution of $3.5' \times 3.5'$ to accentuate large-scale emission, producing the 'SRT+NVSS' combined map with a noise of $3.7 \text{ mJy beam}^{-1}$.

To differentiate between compact emission and the presumed large-scale emission of the cosmic web, VA18 subtracted point sources from the 'SRT+NVSS' map using an image-plane subtraction process. This is described in full in their paper but briefly: the brightest point source in the map was identified, fit with a 2D elliptic Gaussian sitting on top of an arbitrarily oriented plane (to account for background emission), and subtracted. The process was repeated by then subtracting the next brightest source, and so on, until a user-defined threshold was reached. This image subtraction process was performed on the SRT+NVSS map prior to convolving the image from its native $45''$ resolution. The final 'SRT+NVSS-diffuse' map, at $3.5' \times 3.5'$ resolution, has a noise of $3.1 \text{ mJy beam}^{-1}$.^b

The choice to complement existing NVSS data with the deep, single-dish SRT observation arises from the assumption that nearby cosmic web emission will be large-scale, smoothly varying, and highly diffuse. Typical interferometers like the VLA lack very short and 'zero spacing' baselines, and as a result they are likely to be increasingly insensitive to, and eventually 'resolve out', emission on these large angular scales. Single-dish observations like the SRT are sensitive to these large angular scale features but typically have such low resolution that unrelated compact radio sources are blended together. In combining both together, VA18 make use of the strengths of each to get higher resolution data with excellent sensitivity to diffuse, large-scale emission.

Finally, all candidate sources were identified from the SRT+NVSS-diffuse image using a threshold three times greater than the calculated map noise (3σ). The resulting 35 sources were grouped into 10 regions, labelled A through to J. Of these 35, VA18 classify 5 as likely to be the result of imperfect compact source subtraction and 2 as known cluster halos, leaving 28 sources as candidates for large-scale, diffuse synchrotron emission.

3. Radio observations and data processing

In order to independently further investigate the results from VA18, these fields were observed with the MWA and ASKAP.

3.1. Murchison widefield array

The MWA data consist of two distinct datasets that were collected during different configurations of the array, known as 'Phase I'

and 'Phase II', described in detail in Tingay *et al.* (2013) and Wayth *et al.* (2018), respectively. Whilst both configurations consisted of 128 tiles and had identical point source sensitivity, the tiles were arranged differently resulting in a different set of baselines (see Figure 1). Phase I had a maximum baseline length of about 2.6 km as well as a large number of short baselines, many under 100 m. These short baselines gave Phase I excellent surface brightness sensitivity at the expense of poor resolution, which at 154 MHz could be several arcminute depending on the exact baseline weighting scheme used. Phase I is excellent at detecting faint, extended emission, however the poor resolution often necessitates additional, high-resolution observations to discern whether such emission is truly extended or merely the result of blending of nearby sources (e.g., Hindson *et al.* 2014; Zheng *et al.* 2018). Phase II (extended configuration), on the other hand, redistributed the 128 tiles out to a maximum baseline of about 5.4 km and a more sparse sampling of baselines under 500 m. Phase II has higher resolution at about $65''$ at 154 MHz and a better behaved synthesised beam (point spread function) but less sensitivity to diffuse emission. In this follow-up, we make use of observations using both Phase I and II configurations so as to leverage their respective strengths.

The Phase I configuration data are archival observations that were collected at various times from 2013 to 2016 and consist of just over 2 h of observations. The Phase II observations consist of 6 h of observations at 154 MHz from March 2019, plus an additional 30 min of archival observations from the first quarter of 2018. The latter 30 min were observed at high elevations at which the MWA is most sensitive, so contribute a disproportionate amount of signal to the final integration. All MWA observations were made at a central frequency of 154 MHz with a 30.72 MHz bandwidth. The data were originally collected with a 10 MHz and 0.5 s resolution and were averaged down to 40 kHz and 4 s prior to calibration and processing.

MWA calibration and imaging workflows operate independently on short 'snapshot' observations that are typically about 2 min in length; this workflow is necessitated due to the complicated MWA primary beam and the stationary, non-tracking array. Snapshots are short enough in duration that we can assume a constant primary beam model and the MWA, with its more than 8 000 baselines, sufficiently samples the Fourier plane (uv space) such that it is possible to image and deconvolve on timescales as short as 2 min. The downside of such a workflow is that final mosaics are only CLEANed down to the noise level of a single snapshot, making in-field sidelobe confusion the typically dominant source of noise, as well as prohibiting jointly imaging Phase I and Phase II observations together.

For this follow-up, each snapshot was independently calibrated with an 'in-field' sky model using the GLEAM extra-galactic catalogue (Hurley-Walker *et al.* 2017) and the internal MWA tool CALIBRATE (Offringa *et al.* 2016) which calculated full Jones matrix corrections across the band in 120 kHz steps. Additionally, we flagged baselines shorter than 15 wavelengths at the observing frequency, as these baselines tended to pick up significant amounts of nearby galactic emission on scales larger than several degrees.

After the initial sky-model calibration, snapshots were imaged using WSCLEAN (Offringa *et al.* 2014) with a shallow CLEAN and self-calibrated using the CLEAN-component model. A final snapshot image was then produced using a Briggs' 0 weighting of the baselines with a 3σ mask and 1σ threshold. CLEANing was configured to use the WSCLEAN multiscale algorithm with

^bNote that this is different to the value of $2.5 \text{ mJy beam}^{-1}$ given in VA18 and was calculated independently on the supplied final image. We also note that the overall mean of the image is offset from zero by $-2.1 \text{ mJy beam}^{-1}$. When calculating detection contours, we offset multiples of our noise value by this global mean. This independent process has resulted in a small difference between the SRT+NVSS-diffuse contours published here and in VA18.

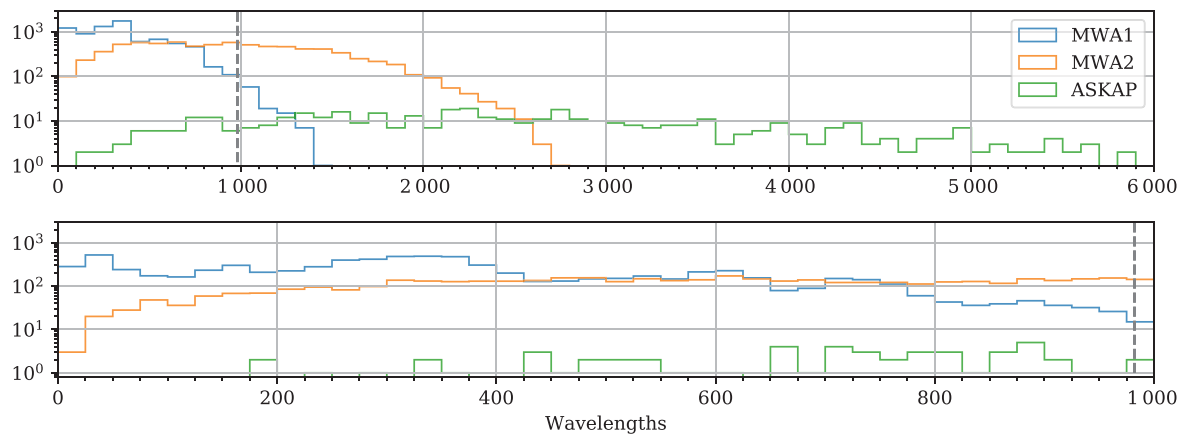


Figure 1. A comparison of baseline lengths for each of MWA Phase I (MWA1), MWA Phase 2 extended configuration (MWA2) and ASKAP. The lengths are measured in wavelengths (i.e. λ/λ_0 , with $\lambda \approx 1.94$ m for the MWA and $\lambda \approx 0.34$ m for ASKAP), which allows us to compare the baseline coverage despite the different observing frequencies. All plots exclude baselines that were flagged. The dashed line indicates a baseline length that would result in a fringe pattern on the sky with angular periodicity of $3.5'$; baselines shorter than this are sensitive to even larger spatial scales. *Top:* The baselines distribution out to 6 000 wavelengths, binned in intervals of 100. *Bottom:* A zoom of the baselines under 1 000 wavelengths, binned in intervals of 25.

default settings as well as joined-channel CLEANing with four channels and two Taylor terms (see Offringa & Smirnov 2017 for a description of the implementation of these algorithms). The final image was primary beam corrected and cross-matched with the GLEAM catalogue to correct for flux. Finally, the full set of snapshots were convolved to a common beam size (using the maximum beam size of any single snapshot), regridded onto a common projection and stacked in the image domain to give the full integration.

This particular field is problematic due to the presence of a number of bright, extended sources within the large MWA field of view, specifically the Crab Nebula, the Orion Nebula, and a number of large-scale supernova remnants. As a result of calibration and beam errors, these bright sources cast artefacts throughout the image and raise the noise level higher than is typical. This is particularly pronounced in the Phase I observations due to the increased power of these extended sources on the shorter baselines.

We provide two images, MWA-1 and MWA-2, using the method described here for each of the Phase I and II configurations, respectively. The properties and noise values for each of these images are provided in Table 1. In addition, we provide a third image—‘MWA-subtracted’—using the Phase II data but using a point source subtraction technique described in Section 3.3.

3.2. ASKAP

ASKAP undertook two observations of this field as part of their early testing programme for their newly built array and data processing pipelines. The ASKAP array is situated at the Murchison Radio Observatory, alongside the MWA. The array consists of 36 tracking dishes distributed quasi-randomly so as to produce baselines ranging in length from 22 m through to a maximum 6.4 km (see Figure 1). This large range of baselines gives ASKAP both high resolution as well as good sensitivity to extended emission, with almost a tenth of the baselines sensitive to emission on angular scales greater than $3.5'$ at 887 MHz. Each dish is 12 m in diameter,

and at 887 MHz the resulting primary beam has a full width half maximum (FWHM) of 1.76° . Additionally, each ASKAP dish is equipped with a phased array feed (PAF) allowing for 36 beams to be formed at once; depending on the configuration of these beams, this can allow for a much larger area of sky to be observed in a single pointing.

The two observations (PI: Vernstrom) occurred on 2019 March 10 and 2019 June 28 for 5 and 8 h, respectively, and were observed at a central frequency of 887 MHz with a bandwidth of 288 MHz. The PAF was configured in the ‘square6x6’ configuration for the first observation and in the ‘closepack36’ configuration for the second (McConnell et al. 2019); both allowed for the simultaneous observation of almost the entire $8^\circ \times 8^\circ$ field.

Both of these observations were independently processed. The initial bandpass and calibration were completed by the automated ASKAPSoft pipelines⁶ using PKS B1934-638 as the primary calibrator providing both bandpass and phase calibration. Note that secondary phase calibrators are not used by ASKAP as the instrumental phases are assumed to remain stable throughout the observation. After this initial calibration, the observation was averaged to 1 MHz channels and 10 s intervals. In addition, we applied two rounds of self-calibration for phase gains, and a final round of combined amplitude and phase gains using CASA (McMullin et al. 2007).

Next, each of the 36 beams were imaged with WSCLEAN using the following CLEANing configuration: 3σ mask, 1σ threshold, multiscale enabled and joined-channels configured with six channels and two Taylor terms. We were forced to exclude the six baselines under 60 m in length due to large-scale fringe patterns across the field caused by these baselines; the origin of these fringes remains unclear. Each of the final 36 beam images were primary beam corrected, truncated at their half-power radius, and mosaiced using their respective primary beam weights. Finally, the

⁶The ASKAPSoft pipeline does not yet have a paper describing its operation; however the current manual is available at <https://www.atnf.csiro.au/computing/software/askapsoft/sdp/docs/current/index.html>.

mosaics from each observation were summed and weighted by the mean noise across each image.

We provide two separate images, ASKAP-B+0.5 and ASKAP-B-1, imaged with Briggs' weightings of 0.5 and -1 , respectively. The former has good sensitivity to extended emission with a synthesised beam of about $20''$, whilst the latter has twice the resolution. Their combination can aid in discerning between the diffuse and compact components of regions of extended emission. Their respective noise values and other details are provided in [Table 1](#). Additionally, we also provide a diffuse emission map, referred hereafter as 'ASKAP-subtracted', with point sources subtracted using the method described in the next section.

3.3. Source subtraction

From each of the MWA Phase II and ASKAP observations we created additional, lower resolution images with point sources subtracted so as to emphasise diffuse emission. Rather than attempt to fit and subtract point sources from the final, deconvolved images as was done to produce the SRT+NVSS-diffuse image, we took advantage of the CLEAN deconvolution process itself. Recall that CLEAN runs in a loop whereby it finds the brightest peak in the dirty image, models a point source at this position with some fraction of the measured peak value (the 'gain' parameter, typically 0.1), and subtracts this from the image (during 'minor cycles') and the visibilities (during 'major' cycles). This loop continues, each time searching for a peak in the residual image and subtracting it out, until some stopping condition is met, typically when the brightest peak remaining falls under some threshold. An output of this process is a final residual image, with the CLEAN components fully subtracted. This residual image will be devoid of any bright sources; however, large-scale, faint emission will typically still be present hidden amongst the noise, and it is this image that we use to construct our diffuse maps.

We used `WSCLEAN` to perform the imaging and deconvolution with stopping conditions controlled by the mask and threshold options. The first of these options constructs a mask such that we only search for peaks within a masked region that is some factor of the noise, and the second determines that we stop CLEANing when there are no more peaks within the masked region greater than this factor of the noise.

For the ASKAP-subtracted image, we set the threshold value to 1.5σ , which is fairly typical; however, we set the mask value to 8σ , which is higher than usual. The result of this is that all bright regions of the map (greater than 8σ) are CLEANed all the way down to 1.5σ , whilst any regions with faint emission beneath this 8σ threshold are left in the final residual map. This first round of CLEANing was run with `WSCLEAN` multiscale disabled. Next, we continued to CLEAN the residual map, but with `WSCLEAN`'s multiscale CLEAN algorithm enabled and with a deeper mask of 3σ . The CLEAN components found in this second round of deconvolution were not subtracted and were either very faint point sources or large-scale extended emission. Finally, this image was convolved up to a resolution of $3.5' \times 3.5'$ so as to emphasise any diffuse emission present whilst suppressing any remaining faint point sources. The final image has a noise of $0.75 \text{ mJy beam}^{-1}$ and identical resolution to the SRT+NVSS-diffuse image.

We used a similar process for the MWA-subtracted image. However, since we image and deconvolve each snapshot independently, we use different values for each of the mask and threshold parameters. Typical 2-min snapshots have a noise of about 12 mJy

beam^{-1} , whilst the final MWA-2 image has a noise of $2.3 \text{ mJy beam}^{-1}$. To obtain the same CLEANing thresholds as in ASKAP would require us to CLEAN to a threshold under the noise of the individual snapshots, which is both unstable and unphysical. Instead, we set each of the mask and threshold to their lowest, stable values of 3 and 1, respectively, meaning the residual images contain faint emission up to approximately 35 mJy beam^{-1} . Since we are already CLEANing down to the limits, the residual images for each snapshot are not further CLEANed using multiscale. Finally, as with the ASKAP-subtracted image, we convolved each snapshot to a resolution of $3.5' \times 3.5'$ and stacked the images. The final MMA-subtracted image has a noise of $5.4 \text{ mJy beam}^{-1}$.

4. Surface brightness sensitivity

Surface brightness sensitivity, σ_{SB} , measures an interferometer's response to extended emission; specifically, it is the minimum surface brightness that is detectable above the noise. As we are searching for large extended emission—which we assume to be smoothly varying—surface brightness is a more useful measure than the more typically quoted point source sensitivity. In this section, we measure and compare the surface brightness sensitivity of each of MWA Phase I, Phase II, and ASKAP.

An interferometer's sensitivity to extended emission is dependent on the same factors that contribute to point source sensitivity (such as system temperature, effective collecting area, number of antennae and baselines) but, crucially, also depends on the geometry of the array. In particular, as the angular scale of emission increases, in visibility space the power spectrum of the source shifts towards the zeroth spacing and therefore short baselines are essential to sample this region.

Surface brightness sensitivity varies based on angular scale of the emission. For sources with an angular scale smaller than the synthesised beam, sensitivity scales approximately with the area of the source, until becoming most sensitive when the scale of the source matches the scale of the synthesised beam. On the other hand, extended emission above a threshold angular scale will have its power spectrum, so condensed around the zeroth spacing that few baselines will properly sample its power and the sensitivity to sources above this scale will drop as we 'resolve out' the source.

We attempt to estimate our surface brightness sensitivity in the following way. We simulate two-dimensional, circular Gaussian sources with constant peak brightness, P [Jy degree^{-2}], and varying FWHM values into the visibilities of the MWA Phase I, Phase II, and ASKAP measurement sets. We then produce dirty images of each and measure the peak flux response S_{peak} [Jy beam^{-1}] at the centre of each Gaussian in the resulting image. We estimate the surface brightness sensitivity as:

$$\sigma_{\text{SB}} = n\sigma_{\text{RMS}} \frac{P}{S_{\text{Peak}}} \quad (2)$$

where σ_{RMS} [Jy beam^{-1}] is the measured noise of our final images as detailed in [Table 1](#), and n is the factor above the noise required for a detection (which was 3σ in all cases). The fraction P/S_{Peak} measures the response to the simulated surface emission and is solely a function of the shape of the synthesised beam (i.e., the PSF); this is constant irrespective of the actual value of the simulated surface emission. Given this constant fraction, [Equation \(2\)](#) allows us to calculate just how bright the simulated surface brightness would need to be for the response to rise above the threshold for detection (i.e., $n\sigma_{\text{RMS}}$).

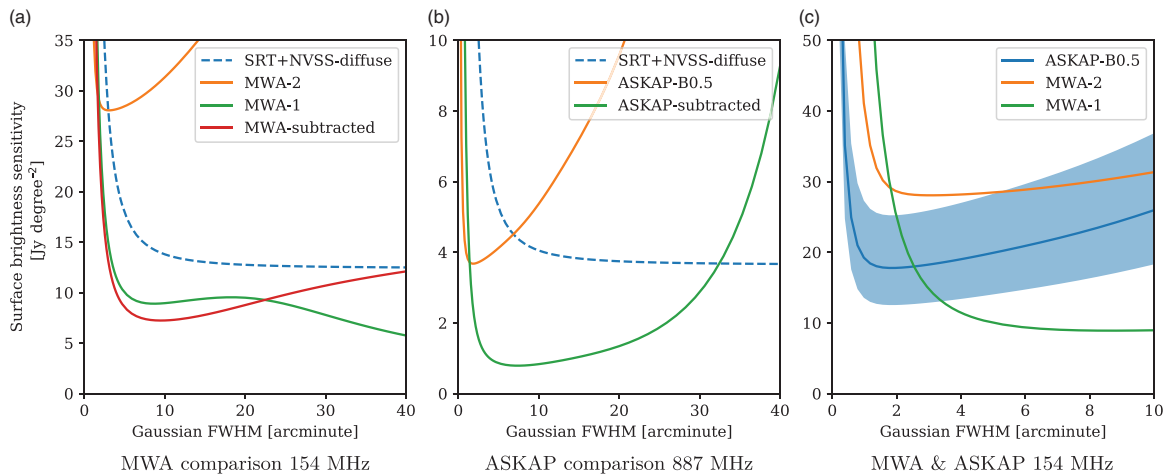


Figure 2. Surface brightness sensitivity values: (a) 154 MHz (MWA-1, MWA-2, and MWA-subtracted); (b) 887 MHz (ASKAP-B+0.5, ASKAP-subtracted). The SRT+NVSS-diffuse values (dashed blue line) are frequency adjusted from 1.4 GHz and represent the minimum surface brightness required to corroborate candidate sources in VA18 assuming a spectral index of -0.7 or steeper. (c) Direct comparison at 154 MHz of MWA and ASKAP surface brightness sensitivity, where ASKAP has been frequency adjusted from 887 MHz assuming a spectral index range $-0.7 < \alpha < -1.1$, with the solid line at the midpoint $\alpha = -0.9$.

In this sensitivity estimation, we use the dirty image as opposed to the deconvolved image as this better simulates how very faint sources are processed. At the limits of surface brightness sensitivity, emission in our images is buried amongst the image noise, and CLEANING thresholds will result in such emission being at most only partially deconvolved. Moreover, deconvolving a source makes it brighter, and so using the dirty images we are properly modelling the worst case.

To compare these values with the SRT+NVSS-diffuse image, we use their stated beam size of $3.5' \times 3.5'$ and simply convolve our Gaussian sky models with a Gaussian beam of this size. From the resulting images, we measure the peak flux response. This process assumes perfect and complete uv coverage with no interfering sidelobes, and so is a lower limit (i.e., best case) for the surface brightness sensitivity of the SRT+NVSS-diffuse image.

There is one further complication. We would like to answer the question: if emission is detectable in the SRT+NVSS-diffuse image at 1.4 GHz, what level of sensitivity is required at 154 and 887 MHz to be able to detect the same emission? To make this comparison, we need to make assumptions about the spectrum of such emission. Shock emission, such as relic, halo, or filamentary accretion shocks typically have spectral indices of approximately -1 or steeper, whilst -0.7 is more typical of AGN emission. We choose here to use the more conservative value of -0.7 . We can then scale the surface brightness sensitivity limits of the SRT+NVSS-diffuse image by this factor for each of the MWA and ASKAP observing frequencies:

$$\sigma_{\min} = \left(\frac{\nu}{1.4 \text{ GHz}} \right)^{-0.7} \sigma_{\text{SB}} \quad (3)$$

This frequency-adjusted limit thus represents the minimum sensitivity required to corroborate detection of a source at the limit of the SRT+NVSS sensitivity for any sources with a spectral index of -0.7 or steeper.

Using this method, Figure 2 compares the surface brightness sensitivity of the MWA and ASKAP with the frequency-adjusted surface brightness of the SRT+NVSS-diffuse image. In Figure 2(a), we compare the surface brightness sensitivity of the 154 MHz

images of the MWA with the SRT+NVSS-diffuse image. We can see that the MWA-2 image surpasses the surface brightness sensitivity of the SRT+NVSS-diffuse image only out to angular scales of approximately $3'$. Emission on angular scales larger than this, however, is increasingly resolved out. It is interesting to note that this reduction in sensitivity occurs on angular scales much smaller than we would expect just from calculating the fringe patterns of the shortest baselines of the MWA phase 2; this discrepancy arises from the weighted addition of each baseline's respective fringe pattern that ultimately forms the shape of the synthesised beam. On the other hand, both MWA-1 and MWA-subtracted have a greater surface brightness sensitivity than the frequency-adjusted SRT+NVSS-diffuse image on all angular scales out to at least $40'$. MWA-1 achieves this by its dense sampling of the inner region of the uv -plane, whilst MWA-subtracted achieves this sensitivity as a result of the extra convolution step that decreased the resolution to $3.5' \times 3.5'$.

In Figure 2(b), we compare the surface brightness sensitivity of ASKAP observing at 887 MHz. The ASKAP-B0.5 image has greater surface brightness sensitivity than SRT+NVSS-diffuse out to angular scales of approximately $7'$. The ASKAP-subtracted image, on the other hand, is able to exceed the frequency-adjusted limit required to corroborate synchrotron emission out to angular scales of approximately $32'$, which is, again, solely a result of the extra convolution step used in the point source subtraction process. We can conclude that both images have the required sensitivity to detect the kind of large-scale emission reported by VA18.

We can also directly compare the surface brightness sensitivity of MWA and ASKAP by frequency adjusting the sensitivity values of ASKAP from 887 MHz down to 154 MHz. As can be seen in Figure 2(c), we use a range of spectral indices, ranging from -0.7 to the steeper -1.1 with a solid line indicating an intermediate spectral index of -0.9 . We find that the ASKAP-B0.5 image is significantly more sensitive than MWA-2 on all angular scales out to approximately $5'$, beyond which the MWA-2 image is more sensitive to those sources with the very steepest spectral indices. ASKAP is more sensitive than MWA-1 on angular scales smaller

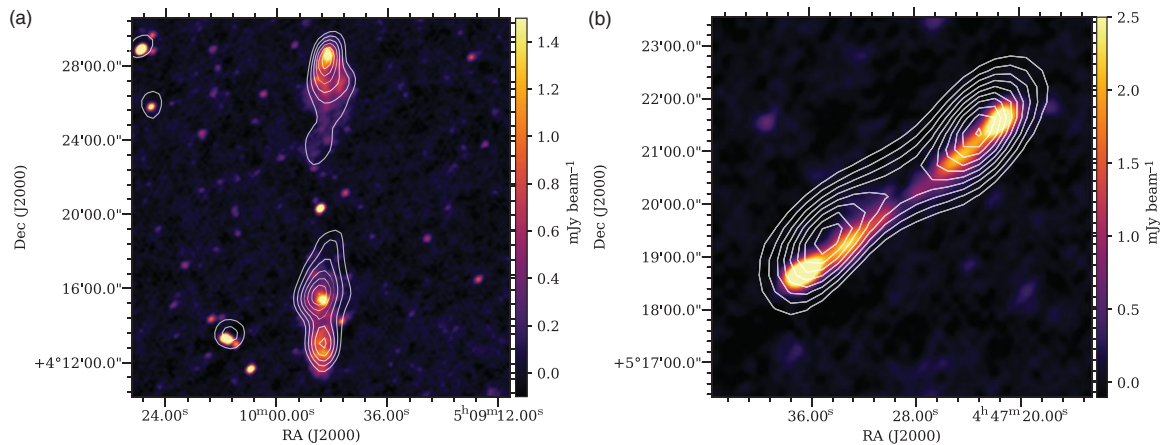


Figure 3. Images from ASKAP-B+0.5 at 887 MHz of two radio galaxies in the field mentioned by VA18. The white contours are MWA-2 at 154 MHz, starting at 3σ and increasing in increments of $+2\sigma$. (a) RA $5^{\text{h}}9^{\text{m}}50^{\text{s}}$ Dec $4^{\circ}20'19''$ and (b) RA $4^{\text{h}}47^{\text{m}}23.9^{\text{s}}$ Dec $5^{\circ}18'50''$.

than approximately $2.5'$; for larger angular scales, the prevalence of short baselines in the MWA phase I array result in MWA-1 having superior surface brightness sensitivity. Nonetheless, this suggests a surprising result: ASKAP is ideally suited to the detection of synchrotron emission on scales both small and large, even for sources with moderately steep spectral indices.

5. Results

In Table 2, we present each of the 35 sources reported by VA18, the maximum significance of their detection in the SRT+NVSS-diffuse image, and whether either MWA (in any of MWA-1, MWA-2, or MWA-subtracted) or ASKAP are able to detect emission in the same region to 3σ significance. In the Appendix, we provide images of every VA18 region. In Figure A.1, we show each of the 35 sources as imaged in ASKAP-B+0.5, with contours from the SRT+NVSS-diffuse (blue) and ASKAP-subtracted (red). In Figure A.2, we present each of the regions as imaged in MWA-2, with contours again from SRT+NVSS-diffuse (blue) and MWA-subtracted (red). Finally, in Figure A.3, we present the full $8^{\circ} \times 8^{\circ}$ region as imaged in MWA-1, with contours from SRT+NVSS-diffuse. This latter image is scaled such that saturated black represents a 5σ detection.

6. Discussion

The known, large-scale synchrotron sources in this field are detected in all our images with strong statistical significance, and this provides a initial validation of the angular sensitivity of our observations. For example, the radio halo in Abell 523 (source A1) is detected in each of ASKAP-subtracted and MWA-subtracted well above the noise (statistical significance of 20σ and 11σ , respectively), as is the radio halo in Abell 520 (source I1; statistical significance of 8σ and 8σ , respectively). Both are also visible in MWA-2 and MWA-1, though in the latter the more compact emission is blended in with the diffuse components. In addition, the large extended lobes of the radio galaxy that VA18 report in region F are visible in all images, as we show in Figure 3(a). The core, on the other hand, is only visible in the higher frequency ASKAP image; this is typical of Galactic core emission which is dominated by free-free mechanisms and thus tends to have

a flatter spectrum at low radio frequencies.^d Similarly, the lobes of the smaller radio galaxy located at RA $4^{\text{h}}47^{\text{m}}24^{\text{s}}$ Dec $5^{\circ}18'50''$ are also clearly detected in all images as shown in Figure 3(b).

Despite demonstrating that we can detect the known synchrotron sources in this field, 23 of the 35 candidate sources are undetected in any of our direct observations as well as our ‘subtracted’ treatments. If we assume that these sources are both real and have spectra that are well approximated by a power law at this frequency range ($S \propto \nu^{\alpha}$), then we can calculate a lower limit value for the spectral index of these sources from ASKAP-subtracted map as $\alpha > 2.5$. The MWA-subtracted map places a less stringent constraint of $\alpha > -0.37$. Such a steep positive spectral index is atypical for synchrotron sources, with the exception of sources that exhibit a turnover due to synchrotron self-absorption or free-free absorption mechanisms. Both these mechanisms, however, are unusual to observe in this frequency range for large, diffuse systems.

We turn now to discuss the sources for which we make a potentially corroborating detection, or are otherwise noteworthy.

6.1. Source B1

Source B1 appears in the SRT+NVSS-diffuse map as a 3σ detection at $04:49:29.06 +08:30:16$, for which we find no radio emission in either ASKAP-subtracted or MWA-subtracted. However, in Figure 4 we present the associated Southern H-alpha Sky Survey Atlas (SHASSA; Gaustad *et al.* 2001) image showing this is a region of strong H-alpha emission, and indicating that this is a Galactic HII region. We propose that source B1 is likely a faint detection of associated thermal free-free emission produced by this Galactic HII region, and that the non-detection by both ASKAP and MWA is due to the typically inverted, blackbody spectrum of such sources, placing its surface brightness below the detection levels of our lower frequency observations.

^dWe also identify an optical candidate for the core of this radio galaxy, which is clearly visible both in Digital Sky Survey (Blanton *et al.* 2017) and Panoramic Survey Telescope and Rapid Response System (Pan-STARRS; Chambers *et al.* 2016) optical surveys and has previously been catalogued in the infrared as WISEA J050950.55+042021.0. The calculations in VA18 that inferred a minimum size of the radio galaxy from the magnitude limit of the DSS survey are therefore invalid.

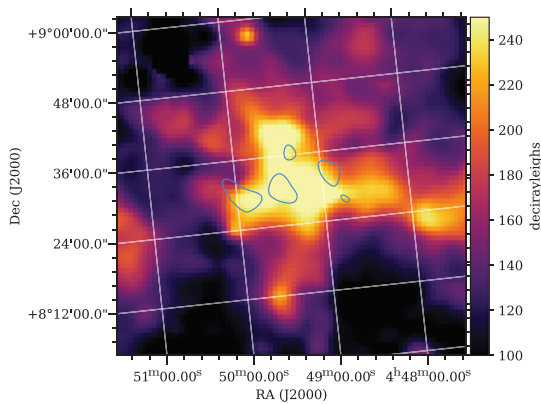


Figure 4. An H-alpha map of region B1 from SHASSA showing the coincident H-alpha emission. SRT+NVSS-diffuse contours (blue) indicate 3σ , 4σ , 5σ , etc.

6.2. Sources C1, C6, C7, C8, C10

VA18 report a very large-scale detection in the vicinity of Abell 539, spanning multiple large-scale islands of emission (C1) as well as numerous small regions of diffuse emission to the west (C2–C10).

In Figure 5, we show the SHASSA image for a large section of region C overlaid with the SRT+NVSS-diffuse contours (blue) and the ASKAP-subtracted contours (magenta). From the contours, we can observe that the ASKAP-subtracted map shows a clearly visible ridge of flux extending approximately 40 arcmin in a north-easterly orientation, approximately joining the regions C7, C8, and C10. This ridge has a peak flux of $6.3 \text{ mJy beam}^{-1}$, whilst it is undetectable in the lower frequency MWA images suggesting a shallow or inverted spectral index. From the background SHASSA map, we observe that this ridge of emission traces a similarly bright region of Galactic H-alpha emission which extends west from the galactic equator through C1 and C6 and peaks along the ridge adjoining C7, C8, and C10.

The coincident emission of H-alpha and radio strongly suggests that the ridge we are observing is a Galactic HII region, and that we are detecting the thermal free-free component of this region in the radio. Moreover, the lack of radio emission in the MWA observations is consistent with the inverted spectrum of thermal free-free emission.

Figure 5 includes, in addition to the bright ridge of emission on the right, regions C1 and C6. We include these regions to suggest the possibility that the western component of C6 as well as the north-east island of C1 (with the exception of the northern ‘C1-zoom’) may also be a detection of the extended Galactic HII region. Indeed, despite C1 lying beyond the half-power point of the ASKAP primary beam, we still detect a radio component coincident with a peak in the H-alpha map. This strongly suggests that the north-east island of C1, which lies closest to the centre of Abell 539, is not extra-galactic in origin.

6.3. Source C1 ‘zoom’

The C1 northern zoom, centred at $05:15:31 +06:49:40$ and located at the very periphery of Abell 539, contains significant diffuse emission that is detected in the MWA (Phase I & II) and ASKAP images. In Figure 6, we show the three-colour optical image from

the Panoramic Survey Telescope and Rapid Response System (Pan-STARRS; Chambers et al. 2016) overlaid with contours from ASKAP-B-1, ASKAP-B+0.5, and MWA-2.

The C1 northern zoom contains a number of bright points of emission. The brightest, located at $5:15:29.52 +6:48:46.23$ (lower right), is resolved into two conjoined points in ASKAP-B-1 with no optical association in Pan-STARRS, whilst in ASKAP-B+0.5 it has a faint extension along the same axis; we propose this source is a pair of radio lobes of a distant, background galaxy and unrelated to the extended emission in this region.

The second brightest source of emission in the C1 north zoom is centred at $5:15:33.93 +6:50:33.3$ and is surrounded by diffuse radio emission. It is clearly extended in the ASKAP-B+0.5 image with a largest angular scale of approximately $180''$. A central hotspot is visible in the ASKAP-B-1 image and in addition, two satellite patches of extended emission appear in ASKAP-B-1 to the south-east and south-west. The source is also visible in all MWA images, and using the MWA-2 and ASKAP-B+0.5 images we can calculate a spectral index for the total integrated flux as -0.97 . In the associated Pan-STARRS image, we observe a candidate host galaxy 2MASX J05153393+0650333 indicated by the arrow sitting near the peak of the emission, for which there is unfortunately no currently available redshift information, as neither of the satellite regions have any optical candidate. Given the existence of a host galaxy and the hotspots, it seems likely that this is diffuse radio galaxy emission. The presence of a bright core suggests this is a Fanaroff & Riley class I (FRI) radio galaxy; however, there are clearly weakly emitting lobes which would suggest the presence of some environmental pressure. The overall morphology of the source is certainly atypical of normal radio jet structure; however, it is suggestive of a head-tail galaxy. Whilst additional observations may aid in understanding its complex morphology, we feel confident to classify this diffuse emission as originating from 2MASX J05153393+0650333.

In addition, a secondary diffuse radio source is visible in the top left of the image. This appears to be an FRII radio galaxy, with the left lobe significantly brighter than the right, possibly due to relativistic beaming. The leftmost lobe is visible in lowest MWA-2 contour, that is, a 3σ detection at 154 MHz. There is no obvious optical candidate visible in Pan-STARRS, suggesting that this is in the background of the 2MASX J05153393+0650333 system.

6.4. Source C9

Source C9 is detected at 3σ significance in MWA-subtracted. The ASKAP-B+0.5 image shows five point sources in a small angular area, and MWA-2 detects and resolves at least three of these. However, the brightest of these sources in MWA-2 is just 13 mJy beam^{-1} , meaning that none of these sources will have been subtracted from individual snapshots; any flux present in the MWA-subtracted image is likely unsubtracted point source emission. In agreement with VA18, source C9 is most likely the result of residual point sources.

6.5. Source E1

There is a trace of a detection at the central peak of E1 in ASKAP-subtracted (peak 3.1σ), whilst there is nothing in MWA, either in MWA-1, 2 or subtracted. In the case of MWA-1, this is a region with no nearby sources that might produce a false-positive result due to blending, and given its superb surface brightness sensitivity, the absence of a lower frequency detection strongly suggests

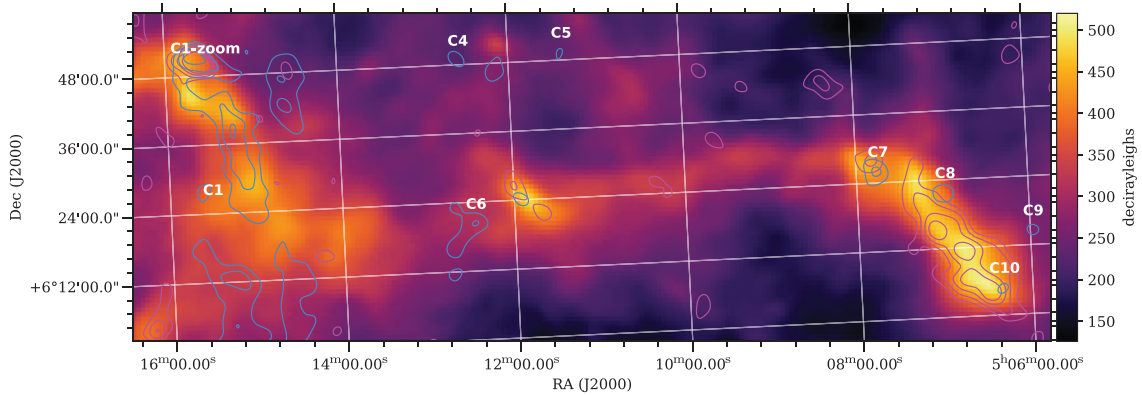


Figure 5. An H-alpha map of region C from SHASSA. SRT+NVSS-diffuse contours (blue) indicate 3σ , 4σ , 5σ , etc. ASKAP diffuse contours (magenta) indicate 2σ , 3σ , 4σ etc.

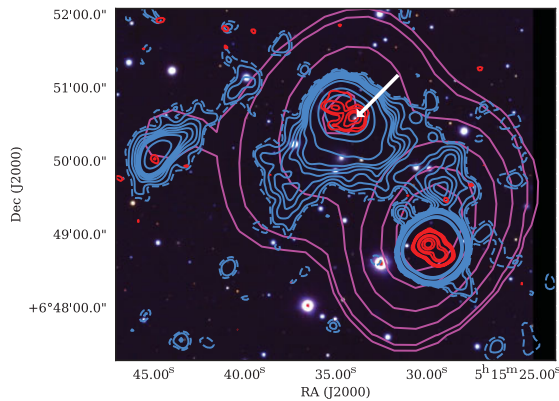


Figure 6. The Pan-STARRS three-colour (bands Y, I, G) image of 'C1-zoom', showing the presumed optical host indicated by the white arrow. The contours are: ASKAP-B+0.5 (blue) at 1.5σ (dashed) and then 2, 3, 4, 5, 6, 7, 10, 20, 30σ ; ASKAP-B-1 (red) at 3, 4, 6, 8, 30, 50, 100, 150σ ; MWA-2 (magenta) at 3, 5, 15, 35, 80, 120σ .

against this region as being synchrotron in origin. SHASSA, however, does not indicate any associated peak in H-alpha emission in this region. Given the low statistical significance of the ASKAP detection, and that the region above the 3σ threshold has a maximum angular extent of just $0.8'$ (compared to a beam size of $3.5' \times 3.5'$), we would be inclined to suggest that this is noise in our own image if it were not so clearly aligned with the SRT+NVSS-diffuse peak contour. We measure a peak brightness of $2.7 \text{ mJy beam}^{-1}$ at 887 MHz, and $14.5 \text{ mJy beam}^{-1}$ in the SRT+NVSS-diffuse image at 1.4 GHz, giving a steep positive spectral index of $+3.7$. Whilst we conclude this is unlikely to be synchrotron, we leave open the possibility that this is emission by some other mechanism with an inverted spectrum.

6.6. Source E2

The MWA-subtracted image detects a small area of diffuse emission at E2, whilst nothing is detected in ASKAP-subtracted. The ASKAP-B+0.5 image resolves five bright radio sources in this small region. At least two of these are very slightly extended in the ASKAP image: the source located at $4:55:07.7 +6:16:31.6$ is a star-forming spiral galaxy with a bright compact core visible

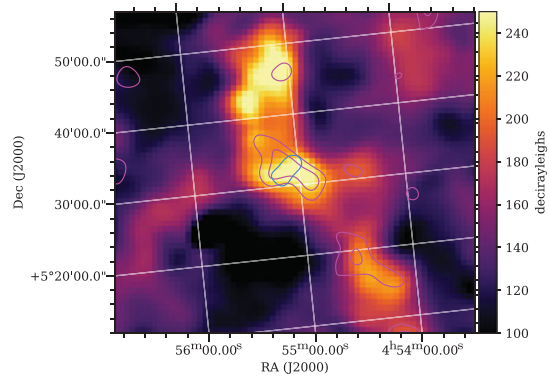


Figure 7. An H-alpha map of region G2 from SHASSA showing the coincident H-alpha emission. SRT+NVSS-diffuse contours (blue) indicate 3σ , 4σ , 5σ , etc. ASKAP-diffuse contours (magenta) indicate 2σ , 3σ , 4σ , etc.

in Pan-STARRS but whose spiral arms are also weakly visible in radio; the source located at $4:54:58.0 +6:17:22.5$ is extended in ASKAP-B+0.5 with an extension towards the north and a bright core or hotspot visible in the ASKAP-B-1 image but no obvious optical counterpart.

As VA18 suggest, the source E2 is most likely due to a blending of numerous radio sources and not due to diffuse radio emission.

6.7. Source F1

VA18 report a small region of 3σ significance located at $05:11:24.89 +03:46:42$. The MWA-subtracted image finds a small region of extended emission offset north of this, which encompasses four distinct radio sources in ASKAP-B+0.5. This extended emission signal is almost certainly just the result of blended emission from these point sources and does not corroborate the F1 candidate region.

6.8. Source G2

In the SRT+NVSS-diffuse image, source G2 is a small 3σ detection. MWA-subtracted makes no detection in this region; however, ASKAP-subtracted makes a similarly weak 3σ detection in the same region. In Figure 7, we show the H-alpha emission in this

region from SHASSA with contour overlays from SRT+NVSS-diffuse (blue) and ASKAP-diffuse (magenta). Once again, we find a correlation between a peak in the H-alpha emission and the detected diffuse radio emission, suggesting that the radio is free-free emission from a Galactic HII region. Indeed, the ASKAP-diffuse 2σ contours appear to trace two additional H-alpha peaks both north and south of G2.

7. Conclusion

We are unable to corroborate the candidate synchrotron sources of VA18. Careful examination of each of the 35 sources suggests five classes: known halo systems (A1, I1); radio galaxies (C1-zoom); HII emission (B1, north-east C1, north-west C6, C7, C8, C10, G2); blended compact sources (C9, F2, E1); and finally one non-synchrotron but otherwise unknown source (E1). The remaining sources are not detected in our observations.

The non-detections strongly suggest against these sources being synchrotron in origin. Synchrotron sources in general exhibit negative spectral indices, and models suggest the shocked emission from the cosmic web proper to have a spectral index $\alpha \approx -1$. These properties ensure that synchrotron sources are brightest at lower radio frequencies, and given the surface brightness sensitivity of the MWA and ASKAP images, any large-scale synchrotron emission should surely be visible at these lower frequencies. As we have noted, the ASKAP non-detection puts a stringent condition on the candidate sources as having a steep, positive spectral index of $\alpha > 2.4$, and this can only be explained if these are regions exhibiting a turnover due to synchrotron self-absorption or free-free absorption.

We suggest three explanations for these non-detections. Firstly, these may be real emission that have a positive spectral index and which renders them undetectable at lower frequencies, for example, thermal free-free emission. However, given the extreme spectral steepness of such a population, we consider this an unlikely scenario. Secondly, given the low 3σ threshold used to identify the candidate sources, some fraction may simply be noise. This may be especially applicable to those regions that were small in angular extent, typically much smaller than the $3.5'$ resolution of the SRT+NVSS-diffuse image. Finally, given the significant image processing employed by VA18, which included combining systematics from both SRT and NVSS, as well as a complex and imperfect point source subtraction process, some fraction of these sources may be the result of spurious image artefacts. VA18 acknowledge this possibility but, as they detailed in Appendix C, their own simulations excluded gain fluctuations from within their pipeline as being significant, and galactic foreground simulations suggested that less than 20% of the candidate sources could be attributed to this foreground.

Whilst this is a disappointing result, we wish to raise the possibility that large-scale, extended emission may be the wrong parameter space for searching for the synchrotron cosmic web. There has been an assumption to date that the synchrotron cosmic web would match the spatial scales of the underlying filaments, which is evident both in the work of VA18 as well as others (see e.g. Brown et al. 2017; Vernstrom et al. 2017). However, the mechanism for synchrotron emission is primarily by way of accretion shocks, which are by definition regions of discontinuity. Such mechanisms may be more likely to produce sharp and smaller-scale emission features as opposed to the broad, smooth, and extended features that have been assumed to date. Indeed, such

compact features can already be observed in simulations (Araya-Melo et al. 2012; Vazza et al. 2015, 2019), suggesting that we may have in fact been looking in the wrong place. Future work in this area will be required to properly understand the characteristic spatial scales of this radio emission and constrain the parameter space as we continue to search for evidence of the synchrotron cosmic web.

Acknowledgements. This scientific work makes use of the Murchison Radio-astronomy Observatory, operated by CSIRO. We acknowledge the Wajarri Yamatji people as the traditional owners of the Observatory site. Support for the operation of the MWA is provided by the Australian Government (NCRIS), under a contract to Curtin University administered by Astronomy Australia Limited. We acknowledge the Pawsey Supercomputing Centre which is supported by the Western Australian and Australian Governments.

The Australian SKA Pathfinder is part of the Australia Telescope National Facility which is managed by CSIRO. Operation of ASKAP is funded by the Australian Government with support from the National Collaborative Research Infrastructure Strategy. ASKAP uses the resources of the Pawsey Supercomputing Centre. Establishment of ASKAP, the Murchison Radio-astronomy Observatory, and the Pawsey Supercomputing Centre are initiatives of the Australian Government, with support from the Government of Western Australia and the Science and Industry Endowment Fund. We acknowledge the Wajarri Yamatji people as the traditional owners of the Observatory site.

This work was supported by resources provided by the Pawsey Supercomputing Centre with funding from the Australian Government and the Government of Western Australia.

References

- Araya-Melo, P. A., Aragón-Calvo, M. A., Brügger, M., & Hoefl, M. 2012, *MNRAS*, 423, 2325
- Blanton, M. R., et al. 2017, *AJ*, 154, 28
- Brown, S., et al. 2017, *MNRAS*, 468, 4246
- Cen, R., & Ostriker, J. P. 1999, *The Astrophysical Journal*, 514, 1
- Chambers, K. C., et al. 2016, The Pan-STARRS1 Surveys (arXiv:1612.05560)
- Chow-Martinez, M., Andernach, H., Caretta, C. A., & Trejo-Alonso, J. J. 2014, *MNRAS*, 445, 4073
- Condon, J. J., Cotton, W. D., Greisen, E. W., Yin, Q. F., Perley, R. A., Taylor, G. B., & Broderick, J. J. 1998, *AJ*, 115, 1693
- de Graaff, A., Cai, Y.-C., Heymans, C., & Peacock, J. A. 2019, *A&A*, 624, A48
- Eckert, D., et al. 2015, *Nature*, 528, 105
- Einasto, M., Einasto, J., Tago, E., Andernach, H., Dalton, G. B., & Müller, V., 2002, *AJ*, 123, 51
- Gaustad, J. E., McCullough, P. R., Rosing, W., & Buren, D. V. 2001, *PASP*, 113, 1326
- Govoni, F., et al. 2019, *Science*, 364, 981
- Hindson, L., et al. 2014, *MNRAS*, 445, 330
- Hotan, A. W., et al. 2014, *PASA*, 31, e041
- Hurlley-Walker, N., et al. 2017, *MNRAS*, 464, 1146
- Macquart, J.-P., et al. 2020, *Nature*, 581, 391
- McConnell, D., et al. 2019, ASKAP Science Observation Guide: Version 1.0 – Pilot Survey Preparation Phase, [https://www.atnf.csiro.au/projects/askap/documents/ASKAP_sci_obs_guide20\(002\).pdf](https://www.atnf.csiro.au/projects/askap/documents/ASKAP_sci_obs_guide20(002).pdf)
- McMullin, J. P., Waters, B., Schiebel, D., Young, W., & Golap, K. 2007, *CASA Architecture and Applications*, 127
- Murgia, M., et al. 2016, *MNRAS*, 461, 3516
- Nicastro, F., Krongold, Y., Mathur, S., & Elvis, M. 2017, *AN*, 338, 281
- Nicastro, F., et al. 2018, *Nature*, 558, 406
- Offringa, A. R., & Smirnov, O. 2017, *MNRAS*, 471, 301
- Offringa, A. R., et al. 2014, *MNRAS*, 444, 606
- Offringa, A. R., et al. 2016, *MNRAS*, 458, 1057
- Prandoni, I., et al. 2017, *A&A*, 608, A40
- Tanimura, H., Aghanim, N., Douspiss, M., Beelen, A., & Bonjean, V. 2019, *A&A*, 625, A67

- Tingay, S. J., et al. 2013, *PASA*, 30
- Vacca, V., et al. 2018, *MNRAS*, 479, 776
- Vazza, F., Ettori, S., Roncarelli, M., Angelinelli, M., Brügger, M., & Gheller, C. 2019, *A&A*, 627, A5
- Vazza, F., Ferrari, C., Brügger, M., Bonafede, A., Gheller, C., & Wang, P. 2015, *A&A*, 580, A119
- Vernstrom, T., Gaensler, B. M., Brown, S., Lenc, E., & Norris, R. P. 2017, *MNRAS*, 467, 4914
- Wayth, R. B., et al. 2018, *PASA*, 35
- Wilcots, E. 2004, *NAR*, 48, 1281
- Zheng, Q., Johnston-Hollitt, M., Duchesne, S. W., & Li, W. T. 2018, *MNRAS*, 479, 730

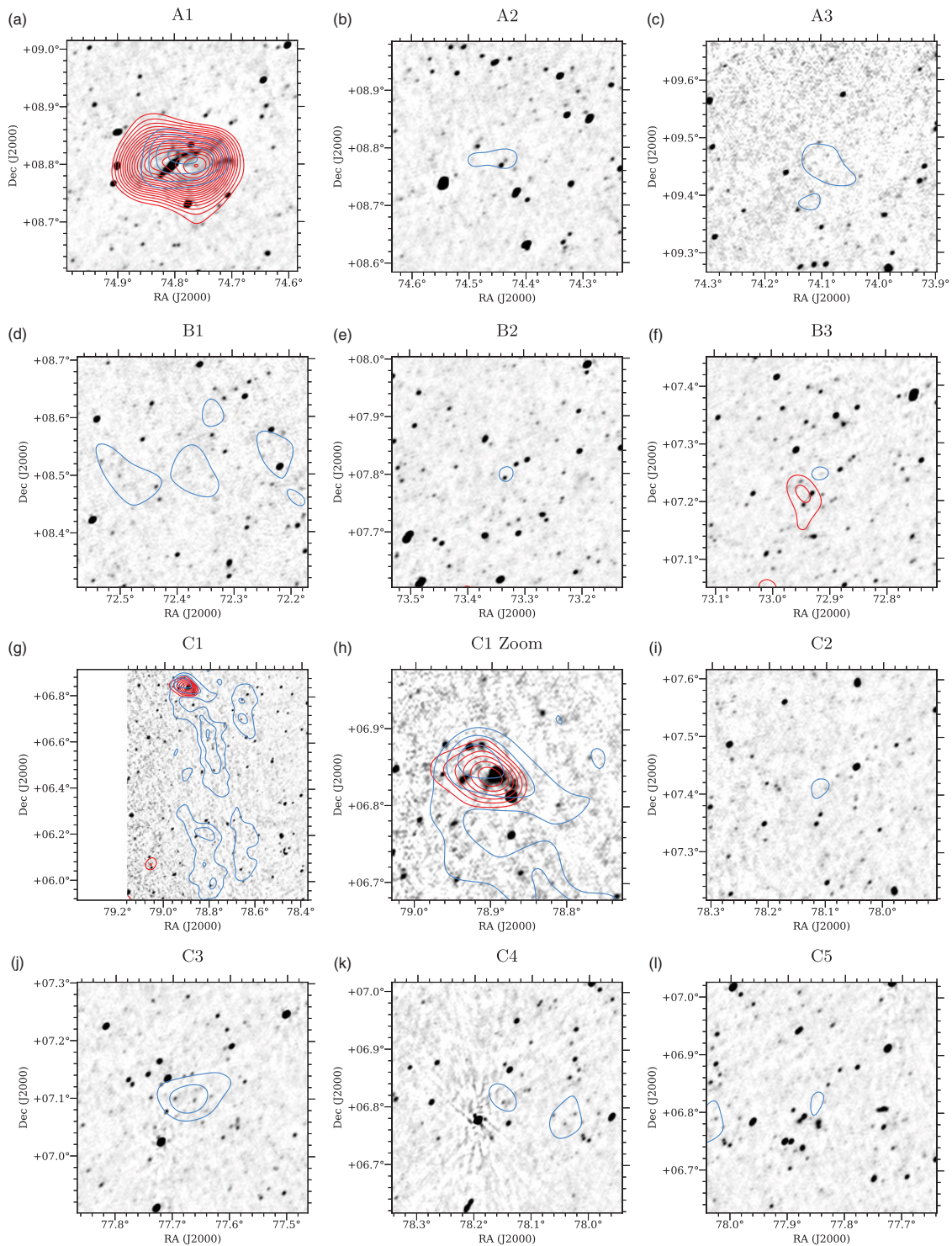


Figure A.1. ASKAP-B+0.5 image with SRT+NVSS-diffuse contours (blue) and ASKAP-subtracted contours (red). Contours start at 3σ of their respective map noise and increase in increments of 1σ . All images scaled linearly from -50 to $1000 \mu\text{J beam}^{-1}$.

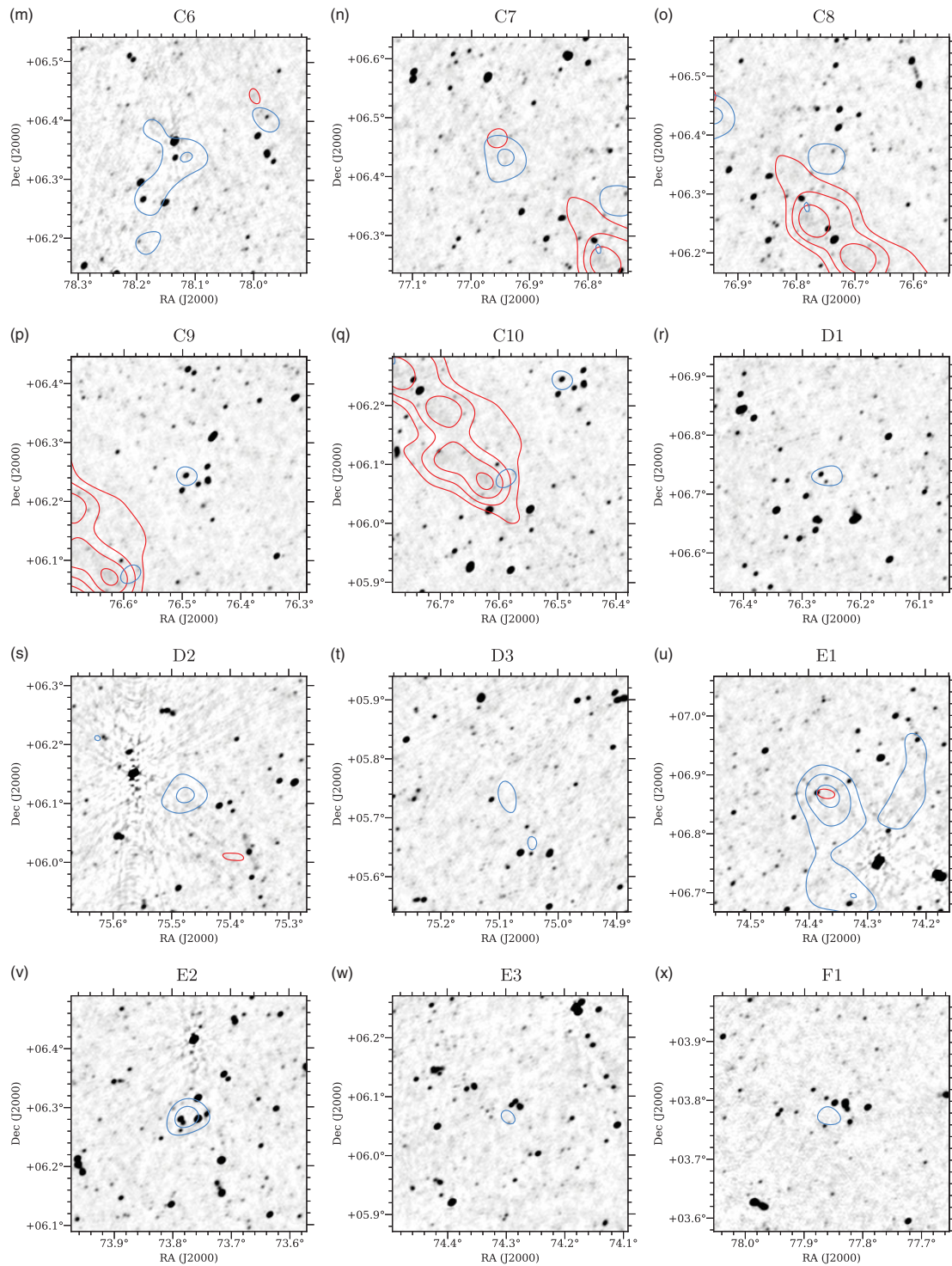


Figure A.1. Continued.

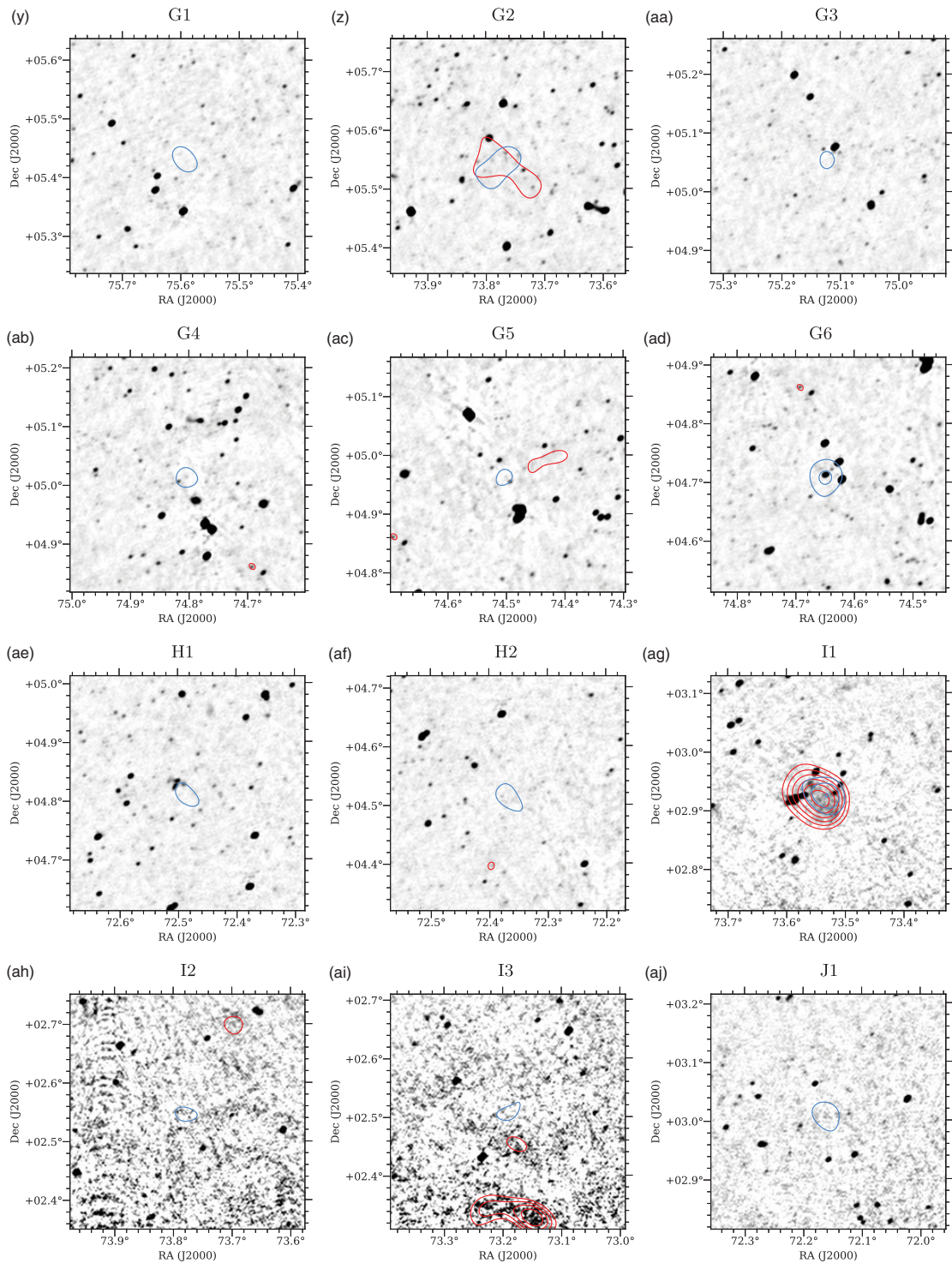


Figure A.1. Continued.

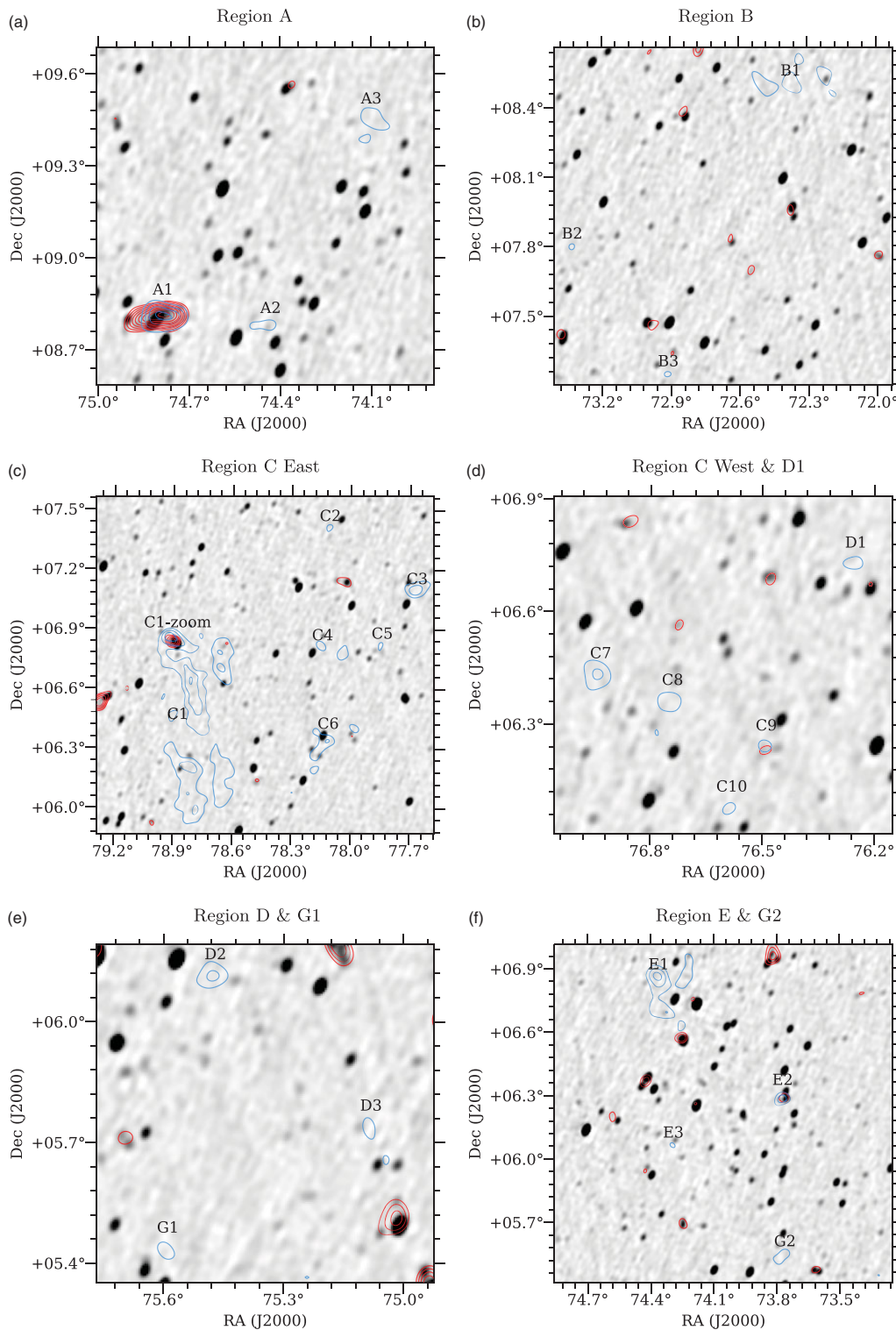


Figure A.2. MWA Phase II at 154 MHz with SRT+NVSS-diffuse contours (blue) and MWA-subtracted contours (red). Contours start at 3σ of their respective map noises and increase in increments of 1σ . Images are scaled linearly from -5 to 50 mJy beam $^{-1}$.

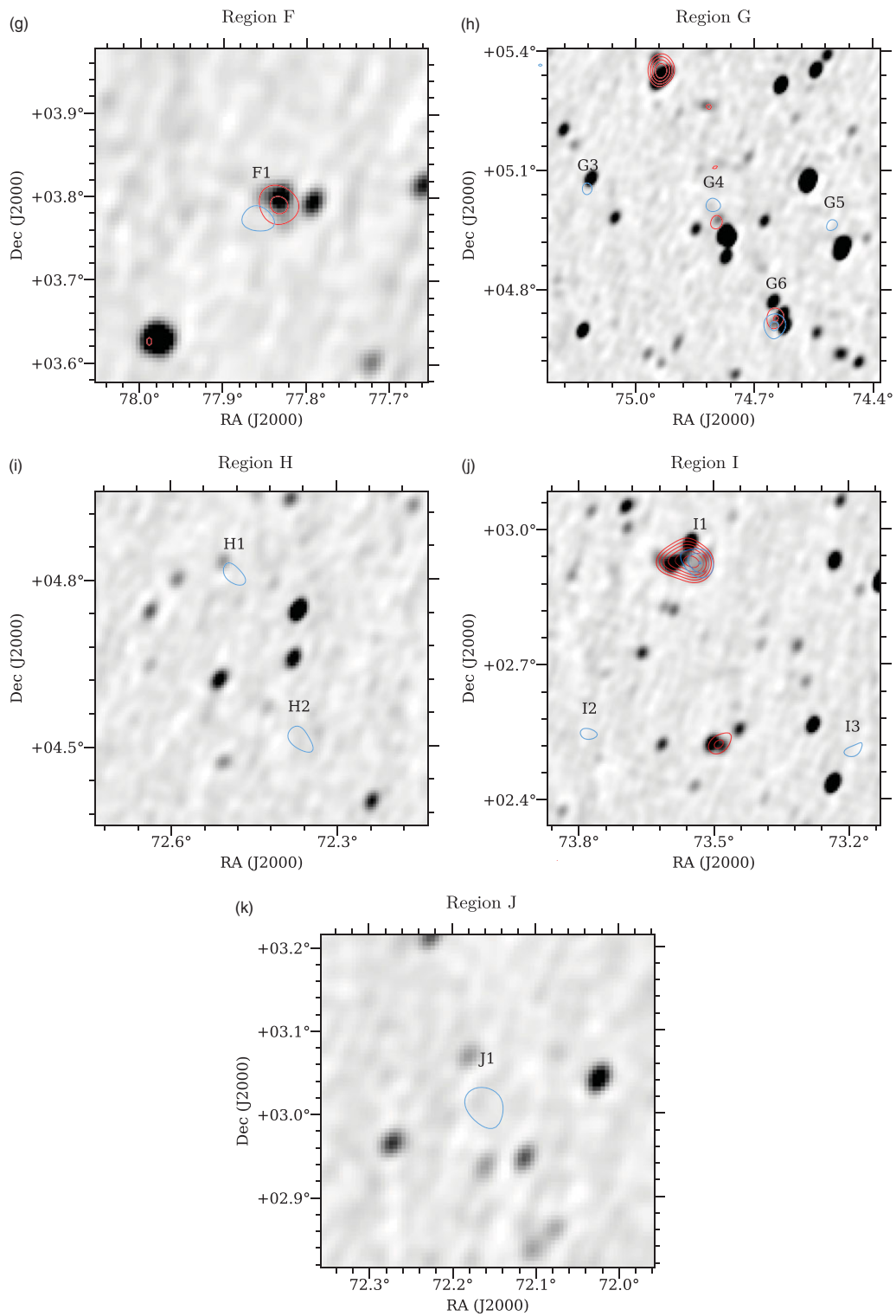


Figure A.2. Continued.

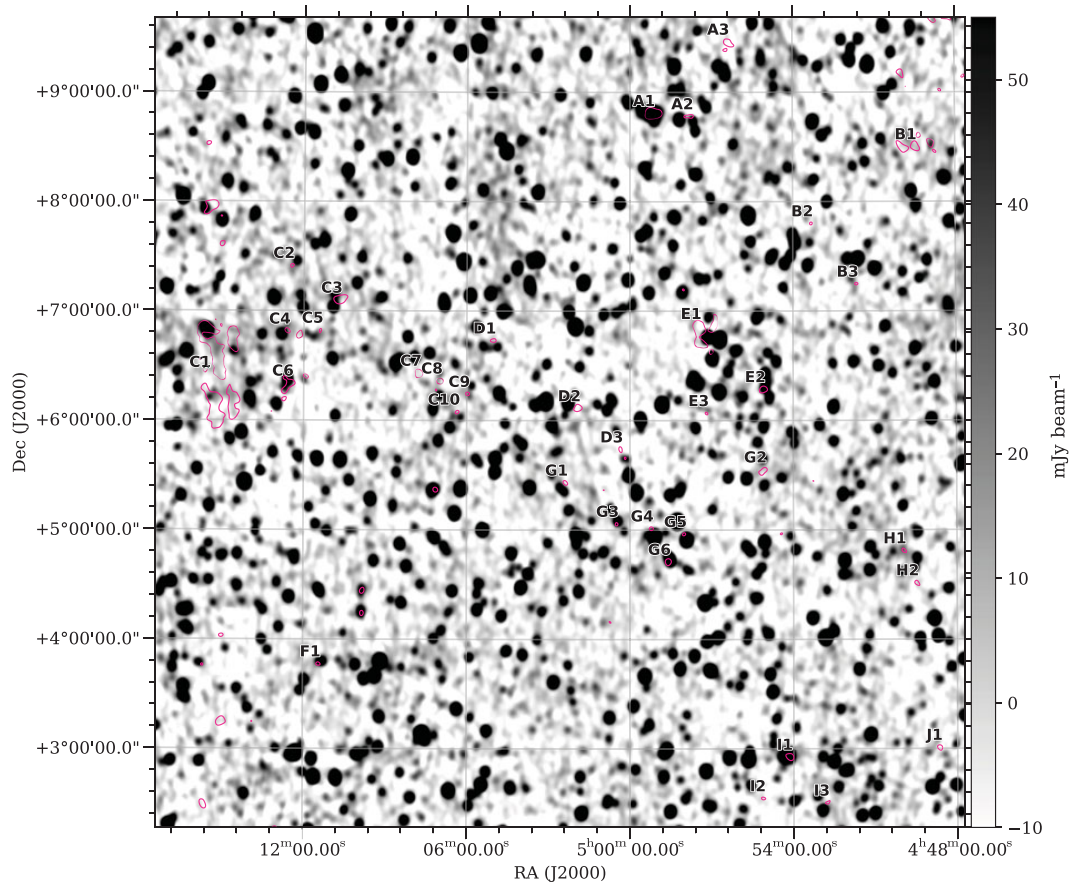


Figure A.3. MWA Phase I at 154 MHz with 3σ SRT+NVSS-diffuse contours in magenta and named regions labelled above and to the left of the contour. The image is scaled linearly between -10 to 55 mJy beam^{-1} so that saturated black indicates a 5σ detection.

B.2 Hodgson et al. (2021b)

Ultra-steep-spectrum radio “jellyfish” uncovered in A2877

[Hodgson, Bartalucci, Johnston-Hollitt, McKinley, Vazza & Wittor \(2021b\)](#)

© AAS 2021. Reproduced with permission.



Ultra-steep-spectrum Radio “Jellyfish” Uncovered in A2877

Torrance Hodgson¹, Iacopo Bartalucci², Melanie Johnston-Hollitt^{1,3}, Benjamin McKinley^{1,4}, Franco Vazza^{5,6,7}, and Denis Wittor⁶

¹ International Centre for Radio Astronomy Research, Curtin University, 1 Turner Avenue, Bentley, 6102, WA, Australia; torrance@pravic.xyz

² INAF-IASF, Via Alfonso Corti 12, I-20133 Milano, Italy

³ Curtin Institute for Computation, Curtin University, GPO Box U1987, Perth, 6845, WA, Australia

⁴ ARC Centre of Excellence for All Sky Astrophysics in 3 Dimensions (ASTRO3D), Bentley, Australia

⁵ Dipartimento di Fisica e Astronomia, Università di Bologna, Via Gobetti 92/3, I-40121, Bologna, Italy

⁶ Hamburger Sternwarte, Gojenbergsweg 112, D-21029 Hamburg, Germany

⁷ INAF, Istituto di Radio Astronomia di Bologna, Via Gobetti 101, I-40129 Bologna, Italy

Received 2020 October 27; revised 2021 January 21; accepted 2021 February 3; published 2021 March 17

Abstract

We report on the discovery of a mysterious ultra-steep-spectrum (USS) synchrotron source in the galaxy cluster A2877. We have observed the source with the Murchison Widefield Array at five frequencies across 72–231 MHz and found the source to exhibit strong spectral curvature over this range, as well as the steepest known spectra of a synchrotron cluster source, with a spectral index across the central three frequency bands of $\alpha = -5.97_{-0.48}^{+0.40}$. Higher-frequency radio observations, including a deep observation with the Australia Telescope Compact Array, fail to detect any of the extended diffuse emission. The source is approximately 370 kpc wide and bears an uncanny resemblance to a jellyfish with two peaks of emission and long tentacles descending south toward the cluster center. While the “USS Jellyfish” defies easy classification, we here propose that the phenomenon is caused by the reacceleration and compression of multiple aged electron populations from historic active galactic nucleus (AGN) activity, a so-called “radio phoenix,” by an as yet undetected weak cluster-scale mechanism. The USS Jellyfish adds to a growing number of radio phoenix in cool-core clusters with unknown reacceleration mechanisms; as the first example of a polyphoenix, however, this implies that the mechanism is on the scale of the cluster itself. Indeed, we show that in simulations, emission akin to the USS Jellyfish can be produced as a short-lived transient phase in the evolution of multiple interacting AGN remnants when subject to weak external shocks.

Unified Astronomy Thesaurus concepts: Galaxy clusters (584); Spectral index (1553); Radio astronomy (1338); Plasma physics (2089); Intracluster medium (858)

1. Introduction

Synchrotron sources typically exhibit power-law behavior in their spectra, such that the observed flux S is related to frequency ν by the relation $S \propto \nu^\alpha$. The spectral index, α , is typically around -0.7 for the lobes of active galactic nuclei (AGNs), and other mechanisms, such as radio halos, relics, and AGN remnants, have been observed to have spectra as steep as -2 . For most of these sources, the spectral index is a well-understood parameter that results from the original injection energy and the aging dynamics of the system.

With the advent of new low-frequency telescopes, in particular the Murchison Widefield Array (MWA; Tingay et al. 2013) and the Low Frequency ARay (LOFAR; van Haarlem et al. 2013), it was widely expected that we would uncover a large, hitherto undetected population of ultra-steep-spectrum (USS) sources only detectable at low frequency (e.g., Enßlin & Röttgering 2002; Cassano et al. 2012, 2015; van Weeren et al. 2019). It was believed that traditionally higher-frequency radio observations introduced an observational bias against sources whose spectra rapidly declined in luminosity with frequency. But these expectations have not been realized. Instead, it appears that the conditions required to produce low-frequency USS synchrotron emission are not particularly common. And for those that we have found, it is all the more important for us to understand the unique conditions that make them possible.

To date, the steepest reported source is in A1033, the so-called “Gently ReEnergised Tail” (GR_{ET}; de Gasperin et al. 2017),

with an integrated spectral index $\alpha = -3.86(3)$. The GR_{ET} is composed of ancient plasma originally ejected from a wide-angle tail radio galaxy and since reaccelerated. The reacceleration mechanism remains unknown, but the authors considered two scenarios: adiabatic compression due to weak shocks and stochastic reacceleration driven by complex turbulence in the tail and interaction with the surrounding intracluster medium (ICM). In this particular instance, they concluded that the latter scenario was more likely. The spectral steepness of the GR_{ET} was so steep that it was only visible at low frequency and became undetectable above 323 MHz.

The GR_{ET} is a kind of radio phoenix, which is a class of synchrotron sources that arises from the reacceleration of ancient but still mildly relativistic ($\gamma > 100$) “fossil” electron populations, usually old AGN cocoons or remnants. Other examples include phoenix in A1664 (e.g., Kale & Dwarakanath 2012), A2256 (van Weeren et al. 2009), and, recently, A1914 (Mandal et al. 2019). In radio phoenix, the underlying fossil electron population is not well mixed with the ICM, and their morphology usually traces out the underlying AGN lobes or tails, albeit made more complex due to diffusion, buoyancy effects, turbulence, and the reacceleration mechanism itself. Radio phoenix rely on a mechanism to reignite an otherwise aged and faded AGN remnant, and adiabatic compression has been suggested as one of these mechanisms (Enßlin & Gopal-Krishna 2001), possibly caused by cluster–cluster interaction. In most radio phoenix to date, however, there is no evidence of shocks, and some are even found in relaxed cool-core clusters, implying that major merger events are not required as a trigger.

Other mechanisms have been suggested, such as the proposed cool-core “sloshing” in the Ophiuchus cluster to account for its giant radio fossil (Giacintucci et al. 2020). Radio phoenix are typically found close to the central cluster region and are usually a few hundred kiloparsecs in size (Feretti et al. 2012). They often exhibit USS ($\alpha < -1.5$) and display spectral curvature, and their spectral index maps typically do not indicate large-scale coherence or trends (see van Weeren et al. 2019 and references therein).

Here we report on the discovery of a diffuse USS radio source to the northwest of A2877, also likely a radio phoenix. The source spans $\sim 740''$ in width, has two bright peaks of emission associated with cluster members, and has tentacles of emission that extend south toward the cluster core, giving the impression of a jellyfish. The “USS Jellyfish” was first detected in images from the Galactic and Extra-galactic All-sky MWA survey (GLEAM; Wayth et al. 2015) by searching for steep-spectrum sources. Due to its extreme spectral steepness, it had no detectable counterpart in the highest-frequency GLEAM images centered at 200.5 MHz and thus did not form part of the original GLEAM catalog (Hurley-Walker et al. 2017). GLEAM was conducted with the lower-resolution phase I of the MWA (Tingay et al. 2013), resulting in a blended source that made determining its morphology difficult. This prompted the follow-up radio observations we present here with the higher-resolution MWA phase II (extended configuration; Wayth et al. 2018) and the Australia Telescope Compact Array (ATCA; Frater et al. 1992), as well as reprocessed archival XMM-Newton X-ray observations.

Throughout, we assume a flat Λ CDM cosmology with Hubble constant $h = 0.677$ and matter density $\Omega_m = 0.307$, of which the baryonic density is $\Omega_b = 0.0486$. All coordinates are with respect to the J2000 epoch. All stated errors indicate one standard deviation.

1.1. A2877

From the southern catalog of Abell (1989), A2877 is a nearby low-mass cluster in the southern sky at a redshift of $z \approx 0.0238$, an estimated mass $M_{500} = 7.103 \times 10^{13} M_\odot$, and radius $r_{500} = 0.6249$ Mpc (Piffaretti et al. 2011). The cluster was classified by Abell as “poor,” having a richness class $R = 0$. It was also cataloged earlier as DC 0107–46 in Dressler (1980), where it was suggested that, in fact, it may form a single cluster with nearby A2870 (DC 0103–47), which is centered approximately 4.9 Mpc away.

The cluster has two distinct substructures, a core and a substructure to the north, which have been identified from optical data of members of the cluster (Girardi et al. 1997; Flin & Krywult 2006).

Cluster A2877 has previously been the subject of radio observations with ATCA at 1.4 GHz as part of the Phoenix Deep Survey (Hopkins et al. 2000). This study detected 15 cluster members at this frequency, of which 14 had spectroscopic observations. These spectra allowed for the classification of six of these galaxies as low-luminosity AGNs, one as a Seyfert 2 galaxy, two as star-forming, and the remaining five indeterminately star-forming, low-luminosity AGNs, or both. The cluster was otherwise radio-quiet.

Table 1
Radio Observations and Respective Image Properties

	Frequency MHz	Weight	Resolution	PA	Noise mJy beam ⁻¹
MWA	87.5	0	$151 \times 97''$	150°	4.9
	118.5	0.5	$123 \times 87''$	150°	1.9
	154.5	1	$108 \times 83''$	150°	1.3
	185.5	1	$93 \times 68''$	151°	0.91
	215.5	1	$77 \times 58''$	151°	0.86
ATCA	1548.5	0	$11.8 \times 4.1''$	15°	0.024
	1998.5	0	$10.1 \times 3.4''$	19°	0.023
	2448.5	0	$8.6 \times 2.8''$	19°	0.027
	2899	0	$8.0 \times 2.5''$	17°	0.030

Note. The MWA observations occurred in 2018 August for a duration of 2.4 hr with 30.72 MHz bandwidths. The ATCA observations occurred in 2018 January for a duration of 14 hr and have been imaged here with bandwidths of 448 MHz. The baseline weight value refers to the Briggs robustness parameter, and the position angle (PA) of the beam is measured north through east.

2. Data and Methods

2.1. ATCA

On 2018 January 16 and 17, A2877 was observed with ATCA across two observation windows for a total of 11 hr. The observations were undertaken at a central frequency of 2.1 GHz with a bandwidth of just over 2 GHz; however, due to radio frequency interference, this band was later truncated below 1325 MHz. The observations were conducted in the 750A configuration, which consists of baselines ranging from 77 to 750 m, with an additional set of baselines ranging in length from 3015 to 3750 m produced by the inclusion of the distant, fixed-position sixth antenna. These shortest baselines give angular sensitivity up to scales of $\sim 9'$ at 1.5 GHz, sufficient to detect the large-scale features of the USS Jellyfish.

Initial calibration and flagging were performed with the *miriad* suite of tools (Sault et al. 1995). The primary calibrator for each observation window was PKS 1934–638, and a secondary calibrator, PKS 0048–427, was observed periodically throughout to ensure phase calibration. We imaged the observation using *WSClean* (Offringa et al. 2014) and the new *WGridder* back end (Arras et al. 2021). The band was separated into four equally sized output channels using its multifrequency synthesis algorithm (Offringa & Smirnov 2017), the baselines were weighted using the Briggs scheme with robustness parameter zero, and cleaning was performed down to the image noise inside a mask set at a factor of 3 times the noise. Three rounds of phase-only self-calibration were performed using *CASA* (McMullin et al. 2007) before producing the final images (see Table 1).

2.2. MWA

The MWA observed A2877 in its phase II extended configuration from 2018 August 4 to 14. The observations spanned a bandwidth of 30.72 MHz and were centered variously at 87.5, 118.5, 154.5, 185.5, and 215.5 MHz. The cluster was observed in 2 minute long “snapshots” cumulatively for about 2.4 hr at each frequency band.

All calibration was performed using an in-field model, in contrast to traditional primary calibration workflows. The radio sky model used here was derived from the GLEAM catalog

(Hurley-Walker et al. 2017) and consisted of the few hundred sources in the field that had an apparent brightness of 1 Jy or more. These sources were predicted into model visibilities based on the primary beam model (Sokolowski et al. 2017) and subsequently used as the model to obtain the calibration Jones matrices.⁸ The calibration was checked after imaging by source finding on the final mosaics and comparing with the input catalog; the median flux ratio for each band was 1.00(1), and the spread was $\leq 3\%$.

Imaging was performed using `WSClean` on individual 2 minute snapshots. This is necessitated by the time-dependent phased-array beam of the MWA, such that 2 minutes is about as long as we can safely assume a constant beam. The images were produced by splitting the 30.72 MHz bandwidth into four equally sized subbands and deconvolved using multiscale cleaning. Each snapshot was phase-rotated to a common phase center and imaged onto a common projection. The final mosaics were produced by the following process: (i) each of the residual images, clean component images, and point-spread function (PSF) images were stacked and weighted inversely by the square of the mean noise of the snapshot and the local beam response; (ii) the stacked PSF was fitted with an elliptical Gaussian; and (iii) this Gaussian was used to convolve the stacked clean components before being recombined with the stacked residuals.

Imaging and cleaning on 2 minute intervals poses significant problems for faint sources. Faint sources remain buried in the noise of individual snapshots and are therefore not cleaned; they only rise to the level of detection when the residuals are themselves stacked. To mitigate this problem, we performed a final joint deconvolution step on the combined mosaics, performing an image-based clean with the combined PSF. The effect of this additional clean procedure was most marked on the lowest band, for which we saw an approximately 20% increase in recovered flux for the USS Jellyfish; on the higher bands, this effect was negligible.

The final weighting, resolution, and noise properties are described in Table 1. The noise properties of these mosaics are the lowest published to date with the MWA and thus provide excellent upper thresholds for detecting the steep radio emission present in A2877.

2.3. Spectral Index and Image Map

The integrated flux of the USS Jellyfish was calculated by using a mask that extended out to the 1σ boundary of the USS Jellyfish in the 87.5 MHz image and summing the flux for each respective MWA image over this mask. Embedded point sources were subtracted from the integrated sum, where their respective flux density was estimated based on fitting simple power-law functions to measurements from all four ATCA bands, the 887 MHz Rapid ASKAP⁹ Continuum Survey (RACS) mosaic (McConnell et al. 2020), and the 215.5 MHz MWA image (see Table 2). To be included, point sources required a detectable counterpart at the 1.5σ level in the highest-frequency MWA image to help constrain the measurement and filter sources that exhibited a turnover at higher frequencies. Errors were calculated in quadrature based on 5%

⁸ This work is the first published work to use an updated and significantly faster reimplementation of the MWA calibration software, which is publicly available at <https://github.com/torrance/MWAjl>.

⁹ Australian Square Kilometre Array Pathfinder.

Table 2
Radio Point Sources that Overlap with the Integrated Flux Mask

R.A. (deg)	Decl. (deg)	S_{200} (mJy)	Spectral Index	Label
17.269	-45.77	12.2(2)	-0.47(1)	A
17.443	-45.78	5.4(5)	-0.85(2)	B
17.480	-45.93	6.4(11)	-0.66(4)	cD
17.444	-45.83	4.4(11)	-0.40(6)	E

Note. Values are derived from fitting a power law to RACS, ATCA, and the 215.5 MHz MWA image.

absolute flux error, 10% point-source error, and local map noise. The local map noise dominates the measurements at the highest frequency due to the large area over which the flux is summed and the proportionally faint emission present.

Spectral index values, both multiband and pairwise, have been calculated using a bootstrapping technique with 100,000 samples to propagate errors. Stated values represent the median value over all samples, and errors indicate the 15.9th and 84.1st percentile values. In the case where the lower error bounds produce negative flux values, we have included only the 84.1st percentile value as an upper bound.

The spectral image map was produced from the lowest three MWA bands at 87.5, 118.5, and 154.5 MHz; the higher band images were not used, as they contained little of the extended diffuse emission. The snapshots at these three bands were imaged with identical pixel resolution, projection, and phase center so as to avoid having to resample and interpolate later. The images were convolved to the common resolution of the 87.5 MHz image. We then employed a bootstrapping technique with 1000 samples to estimate the spectral index and associated error for each pixel across the three images. Point-source subtraction was not performed.

2.4. XMM-Newton

The XMM-Newton observation of A2877 consists of six pointings taken using the European Photon Imaging Camera (Strüder et al. 2001; Turner et al. 2001) for a total exposure time of 475 ks.¹⁰ Each observation was reduced using the Science Analysis System version 18.0.0 and applying the latest calibration files available as of 2019 December. We removed from the analysis observation intervals affected by flares following the procedures described in Pratt et al. (2007), yielding 420 ks of useful time. The pointings were combined to maximize the signal-to-noise ratio. Exposure maps, models of the sky, and instrumental background were computed as described in Bourdin & Mazzotta (2008), Bourdin et al. (2013), and Bogdán et al. (2013). Finally, we identified and removed point sources using the wavelet detection technique of Bogdán et al. (2013).

Unfortunately, the northwest sector of the cluster that hosts the USS Jellyfish is covered by only a single pointing with low exposure time. For this reason, the brightness and temperature maps are not sufficiently deep to investigate the presence of faint or subtle features.

¹⁰ Observation IDs 0801310101, 0693060401, 0693060301, 0655510201, 0560180901, and 0204540201.

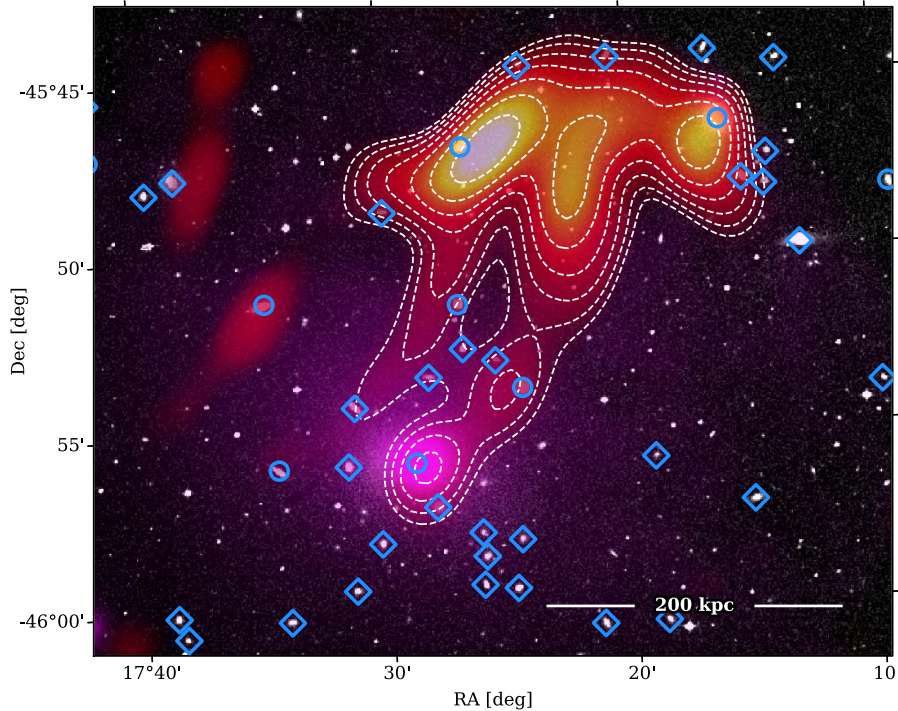


Figure 1. Composite image of the USS Jellyfish in A2877 showing the optical Digitized Sky Survey (background) with XMM X-ray data (magenta overlay) and MWA 118.5 MHz radio data (red-yellow overlay). Contours are provided for the MWA overlay ranging from $7.3 \text{ mJy beam}^{-1}$ and increasing by factors of $\sqrt{2}$, but for clarity, they are restricted only to the USS Jellyfish proper. Blue circles indicate cluster radio sources from Hopkins et al. (2000), and blue diamonds indicate positions of other probable cluster members based on redshift proximity.

3. Results

We present the USS Jellyfish in Figure 1 as a composite image combining the optical Digitized Sky Survey (background) with wavelet-cleaned XMM X-ray data (magenta overlay) and MWA 118.5 MHz radio data (red-yellow overlay). Blue circles indicate known radio-emitting cluster sources from Hopkins et al. (2000), while blue diamonds indicate probable cluster members based on available redshift data. The X-ray emission shows the core overdensity of A2877, to which the radio emission is offset to the northwest. The radio emission resembles a jellyfish, with western and eastern peaks of emission in the head, and likewise western and eastern tentacles that descend south toward the cluster core. The full angular extent of the USS Jellyfish from east to west is $\sim 740''$, which at the redshift of A2877 corresponds to $\sim 370 \text{ kpc}$ in projection.

Figure 2 shows the emergence of the USS Jellyfish from near undetectability at 215.5 MHz to an integrated flux of $1.10(15) \text{ Jy}$ at 87.5 MHz, approximately 275 times more luminous. At this lowest frequency, the integrated flux corresponds to a total radio luminosity of $L_{87.5\text{MHz}} = (1.59 \pm 0.22) \times 10^{24} \text{ W Hz}^{-1}$, assuming a redshift $z = 0.0238$.

The steepness of the spectra is extreme and shows significant curvature, as can be seen in Figure 3. This figure shows the integrated flux measured in each band, linearly interpolated (gray dashed line), while Table 3 additionally provides pairwise spectral

Table 3

The Integrated Flux of the USS Jellyfish at Each MWA Band and Pairwise Spectral Indices

Frequency MHz	Flux Density Jy	Spectral Index
87.5	1.10 ± 0.06	$\alpha_{87.5}^{118.5} = -2.16^{+0.27}_{-0.27}$
118.5	0.57 ± 0.03	$\alpha_{118.5}^{154.5} = -4.87^{+0.38}_{-0.39}$
154.5	0.16 ± 0.01	$\alpha_{154.5}^{185.5} = -7.8^{+1.1}_{-1.3}$
185.5	0.038 ± 0.008	$\alpha_{185.5}^{215.5} < -9.2$
215.5	0.003 ± 0.007	

Note. We provide only an upper bound for the highest-frequency pairwise spectral index, as the integrated flux measurement at 215.5 MHz is consistent with zero.

indices. If we attempt a power-law fit ($S \propto \nu^\alpha$) to the three central bands, we find a spectral index value of $\alpha = -5.97^{+0.40}_{-0.48}$.

Unsurprisingly, higher-frequency observations show no extended emission that is coincident with the USS Jellyfish. The previously stated spectral index would give a total integrated flux at 887 MHz of just $4 \mu\text{Jy}$. Thus, at 887 MHz, the respective RACS mosaic, with a local noise of $220 \mu\text{Jy beam}^{-1}$, shows no emission besides point-source emission from A2877 galaxy members; additional convolution steps to emphasize extended diffuse emission also do not reveal any signal. Similarly, the lowest-frequency band of our ATCA observation at 1548.5 MHz, with a local noise of $52 \mu\text{Jy beam}^{-1}$, does not reveal any of the

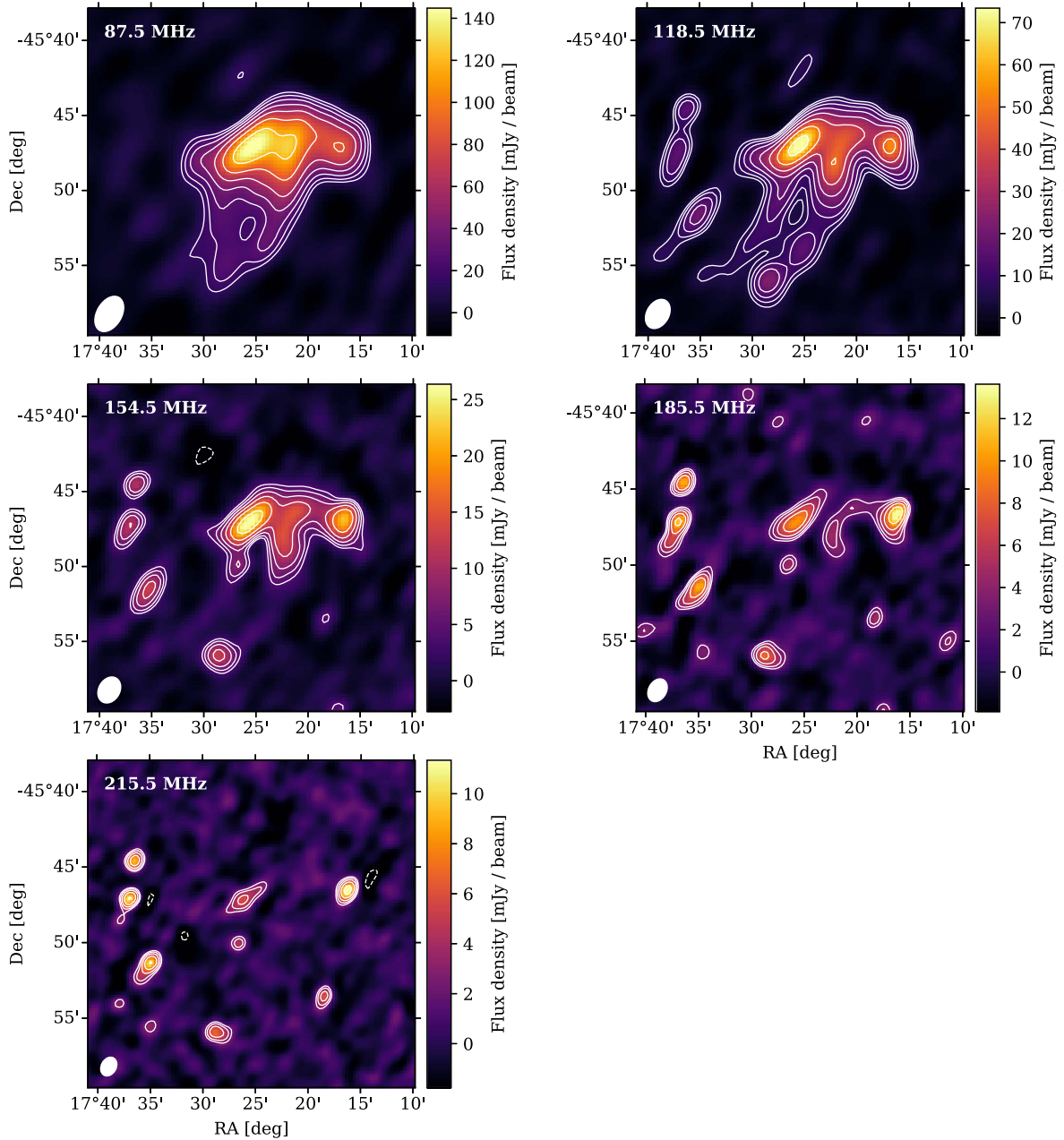


Figure 2. The MWA images of the USS Jellyfish across all five bands. Positive contours start at 3σ , increase by factors of $\sqrt{2}$, and are indicated by solid white lines. Negative contours start at -3σ , scale similarly, and are indicated by dashed white lines.

extended emission of the Jellyfish, nor do the higher-frequency ATCA bands.

There are three radio-emitting members of A2877 entangled in the USS Jellyfish that are detectable in the 215.5 MHz MWA image, and there is a fourth background source. In Figure 4, we show the combined ATCA observation centered at 2223.5 MHz overlaid with contours from the MWA at 215.5 and 118.5 MHz.

In the highest-frequency MWA image, we identify two sources of emission, labeled A and B, that at lower frequencies are closely associated with the bright western and eastern peaks at the head of the USS Jellyfish. At 215.5 MHz, the radio emission at A and the E/S0 galaxy ESO 243 G 045 are well aligned. There is evidence of a slight southeast elongation of the emission, and indeed, at lower frequencies, the western peak shifts slightly southeast from

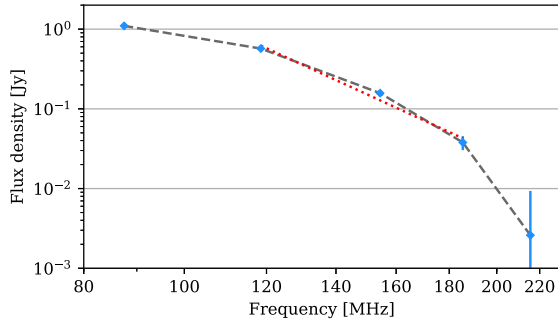


Figure 3. Plotted values of the integrated flux of the USS Jellyfish, which make the curvature apparent. By fitting a power law across the central three frequencies (red), we find a spectral index value of $\alpha = -5.97_{-0.48}^{+0.40}$.

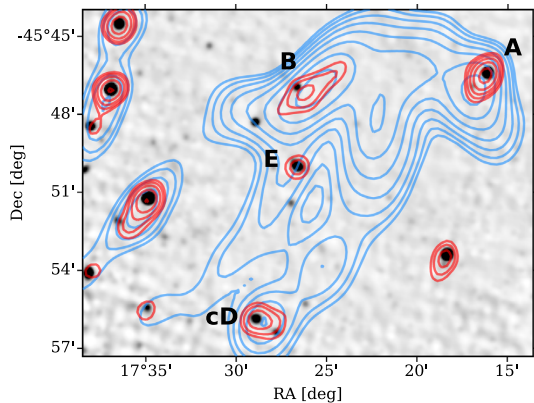


Figure 4. Combined ATCA observation centered at 2223.5 MHz with full 1.8 GHz bandwidth. For display purposes, it is convolved down to a circular $15''$ resolution, giving a local rms noise of $28 \mu\text{Jy beam}^{-1}$. The color scale ranges from -0.1 to 0.5 mJy and is set to saturate the majority of the ATCA sources. Contours show MWA 118.5 (blue) and 215.5 (red) MHz. The labels indicate three cluster members: (A) ESO 243 G 045, (B) WISEA J010946.55–454657.4, and (cD) IC 1633. Additionally, (E) indicates the position of a background radio galaxy.

A. Source B is offset slightly to the southwest of S0 galaxy WISEA J010946.55–454657.4. The northwest alignment of the emission of source B at 215.5 MHz remains visible at lower frequencies, suggesting continuity of the emission source. Hopkins et al. (2000) had previously classified both of these radio sources: ESO 243 G 045 as a low-luminosity AGN and WISEA J010946.55–454657.4 unambiguously as a Seyfert 2 galaxy. Source cD is the central cluster galaxy, IC 1633, and in the lower-frequency bands, the western tentacle bridges this source to the rest of the emission. It is identified by Hopkins et al. (2000) as hosting an AGN, and both their ATCA observation and ours show nearby faint emission to the northeast that may indicate a small jet. A background radio galaxy ($z = 0.545$; Afonso et al. 2005) with resolved $\sim 15''$ jets is also visible in the MWA images and is labeled E.

The spectral index map (Figure 5) shows no overall trend in the spectral index values across the full extent of the emission. Instead, we observe a patchwork of islands of shallower emission, surrounded by more diffuse and steeper emission. Both the western and eastern peaks of emission at the head of

the USS Jellyfish are associated with flatter spectra, as is the emission coincident with the cD galaxy itself and the background radio galaxy E. Note that the lower spectral index values at the western and eastern peaks are not simply caused by a bias introduced from point sources A and B, since both are offset to their respective galaxy counterparts. The rest of the extended emission has a spectral index of around -4 , and at some edges and along the western tentacle, the spectrum tends steeper still.

From the X-ray, we observe that A2877 strongly resembles a cool-core cluster, with the core being X-ray bright and having a temperature of ~ 2 keV. In Figure 6, we show the exposure-corrected and background-subtracted X-ray surface brightness profile of the northwest sector in the 0.5–2.5 keV band (blue points) alongside the radio surface brightness profile of the USS Jellyfish at 118.5 MHz (dashed gray line). There is no evidence for a shock or cold front in this sector; however, it remains possible that this is due to the poor data in this sector or that the feature is intrinsically faint due to projection effects.

4. Discussion

The USS emission on cluster-sized scales points to only a handful of plausible mechanisms to account for its spectral steepness: radio relics and halos, AGN remnants, and reaccelerated AGN plasma or “phoenix.”¹¹ We can readily discount halos, as the emission is significantly offset from the cluster core, and radio halos trace the baryonic content of the cluster. Radio relics trace large-scale cluster shocks and usually appear toward the periphery of a cluster, although they have been observed more centrally. Relics have values for α of typically -1 to -1.5 and often display large-scale coherency in their spectral index map, indicating the direction of the shock, which we do not observe here. Their morphology is usually long and narrow, as they trace the bow of the shock. The spectral index of a relic is related to the shock strength and, assuming diffusive shock acceleration (DSA) on a purely thermal plasma and a conservatively shallow value of $\alpha_{\text{inj}} < -3$, we find a shock Mach number $\mathcal{M} < 1.3$.¹² Modeling of DSA by Hoeft & Brüggén (2007) shows that the efficiency of electron acceleration is strongly dependent on the Mach number, and for shocks $\mathcal{M} < 3$, their models show a rapid and exponential decrease in this efficiency. In the case of the USS Jellyfish, and without recourse to a significant fossil electron population (e.g., see models by Kang & Ryu 2011; Pinzke et al. 2013), such a truly gentle shock is an exceptionally inefficient electron accelerator. For these reasons, we deem the radio relic hypothesis unlikely.

An AGN remnant is another potential scenario, as models for synchrotron aging predict a steepening spectral index, increasing spectral curvature, and decreasing “break frequency” (e.g., Kardashev 1962; Pacholczyk 1970, “KP model”; Jaffe & Perola 1973, “JP model”). None have been observed to be as steep as observed here; however, it is possible that we are observing the remnant in a frequency range above the break frequency. If we assume the break frequency to be < 70 MHz

¹¹ See van Weeren et al. (2019) for an excellent review of each of these phenomena.

¹² It should be noted that Mach numbers derived from radio and X-ray typically disagree, and values derived from radio are overestimated when compared to those derived from X-ray. See review discussion in van Weeren et al. (2019).

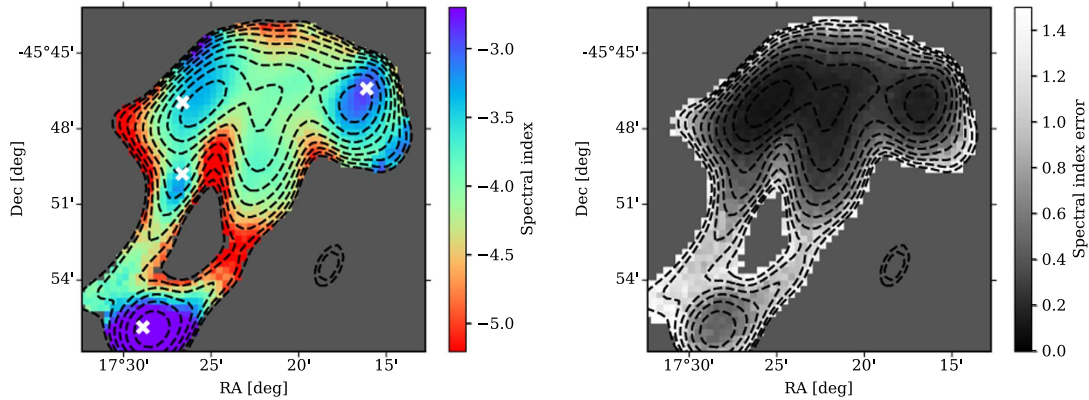


Figure 5. Spectral image map calculated across the lowest three MWA bands, with the locations of point sources from Table 2 indicated with white crosses. The map shows cocoons of shallower-spectrum emission slightly offset from points A and B, as well as aligned with points cD and E, while elsewhere, we observe much steeper emission. Left: spectral index values. Right: respective error map generated using a bootstrapping method.

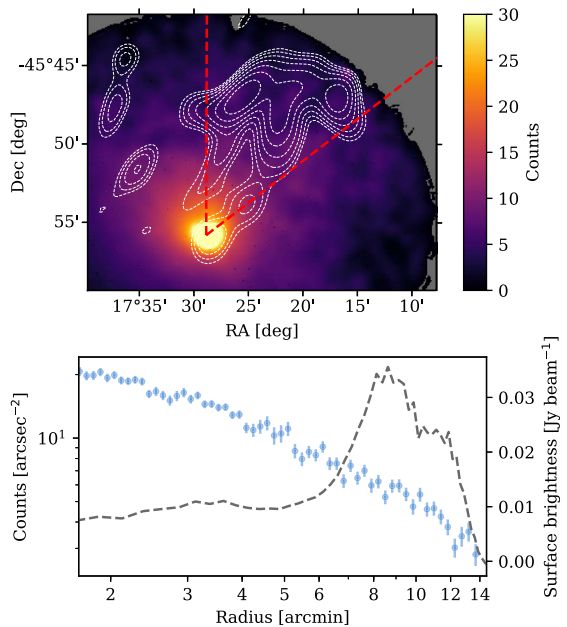


Figure 6. Top: wavelet denoised map of the XMM-Newton image in the 0.5–2.5 keV band produced following Bourdin et al. (2004), with overlay from MWA 118.5 MHz (dashed white lines). Dashed red lines indicate the extent of the northwest sector. Bottom: X-ray count density (blue points) and the MWA 118.5 MHz mean surface brightness (dashed gray line) throughout the northwest sector as a function of radial distance from the cluster core. There is no indication of a shock or cold front.

and the cluster magnetic field strength to be in the range of ≈ 0.01 – $1 \mu\text{G}$,¹³ we find a synchrotron age for the USS Jellyfish of at least 24–220 or 53–490 Myr, based on the KP and JP models, respectively. This is significantly older than any known AGN remnant, and indeed, recent simulations suggest

¹³ For example, measurements of the magnetic field in A3667 find values of approximately 1–3 μG (Johnston-Hollitt 2004; Riseley et al. 2015). The 0.01 μG lower bound is a conservative value derived from equipartition assumptions of the electric and magnetic field.

rapid cooling and dimming of radio lobes after AGN shutdown due to adiabatic losses on the order of just millions of years (Godfrey et al. 2017; English et al. 2019). It is unlikely that the USS Jellyfish is an undisturbed AGN remnant.

Instead, our principal hypothesis is that it is far more likely that the USS Jellyfish is composed of multiple radio phoenix—a polyphoenix—triggered by a common large-scale shock or compression occurring to the northwest of A2877. The strongest evidence for this consists of the western and eastern peaks of emission and their association with nearby point sources A and B, respectively. Both peaks are the least steep components of the spectral image map, indicating a cocoon of younger, more energetic electrons that envelop cluster members ESO 243 G 045 and WISEA J010946.55–454657.4. We suggest that the shallower-spectrum component at the western peak, though it is offset to the southeast of source A, is directly related to emission from ESO 243 G 045. We also suggest that the elongated eastern peak is the product of a pair of weak AGN jets originating from source B, WISEA J010946.55–454657.4; the slight offset likely indicates that this activity was historic. Moreover, the eastern spur of the jellyfish head can be explained by deflection of the south-eastern jet of source B by the denser, more central ICM. While both electron populations would have rapidly dimmed if unperturbed, we suggest that they have been compressed and reignited by some external mechanism(s).

The large-scale, more diffuse emission of the USS Jellyfish, as well as its tentacles, remains difficult to explain. The eastern extension from ESO 243 G 045 that is visible at 185.5 MHz is suggestive of either a lobe from a previously active epoch of AGN activity or a tail. If it is the latter, one plausible explanation is that both tentacles are the reenergized tail of ESO 243 G 045 that sweeps south toward the core of the cluster. An alternative explanation would be to invoke the cD galaxy IC 1633 as a third electron source, since the western tentacle, and to some degree the eastern, establishes a bridge of emission to this source.

The fact that multiple disparate electron populations have been reaccelerated strongly suggests a common large-scale reacceleration mechanism. As the XMM observation shows, there is presently no evidence of a shock in the northwest sector; moreover, it appears that A2877 is a relaxed, cool-core

cluster and therefore unlikely to be currently subject to disruptive merger events or other large-scale structure formation processes that could trigger such a large-scale shock. Cool-core sloshing, which is identified in the X-ray by the presence of spiral or arc-shaped cold fronts about the central core, is an alternative mechanism that is triggered by instabilities acting upon the deep gravitational well at the centers of cool-core clusters (e.g., see Ascasibar & Markevitch 2006; Ghizzardi et al. 2010; Vazza et al. 2012). Indeed, the previously identified northern substructure in A2877 may provide just such an instability. While this mechanism has typically been invoked to explain centrally located “mini-halos” (e.g., Giacintucci et al. 2014), cold fronts associated with cool-core sloshing have been observed up to 1 Mpc away (Simionescu et al. 2012; Rossetti et al. 2013). However, until we can obtain both high-resolution and high-sensitivity X-ray observations of the cluster, the existence and nature of any shocks in the system must remain purely speculative.

Of special note, the spectral index map of the USS Jellyfish indicates spectra that are still strongly correlated with the original plasma age. In a standard DSA scenario, a strong shock would have imprinted the strength of the shock itself on the spectrum of the plasma and would display the same kind of large-scale coherence observed in the spectral index maps of many relics. We can thus infer a particularly gentle shock, and, based on our current understanding of DSA physics and the inefficiency of weak shocks, we can also infer the existence of a significant population of suprathermal electrons throughout the northwest sector of A2877, further reinforcing the phoenix hypothesis. Additionally, adiabatic compression of AGN cocoons akin to that originally described in Enßlin & Gopal-Krishna (2001) is another complimentary mechanism. Indeed, due to the higher speed of sound in the cocoon environment, shock waves will only poorly penetrate the AGN cocoons, and DSA would thus be of negligible effect. Their modeling suggests that adiabatic compression can boost the luminosity of the AGN cocoons without a significant flattening of the original spectrum, thus preserving the underlying aged spectra. Such compression, however, is unlikely to explain the large-scale diffuse radio emission observed exterior to the AGN cocoons. We also raise the possibility of a third reacceleration mechanism, local turbulence in the wake of a weak shock between interacting AGN lobes, powering Fermi II acceleration processes.

To explore a possible formation scenario for the USS Jellyfish, we turn to a recent suite of magnetohydrodynamical simulations by Vazza et al. (submitted). In one of these scenarios, we have identified a polyphoenix akin to the USS Jellyfish as a transient feature in the evolving ICM. In these simulations, light jets (i.e., filled by hot gas and magnetic fields) were released by AGN particles in the simulation within a forming galaxy cluster with a total mass of $M_{100} \approx 1.5 \times 10^{14} M_{\odot}$. For the runs used in this comparison, the AGN jets were initiated at the same epoch for the four most massive AGNs in the simulation, all located within $\sim 1 \text{ Mpc}^3$ (comoving) and each releasing $\sim 10^{57}$ erg of feedback energy into the surrounding medium in the form of kinetic, thermal, and magnetic energy. The model for the spectral energy evolution of relativistic electrons is similar to the one presented in Vazza et al. (2021) and we describe it briefly here. The spatial propagation of relativistic electrons injected by AGNs is followed in postprocessing using a Lagrangian advection

algorithm, as detailed in Wittor et al. (2020). The spectral energy evolution is modeled by numerically integrating Fokker–Planck equations of an initial power-law distribution of electron momenta, $N(\gamma) \propto \gamma^{-2}$, in the range of $\gamma_{\min} = 50$ and $\gamma_{\max} = 10^5$ (where γ is the Lorentz factor of electrons). We consider continuous energy transfer via synchrotron emission, inverse Compton scattering, Coulomb collisions, adiabatic compression/expansion, and injection and reacceleration of electrons from shock induced DSA (e.g., Kang et al. 2012). The AGNs produced by such a model are compatible with FR II morphologies and start with a radio luminosity of $\sim 10^{40} - 10^{41} \text{ erg s}^{-1} \text{ Hz}^{-1}$ at 120 MHz. The lobes of these AGNs spatially evolve by diffusing into the ICM and rapidly fade in the radio band due to adiabatic losses and radiative cooling, except when perturbations in the ICM reaccelerate fossil electron spectra via adiabatic compression and, most importantly, DSA processes. Turbulent reacceleration processes have not been included.

By visually inspecting the radio emission maps of all snapshots in the simulation, we identified a short ($\sim 100 - 250 \text{ Myr}$) evolutionary stage, some 2.2 Gyr after the original AGN outburst, during which the aging lobes released by three of the four AGNs produced a radio morphology that loosely resembles the USS Jellyfish in extent, total power, and radio spectral slope.¹⁴ In the epochs prior, the AGN lobes rapidly dimmed; however, a confluence of factors causes a transient rebrightening coinciding with the mixing of three of the four ancient lobes at the same time as the passing of several weak shocks ($M < 2$) triggered by both cluster growth and interactions of the AGN lobes themselves. The top panel of Figure 7 shows the contours of radio emission at 120 MHz from this snapshot if the source were placed at the same distance as A2877, with contours marking $\geq 7 \text{ mJy beam}^{-1}$ regions, while the colors give the spectral index in the 87–150 MHz frequency range. At least qualitatively, the detectable emission in the simulated emission map resembles the complex shape of the real USS Jellyfish, including its elongated threads and radio substructures in the “head.” The spectral index map has a rather uniform distribution with $\alpha \sim -3$, with some patches of steeper emission in the threads. This model takes into account the role of weak shock (re)acceleration in the ICM, driven by matter accretion events that took place in the host cluster after the injection of jets. The middle panel shows the same snapshot but without “cluster weather”—that is, excluding all ICM interactions, such as weak shocks induced by gas motions associated with cluster growth—and points to the necessity in this particular case for these external mechanisms to draw out the tentacles and filamentary structures. The bottom panel shows the dark matter density, which, as a proxy for the location of galaxies in the simulation, shows that three of the peaks in the radio emission still closely align with their host galaxies, even after significant evolution of the system.

This simulation tentatively suggests that multiple aging and interacting AGN plasmas, alongside weak shock-induced adiabatic compression and DSA, are a plausible and sufficient explanation for diffuse and very steep cluster emission like the USS Jellyfish, and that alternative mechanisms, such as those developed to explain the GReET, are not necessarily required here. The simulation also shows the potential rarity of the

¹⁴ Movies of the evolution of radio emission in these simulations are available at <https://vimeo.com/491986204> and <https://vimeo.com/491983312>.

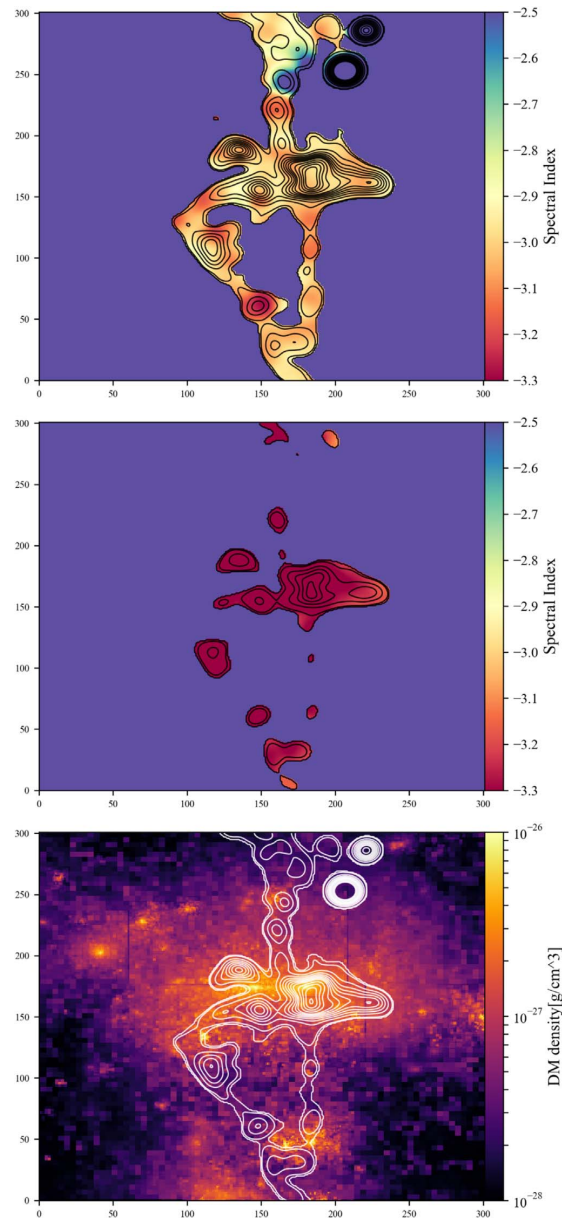


Figure 7. Top: simulated radio emission contours at 120 MHz for our baseline model for electrons. Contours start at 7 mJy beam^{-1} and increase by factors of $\sqrt{2}$. The emission has been convolved to the stated resolution of the MWA 118.5 MHz image, $123'' \times 87''$, and the spatial scale in the image is 5 kpc pixel^{-1} . Middle: same as the top panel but without the inclusion of “cluster weather.” Bottom: dark matter density, where concentrations indicate the presence of galaxies and show the approximate alignment of radio peaks with their original host galaxies.

scenario due to both its short-lived, transient nature in a lengthy 2.2 Gyr evolution and the requirement for an otherwise radio-quiet cluster across the remainder of that evolution.

5. Conclusion

We have reported on the discovery of the steepest-spectrum synchrotron source to date, the USS Jellyfish, which lies to the northwest of the cluster A2877. We have argued that the source is a polyphoenix: that is composed of multiple aged and mixed AGN populations reaccelerated by a common large-scale event. The currently available X-ray data do not show the presence of cold fronts, sloshing, or other shock systems in the cool-core cluster; however, the quality of these data likely means that weak shocks are undetectable. We have also presented recent magnetohydrodynamic simulations showing that a combination of weak shocks inducing standard DSA and adiabatic compression and acting upon ancient interacting AGN plasmas are capable of producing diffuse, USS emission akin to the USS Jellyfish without recourse to other, more exotic (re) acceleration mechanisms. These same simulations show that the USS Jellyfish may also be a short-lived, transient phase in the evolution of the system.

Follow-up work on A2877 should make high-sensitivity and high-resolution X-ray observations of A2877 a priority in an effort to discern the presence and nature of any shocks in the northwest and detect telltale signs of cool-core sloshing that may be present. Additionally, both higher-resolution and higher-sensitivity radio observations of the USS Jellyfish may provide us with a better picture of its morphology; however, the incredible steepness of its spectrum makes follow-up observations above 300 MHz unlikely to detect any of the extended emission. We may have to wait for the development of SKA Low for a higher-resolution, low-frequency telescope able to observe so far south.

The authors thank Benjamin Quici for helpful discussions during the preparation of this manuscript. This scientific work makes use of the Murchison Radio-astronomy Observatory, operated by CSIRO. We acknowledge the Wajarri Yamatji people as the traditional owners of the observatory site. Support for the operation of the MWA is provided by the Australian Government (NCRIS) under a contract to Curtin University administered by Astronomy Australia Limited. We acknowledge the Pawsey Supercomputing Centre, which is supported by the Western Australian and Australian Governments. The Australia Telescope Compact Array is part of the Australia Telescope National Facility, which is funded by the Australian Government for operation as a National Facility managed by CSIRO. F.V. acknowledges financial support from the ERC Starting grant MAGCOW, No. 714196. The cosmological simulations in Section 4 were performed with the ENZO code (<http://enzo-project.org>) under projects “stressicm” and “hhh44” at the Jülich Supercomputing Centre (PI: F. Vazza). D.W. is funded by the Deutsche Forschungsgemeinschaft (DFG, German Research Foundation) 441694982.

ORCID iDs

Torrance Hodgson <https://orcid.org/0000-0003-3443-7123>

Iacopo Bartalucci <https://orcid.org/0000-0001-7703-9040>

Melanie Johnston-Hollitt <https://orcid.org/0000-0003-2756-8301>

Benjamin McKinley <https://orcid.org/0000-0002-9006-1450>

Franco Vazza <https://orcid.org/0000-0002-2821-7928>

References

- Abell, G. O., Corwin, H. G. J., & Olowin, R. P. 1989, *ApJS*, **70**, 1
- Afonso, J., Georgakakis, A., Almeida, C., et al. 2005, *ApJ*, **624**, 135
- Arras, P., Reinecke, M., Westermann, R., & Enßlin, T. A. 2021, *A&A*, **646**, A58
- Ascasibar, Y., & Markevitch, M. 2006, *ApJ*, **650**, 102
- Bogdán, Á., Forman, W. R., Vogelsberger, M., et al. 2013, *ApJ*, **772**, 97
- Bourdin, H., & Mazzotta, P. 2008, *A&A*, **479**, 307
- Bourdin, H., Mazzotta, P., Markevitch, M., Giacintucci, S., & Brunetti, G. 2013, *ApJ*, **764**, 82
- Bourdin, H., Sauvageot, J. L., Slezak, E., Bijaoui, A., & Teyssier, R. 2004, *A&A*, **414**, 429
- Cassano, R., Bernardi, G., Brunetti, G., et al. 2015, Proc. Advancing Astrophysics with the Square Kilometre Array (AASKA14) (Trieste: SISSA), 73
- Cassano, R., Brunetti, G., Norris, R. P., et al. 2012, *A&A*, **548**, A100
- de Gasperin, F., Intema, H. T., Shimwell, T. W., et al. 2017, *SciA*, **3**, e1701634
- Dressler, A. 1980, *ApJS*, **42**, 565
- Enßlin, T. A., & Gopal-Krishna 2001, *A&A*, **366**, 26
- Enßlin, T. A., & Röttgering, H. 2002, *A&A*, **396**, 83
- English, W., Hardcastle, M. J., & Krause, M. G. H. 2019, *MNRAS*, **490**, 5807
- Feretti, L., Giovannini, G., Govoni, F., & Murgia, M. 2012, *A&ARv*, **20**, 54
- Flin, P., & Krywult, J. 2006, *A&A*, **450**, 9
- Frater, R. H., Brooks, J. W., & Whiteoak, J. B. 1992, *JEEEA*, **12**, 103
- Ghizzardi, S., Rossetti, M., & Molendi, S. 2010, *A&A*, **516**, A32
- Giacintucci, S., Markevitch, M., Johnston-Hollitt, M., et al. 2020, *ApJ*, **891**, 1
- Giacintucci, S., Markevitch, M., Venturi, T., et al. 2014, *ApJ*, **781**, 9
- Girardi, M., Escalera, E., Fadda, D., et al. 1997, *ApJ*, **482**, 41
- Godfrey, L. E. H., Morganti, R., & Brienza, M. 2017, *MNRAS*, **471**, 891
- Hoefl, M., & Brügger, M. 2007, *MNRAS*, **375**, 77
- Hopkins, A., Georgakakis, A., Cram, L., Afonso, J., & Mobasher, B. 2000, *ApJS*, **128**, 469
- Hurley-Walker, N., Callingham, J. R., Hancock, P. J., et al. 2017, *MNRAS*, **464**, 1146
- Jaffe, W. J., & Perola, G. C. 1973, *A&A*, **26**, 423
- Johnston-Hollitt, M. 2004, in Proc. The Riddle of Cooling Flows in Galaxies and Clusters of Galaxies, ed. T. Reiprich, J. Kempner, & N. Soker (Charlottesville, VA: Univ Virginia), 51
- Kale, R., & Dwarakanath, K. S. 2012, *ApJ*, **744**, 46
- Kang, H., & Ryu, D. 2011, *ApJ*, **734**, 18
- Kang, H., Ryu, D., & Jones, T. W. 2012, *ApJ*, **756**, 97
- Kardashev, N. S. 1962, *SvA*, **6**, 317
- Mandal, S., Intema, H. T., Shimwell, T. W., et al. 2019, *A&A*, **622**, A22
- McConnell, D., Hale, C. L., Lenc, E., et al. 2020, *PASA*, **37**, e048
- McMullin, J. P., Waters, B., Schiebel, D., Young, W., & Golap, K. 2007, in ASP Conf. Ser., 376, Astronomical Data Analysis Software and Systems XVI, ed. R. A. Shaw, F. Hill, & D. J. Bell (San Francisco, CA: ASP), 127
- Offringa, A. R., McKinley, B., Hurley-Walker, N., et al. 2014, *MNRAS*, **444**, 606
- Offringa, A. R., & Smirnov, O. 2017, *MNRAS*, **471**, 301
- Pacholczyk, A. G. 1970, Radio Astrophysics. Nonthermal Processes in Galactic and Extragalactic Sources (San Francisco, CA: Freeman)
- Piffaretti, R., Arnaud, M., Pratt, G. W., Pointecouteau, E., & Melin, J. B. 2011, *A&A*, **534**, A109
- Pinzke, A., Oh, S. P., & Pfrommer, C. 2013, *MNRAS*, **435**, 1061
- Pratt, G. W., Böhringer, H., Croston, J. H., et al. 2007, *A&A*, **461**, 71
- Riseley, C. J., Scaife, A. M. M., Oozeer, N., Magnus, L., & Wise, M. W. 2015, *MNRAS*, **447**, 1895
- Rossetti, M., Eckert, D., De Grandi, S., et al. 2013, *A&A*, **556**, A44
- Sault, R. J., Teuben, P. J., & Wright, M. C. H. 1995, in ASP Conf. Ser., 77, Astronomical Data Analysis Software and Systems IV, ed. R. A. Shaw, H. E. Payne, & J. J. E. Hayes (San Francisco, CA: ASP), 433
- Simionescu, A., Werner, N., Urban, O., et al. 2012, *ApJ*, **757**, 182
- Sokolowski, M., Colegate, T., Sutinjo, A. T., et al. 2017, *PASA*, **34**, e062
- Strüder, L., Briel, U., Dennerl, K., et al. 2001, *A&A*, **365**, L18
- Tingay, S. J., Goeke, R., Bowman, J. D., et al. 2013, *PASA*, **30**, e007
- Turner, M. J. L., Abbey, A., Arnaud, M., et al. 2001, *A&A*, **365**, L27
- van Haarlem, M. P., Wise, M. W., Gunst, A. W., et al. 2013, *A&A*, **556**, A2
- van Weeren, R. J., de Gasperin, F., Akamatsu, H., et al. 2019, *SSRv*, **215**, 16
- van Weeren, R. J., Intema, H. T., Oonk, J. B. R., Röttgering, H. J. A., & Clarke, T. E. 2009, *A&A*, **508**, 1269
- Vazza, F., Roediger, E., & Brügger, M. 2012, *A&A*, **544**, A103
- Vazza, F., Wittor, D., Brunetti, G., & Brügger, M. 2021, *A&A*, submitted (arXiv:2102.04193)
- Wayth, R. B., Lenc, E., Bell, M. E., et al. 2015, *PASA*, **32**, e025
- Wayth, R. B., Tingay, S. J., Trott, C. M., et al. 2018, *PASA*, **35**, 33
- Wittor, D., Vazza, F., Ryu, D., & Kang, H. 2020, *MNRAS*, **495**, L112

B.3 Hodgson et al. (2021a)

FIGARO simulation: Filaments and GALactic RadiO simulation

[Hodgson, Vazza, Johnston-Hollitt & McKinley \(2021a\)](#)

© The authors 2021. Reproduced with permission.

Research Paper

FIGARO simulation: Filaments & GALactic RadiO simulation

Torrance Hodgson^{1,*} , Franco Vazza^{2,3,4}, Melanie Johnston-Hollitt^{1,5} and Benjamin McKinley^{1,6}

¹International Centre for Radio Astronomy Research (ICRAR), Curtin University, 1 Turner Ave, Bentley, WA 6102, Australia, ²Dipartimento di Fisica e Astronomia, Università di Bologna, Via Gobetti 92/3, Bologna 40121, Italy, ³Hamburger Sternwarte, Gojenbergsweg 112, Hamburg 21029, Germany, ⁴INAF, Istituto di Radio Astronomia di Bologna, Via Gobetti 101, Bologna 40129, Italy, ⁵Curtin Institute for Computation, Curtin University, GPO Box U1987, Perth, WA 6845, Australia and ⁶ARC Centre of Excellence for All Sky Astrophysics in 3 Dimensions (ASTRO3D), Bentley, Australia

Abstract

We produce the first low to mid-frequency radio simulation that incorporates both traditional extragalactic radio sources as well as synchrotron cosmic web emission. The Filaments & GALactic RadiO (FIGARO) simulation includes 10 unique $4^\circ \times 4^\circ$ fields, incorporating active galactic nuclei (AGNs), star-forming galaxies (SFGs), and synchrotron cosmic web emission out to a redshift of $z = 0.8$ and over the frequency range 100–1 400 MHz. To do this, the simulation brings together a recent 100^3 Mpc³ magnetohydrodynamic simulation (Vazza et al. 2019, A&A, 627, A5), calibrated to match observed radio relic population statistics, alongside updated ‘T-RECS’ code for simulating extragalactic radio sources (Bonaldi et al. 2019, MNRAS, 482, 2). Uniquely, the AGNs and SFGs are populated and positioned in accordance with the underlying matter density of the cosmological simulation. In this way, the simulation provides an accurate understanding of the apparent morphology, angular scales, and brightness of the cosmic web as well as—crucially—the clustering properties of the cosmic web with respect to the embedded extragalactic radio population. We find that the synchrotron cosmic web does not closely trace the underlying mass distribution of the cosmic web, but is instead dominated by shocked shells of emission surrounding dark matter halos and resembles a large, undetected population of radio relics. We also show that, with accurate kernels, the cosmic web radio emission is clearly detectable by cross-correlation techniques and this signal is separable from the embedded extragalactic radio population. We offer the simulation as a public resource towards the development of techniques for detecting and measuring the synchrotron cosmic web.

Keywords Cosmic web (330) – Warm-hot intergalactic medium (1786) – radio astronomy (1338) – extragalactic magnetic fields (507)

(Received 6 May 2021; revised 17 June 2021; accepted 25 June 2021)

1. Introduction

The term ‘cosmic web’ has been used to evoke the distribution of matter in our Universe on the very largest of scales. In this model, perturbations shortly after inflation have been amplified by gravitational instability to drive a process of hierarchical structure formation: low-density regions have evolved into giant voids, high-density regions have seeded galaxies, groups, and clusters, and these are connected by a network of low-density filaments and sheets (e.g. Baugh et al. 2004). Outside of galaxies and cluster cores, some 40–50% of the baryonic mass of the Universe is believed to trace this cosmic web structure, existing as a diffuse, highly-ionised, warm-hot intergalactic medium (e.g. Cen and Ostriker 1999; Davé et al. 2001).

Until recently, the existence of the WHIM and its distribution in a cosmic web was primarily inferred from simulations of Universe evolution. Tentative empirical results have begun to support this model (e.g. Eckert et al. 2015; Nicastro et al. 2018; de Graaff et al. 2019; Tanimura et al. 2019). Most recently, Macquart et al. (2020) provided compelling evidence in support of this hypothesis by tracing the dispersion measure of a small collection of fast radio bursts, the origins of each having been traced to a known host galaxy. Despite the small sample size, this result

has provided the strongest evidence yet for these missing baryons residing along the line of sight in the intracluster medium.

The *synchrotron* cosmic web is the expected radio component emitted by this large-scale structure (Brown 2011). As part of the ongoing process of large-scale structure formation, simulations such as Vazza et al. (2015, 2019) have modelled large-scale accretion processes and shown them capable of producing shocks surrounding filaments and the outermost regions of galaxy clusters many times the local speed of sound, with Mach numbers as high as $\mathcal{M} \sim 10$ –100. Such shocks are capable of producing high-energy electrons by way of diffusive shock acceleration (DSA) and, in the presence of large-scale intracluster magnetic fields, this suprathermal population will in turn produce synchrotron emission (e.g. Keshet et al. 2009). The strength of this emission is predicted to be extremely weak, however, and in previous modelling, it was predicted to be at or below the level of detectability of the current generation of low-frequency radio instruments (Vazza et al. 2015). Using more recent cosmological numerical simulations as guidance, Gheller and Vazza (2020) tested the detectability of a number of observables that trace the gas in the cosmic web using a cross-correlation technique. They reported that the observables with the strongest cross-correlation with the underlying distribution of galaxies should be those involving the Sunyaev–Zeldovich effect and, in spite of the difficulty of its detection, the diffuse synchrotron radio emission from the shocked cosmic web.

Two separate papers by Brown et al. (2017) and Vernstrom et al. (2017) both attempted a statistical detection using a

* Author for correspondence: Torrance Hodgson, E-mail: torrance@pravic.xyz

Cite this article: Hodgson T, Vazza F, Johnston-Hollitt M and McKinley B. (2021) FIGARO simulation: Filaments & GALactic RadiO simulation. *Publications of the Astronomical Society of Australia* 38, e047, 1–18. <https://doi.org/10.1017/pasa.2021.32>

cross-correlation analysis. Vernstrom *et al.* (2017) used a deep, 180 MHz observation of a $21.8^\circ \times 21.8^\circ$ field using the Murchison Widefield Array (MWA; Tingay *et al.* 2013) and cross-correlated this (residual) map with galaxy density maps at various redshifts, smoothed to scales ranging from 1 to 4 Mpc. Their expectation was that there would be a peak in the cross-correlation at 0° offset, and this expectation was rooted in an assumption that cosmic web emission broadly traced the large-scale mass distribution of the Universe. However, other radio sources such as active galactic nuclei (AGNs) and star-forming galaxies (SFGs) also correlate with galaxy density maps, making it necessary to accurately model these related emission populations to distinguish their signals. Indeed, despite the authors detecting a peak in the correlation at 0° offset, it was this confounding factor that prohibited any claim to a positive detection.

Brown *et al.* (2017) similarly attempted to use a cross-correlation analysis using the S-Band Polarization All-Sky Survey observed with Parkes at 2.3 GHz (Carretti *et al.* 2013). However, rather than using galaxy density as a proxy for the cosmic web, they used cosmological simulations that were constrained to reproduce the local large-scale structure and which tracked the evolution of thermal gas and magnetic field strengths. The resulting synchrotron cosmic web emission S was modelled as a function of thermal electron density n_e and magnetic field strength B in the form $S \propto n_e B^2$. From this, they produced a large-scale, low-resolution map of the local synchrotron cosmic web showing that it broadly and smoothly traced out the underlying mass density of the local Universe. The cross-correlation showed no statistically significant detection.

Both papers point to the great difficulty of making a detection of the synchrotron cosmic web. In particular, they point to the need for future detection attempts to be able to accurately model how the radio emission traces the underlying matter density, as well as to understand the much brighter population of AGN and SFG radio sources, how these cluster with respect to the underlying synchrotron cosmic web, and how their emission may produce confounding signals.

Most recently, Vernstrom *et al.* (2021) have claimed the first definitive detection of the synchrotron cosmic web. By using luminous red galaxies as tracers of cluster cores, Vernstrom *et al.* stacked nearby cluster pairs found in low-frequency radio data produced both by the MWA as well as Owens Valley Radio Observatory Long Wavelength Array (OVRO-LWA Eastwood *et al.* 2018) and identified a residual signal produced in the spanning intracluster medium. The authors argue against alternative explanations for the signal such as intervening cluster emission or overdense AGN and SFG emission spanning the filaments; whilst the results of this experiment are promising, the work also points to the need to accurately understand and model the combined extragalactic population alongside cosmic web emission so as to provide robust constraints on possible contamination within the stacking signal.

In response to the need for such simulations, we present the first sky model providing both the synchrotron cosmic web alongside a realistically clustered AGN and SFG radio population, the ‘Filaments & Galactic RadiO’ (FIGARO) simulation. We provide this model in the form of $10 \ 4^\circ \times 4^\circ$ light cones out to a redshift of $z = 0.8$, and valid for observing frequencies ranging from 100 to 1 400 MHz. To do this, we have combined cosmic web emission extracted from the magnetohydrodynamic (MHD) simulations by Vazza *et al.* (2019) and have populated the light cone with AGN and SFG radio sources using the Tiered Radio Extragalactic

Continuum Simulation (T-RECS) codebase produced by Bonaldi *et al.* (2019). Uniquely, this latter population are positioned and clustered realistically with respect to the underlying mass density of the cosmological simulation. We expect this simulation to be important in developing observing and detection strategies for detecting the cosmic web with both current as well as upcoming low to mid-frequency radio telescopes.

This paper is structured as follows. We begin by discussing the construction of this simulation as well as the verification steps taken during that process. In Section 2, we discuss the underlying MHD simulation, the extraction of synchrotron cosmic web emission from the snapshots and the calibration of this emission against the small known population of radio relics. In Section 3, we discuss the extraction and validation of dark matter halos from the simulation, taking care to verify their number density and clustering properties as this population are a key input for the T-RECS simulation. Section 4 details the light cone construction process itself, stacking the cosmic web and dark matter halos out to a redshift depth of $z = 0.8$. Finally, in Section 5, we discuss how we use the halo light cones to position the AGN and SFG radio population using the T-RECS simulation codebase, before presenting the completed simulation catalogue in Section 6. We finish in Section 7 with a discussion oriented around the possibility of detection of the cosmic web with the latest generation of radio telescopes.

Throughout this paper, and including the original cosmological simulation, a Λ CDM cosmological model is assumed, with density parameters $\Omega_{\text{BM}} = 0.0478$ (baryonic matter), $\Omega_{\text{DM}} = 0.2602$ (dark matter), and $\Omega_{\Lambda} = 0.692$, and the Hubble constant $H_0 = 67.8 \text{ km s}^{-1} \text{ Mpc}^{-1}$. All stated observing resolutions refer to the full width at half maximum (FWHM) of a circular Gaussian.

2. Cosmological simulation and snapshots

In beginning to build FIGARO, we must start with an underlying and evolving cosmological simulation. We have used the MHD simulation detailed in Vazza *et al.* (2019), which was produced using ENZO.^{a,b} This simulation encompassed a comoving volume of 100^3 Mpc^3 with a uniform grid of $2\ 400^3$ cells and $2\ 400^3$ dark matter particles, each with a fixed mass set at $8.62 \times 10^6 M_{\odot}$. This gives a spatial resolution of 41.6^3 kpc^3 (comoving) per cell. The simulation was initialised at $z = 45$ with a simple uniform magnetic field of $B_0 = 0.1 \text{ nG}$, and these fields were evolved in time using the MHD method of Dedner *et al.* (2002).

Whilst larger, purely dark matter simulations do exist, a full MHD treatment is significantly more computationally expensive. The simulation used here is the largest of its kind to date, and presents a careful computational trade-off between cellular resolution and total volume. In the latter case, the volume is large enough to allow the simulation of a small population of $\sim 10^{14} M_{\odot}$ clusters and galaxy groups.

An important caveat to note is that the simulation does not include either radiative gas cooling or feedback processes due to star formation and AGN, both of which are important to the evolution of cluster interiors, nor was the spatial resolution sufficiently high to capture turbulent dynamo effects of the dense cluster regions that can significantly magnify magnetic fields. Our regions of interest for this catalogue, however, are the filaments

^awww.enzo-project.org.

^bNote that the cosmological parameters are incorrectly stated in Vazza *et al.* (2019), and are instead those given in this paper.

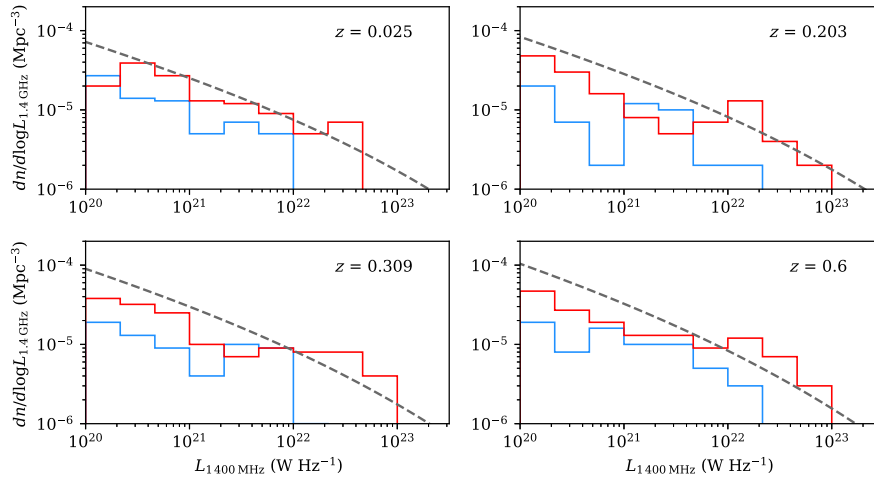


Figure 1. A comparison of the radio relic luminosity function (RRLF) from Nuza et al. (2012) (dashed grey) with the the measured relics in each snapshot volume for HB07 (blue) and HB07 with additional fossil electrons (red). Relic statistics were calculated by summing emission in the annulus around dark matter halos with radii $0.5 \cdot r_{200} < r < 1.5 \cdot r_{200}$.

and cluster peripheries and these regions are sufficiently distant from core cluster environs that these effects, at least to first order, are not especially relevant.

2.1. Radio

Synchrotron radio emission is produced by electrons at relativistic energies interacting with background magnetic fields. In this simulation we trace synchrotron emission solely as a result of diffusive shock acceleration (DSA) typically associated with accretion shocks, cluster mergers, and other large-scale structure formation processes (e.g. Ryu et al. 2003).

In DSA, a small fraction of ambient electrons are accelerated to relativistic energies, which then radiate due to their interaction with non-negligible intracluster magnetic fields. We model the resulting radio power based on Hoeft and Brüggén (2007), henceforth HB07:

$$P_\nu \propto S \cdot n_d \cdot \xi(M, T) \cdot \nu^\alpha \cdot T_d^{3/2} \cdot \frac{B^{1-\alpha}}{B_{\text{CMB}}^2 + B^2}, \quad (1)$$

where S is the shock surface area; n_d is the downstream electron density; $\xi(M, T)$ is the electron acceleration efficiency which is a function of Mach number and temperature; ν is the frequency and α is the spectral index of the radio emission; T_d is the downstream electron temperature; B is the magnetic field in each cell; and B_{CMB} is the equivalent magnetic field strength of the CMB where $B_{\text{CMB}} \approx 3.25(1+z)^2 \mu\text{G}$.

Both B and $\xi(M, T)$ are poorly understood, especially in the highly diffuse filaments and cluster outskirts, yet are key parameters in calculating the radio power. The magnetic field strength along filaments is primarily the result of adiabatic gas compression, and in these low-density regions, the field strength is closely related to the magnetic field seeding scenario (e.g. Vazza et al. 2015). The seed strength, however, is unknown and thus predictions of these magnetic fields vary between cosmological simulations in the range of 10^{-4} – 0.1 nG. At best, we have upper limits provided by Planck from CMB observations which limit the magnetic field strengths to a few nG on scales of 1 Mpc (Planck

Collaboration 2016). In this simulation, the magnetic field was seeded uniformly at 0.1 nG—an order of magnitude lower than these limits—but there is latitude in the choice of this parameter. Moreover, for values of $B \ll B_{\text{CMB}}$, the radio power scales $P \propto B^2$, making the simulation particularly sensitive to the seed strength.

The electron acceleration efficiency $\xi(M, T)$ is a second, crucial parameter that is difficult to model. This parameter estimates the fraction of thermal electrons that are accelerated to relativistic energies as a result of a shock. The model used here is based on HB07 which depends upon the strength of the shock and the thermal temperature of the downstream electrons. However, this model does not exceed $\sim 10^{-3}$ for reasonable Mach values, and this value is insufficient to account for many observed radio relics (e.g. Botteon et al. 2020). For these events, we now believe ‘fossil’ electron populations—those which have been previously accelerated by, for example, AGN activity or previous DSA shocks—allow for a much higher effective electron acceleration efficiency (e.g. Pinzke, Oh, & Pfrommer 2013). As shocks were here calculated in post-processing, this simulation does not have a ‘memory’ of previous shocks nor does it model AGN activity; at each snapshot, the electron population is therefore always assumed to be at thermal equilibrium resulting in underestimated radio emission, especially in dense cluster environments.

As a mitigation, we introduce a modified HB07 model (herein: ‘HB07 + fossil’) for the acceleration efficiency. This mitigation builds upon HB07 with a special case for weak shocks in dense environments: for shocks with $\mathcal{M} < 5$ and thermal temperature $T > 10^7$ K, we arbitrarily set $\xi(M, T) = 10^{-2}$. The final HB07+fossil model was then a weighted sum of the original HB07 model with this special case, with weightings 0.95 and 0.05, respectively.

These weightings were chosen to best reproduce the radio relic luminosity function (RRLF) derived by Nuza et al. (2012). Radio relics are a known class of radio source produced by DSA at the periphery of clusters and is driven by shocks from large-scale structure formation processes. Radio relics should be well modelled by our simulation and provide a means by which to calibrate the radio emission of our models. In Figure 1, we compare the relic

Table 1. The simulation snapshots used to construct the light cone and associated halo catalogues.

Snapshot no.	Redshift	Luminosity density (1.4 GHz)
	z	($\text{erg s}^{-1} \text{Hz}^{-1} \text{Mpc}^{-3}$)
188	0.025	4.45×10^{24}
166	0.2	6.20×10^{24}
156	0.3	3.58×10^{24}
122	0.6	4.44×10^{24}

counts for both the HB07 (blue) and HB07+fossil (red) models for each of the snapshot volumes of our simulation^c with the Nuza *et al.* (2012) RRLF in dashed grey.^d We can observe that the standard HB07 model results in significantly under-powered relics by about one order of magnitude, whilst the modified HB07 + fossil weighted model brings the relic counts into good agreement.

2.2. Snapshots

We have extracted four ‘snapshots’ of the simulation at redshifts ranging from $z = 0.025$ to $z = 0.6$, as detailed in Table 1, and these snapshots have formed the basis for constructing our light cones. This selection of snapshots was driven purely by the data still available. Amongst the observables produced by the simulation, the three of note to this work are: dark matter density cubes; the calculated luminosity of the synchrotron emission at 1 400 MHz; and the shock values (i.e. cell Mach numbers).

3. Halo finding

Alongside the radio emission, the mass distribution, and in particular the dark matter halo positions, are a key ingredient in building the FIGARO simulation. This arises because T-RECS relies on dark matter halos to position AGN and SFG and thus accurately mimic the clustering properties of these sources with respect to the cosmic web emission. Thus for each snapshot, we needed to identify dark matter halos in post-processing using each snapshot’s associated dark matter cube. The processed outputs of the simulation have been smoothed using a Cloud-In-Cell (CIC) kernel, prohibiting traditional ‘friend of friend’ algorithms. Instead, to identify dark matter halos we used the following simple algorithm: a sphere was progressively grown around the most massive voxel until the mean density of the enclosed volume reduced beneath a threshold density $\bar{\rho}$, in this case $\bar{\rho} = 200\rho_c$, where ρ_c is the critical density of the Universe at that respective redshift. From this, we could then interpolate the virial radius r_{200} and mass M_{200} of the halo. The mass of enclosed voxels was set to zero and the process was repeated on the next most massive voxel in the snapshot, and so on, until exhausting the volume of resolved halos.

To provide enough potential source positions, T-RECS requires that we find halos down to $\sim 10^{9.5} M_\odot$. Given the relatively coarse spatial and mass resolution of our simulation, detecting these low-mass halos is challenging. To achieve this we set the minimum allowable halo size as having a radius of 1 voxel, that is,

^cRelics were measured by summing the luminosity about dark matter halos in the annular cylinder defined with radii $0.5 \cdot r_{200} < r < 1.5 \cdot r_{200}$ and depth $3 \cdot r_{200}$. To avoid double counting in the case of nearby relics, we processed halos in order of most massive to least massive, and excluded regions that had already been counted.

^dThe calculation of this RRLF required the convolution of a halo mass function, for which we used Angulo *et al.* (2012).

incorporating just 7 voxels in total. At this limit, however, we are especially wary of the introduction of errors or bias due to discretisation effects, and we have therefore performed a number of sanity checks upon our halo catalogue.

In Figure 2 we show the halo counts, binned by mass, for each respective snapshot. We compare these counts with the halo mass function by Angulo *et al.* (2012) (produced using HMFCalc by Murray *et al.* 2013) and we observe good agreement down to about $10^{10.5} M_\odot$, below which our catalogue becomes increasingly incomplete. The lowest mass halos range from $10^{9.87} M_\odot$ at $z = 0.025$ to $10^{9.57} M_\odot$ at $z = 0.6$, where this lower limit steadily decreases due to the decreasing cosmological scale factor and corresponding increased resolution of the simulation at earlier epochs.

As a second sanity check, in Figure 3, we compare the clustering properties of the FIGARO halos with those from the Millennium II (MII) and Planck Millennium (PM) simulations by calculating the two-point correlation functions of each respective halo population (for details, see Appendix A). Both the MII and PM simulations are of sufficiently high resolution so as to be able to properly resolve low-mass halos on the order of $10^{9.5} M_\odot$ and therefore provide a good benchmark for comparison. What we observe is good agreement between the simulations across all mass ranges for scales greater than 0.3 Mpc. For scales less than this, both MII and PM turnover slightly, whereas FIGARO continues its power law behaviour. This discrepancy exists for all mass bins and so is not directly related to the discretisation of the simulation, although its cause is unknown.

These sanity checks satisfy to us that our halo catalogue is sufficiently robust, despite the coarse resolution of our simulation.

4. Light cone construction

With both the synchrotron cosmic web and the dark matter halos catalogued for each of our underlying snapshot volumes, we can now proceed to tile these volumes so as to construct the FIGARO light cones. This cone was constructed spanning a $4^\circ \times 4^\circ$ angular extent and with a depth extending to a redshift of $z = 0.8$. The simulation volume, with sides of length 100 Mpc (comoving) only extends out to $z = 0.023$, and the field of view exceeds a comoving transverse distance of 100 Mpc at $z = 0.35$. This necessitates replicating the simulation volume along the length of the light cone a total of 34 times, as well as laterally tiling the volume beyond $z = 0.35$. We discuss here the construction of this light cone.

The web and halo light cones were constructed identically. In both cases, we began with a catalogue of voxel positions and properties. For the web, these properties were the voxel luminosity and shock value; for the halos these were the halo mass and radius. Each cone was constructed by appending the snapshot catalogue in 100 Mpc increments along the length of the light cone. To mitigate repeating structures along the line of sight, we introduced a random transverse offset on each iteration as well as sequentially rotating the volume through each of its three axes. Then, for each entry in the snapshot catalogue, we calculated its redshift, latitude and longitude and, if these latter values fit within the $4^\circ \times 4^\circ$ field of view, they would be appended to the final catalogue. Note that throughout, we assume the field of view is small enough that we can safely assume a flat screen projection.

As noted, at redshifts of about $z = 0.35$ it becomes necessary to tile the simulation volume so as to fully cover the field of view. Since the simulation volume wraps at its edges, this tiling does not

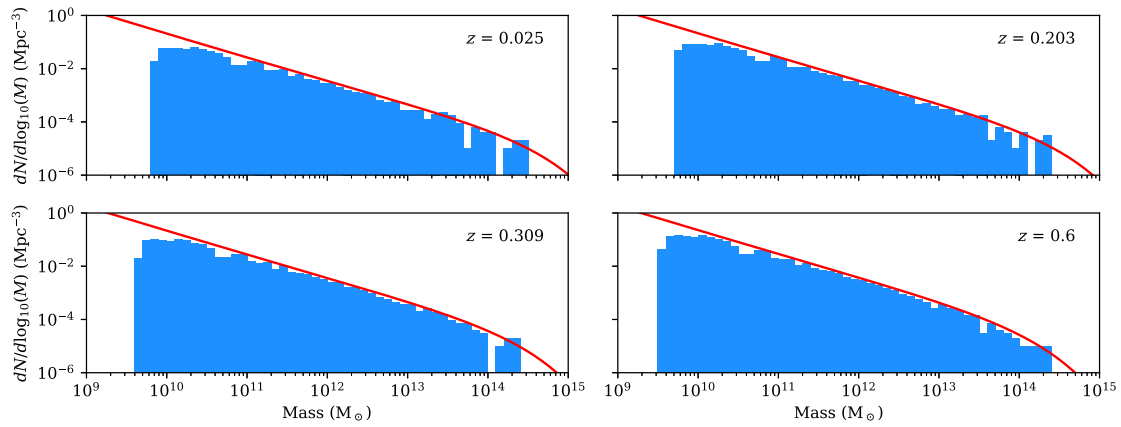


Figure 2. Halo counts for each snapshot, compared with the halo mass function by Angulo et al. (2012) (produced using HMFCalc by Murray et al. 2013) at the respective redshifts. The halos are binned by mass into intervals of 0.1 dex.

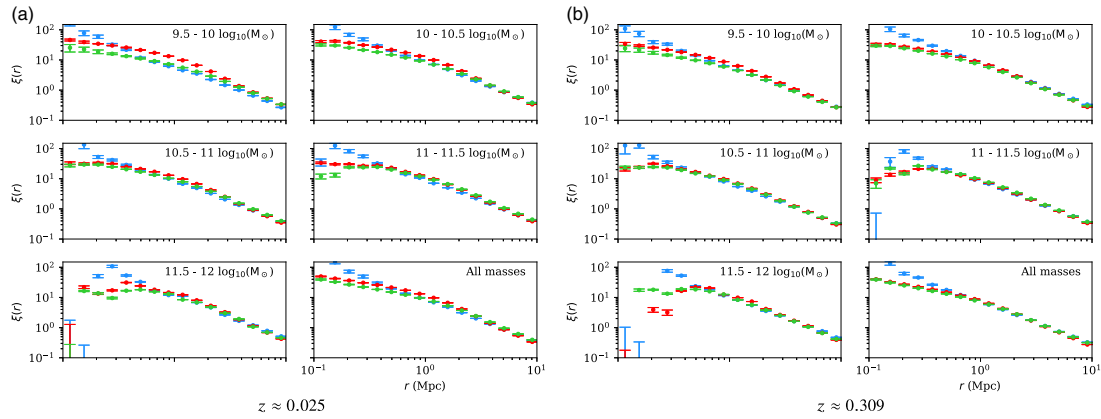


Figure 3. The two-point correlation of halos for the FIGARO (blue), Millennium II (MII; red), and Planck Millennium (PM; green) simulations. The results are shown at redshifts $z \approx 0.025$ and $z \approx 0.309$ and are binned by mass in $0.5 \log_{10}(M_{\odot})$ increments. Additionally, an all mass result is also shown. In all, the halo clustering properties of FIGARO are consistent with both MII and PM simulations with the exception of scales under ~ 0.3 Mpc.

cause discontinuities or edges in the final light cone. The volume was tiled in a 2×2 arrangement from $z = 0.35$.

The random transverse offset allows us to additionally produce multiple light cones or ‘realisations’ which, especially at low redshifts, can be significantly different to each other. In one realisation, for example, the low redshift cone may be largely empty whilst in another, just by chance, there may be a massive galaxy cluster within the field of view. This reflects the kind of cosmic variance we should expect. We have produced 10 realisations in total.

In the case of the halos, their properties were simply appended to a catalogue. In the case of the web emission, however, some additional processing was required. For each web voxel, we calculated its flux S_v from the simulation luminosity values L_v using the standard radio luminosity function with k -correction:

$$S_v(z) = L_v \frac{(1+z)^\alpha}{4\pi D_L^2}, \quad (2)$$

where D_L is the luminosity distance at the redshift z of the voxel and α is the voxel’s spectral index. In turn, the spectral index α was calculated from the voxel’s associated Mach number \mathcal{M} using the relation:

$$\alpha = \frac{\mathcal{M}^2}{1 - \mathcal{M}^2}, \quad (3)$$

where the power law relation uses the positive sign convention $S \propto \nu^\alpha$. This latter relation is also used to scale the luminosity values from the 1 400 MHz output of the simulation to the observing frequency. Finally, this flux value was appended to a map spanning the field of view with $3'' \times 3''$ resolution.

The relatively small volume of the simulation raises issues as we go deeper in redshift space. Whilst the simulation volume is large enough to give a good representative sample of the Universe for small and medium mass clusters, it is, however, just large enough to simulate a single massive galaxy cluster, on the order of $10^{15} M_{\odot}$. As we have shown in Table 2, at low redshifts, we sample only a very small fraction of the total simulation volume; since

Table 2. The comoving volume enclosed by regular $\Delta z = 0.05$ redshift slices and the $4^\circ \times 4^\circ$ field of view. For higher redshifts ($z \gtrsim 0.15$), the volume as a fraction of the total simulation volume is sufficiently large enough that different realisations will be increasingly similar. For redshift slices greater than approximately $z = 0.25$, it becomes necessary to duplicate the simulation volume more than once.

Redshift slice		Comoving volume	Fractional volume
z_{\min}	z_{\max}	(Mpc^3)	
0	0.05	1.7×10^4	0.02
0.05	0.1	1.1×10^5	0.11
0.1	0.15	3.0×10^5	0.30
0.15	0.2	5.5×10^5	0.55
0.2	0.25	8.6×10^5	0.85
0.25	0.3	1.2×10^6	1.21
0.3	0.35	1.6×10^6	1.60

this sample will primarily be low or medium mass clusters, it is a reasonable representation of the Universe as whole. Moreover, at these low redshifts, the differences between realisations should give an accurate picture of the effect of cosmic variance. However, as we go deeper in redshift and as the fractional volume increases towards unity, the different realisations will increasingly sample from the same parts of the simulation, thus becoming self-similar. Moreover, the particular statistics associated with the small population of high mass clusters in our volume, which also host the most luminous cosmic web emission, will begin to dominate statistics derived from these redshift slices. Finally, at redshifts of around $z = 0.35$, where tiling becomes necessary, the most massive galaxy cluster in the volume will be replicated in every single 100 Mpc increment. This single cluster and its unique evolution will dominate most statistics derived from these deeper redshift slices. This is a limitation we will need to consider when we later discuss the statistics of cosmic web emission.

5. T-RECS

T-RECS (Bonaldi *et al.* 2019) is a simulation of the continuum radio sky from 150 MHz to 20 GHz that models radio emission from AGN and SFG using a number of empirically derived relations, and forms the final ingredient required for FIGARO. The simulation provides a thorough range of properties for each radio source, ranging from general properties of intrinsic luminosity, redshift, and physical size to more specific properties such as AGN classification, radio jet angle, and SFG ellipticity. Each of the two general populations were further broken down into subpopulations. The AGNs consisted of: steep-spectrum sources (SS-AGNS), flat-spectrum radio quasars (FSRQ), and BL Lac. The SFGs were also further subdivided into three subpopulations: late-type, spheroidal, and lensed spheroidal galaxies.

The T-RECS simulation was constructed with careful attention paid to the spatial clustering of radio sources. This clustering was implemented by associating each AGN and SFG radio source with a dark matter halo extracted from a $5^\circ \times 5^\circ$ light cone that Bonaldi *et al.* (2019) had constructed, originally derived from the PM simulation. Bonaldi *et al.* (2019) describe in detail the way in which each radio population was associated with dark matter halos of a particular mass range, which we briefly summarise here. In the first case, the AGN subpopulations were associated with dark matter

halos by first relating a stellar mass M_* to each halo mass M_h (i.e. $M_* = F(M_h)$), and then in turn calculating the fraction of galaxies hosting an AGN (radio loud or radio quiet) as a function of that host galaxy mass. The SFGs, on the other hand, used an abundance matching process to relate the known distribution of halo masses and the known distribution of SFG luminosities. This allowed for associating the most luminous SFGs with dark matter halos, whilst for SFGs where the luminosity implied a dark matter halo mass smaller than allowed for by the resolution of the PM simulation, a random distribution on the sky was instead assumed.

Crucially for our purposes, Bonaldi *et al.* (2019) also made the simulation code publicly available. This has allowed us to run the simulation ourselves, and in the process input our own dark matter halo catalogue for each of the respective realisation light cones. Thus the output extragalactic catalogue positions AGN and SFG sources with respect to the underlying matter density of our light-cones, and in this way we accurately model how the cosmic web and the embedded radio population cluster with respect to each other.

We made use of the T-RECS codebase largely without modification, with the exception of a bug fix that corrected a random number generation routine that incorrectly produced strongly biased results. We provided the halo catalogues of each light cone realisation in the format T-RECS expected and ran the simulation for a $4^\circ \times 4^\circ$ field of view, with a lower flux threshold of $S_{1400\text{MHz}} = 0.1 \mu\text{Jy}$, and for a redshift range that encompassed the full cosmic web light cone. The choice of lower flux threshold was selected so as to fully simulate classical confusion noise in the frequency range 150–1400 MHz assuming a highest resolution of $8''$ (see Appendix B).

Finally, we also note the ease with which future improvements to T-RECS modelling of AGN and SFG populations can readily be regenerated into this simulation, especially as deeper, large-field surveys provide more accurate statistics of these faint sources (e.g. Prandoni 2021).

5.1. Clustering of the radio population

To validate the spatial distribution of the resulting radio catalogue, we turn to the angular two-point correlation function. This function $\omega(\theta)$ describes the apparent two-dimensional clustering of radio sources based on their angular separation, without reference to their redshift. Here, we compare the results of two recent empirical measurements of this value, by Magliocchetti *et al.* (2017) and Hale *et al.* (2018), against that of our simulation.

Magliocchetti *et al.* (2017) reported a measurement of the angular two-point correlation function based on a catalogue of sources derived from observations at 1.4 GHz of a 2 deg^2 region of the COSMOS field. By setting a lower flux threshold of 0.15 mJy, above which value the catalogue was considered complete, and assuming $\omega(\theta)$ to be a power law of the form $\omega(\theta) = A\theta^{1-\gamma}$ where γ was set to 2, they were thereby able to derive a value for the constant of proportionality as $A = 2.2 \pm 0.4 \times 10^{-3}$. Hale *et al.* (2018) similarly used observations of a 2 deg^2 region of the COSMOS field, but at the higher frequency range of 2–4 GHz and using a much lower flux threshold $12.65 \mu\text{Jy}$ (5.5 times the median image noise). They assumed the same power law form but instead fixed $\gamma = 1.8$ and thereby derived a value for the constant of proportionality as $\log_{10} A = -2.8 \pm 0.1$.

In Figure 4, we compare these measurements against those of our simulation. We estimate the angular version of the

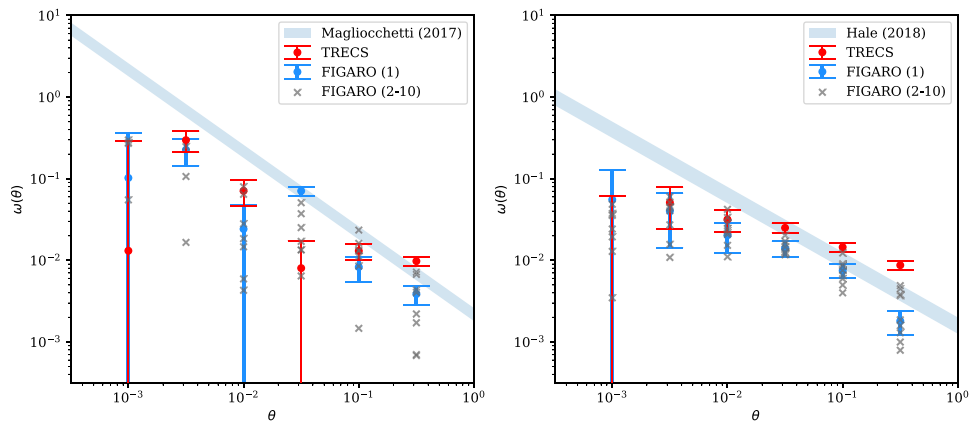


Figure 4. The angular two-point correlation of all radio sources (AGN, SFG, and all subtypes) for FIGARO (realisation 1; blue), the original T-RECS (red), and other FIGARO realisations (grey crosses), calculated across the redshift range $0 < z < 0.8$. *Left:* Comparison to Magliocchetti et al. (2017) using their minimum flux threshold of 0.15 mJy at 1.400 MHz . *Right:* Comparison to Hale et al. (2018) using their minimum flux threshold of $12.65 \mu\text{Jy}$ at 3 GHz .

two-point correlation function using the equation described in Appendix A with the exception that the Euclidean metric r is replaced with the apparent angular separation θ between sources. All error estimates are calculated using bootstrap sampling with 100 iterations. The function was calculated for angular separations $10^{-3.25} < z < 10^{-0.25}$ in equal logarithmically spaced bins of width $\log_{10} \Delta\theta = 0.5$.

In the left panel, we compare the measurement of Magliocchetti et al. (2017) (shaded blue region) with those of realisation 1 from FIGARO (blue, error bars indicate three standard deviations). We also calculate $\omega(\theta)$ for the other realisations (grey crosses), which indicate the variation in this function purely as a result of cosmological variance; however, for clarity we have not included their associated error bars. For reference, we also plot $\omega(\theta)$ of T-RECS using its PM cosmology for the matching redshift range $0 < z < 0.8$.^e The simulated catalogues have had a flux threshold of $S_{1.4\text{GHz}} > 0.15 \text{ mJy}$ applied. On the right, we compare the measurement of Hale et al. (2018) with the same set of simulations except subject to a flux threshold of $S_{3\text{GHz}} > 12.65 \mu\text{Jy}$.

In both cases, FIGARO is reasonably consistent with these empirical measurements for $\theta \gtrsim 10^{-1.75}$, especially when we take into account the spread of values measured from different realisations, as well as with the original T-RECS. FIGARO (and the original T-RECS), however, appears to be under-clustered on angular scales smaller than this. One partial explanation for this is a result of our coarse simulation volume. The resolution of our simulation (and therefore the halo catalogue) was 41.7 kpc , which at a redshift of $z = 0.1$ corresponds to a minimum angular resolution of $19.9''$ and even at a redshift of $z = 0.3$ the minimum angular resolution of $7.0''$ is still greater than the smallest bin for which we have calculated $\omega(\theta)$. As a result, for a given redshift slice, we should expect $\omega(\theta)$ will decline for values of θ smaller than the respective minimum angular scale, and this will introduce an

under-clustering bias to our results on these small angular scales. The second contributing factor is the absence of higher redshift ($z > 0.8$) sources, although a comparison of the two-point statistics for the full T-RECS catalogue against the redshift limited catalogue shows this effect to be small. Nonetheless, we consider our results to be at least as good as the original T-RECS catalogue and sufficient for our present purposes.

6. Results

Combining the final cosmic web light cones and T-RECS catalogues, we produce $10 \text{ } 4^\circ \times 4^\circ$ realisations of the radio sky encompassing the redshift range $0 < z < 0.8$. We additionally provide a background catalogue consisting only of T-RECS sources in the redshift range $0.8 < z < 8$; these sources were not clustered but were instead positioned randomly across the field of view using a uniform distribution, which was uniquely generated for each realisation. Figure 5 is illustrative of the final cosmic web catalogue, where in the top image, we present realisation 5 encompassing the full simulated redshift range of cosmic web emission ($0 < z < 0.8$) and T-RECS sources ($0.8 < z < 8$) at 900 MHz , and convolved to a beam resolution of $20''$. The density fluctuations of the extragalactic radio populations are subtly visible, and using this colour scale we can also identify a small handful of peaks in the cosmic web emission. In the bottom panel, we present the cosmic web emission only, presented using a logarithmic colour scale.

Accompanying this paper, we also make available a full data release of the simulation for each realisation, which includes catalogues describing their respective halos, cosmic web maps, and AGN and SFG populations along the length of the redshift cone. For each realisation, we provide the full data in Hierarchical Data Format 5 (HDF5), with five named datasets. These dataset names and their corresponding schemas are: `halos` (Table 3), `web` (Table 4), `sfg` (Table 5), and `agn` (Table 6).

The cosmic web radio emission itself is provided as a four-dimensional array, with the first axis spanning integrated redshift slices in 0.05 increments, the next two axes spanning the full $4^\circ \times 4^\circ$ field of view, and the final two a tuple containing the flux value and spectral index. The field of view is approximated

^eWe note that the T-RECS two-point statistics are notably lower than those published by Bonaldi et al. (2019). This is not caused solely by the reduced redshift range, as their two-point statistics are similarly lower when calculated over the full redshift range out to $z = 8$; instead, the most likely cause for this deviation is the bug fix to the random number generator.

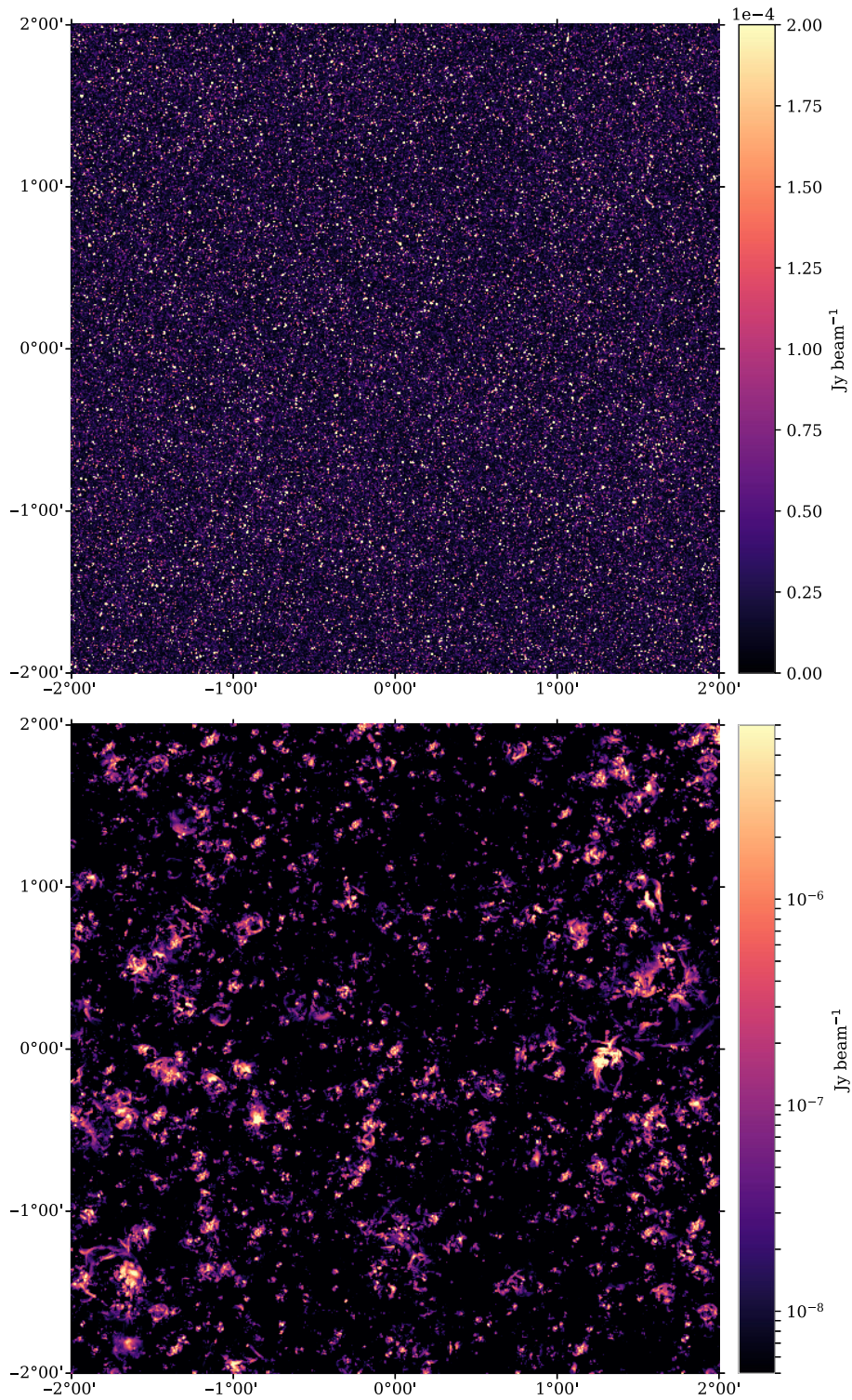


Figure 5. A full-field ($4^{\circ} \times 4^{\circ}$) image of realisation 5 at 900 MHz encompassing the redshift range $0 < z < 0.8$ for the cosmic web and $0 < z < 8$ for T-RECS sources, and convolved to a beam resolution of $20''$. *Top:* The combined simulation with T-RECS extragalactic sources and faint, background cosmic web emission. The colour scale ranges from 0 to saturate at $200 \mu\text{Jy}$. *Bottom:* Cosmic web emission only, using a logarithmic colour scale.

Table 3. Halo dataset schema which describes the properties of dark matter halos along the length of a realisation’s redshift cone.

Column	Name	Units	Description
1	x_coord	degree	The x angular coordinate of the halo
2	y_coord	degree	The y angular coordinate of the halo
3	redshift		The redshift of the halo
4	R200	Mpc	The R200 virial (spherical) radius of the halo
5	M200	$\log_{10} M_{\odot}$	The total mass of the volume enclosed the by the R200 virial radius

Table 4. Cosmic web array with four dimensions. The values for x_coord and y_coord denote the centre of the pixel, with each pixel having a value of Jy and occupying an area $\sim 3'' \times 3''$. The formulas above assume zero indexing (i.e. $i \in [0, 1, \dots]$).

Axis	Length	Name	Description
0	7	i	For $i = 0$, this array contains the full sum of cosmic web emission out to redshift $z < 0.8$. The indexes $i \in [1, 2, \dots, 7]$ contain the cosmic web emission in redshift slices of depth $\Delta z = 0.05$ spanning $0 < z \leq 0.3$
1	4800	j	The x angular coordinate of the pixel, where $x_coord = (j + 0.5)/1200 - 2$ degrees
2	4800	k	The y angular coordinate of the pixel, where $y_coord = (k + 0.5)/1200 - 2$ degrees
3	2	l	The tuple $(S_{900\text{MHz}}, \alpha)$ where $S(\nu) = S_{900\text{MHz}} (\nu/900\text{MHz})^{\alpha}$

Table 5. SFG dataset schema which describes the properties of SFG radio sources along the length of a realisation’s redshift cone.

Column	Name	Units	Description
1	logSFR	$\log_{10}(M_{\odot})/\text{year}$	Star formation rate
2:7	l_freq	Jy	Total flux density of the source for frequencies $\nu \in (100, 300, 600, 900, 1400, 3000)$ MHz
8	x_coord	degree	The x angular coordinate of the SFG
9	y_coord	degree	The y angular coordinate of the SFG
10	redshift		The redshift of the SFG
11	size	arcsecond	Projected apparent size of the disc
12	e1		First ellipticity component
13	e2		Second ellipticity component
14	PopFlag		Population flag: 1 \Rightarrow late-type, 2 \Rightarrow spheroidal, 3 \Rightarrow lensed spheroidal

as a flat screen, with each pixel coordinate offset by $3''$; with this approximation, each pixel occupies approximately $3'' \times 3''$ with a maximum error at the edge of 0.06%.

6.1. Morphology and the ubiquity of relics

In Figure 5, we showed the full $4^{\circ} \times 4^{\circ}$ image of a typical realisation, with the lower figure showing just the cosmic web emission with logarithmic scaling. The phrase ‘cosmic web’ has been evoked to describe the large-scale structure of the Universe as a kind of sponge, and the synchrotron component has often been expected

Table 6. AGN dataset schema which describes the properties of AGN radio sources along the length of a realisation’s redshift cone.

Column	Name	Units	Description
1	Lum1400	$\log_{10}(\text{erg s}^{-1} \text{ Hz}^{-1})$	Luminosity at 1400 MHz
2:7	l_freq	Jy	Total flux density of the source for frequencies $\nu \in (100, 300, 600, 900, 1400, 3000)$ MHz
8	x_coord	degree	The x angular coordinate of the AGN
9	y_coord	degree	The y angular coordinate of the AGN
10	redshift		The redshift of the AGN
11	length	Kpc	The physical length of the core plus jet emission
12	angle	degree	Viewing angle between the jet and line of sight
13	Rs		Ratio between the distance between the spots and total size of the jets
14	PopFlag		Population flag: 4 \Rightarrow FSRQ, 5 \Rightarrow BL Lac, 6 \Rightarrow SS-AGNs

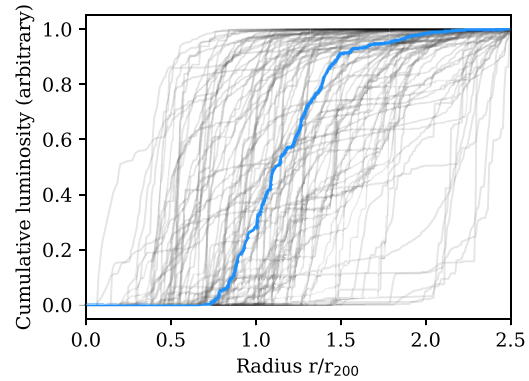


Figure 6. The cumulative radio luminosity contained within the spherical volume surrounding each of the 100 most massive dark matter halos as a function of radius, for the snapshot volume at $z = 0.025$. The luminosity has been normalised to the value at $r = 2.5 \cdot r_{200}$ for each curve. The median value across all halos is indicated in blue.

to follow the same hierarchy of structures with sheets, filaments and dense clusters. However, this is not what we observe. Instead, we observe ubiquitous relic-like, shocked shells of emission that surround dark matter halos. Indeed, these are the primary source of emission in the volume. These shocked shells envelop dark matter halos and in the lowest redshift snapshot, for example, $\sim 96\%$ of the total power in the volume is located in the spherical shell ($r < 1.5 \cdot r_{200}$) of the 100 most massive dark matter halos. The connecting filaments or inflows are not easily discernible, even in a logarithmically scaled image.

In Figure 6, we show the distribution of power for the $z = 0.025$ snapshot by plotting the cumulative radio luminosity contained within the spherical volume surrounding each of the 100 most massive dark matter halos, as a function of radius. The cumulative luminosity is plotted in grey for each of the halos, and in blue we plot the mean cumulative luminosity. The universal absence of

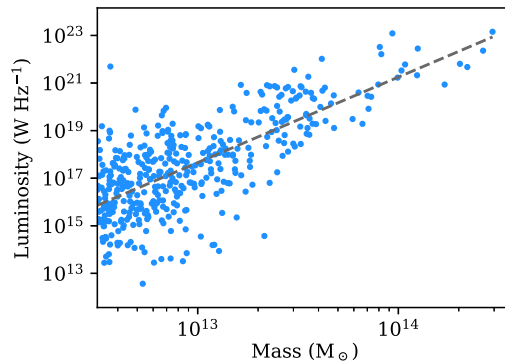


Figure 7. Cosmic web power across the snapshot volume $z = 0.025$ within the dark matter halo spheres $r < 1.5 \cdot r_{200}$ as a function of dark matter halo mass. There is a power law trend indicated by dashed line ($L \propto M^{3.6}$), but significant scattering occurs primarily as a result of the interaction and merger histories of specific clusters.

emission at the core reminds us that in this simulation we do not model Fermi II shock processes such as radio halos. Instead, in general, we observe DSA processes occurring and most luminous in the range $0.75 \cdot r_{200} < r < 1.5 \cdot r_{200}$, although with significant spread in this range from as low as $0.25 \cdot r_{200}$ out to greater than $2 \cdot r_{200}$. The shells themselves are far from isotropic, having complex, filamentary structures with knots and shock fronts orders of magnitude more luminous than elsewhere in the shell.

The absence of significant DSA processes in the innermost cores of dark matter halos is primarily due to the increased matter density and corresponding increase to the speed of sound, as well as the proportionally small area of the shock front; shocks in these regions are therefore not effective electron accelerators despite these regions containing the highest density electron population and magnetic field strengths (Vazza *et al.* 2012). As the shock proceeds significantly far away from the cluster core it loses energy, encounters an increasingly sparse electron environment, and magnetic field strengths decline; thus similarly these outermost environments are ineffective at producing synchrotron emission. In between, however, there exists a sweet spot which maximises the synchrotron output, precisely as we observe in the simulation.

Moreover, the majority of radio power within the volume surrounds just a handful of interacting clusters. In Figure 7, we plot the power contained within the spheres centred on dark matter halos with radius $r = 1.5 \cdot r_{200}$ as a function of halo mass. We observe a power law correlation between mass and the cumulative radio power ($L \propto M^{3.6}$; dashed grey line), although we observe significant scattering around this trend that shows the dependence on the specific interaction and merger histories of individual clusters. The plot also makes it clear that just handful of dark matter halo environments account for the majority of the power output in the volume: 90% of total power is located within the spheres of radius $r = 1.5 \cdot r_{200}$ surrounding just 12 dark matter halos, which cumulatively account for 0.45% of the total volume.

6.2. A brief survey of the brightest, most detectable features

To further illustrate the typical emission morphologies, in Figure 8, we provide a small sample of emission regions drawn from redshift slices $0.10 < z < 0.15$ and $0.15 < z < 0.20$ of realisations 1 and 2, observed at 900 MHz and with a $20''$ resolution.

These sources were chosen as they are amongst the brightest emission and provided a good range of morphologies that are present throughout the catalogue. In contrast to previous figures, these are presented using a linearly-scaled colour map, ranging from 0 to the 99.5th percentile pixel, to make clear the morphology and angular size of the emission structures as would actually be observed. This is to correct for the impression of broad, diffuse emission that may be taken from logarithmic colour scales, when in fact the emission landscape we observe is one with bright ‘knotty’ peaks of emission and otherwise extremely faint surrounding islands of emission. The contours, however, are logarithmically scaled, indicating 0.1, 0.01, and 0.001 of the 99.5th percentile value. The r_{200} radius of nearby dark matter halos are indicated by red dashed circles.

The most recognisable features in this collection are the very traditional double relic morphologies, which can be seen in Figure 8(a), (b), (c), and (d). These examples clearly show matching pairs of arced emission structures as shocked waves travel outwards from the dark matter halo centre, with very classic bow wave morphology. Figure 8(e) is more complex but still recognisable as a relic system, whilst 8f is asymmetric and appears as single relic system.

The remaining examples demonstrate the effect of projection angle on what are otherwise similarly structured shells of emission about dark matter halos. Figure 8(g), (h), and (i), for example, appear in projection to have centrally located emission. Figure 8(j) has two apparently point-like peaks of emission that are amongst the brightest features in this collection, with the brightest peaking at $8 \mu\text{Jy beam}^{-1}$; these ‘points’ are aided in their apparent brightness by summing long, narrow emission structures in the radial direction.

Figure 8(k) and (l) are the most complex in this set of examples, and both involve numerous interacting dark matter halo systems. They are also the most luminous, presumably aided by these cluster interactions. The two Southern peaks in Figure 8(k) peak at approximately $12 \mu\text{Jy beam}^{-1}$, whilst the central peak of emission in Figure 8(l) measures $52 \mu\text{Jy beam}^{-1}$.

Crucially, note the absence of broad emission features, connecting filamentary bridges between dark matter halos, and in general, emission that isn’t associated with shocked shells surrounding dark matter halos.

6.3. The embedded radio population

We now consider the addition of the T-RECS sources. In Figure 9, we show a $50' \times 50'$ field of view showing the redshift range $0.15 < z < 0.2$ extracted from realisation 3 and centred on a massive cluster system. This redshift range has a comoving depth of 203 Mpc, and so this extraction incorporates the full simulation volume stacked twice in the radial direction. The panels allow us to compare the distribution of the synchrotron cosmic web in comparison to the underlying mass distribution as well as the embedded radio population.

The left panel shows the cosmic web emission component of this redshift range observed at 900 MHz and at a resolution of $20''$. The colour scale in the image spans seven orders of magnitude from the plausibly detectable $10 \mu\text{Jy beam}^{-1}$ at the heart of the most massive dark matter halo in the field of view, to 10 nJy beam^{-1} on the virial periphery, to under 1 nJy beam^{-1} along the filaments. Around the most massive cluster, we observe a number

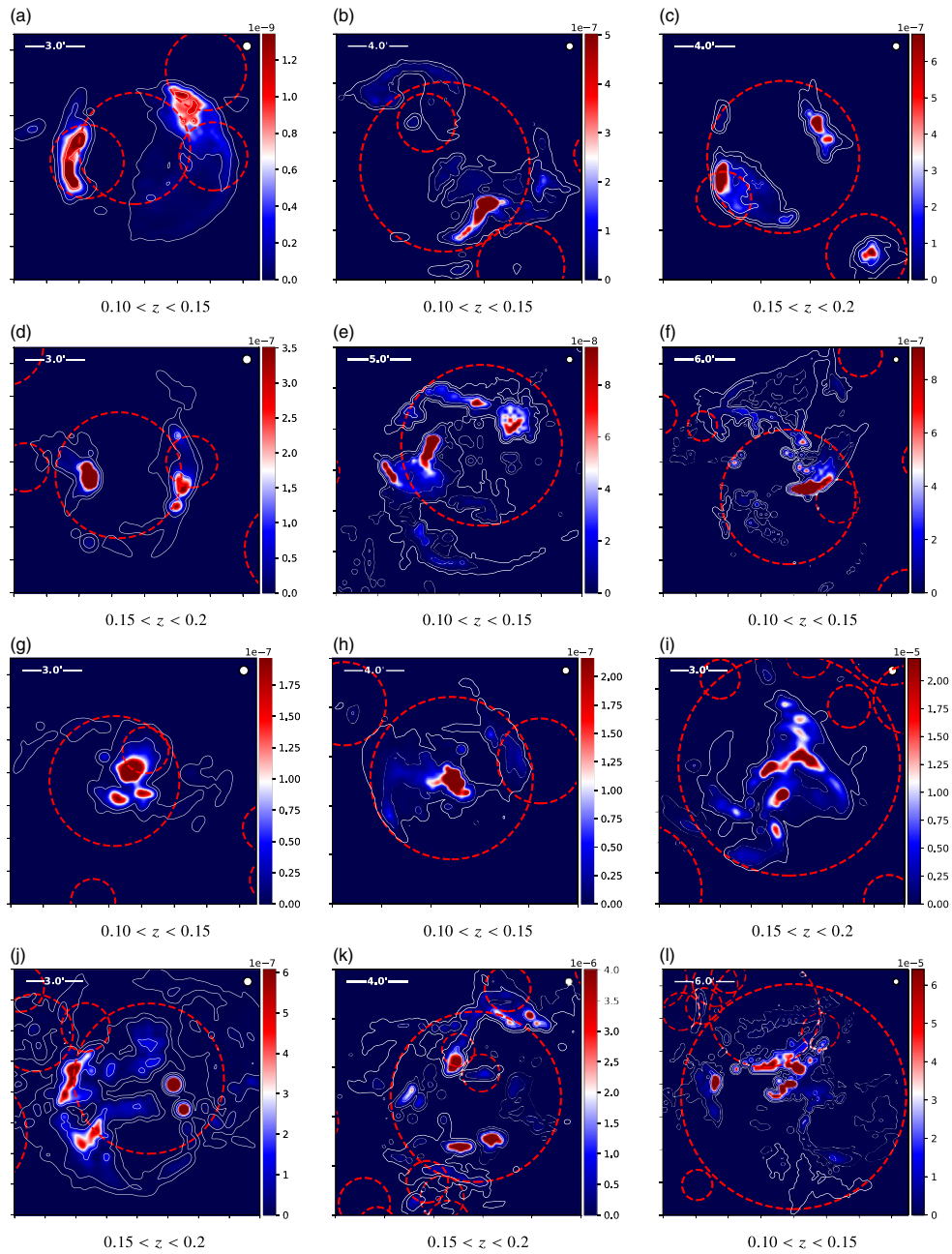


Figure 8. A sample of emission features at 900 MHz from various realisations showing both familiar relic formations as well as more unusual shock morphologies. Each image has been convolved to a resolution of 20'' (beam size indicated by white circle in top right), and the colour map (Jy beam^{-1}) is varyingly scaled from 0 Jy beam^{-1} to the value of the 99.5th percentile pixel. Red circles indicate the r_{200} dark matter halo extent for halos with $M_{200} > 10^{12} M_{\odot}$. Note that all emission occurs outside the core region of dark matter halos, and only appears to be centrally located due to projection effects.

of shocked shells of radio emission; these surround the cluster core, however, projection effects mean the brightest emission appears to align with the core region of the cluster.

The central panel shows the mass distribution within the field of view, where we have also overlaid the dark matter halos detected

by our halo finding algorithm with mass $M > 10^{12.5} M_{\odot}$. We can observe that this is in fact a merging system of two massive systems at the centre of the field, and it is clear that a bridge of increased mass density extends between the two systems. As we observed prior, the northern, most massive system is enshrouded

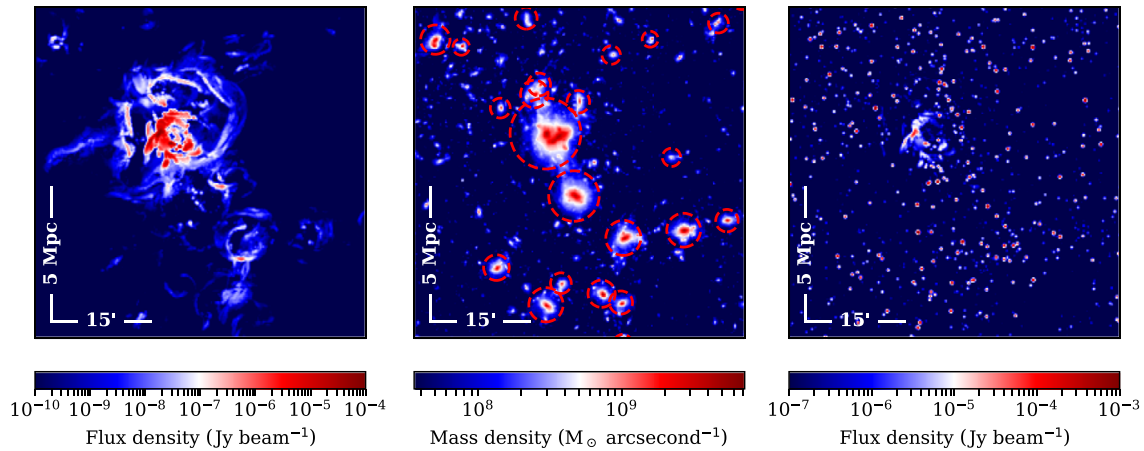


Figure 9. A $50 \times 50'$ field of view showing redshift range $0.15 \leq z < 0.2$ extracted from realisation 3. This redshift range has a comoving depth of 203 Mpc, and so this extraction incorporates the full simulation volume stacked twice in the radial direction. The 5 Mpc scale has been calculated at the mean redshift $z = 0.175$. *Left:* The synchrotron cosmic web emission at 900 MHz with resolution $20''$. *Middle:* The associated mass distribution with halos of mass $M > 10^{12.5} M_{\odot}$ indicated by dashed red circles of radii r_{200} . *Right:* The combined cosmic web emission and T-RECS radio population for this redshift range at 900 MHz with resolution $20''$. The T-RECS radio population are modelled as simple point sources.

by shocked shells of cosmic web emission, whilst the southern is comparatively quiet in this regard, and there is no significant emission associated with the bridge.

In the rightmost panel of Figure 9 we show the associated T-RECS radio populations, with both AGN and SFG modelled as simple point sources. The T-RECS sources are not uniformly distributed and display clustering coincident with the most massive portions of the field of view, as well as less dense regions coincident with the dark matter voids. A number of bright T-RECS sources overlap with the peak of the cosmic web emission. Whilst we have modelled the T-RECS sources as simple point sources, at this redshift and at a resolution of $20''$ the lobes of radio loud AGN can be resolved. In this sense, the rightmost panel represents a best-case view of the cosmic web, whereas a more sophisticated representation of the T-RECS catalogue would likely occlude the underlying cosmic web emission much more significantly.

7. Discussion

We orient the discussion of FIGARO primarily around practical questions of the detectability of the cosmic web with current and future radio instruments. This discussion will include its apparent flux distribution, characteristic angular scales, its correlation with the much brighter AGN and SFG populations and, ultimately, the possibility of its detection with the cross-correlation method discussed in the introduction.

To make these comparisons, we will make reference to three idealised instruments that map approximately to: the MWA in its phase 2 configuration (Wayth *et al.* 2018); the Australian Square Kilometre Array Pathfinder (ASKAP; Hotan *et al.* 2021); and the proposed Square Kilometre Array Low (SKA Low).^f For our purposes, we characterise these instruments simply by an

^f<https://www.skatelescope.org/>.

Table 7. Idealised observing configurations that approximately map to the MWA, SKA Low, and ASKAP radio interferometers. The resolution refers to the FWHM of a circular Gaussian beam.

Name	Frequency	Resolution	Noise
MWA	150 MHz	$60''$	1 mJy beam^{-1}
SKA low	150 MHz	$10''$	$200 \mu\text{Jy beam}^{-1}$
ASKAP	900 MHz	$20''$	$40 \mu\text{Jy beam}^{-1}$

observing frequency, resolution, and noise limit, as shown in Table 7.

7.1. Flux comparison

In this section, we quantify flux differences between the embedded radio population and the synchrotron cosmic web. We begin by examining the flux sum across various redshift slices. In Table 8, we show the flux sum at 150 MHz for both of the embedded radio population and the cosmic web emission, computed across all 10 realisations. Across the depth of the redshift cone out to $z = 0.8$, the total flux attributed to AGN and SFG sources is 3.95 Jy deg^{-2} , whilst the cosmic web emission over this depth is almost a factor of 150 lower, at $0.027 \text{ Jy deg}^{-2}$. The full flux of the AGN and SFG sources out to $z = 8$ is 8.95 Jy , for which we have no commensurate cosmic web flux values. If we bin the length of the light cones in $\Delta z = 0.05$ slices, we see that the cosmic web emission peaks in the two redshift slices $0.05 < z < 0.1$ and $0.1 < z < 0.15$, each providing a fractional signal of about 0.09% of the total flux of the simulation.

Table 8 also shows the flux-weighted spectral index, which appears as the exponent value, and which allows for extrapolation of the flux sum up to 1400 MHz. These spectral index values do not appear to be redshift dependent across the nearby redshift range we have considered, and show a consistent $\alpha \approx -0.8$

Table 8. Flux statistics across all 10 realisations at 150 MHz. For average flux density values, we also provide the flux-weighted mean spectral index (as the exponent) allowing for extrapolation up to 1 400 MHz. Whilst the flux sums only depend on frequency, the final two columns, the 100th and 99.9th percentile values, are calculated with respect to the idealised MWA configuration.

Redshift range	T-RECS flux (Jy deg ⁻²)	Web flux (Jy deg ⁻²)	Web 100th (mJy beam ⁻¹)	Web 99.9th (mJy beam ⁻¹)
$0 < z < 8$	$9.06 \times (\nu/150 \text{ MHz})^{-0.81}$	—	—	—
$0 < z < 0.8$	$3.95 \times (\nu/150 \text{ MHz})^{-0.83}$	$0.027 \times (\nu/150 \text{ MHz})^{-1.24}$	21	0.90
$0 < z < 0.05$	$0.064 \times (\nu/150 \text{ MHz})^{-0.81}$	$0.0022 \times (\nu/150 \text{ MHz})^{-1.26}$	3.9	0.12
$0.05 < z < 0.1$	$0.12 \times (\nu/150 \text{ MHz})^{-0.80}$	$0.0033 \times (\nu/150 \text{ MHz})^{-1.26}$	21	0.20
$0.1 < z < 0.15$	$0.18 \times (\nu/150 \text{ MHz})^{-0.84}$	$0.0034 \times (\nu/150 \text{ MHz})^{-1.24}$	20	0.13
$0.15 < z < 0.2$	$0.17 \times (\nu/150 \text{ MHz})^{-0.85}$	$0.0028 \times (\nu/150 \text{ MHz})^{-1.22}$	11	0.12
$0.2 < z < 0.25$	$0.21 \times (\nu/150 \text{ MHz})^{-0.82}$	$0.0027 \times (\nu/150 \text{ MHz})^{-1.22}$	10	0.11
$0.25 < z < 0.3$	$0.23 \times (\nu/150 \text{ MHz})^{-0.82}$	$0.0021 \times (\nu/150 \text{ MHz})^{-1.23}$	7.1	0.11

for extragalactic sources and $\alpha \approx -1.25$ for cosmic web emission.⁸ Thus, whilst at 150 MHz, the total cosmic web emission is a factor of ~ 150 times fainter than the embedded extragalactic emission, at 900 MHz this ratio increases to ~ 300 . All things being equal, the cosmic web signal is most detectable at these lower frequencies. It's also important to note that the presence of fossil electron populations, which are not part of our model, may bias the cosmic web emission steeper still.

To further draw out the flux differences between these two populations, we next consider the distribution of flux values on the sky; this is dependent on the observing configuration, and in particular the beam resolution. In Figure 10, we bin pixels by flux density ($\log_{10} \Delta S = 0.25$) and show the proportion of the sky covered by these values, for each of the cosmic web and extragalactic sources when mapped according to the observing configurations in Table 7. Vertical dotted lines indicate the noise threshold of each observing configuration. As before, extragalactic sources are modelled simply as point sources. The peak flux distribution of the two populations differs by about two–three orders of magnitude for all configurations, with the vast majority of the cosmic web area of emission more than four–five orders of magnitude fainter than the bulk of the extragalactic emission. Only a small proportion of the cosmic web is either directly or statistically (e.g. via cross-correlation) detectable. If we refer back to Table 8, the final two columns show the peak (i.e. 100th percentile) and 99.9th percentile flux density values when observed in the MWA configuration. The peaks are bright enough that they are directly detectable with the MWA; their morphology, however, tends to resemble the aforementioned apparently point-like knots, making them hard to correctly identify. The extended emission surrounding these knots rapidly declines in brightness, and this can be seen in the 99.9th percentile flux values which are already a factor of ~ 10 lower than the current best noise limits of the MWA.

What is not apparent here is the variability of the cosmic web flux distribution between different realisations. In the lowest redshift slice, the relatively small volume contained within the $4^\circ \times 4^\circ$, $0 < z < 0.05$ cone slice results in a highly variable flux distribution which reflects the real degree of cosmic variance of the very nearby

Universe; thus for this nearest redshift slice, the realisations differ in total flux by five orders of magnitude depending on whether they sample from a void, a filament or, by chance, the core region of a massive cluster. By $z > 0.1$, this variability has significantly reduced as the enclosed volume of each redshift slice encompasses greater proportions of the simulation volume; the redshift slice $0.1 < z < 0.15$, for example, differs by just one order of magnitude across all realisations.

7.2. Cosmic web angular scale

We next consider the characteristic angular extent of cosmic web sources, quantified through the radial autocorrelation function. This is described in Appendix C with the modification that we cross-correlate the map against itself (i.e. we set $\text{map } A = B$). Figure 11 shows the radial autocorrelation as a function of angular offset, $R(\theta)$, for a number of redshift slices out to redshift $z = 0.3$. This redshift range is typical of previous detection attempts, for example, Brown (2011) which only extended as deep as $z = 0.05$ and Vernstrom et al. (2017) which had a mean redshift depth of $z = 0.2$. The autocorrelation of each specific realisation is shown in grey, and the mean across all 10 realisations is shown in blue; the large spread of results, especially at low redshifts, is primarily a result of cosmic variance.

To compare results, Table 9 compiles the minimum, mean, and maximum FWHM values for each redshift slice. In the lowest redshift bin ($0 < z < 0.05$), θ_{FWHM} varies from as small as $55''$ to as much as $149''$; for redshift bin ($0.05 < z < 0.1$) the range is 28 – $58''$; and for the redshift bin ($0.1 < z < 0.15$) the range is much more narrow at 28 – $43''$. Given that these volumes are much smaller than the simulation volume (refer to Table 2), we believe that these ranges are likely representative of the real spread. The deepest three redshift bins in Figure 11 have mean values for θ_{FWHM} of $28''$, $22''$, and $22''$, respectively, however, these values are increasingly likely to be affected by systematics arising from the limited simulation volume.

These angular sizes are significantly less than the typical angular length of intracluster filaments at their respective redshifts, and this latter scale has often been used as a proxy for the expected angular extent of cosmic web emission (e.g. Vernstrom et al. 2017). This smaller than expected angular extent arises as a result of the ‘knotty’ morphology of most emission structures, combined with our previous observation that the emission does not, in

⁸Since the flux-weighted spectral index values of the extragalactic sources are calculated over the frequency range 100–1 400 MHz, they will be dominated by the steeper AGN population which are especially luminous at lower frequencies; these values will therefore be steeper than those calculated over higher frequency ranges.

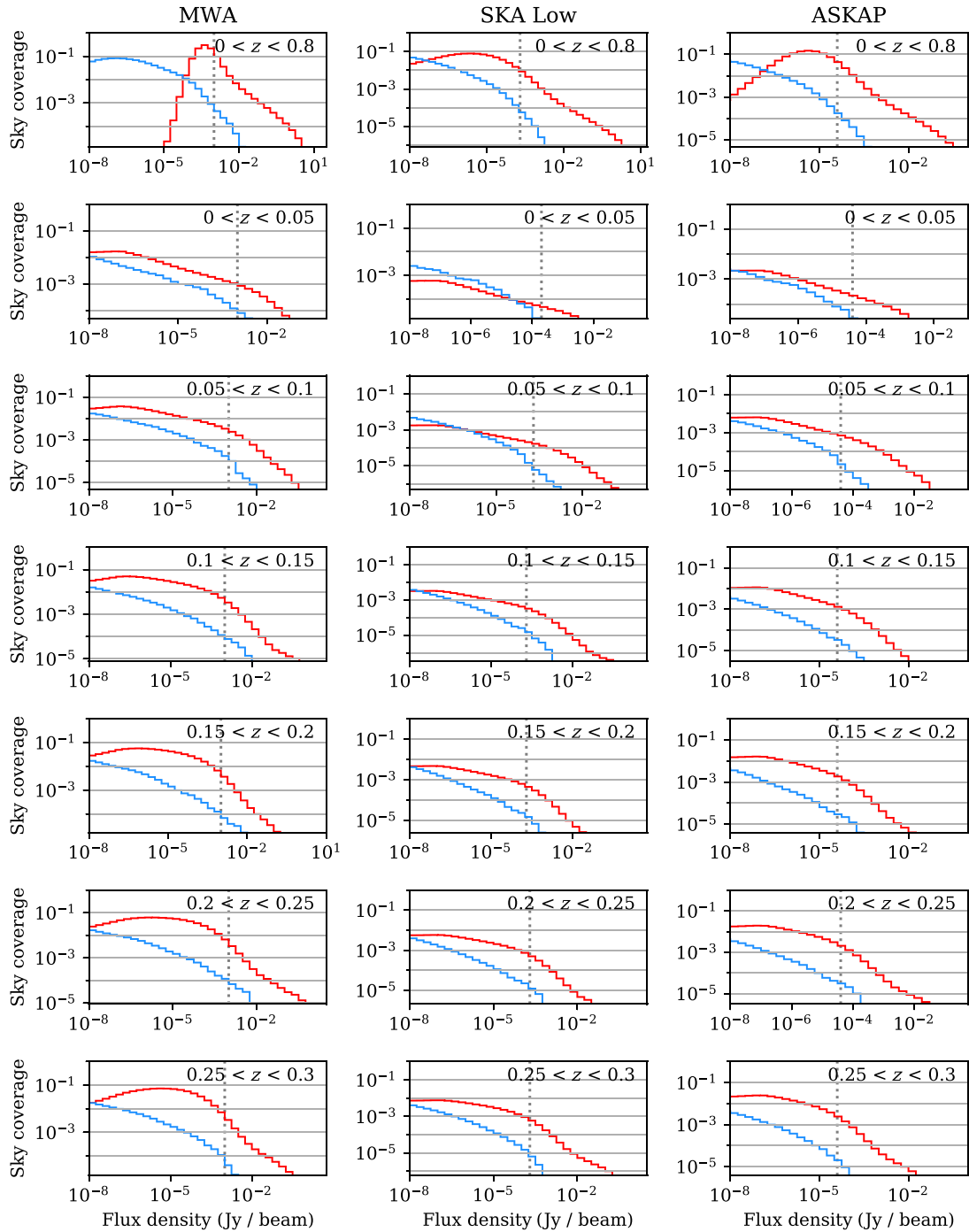


Figure 10. The sky coverage of the cosmic web (blue) and embedded extragalactic (red) emission as a function of flux density binned in $\log_{10} S = 0.25$ increments. We show the sky coverage both as a function of redshift slice, as well as idealised observing configurations for MWA (150 MHz, $60''$), SKA Low (150 MHz, $10''$), and ASKAP (900 MHz, $20''$). Vertical dotted lines indicate the noise threshold for each configuration.

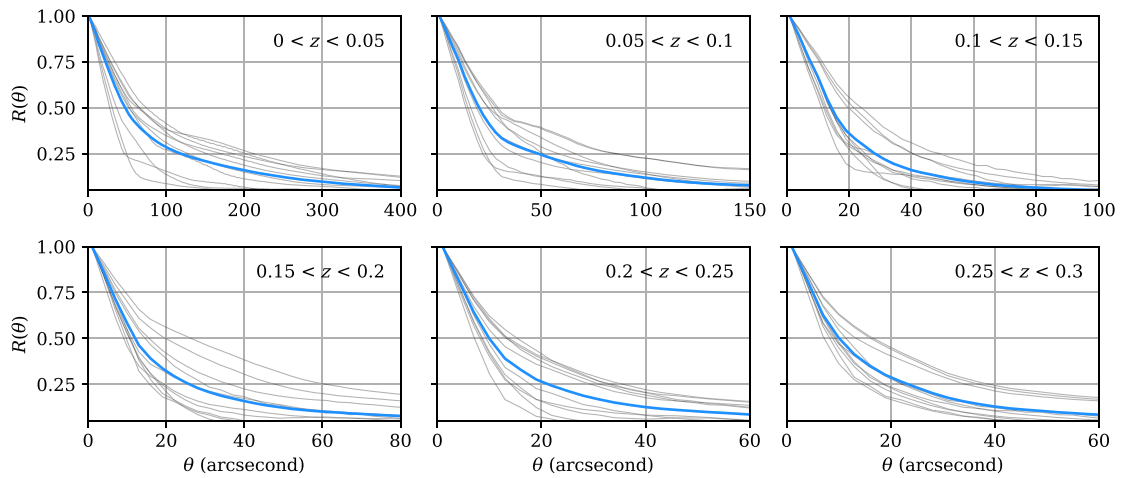


Figure 11. The radial autocorrelation as a function of angular offset, $R(\theta)$, for redshift slices ($\Delta z = 0.05$) out to redshift $z = 0.3$. The autocorrelation of each specific realisation is shown in grey, and the mean across all 10 realisations is shown in blue.

Table 9. The characteristic angular scale of cosmic web emission, measured here by the FWHM of the autocorrelation of the cosmic web maps, for redshift slices of $\Delta z = 0.05$ out to $z = 0.3$. The minimum, mean, and maximum are calculated across each of the 10 realisations and are indicative of the expected cosmic variance between $4'' \times 4''$ fields.

Redshift	min(θ) (arcsec)	mean(θ) (arcsec)	max(θ) (arcsec)
$0 < z < 0.05$	55	105	149
$0.05 < z < 0.1$	28	43	58
$0.1 < z < 0.15$	22	31	48
$0.15 < z < 0.2$	18	28	53
$0.2 < z < 0.25$	14	22	31
$0.25 < z < 0.3$	14	22	33

general, bridge cluster pairs but rather is restricted to halo shells. Whilst previous detection attempts, such as Vacca et al. (2018), have deliberately chosen observing strategies to ensure sensitivity to extended and diffuse emission structures presumed to have angular scales that are multiple arcminutes in extent, these results suggest that a much finer resolution on the order of 20–40'' is best for nearby cosmic web emission.

7.3. Cross-correlating the cosmic web

The cosmic web signal is too faint to detect directly, with the exception of outlier emission knots, and so one promising method is the radial cross-correlation method used by both Brown et al. (2017) and Vernstrom et al. (2017). In this method, a kernel image is first constructed and weighted based on where cosmic web emission is believed to concentrate across a map. This ‘best guess’ map for the cosmic web is then cross-correlated and radially averaged in an effort to bring out the cosmic web signal that is otherwise hidden beneath the image noise; a peak at or very near 0° offset suggests a possible detection of the cosmic web. In Vernstrom et al. (2017), the correlation kernel was produced by using galaxy

density maps, which were believed to be a proxy for large-scale mass density and in turn for the synchrotron component of the cosmic web. A challenge with this approach is that the extragalactic radio population also correlates with this density map, producing an excess cross-correlation signal that is difficult to separate from any potential cosmic web signal.

We here attempt to reproduce this ‘false’ correlation by cross-correlating FIGARO with the mass density maps pertaining to redshift slices of depth $\Delta z = 0.05$, for the redshift range $0.05 < z < 0.3$. Prior to cross-correlation, the mass density maps were smoothed with a Gaussian kernel having a FWHM of 1 Mpc pertaining to the mean redshift of the respective slice. In Figure 12, we show the cross-correlation of FIGARO for each of the idealised observing configurations with these mass density maps (solid line), as well as a ‘null’ result where the underlying cosmic web emission has been spatially flipped (dashed line). All AGN and SFG sources (spanning the full redshift range $0 < z < 8$) have been represented as simple point sources and have been cleaned down to the noise threshold of the respective observing configuration. We observe that all results peak at zero, indicating a positive correlation with the mass density maps. In the case of the null result (dashed line), this correlation is solely the result of the AGN and SFG populations clustering similarly to the underlying mass distribution; this ‘false’ signal is precisely the issue Vernstrom et al. (2017) encountered. However, we also observe an excess correlation in the solid line, and this is due to the additional presence of the cosmic web. The degree of this excess is quite significant, accounting for more than half of the signal in the closest redshifts, and reducing somewhat at higher redshifts. We should note that the presence of other cluster emission that is not modelled in our simulation, such as radio halos, faint and diffuse AGN remnants, and radio phoenix, would further strengthen the ‘null’ result signal and reduce the relative excess; these populations are not well understood and it is very difficult at this time to model their additional contribution to the cross-correlation signal.

This spatial alignment of unrelated cluster emission and cosmic web emission makes detection extremely challenging. Nonetheless, we can still ask the question: if we had perfect

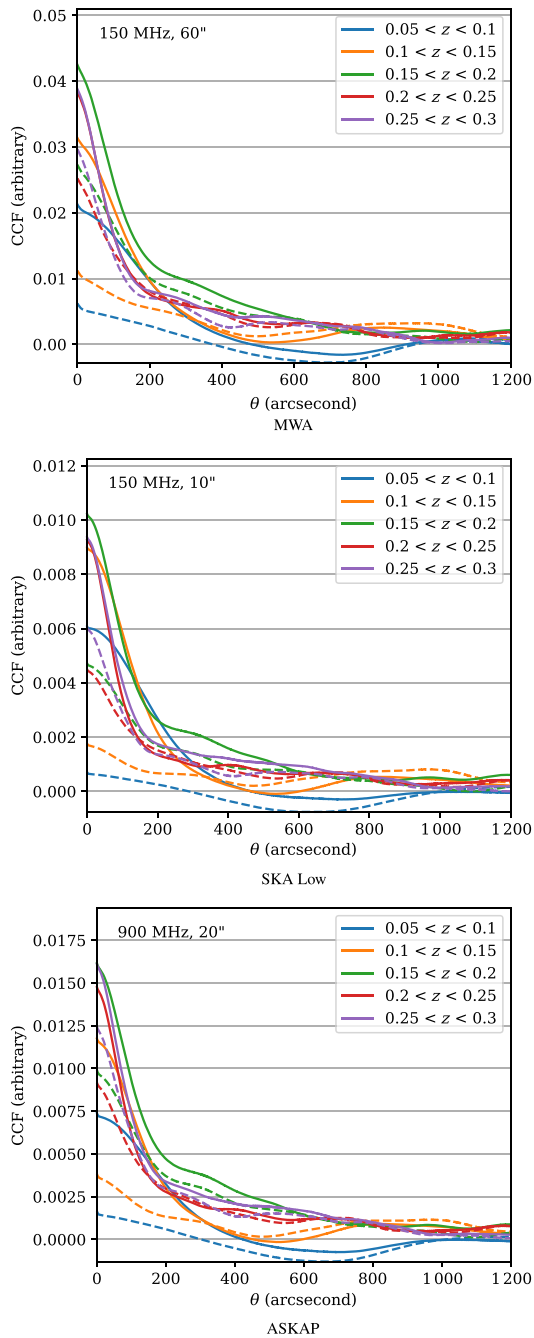


Figure 12. Cross-correlation of mass density with the FIGARO simulations, for a variety of redshift slices (solid lines), and compared with the ‘null’ case where the underlying cosmic web emission has been flipped (dashed). The excess correlation versus the null result therefore shows the cosmic web component of the cross-correlation result.

knowledge of the distribution of the cosmic web, can we avoid the cross-correlation from being polluted by extragalactic population? To answer this, we have computed the cross-correlation of the full FIGARO maps (cosmic web, AGN, and SFG sources combined) with a kernel that is the cosmic web emission located in webshift slices of depth $\Delta z = 0.05$. We do this for all three observing configurations and have cleaned each map down to its respective noise threshold to produce a residual image. In Figure 13, we present the results of this cross-correlation and also additionally a ‘null’ result where we have spatially flipped the cosmic web signal in the map. The cosmic web kernel correlates strongly with itself, as expected, even in amongst the additional AGN and SFG residual sources; and moreover, this correlation seems to peak in the redshift slice $0.1 < z < 0.15$ suggesting this is a sweet spot that maximises cosmological volume against the fading brightness that arises with increasing luminosity distance. The strongest correlation is observed in the MWA configuration, which by observing at 150 MHz takes advantage of the steep spectral index of cosmic web emission, but which is also advantaged by its lower resolution beam that is approximately at the characteristic scale of the cosmic web emission. Despite the disadvantage of observing at a higher frequency, the ASKAP configuration also produces a strong correlation signal suggesting this might well be a valid observing configuration.

Most significantly, however, we observe no significant signal in the null results in Figure 13, and in fact in many cases this signal is not only weak, it is also weakly negative indicating anti-correlation. This is an important result: on average, the cosmic web signal is spatially separate and distinct from the extragalactic radio population, and they do not cluster in the same way. Whilst this provides for the possibility of devising a kernel that does not correlate with other cluster emission, of course any real detection attempt will not be blessed with perfect knowledge of the cosmic web distribution. The much more difficult task will be in devising kernels based only on approximate knowledge and proxies such as the mass distribution, but which do not strongly correlate with central cluster emission. We leave the development of kernels based only on limited knowledge of the Universe to future work.

8. Conclusion

We have released the FIGARO simulation: the first combined simulation of the cosmic web and its embedded extragalactic radio population spanning 10 unique $4^\circ \times 4^\circ$ fields, out to a redshift of $z = 0.8$, and valid over a frequency range 100–1 400 MHz. In doing this, we have brought together the largest MHD simulation to date encompassing 100^3 Mpc^3 —from which we have derived a model of synchrotron cosmic web emission, calibrated to match observed radio relic population statistics—and combined this simulation with the previously released T-RECS codebase to model the embedded extragalactic AGN and SFG embedded populations. Uniquely, these latter populations have been positioned such that they follow the underlying mass distribution of the MHD simulation, and thus cluster realistically alongside the associated cosmic web emission. We make these simulations publicly available as we believe they can be helpful in developing cosmic web detection techniques, as well as in modelling and constraining confounding signals that may arise in the course of these detection attempts.

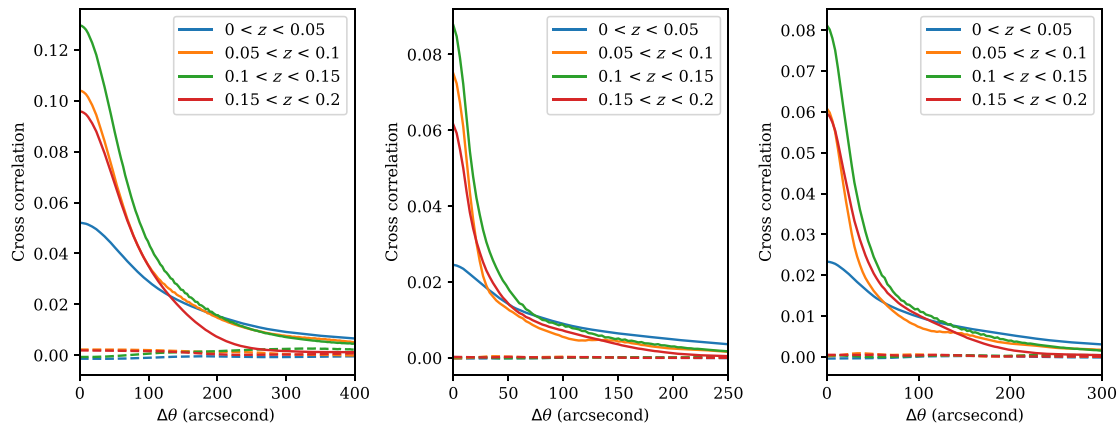


Figure 13. Cross-correlation of the all FIGARO realisations with kernels of the *known* cosmic web signal for a variety of redshift slices (solid line), in comparison with a ‘null’ result where the cosmic web signal has been spatially flipped (dashed line). The cosmic web emission is easily detectable even amongst the extragalactic sources. Note the lack of correlation peak for the null result, showing the extragalactic sources do not cluster in the same way as the cosmic web emission. *Left:* MWA, 150 MHz, 60'' resolution. *Middle:* SKA Low, 150 MHz, 10'' resolution. *Right:* ASKAP, 900 MHz, 20'' resolution.

In addition, we have provided an early analysis of the FIGARO simulation and its properties. Foremost amongst these results is to emphasise the spatial distribution and morphology that the cosmic web takes: as opposed to a sponge-like, filamentary structure that traces the underlying mass distribution, we find that the radio cosmic web is composed of ubiquitous, relic-like shells, principally in the spherical annuli $0.75 \cdot r_{200} < r < 1.5 \cdot r_{200}$ enshrouding dark matter halos. The filaments proper are largely empty of any significant emission. Moreover, the actual distribution of power in these shells is irregular and ‘knotty’. The brightest of these knots rise to the level of detection with the current generation of instruments whilst the surrounding emission rapidly declines in brightness, with a characteristic angular extent of $\lesssim 58''$ already by $z \gtrsim 0.05$, much more compact than has been previously assumed. Indeed, some of these bright, knotty peaks of cosmic web emission are of an angular size that they could be easily confused with more compact emission sources, and indeed may already be present in the current generation of sky surveys.

Our simulation gives hope to the future detection of the cosmic web, primarily since the cosmic web emission and the extragalactic radio sources do not cluster in the same way. Our cross-correlation analysis shows the cosmic web emission is clearly detectable both at 150 and 900 MHz by way of cross-correlation, even in the presence of the much more luminous AGN and SFG sources; and that these embedded sources show negligible correlation, and in many cases, weak anti-correlation, with the cosmic web emission. In this case, the kernel used in the cross-correlation was the known cosmic web map itself; in a real detection attempt, a kernel will need to be devised with only approximate knowledge of the distribution of cosmic web flux. We hope the present simulation can aid in the development of such a kernel.

Besides the AGN and SFG populations, there are additional confounding factors that may impact detection techniques. One such factor in particular is the radio halo population which consists of large, extended low-surface brightness features that are centrally located in cluster and group cores, and which without careful consideration could contribute to false or exaggerated signals. The introduction of this population into FIGARO could prove a useful direction in future work.

Acknowledgements. F.V. acknowledges financial support from the ERC Starting Grant ‘MAGCOW’, no. 714196. The cosmological simulations on which this work is based have been produced using the ENZO code (<http://enzo-project.org>), running on Piz Daint supercomputer at CSCS-ETHZ (Lugano, Switzerland) under project s805 (with F.V. as PI, and the collaboration of C. Gheller and M. Brüggen). We also acknowledge the usage of online storage tools kindly provided by the INAF Astronomical Archive (IA2) initiative (<http://www.ia2.inaf.it>).

References

- Angulo, R. E., Springel, V., White, S. D. M., Jenkins, A., Baugh, C. M., & Frenk, C. S. 2012, *MNRAS*, **426**, 2046
- Baugh, C. M., et al. 2004, *MNRAS*, **351**, L44
- Bonaldi, A., Bonato, M., Galluzzi, V., Harrison, I., Massardi, M., Kay, S., De Zotti, G., & Brown, M. L. 2019, *MNRAS*, **482**, 2
- Botteon, A., Brunetti, G., Ryu, D., & Roh, S. 2020, *A&A*, **634**, A64
- Brown, S. D. 2011, *JApA*, **32**, 577
- Brown, S., et al. 2017, *MNRAS*, **468**, 4246
- Carretti, E., Staveley-Smith, L., Govoni, F., Feretti, L., Murgia, M., Giovannini, G., Vacca, V., & Brown, S. 2013, Parkes-ATCA Cluster Survey (PACS): Single-dish and interferometric imaging of radio halos in Galaxy Clusters, ATNF Proposal
- Cen, R., & Ostriker, J. P. 1999, *ApJ*, **514**, 1
- Davé, R., et al. 2001, *ApJ*, **552**, 473
- Dedner, A., Kemm, F., Kröner, D., Munz, C. D., Schnitzer, T., & Wesenberg, M. 2002, *JCP*, **175**, 645
- de Graaff, A., Cai, Y.-C., Heymans, C., & Peacock, J. A. 2019, *A&A*, **624**, A48
- Eastwood, M. W., et al. 2018, *AJ*, **156**, 32
- Eckert, D., et al. 2015, *Natur*, **528**, 105
- Gheller, C., & Vazza, F. 2020, *MNRAS*, **494**, 5603
- Hale, C. L., Jarvis, M. J., Delvecchio, I., Hatfield, P. W., Novak, M., Smolčić, V., & Zamorani, G. 2018, *MNRAS*, **474**, 4133
- Hoefl, M., & Brüggen, M. 2007, *MNRAS*, **375**, 77
- Hotan, A. W., et al. 2021, *PASA*, **38**, e009
- Keshet, U., Katz, B., Spitkovsky, A., & Waxman, E. 2009, *ApJ*, **693**, L127
- Landy, S. D., & Szalay, A. S. 1993, *ApJ*, **412**, 64
- Ling, E. N., Frenk, C. S., & Barrow, J. D. 1986, *MNRAS*, **223**, P21
- Macquart, J.-P., et al. 2020, *Natur*, **581**, 391
- Magliocchetti, M., Popesso, P., Brusa, M., Salvato, M., Laigle, C., McCracken, H. J., & Ilbert, O. 2017, *MNRAS*, **464**, 3271
- Murray, S. G., Power, C., & Robotham, A. S. G. 2013, *A&C*, **3**, 23

- Nicastro, F., Kaastra, J., Krongold, Y., Borgani, S., Branchini, E., Cen, R., Dadina, M., Danforth, C. W., Elvis, M., Fiore, F., Gupta, A., Mathur, S., Mayya, D., Paerels, F., Piro, L., Rosa-Gonzalez, D., Schaye, J., Shull, J. M., Torres-Zafra, J., Wijers, N., & Zappacosta, L. 2018, *Natur*, **558**, 406
- Nuza, S. E., Hoeft, M., van Weeren, R. J., Gottlöber, S., & Yepes, G. 2012, *MNRAS*, **420**, 2006
- Pinzke, A., Oh, S. P., & Pfrommer, C. 2013, *MNRAS*, **435**, 1061
- Planck Collaboration 2016, *A&A*, **594**, A19
- Prandoni, I. New constraints on the faint radio source population from the LoTSS deep fields SKA Observatory Virtual Conference: A Precursor View of the SKA Sky
- Ryu, D., Kang, H., Hallman, E., & Jones, T.W. 2003, *ApJ*, **593**, 599
- Tanimura, H., Aghanim, N., Douspis, M., Beelen, A., & Bonjean, V. 2019, *A&A*, **625**, A67
- Tingay, S. J., et al. 2013, *PASA*, **30**, e007
- Vacca, V., et al. 2018, *MNRAS*, **479**, 776
- Vazza, F., Brüggén, M., van Weeren, R., Bonafede, A., Dolag, K., & Brunetti, G. 2012, *MNRAS*, **421**, 1868
- Vazza, F., Etori, S., Roncarelli, M., Angelinelli, M., Brüggén, M., & Gheller, C. 2019, *A&A*, **627**, A5
- Vazza, F., Ferrari, C., Brüggén, M., Bonafede, A., Gheller, C., & Wang, P. 2015, *A&A*, **580**, A119
- Vernstrom, T., et al. 2014, *MNRAS*, **440**, 2791
- Vernstrom, T., Gaensler, B.M., Brown, S., Lenc, E., & Norris, R. P. 2017, *MNRAS*, **467**, 4914
- Vernstrom, T., Heald, G., Vazza, F., Galvin, T., West, J., Locatelli, N., Fornengo, N., & Pinetti, E. 2021, arXiv e-prints, p. arXiv:2101.09331.
- Wayth, R. B., et al. 2018, *PASA*, **35**, 33

A. Two-point correlation function

To compare clustering properties, we make use of the two-point correlation function $\xi(r)$. For a given set of points in a volume, this function estimates the probability of finding two points separated by some distance r with respect to a set of points that were randomly (uniformly) distributed. We have calculated this function using the estimator provided by Landy and Szalay (1993):

$$\xi(r) = \frac{\langle D, D \rangle - 2f\langle D, R \rangle + f^2\langle R, R \rangle}{f^2\langle R, R \rangle} \quad (\text{A1})$$

In this equation the notation $\langle A, B \rangle$ indicates the number of unique pairs of points (a, b) , where $a \in A$ and $b \in B$, for which the condition $r < |a - b| < r + dr$ is satisfied. The set D is our data, and contains the set of points for which we wish to calculate the two-point correlation function; the set R is a set of points randomly assigned to the same volume according to a uniform distribution; $f = \text{length}(D)/\text{length}(R)$ is a normalisation constant to account for any differences in the number of points in each set. To calculate the error in this estimate, we use the ‘bootstrap resampling’ method (see, e.g. Ling et al. 1986) whereby we repeat the calculation for a number of independently generated R , over which we can calculate the mean and standard deviation of the resulting values.

In the case of the angular two-point correlation function, the Euclidean distance is replaced by the apparent angular distance in projection on the celestial sphere.

B. Confusion limit calculation

The choice of lower flux threshold when generating the T-RECS catalogue was selected so as to fully simulate classical confusion noise in the frequency range 150–1400 MHz assuming a maximum resolution of $8''$. We make use of the ‘probability of deflection’ or $P(D)$ technique that is described in Vernstrom et al.

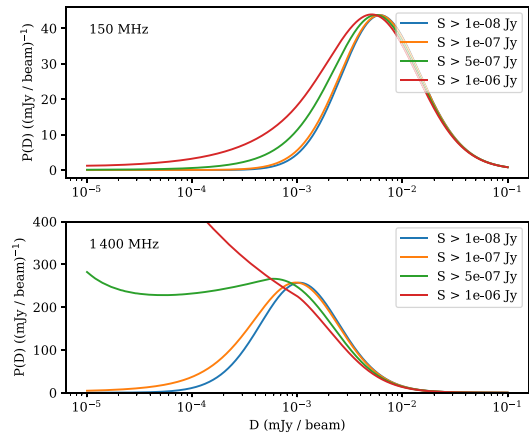


Figure B.1. The probability of deflection for the T-RECS catalogue at 150 and 1400 MHz with an $8''$ circular Gaussian beam. Each curve shows the distribution for a different lower 1400 MHz threshold cutoffs, showing that simulating sources down to $0.1\mu\text{Jy}$ at 1400 MHz is sufficient to simulate the classical confusion noise across this frequency range.

(2014), and references therein, to calculate the classical confusion noise. This technique allows for us to calculate, for any given point on the sky, the probability distribution of the flux density per beam based upon two inputs: a differential source count (dN/dS) and a synthesised beam shape. The classical confusion noise can then be estimated from the width of the peak in this distribution. In this case, we calculated the differential source count from the T-RECS catalogue itself, calculated independently at 150 and 1400 MHz, and for the synthetic beam shape we assumed a circular Gaussian with FWHM of $8''$. In Figure B.1, we compare the $P(D)$ distribution that results from a range of lower flux thresholds, that is to say, by setting $\frac{dN}{dS_{1400}}(S < S_0) = 0$ for a range of S_0 . At 150 MHz, for all the lower flux thresholds considered, we can see the central peak is well formed indicating that the confusion noise (at $\sim 18\mu\text{Jy beam}^{-1}$) is well simulated. At 1400 MHz, on the other hand, we can see that for the lower flux thresholds of $5 \times 10^{-7}\text{Jy}$ and 10^{-6}Jy the peaks are malformed, and only at 10^{-7}Jy and below is the confusion noise (at $\sim 3\mu\text{Jy beam}^{-1}$) well simulated.

C. Radial cross-correlation

The radial cross-correlation of discrete maps A and B is constructed by first calculating its 2D cross-correlation function, which is defined as

$$R(\Delta x, \Delta y) = \sum_{ij} \frac{(A(i, j) - \bar{A})(B(i + \Delta x, j + \Delta y) - \bar{B})}{N(\Delta x, \Delta y) \cdot \sigma_A \sigma_B}, \quad (\text{C1})$$

where $A(i, j)$ is the (i, j) th component of map A , \bar{A} is the map mean, σ_A is the standard deviation across the map, and $N(\Delta x, \Delta y)$ is a normalisation function. In essence, the maps are offset from each other by $\Delta x, \Delta y$ and we sum the product of all overlapping values, where the normalisation function simply counts the number of overlapping cells. The radial autocorrelation function is simply the radial average of this function, with $r = \sqrt{\Delta x^2 + \Delta y^2}$, and where in practice, we discretise radial values into bins and average over the 2D values of the function that fall within the bin.

B.4 Hodgson et al. (2022b)



Searching for the synchrotron cosmic web again: A replication attempt

[Hodgson, Johnston-Hollitt, McKinley & Hurley-Walker \(2022a\)](#)

© The authors 2022. Reproduced with permission.

Research Paper

Searching for the synchrotron cosmic web again: A replication attempt

Torrance Hodgson^{1,2}, Melanie Johnston-Hollitt², Benjamin McKinley^{1,3} and Natasha Hurley-Walker¹¹International Centre for Radio Astronomy Research (ICRAR), Curtin University, 1 Turner Ave, Bentley, WA 6102, Australia, ²Curtin Institute for Computation, Curtin University, GPO Box U1987, Perth, WA 6845, Australia and ³ARC Centre of Excellence for All Sky Astrophysics in 3 Dimensions (ASTRO3D), Bentley, Australia

Abstract

We follow up on the surprising recent announcement by Vernstrom et al. (2021, MNRAS) of the detection of the synchrotron cosmic web. We attempt to reproduce their detection with new observations with the Phase II, extended configuration of the Murchison Widefield Array at 118.5 MHz. We reproduce their detection methodology by stacking pairs of nearby luminous red galaxies (LRGs)—used as tracers for clusters and galaxy groups—contained in our low-frequency radio observations. We show that our observations are significantly more sensitive than those used in Vernstrom et al. and that our angular sensitivity is sufficient. And yet, we make no statistically significant detection of excess radio emission along the bridge spanning the LRG pairs. This non-detection is true both for the original LRG pair catalogue as used in Vernstrom et al., as well as for other larger catalogues with modified selection criteria. Finally, we return to the original data sets used in Vernstrom et al., and find that whilst we clearly reproduce the excess X-ray emission from ROSAT, we are not able to reproduce any kind of broad and extended excess intercluster filamentary emission using the original 118.5 MHz MWA survey data. In the interests of understanding this result, as part of this paper we release images of the 14 fields used in this study, the final stacked images, as well as key components of our stacking and modelling code.

Keywords: cosmic web (330) – warm-hot intergalactic medium (1786) – radio astronomy (1338)

(Received 3 December 2021; revised 16 February 2022; accepted 17 February 2022)

1. Introduction

The ‘cosmic web’ is a term used to evoke the structure of the Universe on the very largest of scales. In this model, dense clusters and galaxy groups are connected by diffuse filaments, forming a web like structure, and are interspersed with large, empty voids. Galaxy surveys have provided a strong empirical basis for this model (e.g. Baugh et al. 2004), whilst cosmological simulations have shown it to be a consequence of gravitational instabilities acting upon small density perturbations in the early Universe (e.g. Cen & Ostriker 1999; Davé et al. 2001). These same simulations, however, have predicted something more: that up to 40% of the baryonic content of the Universe resides along these filaments and around the periphery of clusters and galaxy groups, existing in a diffuse, highly ionised plasma, the so-called ‘warm-hot intergalactic medium’ (WHIM). To date, the WHIM has proven difficult to detect, however a number of recent works in this area have made increasingly convincing claims to have made detection (see, e.g.: Eckert et al. 2015; Nicastro et al. 2018; Tanimura et al. 2019; Tanimura et al. 2020; Macquart et al. 2020).

This sparse, weakly magnetised WHIM is also predicted to have an associated radio signature, the ‘synchrotron cosmic web’ (see: Brown 2011; Vazza et al. 2015; Vazza et al. 2019). As part of ongoing large-scale structure formation, cosmological simulations

predict strong accretion shocks—having Mach numbers in the range $\mathcal{M} \sim 10\text{--}100$ —from in-falling matter along filaments and around the outskirts of clusters. These shocks should be capable of accelerating the electrons from within the WHIM to high energies by way of diffusive shock acceleration and this population of high energy electrons, in turn, are expected to radiate this energy as synchrotron emission as they interact with weak intercluster magnetic fields. In this way, the cosmic web is expected to have a synchrotron radio signature that traces out accretion shocks along its boundaries. The detection and confirmation of this radio emission would allow us to validate models of the large-scale structure of the Universe, as well as giving us insight into the poorly understood intercluster magnetic environments at the sites of these shocks.

This synchrotron cosmic web, however, is predicted to be extremely faint and has proven especially difficult to detect. Large-scale magnetohydrodynamic simulations by Vazza et al. (2019), for example, point to a large population of radio-relic-like shocks well below the level of direct detection of any current or future radio telescopes. Only a small fraction of the very brightest knots in these shocks rise to the level of direct detection, and these are located principally around the most massive galaxy clusters (Hodgson et al. 2021b). Vacca et al. (2018) did in fact claim direct detection of numerous large-scale synchrotron sources associated with the cosmic web, but follow-up observations by Hodgson et al. (2020) rebuffed these claims. More recently, Govoni et al. (2019) claimed the detection of a radio ‘ridge’ extending between clusters Abell 309 and 401, suggesting a diffuse, energetic and magnetised plasma extending between the merging clusters. Whilst this detection goes some way to validating our models, in this particular case

Corresponding author: Torrance Hodgson, email: torrance@pravic.xyz

Cite this article: Hodgson T, Johnston-Hollitt M, McKinley B and Hurley-Walker N. (2022) Searching for the synchrotron cosmic web again: A replication attempt. *Publications of the Astronomical Society of Australia* 39, e013, 1–24. <https://doi.org/10.1017/pasa.2022.9>

the energy is provided by the merging dynamics of the clusters and is qualitatively different to the more general mechanisms of the synchrotron cosmic web.

Other attempts to detect the synchrotron cosmic web have turned to statistical detection techniques to reveal faint emission sources buried beneath the noise of our current observations. Foremost among these methods is the cross-correlation technique. This method involves constructing a ‘best guess’ kernel of the probable locations of cosmic web emission, and performing a radial cross-correlation of this kernel with the radio sky. A positive correlation at 0° offset is, in theory, indicative of a detection. In this way, this method hopes to reduce the noise by effectively integrating over a large enough area of the sky. Both Brown *et al.* (2017) and Vernstrom *et al.* (2017) used cross-correlation methods, and both were unable to make a definitive detection. In the former study, no positive correlation was detected. In the latter, Vernstrom *et al.* (2017) did indeed report a correlation, however the association of other sources such as active galactic nuclei (AGNs), star forming galaxies (SFGs), and other cluster emission with their correlation kernel meant they were unable to attribute the peak at 0° to the cosmic web alone.

Recently, however, Vernstrom *et al.* (2021) (herein: V2021) have reported definitive detection of the synchrotron cosmic web using an alternative statistical method known as stacking. Their method attempted to measure the mean intercluster radio emission between pairs of close-proximity luminous red galaxies (LRGs). LRGs are known to have a strong association with the centre of clusters and galaxy groups (Hoessel, Gunn, & Thuan 1980; Schneider, Gunn, & Hoessel 1983; Postman & Lauer 1995). Close-proximity pairs of LRGs therefore are likely to indicate close-proximity overdense regions of our Universe, and in turn we expect some fraction of these to be connected by a filament. Thus, V2021 stacked hundreds of thousands of low-frequency radio images of such pairs, which were rotated and rescaled so as to align all pairs to a common grid, before being averaged so as to find the mean image. After subtracting out a model for the LRG and cluster contribution, they reported finding excess emission with $>5\sigma$ significance along the length of the intercluster region. Moreover, this excess was detected by two independent instruments—in the Galactic and Extragalactic All-sky MWA^a survey (Wayth *et al.* 2015; Hurley-Walker *et al.* 2017b) and by the Owens Valley Radio Observatory Long Wavelength Array (OVRO-LWA; Eastwood *et al.* 2018)—and across four frequencies ranging from 73–154 MHz. A null test, formed by stacking physically distant LRG pairs for which we do not expect a connecting filament to exist, returned no excess emission. After excluding multiple alternative explanations, V2021 suggested the most likely explanation for this excess intercluster signal was the cosmic web itself.

The result reported in V2021 is convincing, but it is also surprising. Previous intercluster magnetic field estimates provided upper limits on the order of just a few nG (e.g. Pshirkov, Tinyakov, & Urban 2016; O’Sullivan *et al.* 2019; Vernstrom *et al.* 2019). However, the reported excess emission supports intercluster magnetic field strengths averaging 30–60n G, and moreover these estimates are strictly a lower limit as some significant fraction of stacked pairs will not in fact be connected by a filament. More recent follow-up work by Hodgson *et al.* (2021a), which stacked

a simulated radio sky—including cosmic web emission—from the Filaments and Galactic RadiO (FIGARO; Hodgson *et al.* 2021b) simulation, failed to reproduce excess intercluster emission. With perfect knowledge of their simulated sky, this work stacked the known locations of dark matter halos rather than LRGs. They reported excess emission being detected on the immediate interior of halo pairs, associated with asymmetric accretion shocks onto clusters and galaxy groups, but no detectable emission along the true intercluster region. This work also explored the role of other contaminating sources, such as AGN, SFG, and radio halo populations, as well as the effect of sidelobes from the dirty interferometric beam, finding none of these to be significant. The discrepancy between V2021 and these simulated results, which build on our current best simulations of the cosmic web, remain difficult to explain.

Given the importance of the result of V2021, in this present study we attempt to reproduce and corroborate their result. We do so using the upgraded MWA Phase II instrument (Wayth *et al.* 2018), observing at 118 MHz, and take advantage of improvements to calibration and imaging pipelines that have appeared since the original GLEAM survey. We image 14 fields spanning the same LRG pairs as used in V2021, which we then stack using independent stacking and modelling pipelines. Our aim is to closely adhere to the methodology used in V2021 whilst seeking to measure the excess intercluster emission more accurately, thanks to the improved noise characteristics of our observations.

Throughout this paper, we assume a Λ CDM cosmological model, with density parameters $\Omega_{\text{BM}} = 0.0478$ (baryonic matter), $\Omega_{\text{DM}} = 0.2602$ (dark matter), and $\Omega_{\Lambda} = 0.692$, and the Hubble constant $H_0 = 67.8 \text{ Km s}^{-1} \text{ Mpc}^{-1}$. All stated errors indicate one standard deviation.

2. Luminous red galaxy pairs

Only a few thousand clusters are currently catalogued with robust X-ray or Sunyaev–Zeldovich measurements (e.g. Piffaretti *et al.* 2011; Planck Collaboration *et al.* 2016). This number is much smaller than the expected number of clusters and galaxy groups (e.g. Wen, Han, & Yang 2018), and is also too few to be useful for our present purposes as we do not expect the faint, intercluster emission to become detectable above our field noise after stacking so few images. Instead, as with V2021, we turn to using LRGs as a proxy for such overdense regions. LRGs are massive, especially luminous early-type galaxies, and are closely associated with overdense regions of the Universe. This association, however, comes with some caveats as explored in detail in Hoshino *et al.* (2015). To summarise briefly here, in the first instance not all massive clusters have a LRG as their central galaxy: for the most massive clusters the probability of this association peaks at 95%, however this association steeply drops off for lower mass systems, reaching just 70% for clusters of mass $M_{200} = 10^{14} M_{\odot}$. An additional error introduced from the brightest LRGs located in clusters that do not align with the cluster centre, and this ‘miscentred’ fraction is substantial at 20–30%. Nonetheless, as with V2021, these caveats are acceptable given the vastly greater number of potential clusters that LRGs allow us to identify. It does, however, mean that any excess emission attributed to intercluster regions are strictly lower limits.

As with V2021, we use the LRG catalogue from Lopes (2007). This catalogue incorporates approximately 1.4 million LRGs extracted from the fifth data release of the Sloan Digital Sky Survey

^aMurchison Widefield Array (MWA; Tingay *et al.* 2013).

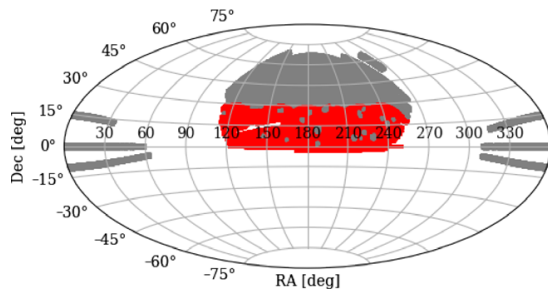


Figure 1. LRG pair distribution on the sky. The red points indicate pairs used in our stacks, whilst the grey are those pairs either outside our field or are within an exclusion zone.

(York et al. 2000), out to a redshift of $z < 0.70$. Lopes (2007) have used an empirical based method to calculate spectroscopic redshifts for this population from just three bands (*gri*), with an estimated error $\sigma = 0.027$ for $z < 0.55$, and $\sigma = 0.040$ up to $z = 0.70$.

In V2021, a list of LRG pairs was calculated that met the following set of conditions. First, the separation between the pairs was less than 15 Mpc. The metric used was the comoving distance, and this condition also included a lower bound of 1 Mpc (T. Vernstrom, personal communication). Additionally, the pairs were required to have an angular separation on the celestial sphere in the range $20' < \theta < 180'$. We find 1 078 730 such valid pairs, of which 601 435 ultimately overlap with our fields, and label this catalogue ‘Max 15 Mpc’. In Figure 1 we show the location of the LRG pair population on the celestial sphere, with those in red overlapping with our fields.

V2021 reported finding just 390 808 pairs that satisfied these conditions. As it turns out, this reduced catalogue was the result of a bug in their code (T. Vernstrom, personal communication). Therefore, to compare like for like, we additionally include this abridged catalogue as ‘LRG-V2021’.

We also provide two additional catalogues of LRG pairs with differing selection criteria. In the first, we reduce the maximum spatial separation to 10 Mpc (‘Max 10 Mpc’), of which there are 270 458 (153 433 overlapping) entries. The motivation for this catalogue arises from our expectation that intercluster emission should be brighter for cluster pairs in closer proximity to each other where they are more likely to be interacting, possibly triggering pre- or post-merger shocks known to produce synchrotron emission. We also include a final catalogue with modified angular constraints, such that the minimum and maximum angular separations are shifted to $15'$ and $60'$, respectively (‘Max $60'$ ’). This catalogue contains 824 773 (436 899 overlapping) entries, and is motivated by concerns about resolving out large-scale angular structures, which is an aspect we discuss later in Subsection 5.2.

In Figure 2, we show the redshift, angular separation and spatial separation distributions of each of these LRG catalogues, for those LRG pairs that overlap with our fields and are included in our stacks. Note the double peak structure present in the redshift distribution of the Max 15 Mpc and Max $60'$ catalogues: this is a function of the underlying distribution of the LRG catalogue which exhibits a small peak around $z = 0.08$ and much larger peak around $z = 0.5$, combined with the effect at increasing redshifts of the dual constraints of the minimum angular separation and

the maximum spatial separation. In the case of the 15 Mpc criterion, we find a mean redshift of $\langle z \rangle = 0.185$, a mean separation of $\langle r \rangle = 11.6$ Mpc, and a mean angular separation of $\langle \theta \rangle = 67'$. The mean values for the other LRG pair catalogues are provided in Table 1.

3. Observations & data processing

3.1. Data selection

The original GLEAM survey, which was used in V2021, was observed using the MWA Phase I (Tingay et al. 2013). This consisted of 128 tiles positioned to give a maximum baseline of approximately 3 km when observing at zenith, and a large number of baselines under 100 m; when observing near the horizon these baselines are significantly foreshortened. The upgrade to the MWA Phase II (Wayth et al. 2015) in late 2017 was primarily a reconfiguration of the tile positions: the same 128 tiles were positioned to give an increased maximum baseline of almost 6 km as well as a much smoother distribution of baselines. The effect of these changes was to give Phase II almost twice the resolution as well as a better behaved dirty beam with reduced sidelobes, whilst otherwise leaving the point-source sensitivity unchanged. Sidelobe confusion is a major source of noise in Phase I observations, whereas in Phase II observations the higher resolution allows much deeper cleaning, which has flow on effects to further reduce image noise even when accounting for the resolution difference. In the observations used in this study, we take advantage of these improved characteristics of the MWA Phase II.

We have drawn our observations from those made in preparation for the upcoming GLEAM-X survey (Hurley-Walker et al. 2017a). GLEAM-X has observed the sky at frequencies ranging from 72–231 MHz in short duration ‘snapshots’ of approximately 2 min. These observation runs are typically observed at a fixed pointing in a ‘drift scan’ mode, where the celestial sphere is allowed to freely rotate through the primary beam.

We have identified 14 fields to image that best span the LRG population. These fields are centred at declinations of $\delta = \{+2^\circ, +18^\circ\}$ and spanning the right ascension range of $120^\circ \leq \alpha \leq 240^\circ$ at intervals of 20° . From the archive of GLEAM-X observations, we filter for snapshots observed at 118.5 MHz and where their pointing centres are located near the centre of these 14 fields, with a tolerance $\alpha \pm 5^\circ$ and $\delta \pm 3^\circ$. There are 512 observations that match this criteria, made during runs in 2018 February–March, 2018 May–June, 2019 January–February, and 2019 March. After calibration, imaging, and quality control checks, however, this number is reduced to 291 snapshots, constituting approximately 10 h of observations. In Table 2 we tabulate these 14 fields and some of their properties.

3.2. Data processing

All observations are centred at 118.5 MHz, of 112 s duration, spanning a bandwidth of 30.72 MHz, and correlated at a resolution of 10 kHz and 0.5 s. This is further averaged to 40 kHz and 4 s prior to calibration and imaging to ease data storage and processing requirements. All subsequent data processing occurs on a per snapshot basis until final mosaicing.

Calibration is performed using an in-field radio sky model. This sky model has been constructed in preparation for the

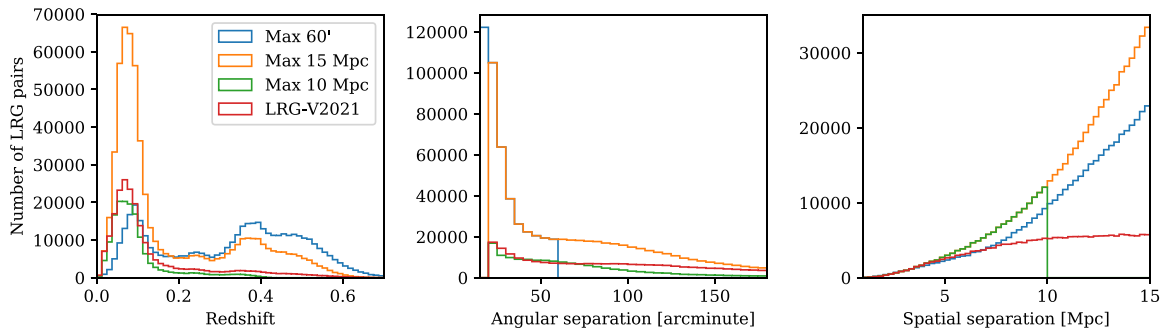


Figure 2. The LRG pair distributions by redshift (left), angular separation (centre), and spatial separation (right), for each of the LRG pair catalogues used in our stacks.

Table 1. LRG pair statistics comparison between each of the LRG pair catalogues. We show the spatial and angular selection criteria for each catalogue, the number of LRG pairs that overlap with our fields (and the total pairs), their mean redshift, their mean angular separation, and their mean spatial separation, respectively. Spatial distances use a comoving metric.

	Spatial criteria (Mpc)	Angular criteria (arcminute)	N	$\langle z \rangle$	$\langle \Delta r \rangle$ (arcminute)	$\langle \Delta \theta \rangle$ (Mpc)
Max 15 Mpc	$1 < r < 15$	$20 < \theta < 180$	601 435 (1 078 730)	0.18	11.5	67.8
Max 10 Mpc	$1 < r < 10$	$20 < \theta < 180$	153 433 (270 458)	0.098	7.6	65.8
Max 60'	$1 < r < 15$	$15 < \theta < 60$	436 899 (824 773)	0.32	11.4	28.5
LRG-V2021	$1 < r < 15^*$	$20 < \theta < 180^*$	219 684 (390 808)	0.14	10.3	83.8

*Due to an error in the work of V2021, the LRG-V2021 catalogue is an incomplete catalogue that nonetheless adheres to these ranges.

Table 2. A summary of the 14 fields imaged, observed by the MWA Phase II instrument at 118 MHz. The fields span the right ascension range 120° to 240° in 20° increments, at declinations of 3° and 18° . We indicate the number of 112 s duration snapshots used in each field mosaic, and the resulting noise at the centre of the field. The model deviation describes the ratio of the measured flux density of sources after performing source finding, in comparison to the original calibration sky model; the μ term describes the mean values of these ratios, whilst σ shows the standard deviation of these ratios.

ID	RA (deg)	Dec (deg)	Snapshots	Noise (mJy beam ⁻¹)	Model deviation μ σ (dex)	Notes
1	120	3	19	8.2	0.000/0.025	
2	140	3	35	5.8	0.001/0.021	Hydra A present in field, peaking at ~ 260 Jy beam ⁻¹
3	160	3	28	7.1	0.000/0.022	Affected by sidelobes from Virgo A
4	180	3	35	6.6	-0.002/0.028	Virgo A present in field peaking at ~ 526 Jy beam ⁻¹ , and second bright source present 3C 273 peaking at ~ 105 Jy beam ⁻¹
5	200	3	31	8.8	0.000/0.022	Large-scale sidelobe pattern present from Centaurus A which is positioned south out-of-field in sidelobe of the primary beam. Virgo A also present in field.
6	220	3	15	8.4	0.001/0.026	
7	240	3	11	10.0	-0.001/0.022	Hercules A present in field peaking at ~ 377 Jy beam ⁻¹
8	120	18	11	8.0	-0.002/0.027	
9	140	18	17	6.2	0.000/0.026	Large-scale sidelobe pattern from Virgo A in south, out-of-field
10	160	18	20	6.4	-0.001/0.030	
11	180	18	24	6.8	-0.001/0.035	Both Virgo A and 3C 273 present in field
12	200	18	19	9.5	-0.004/0.037	Virgo A present, as well as large-scale sidelobe pattern from Centaurus A, positioned south out-of-field
13	220	18	11	11.1	-0.003/0.036	
14	240	18	7	14.6	0.001/0.031	

GLEAM-X survey, and is principally based on the GLEAM sky catalogue. It does, however, include a number of additional sources, including better models for the so-called ‘A-team’ of extremely bright radio sources, such as Hydra A, Virgo A, Hercules A, and

Centaurus A, all of which populate our fields. The GLEAM sky catalogue is known to have an error of 8.0(5)% up to declination 18.5° , and an uncertainty of 11(2)% for more Northern declinations. We calibrate on all sources from this sky model that are

within a 20° radius of our field centre, and having a primary beam-attenuated apparent flux density of at least 700 mJy. These sources are predicted into the visibilities using the full embedded element primary beam model (Sokolowski et al. 2017).

Calibration is performed using the updated MWA calibrate tool,^b which finds a full Jones matrix solution for each antenna, independently for each pair of channels, and with the solution interval set to the duration of the snapshot. Baselines longer than approximately 3.7 km are excluded from consideration during calibration, since these baselines are increasingly sensitive to angular scales of a higher resolution than the original GLEAM catalogue. Calibration solutions are visually inspected, and any antennae which have failed to well converge are flagged at this time. No self-calibration is performed, as in practice we have found this to be unnecessary.

Imaging is performed using `wsclean` (Offringa et al. 2014). We weight baselines using the Briggs formulation, with a robustness factor of +1; additionally baselines smaller than 15λ , which are sensitive to emission on angular scales larger than 3.8° , are excluded to avoid any kind of large-scale contamination from Galactic emission. Cleaning is then performed down to a threshold that depends on two factors: cleaning continues until first the ‘auto-mask’ threshold is reached, which is set at a factor of 3 times the residual map noise, and then cleaning continues only on those pixels previously cleaned down to the ‘auto-threshold’ limit, which we set as the estimated residual map noise. Typical values for the residual map noise of these individual snapshots is around 15–20 mJy. During imaging, we split the 30.72 MHz band into four equally sized channels to account for the typical flux density changes of sources over this frequency range due both to intrinsic properties and beam attenuation. We do, however, perform joint-channel cleaning, where clean peaks are chosen based on a full-bandwidth mean map, and the peak value is estimated using a linear fit across each output channel. Note that whilst `wsclean` does have multiscale clean functionality, we have chosen not to use this, so that any faint, extended emission sources *remain* in the residual maps after cleaning. We image and clean instrumental polarisations (e.g. XX, XY, YX, YY) independently, which is important since sources at this low elevation become strongly polarised as a result of the primary beam. These instrumental polarisation images are later combined based on the primary beam model to produce Stokes I images. Finally, after imaging is completed, we keep both the restored and residual Stokes I images for each snapshot for later processing: the restored map is used to verify and correct field calibration, whilst the residual map provides us with a point-source subtracted map to be ultimately used in stacking, without the need for complex wavelet subtraction techniques as used in V2021.

As a first order effect of ionospheric electron density variations, we observe direction-dependent shifts in the apparent position of radio sources, and these effects become increasingly strong at the low frequencies observed by the MWA. Without resolving this positional error, we not only risk introducing astrometric errors, but additionally sources in the final mosaic can appear blurred and point sources have a peak to integrated flux density ratio that is less than unity. To resolve this, typical MWA workflows make image-based corrections to ‘warp’ the image, and align the apparent position of sources with their position in the sky model (for

example, see Hurley-Walker & Hancock 2018). We follow this method by first source finding on the restored image using `Aegean` (Hancock, Trott, & Hurley-Walker 2018), and cross-matching these sources with our sky model. We include only those sources that are isolated by at least $1'$ radius from any other sky model source to avoid any ambiguous matches, and as a quality control check we require at least 200 cross-matches in a snapshot or else it is discarded. Then by measuring the angular offset of apparent position to that of the sky model, we interpolate across these deviations and thus warp the image to correct for this effect.

In an effort to match the sensitivity to extended emission of the MWA Phase II instrument to that of its Phase I counterpart, we proceed by convolving both the restored and residual images. At 118.5 MHz, a typical dirty beam size at Briggs +1 weighting has major and minor axes of approximately $2.3' \times 1.8'$, whilst this size varies significantly by declination due to the foreshortening effect of the array at low elevations. We use `miriad` (Sault, Teuben & Wright 1995) to convolve each snapshot to a circularised resolution of $3'$, defined at zenith. We discuss the effects of this convolution step, and our sensitivity to extended emission, in Subsection 5.2.

Our snapshots are ready to be stacked and mosaiced. To do this we must first ensure all images are on the same projection, which are presently in a slant orthographic projection (‘SIN’) with the projection origin at each snapshot’s zenith. To minimise reprojection errors, which can be significant, we choose to reproject each snapshot onto the mean projection shared amongst the snapshots for a particular field, leaving the SIN projection origin approximately at the MWA zenith. We additionally mask the region within 15° of the horizon for each snapshot, as these low-elevation observations are subject to significant errors. With these steps completed, we perform the weighted mean of all snapshots, with the weight based on the estimated local map noise σ , as $\frac{1}{\sigma^2}$.^c A final quality check is included during this mosaicing step, whereby any snapshot with a map noise in excess of 35 mJy beam^{-1} (increased to 45 mJy beam^{-1} for field 14) is discarded. In this way, we create mosaics of the residuals, the restored images, as well as the estimated noise.

Finally, we verify our calibration by source finding on the final mosaic and comparing the measured flux density to the sky model flux density. As reported by Hurley-Walker et al. (2017b), we observe a declination-dependent flux density error. In Figure 3, we present the kind of diagnostic used to check the flux density values for each field. For example, the top panel of this figure shows this error across field 10, showing the measured to model integrated flux density ratio increases from approximately unity to as high as 1.3 times at declination $+30^\circ$. To correct for this effect, we model this error as a simple linear function of declination, as depicted by the dashed black line, and scale the image accordingly. The centre panel in Figure 3 shows the effect of this correction: the mean flux density ratio is reduced from 0.044 dex to -0.001 dex; the spread of ratios is reduced from a standard deviation of 0.0436 dex to 0.030 dex; and in this particular instance, the apparently

^cThe local noise map is calculated using the median absolute deviation from the median (MADM) applied to a residual image that has *not* been primary beam corrected. We choose to use this image for our noise estimation as it has had bright sources removed and, prior to beam correction, the noise does not vary spatially, thus allowing for the easy calculation of a global value. We then apply a beam correction to this constant noise map so as to obtain an estimate of the local noise map, which varies spatially as a function of the primary beam.

^bSee <https://github.com/torrance/MWAjl/>.

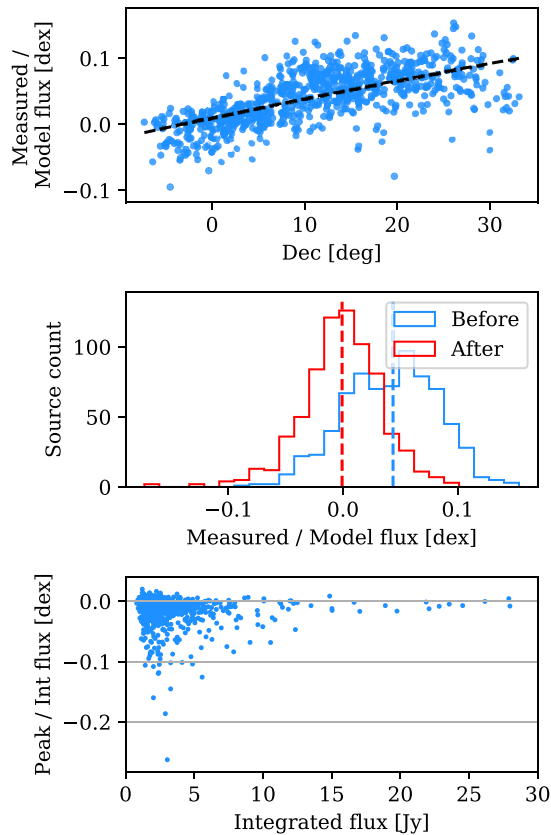


Figure 3. Example calibration diagnostics for field 10, showing the declination correction. The 731 measured sources are compared to the calibration model. Prior to correction, their ratio has mean 0.044 dex and standard deviation 0.044 dex; after correction the mean becomes -0.001 dex and standard deviation 0.030 dex. *Top:* The measured to model flux density ratio, as a function of declination. The dashed line indicates the fit which is later used as an image-based correction. *Centre:* The distribution of measured to model flux density ratios for all 731 sources prior to (blue) and after (red) correction. Note in this case, the simple declination correction resolves the initial bimodal distribution. *Bottom:* The measured ratio of peak to integrated flux density, showing peak and integrated flux density of point sources are very nearly identical.

bimodal distribution is corrected to appear much more normally distributed. As shown in Table 2, the mean flux density ratio across all fields is very nearly 0 dex after this correction, whilst the standard deviation lies in the range 0.021–0.037 dex. These values are well within the stated errors of the GLEAM sky model. As a final sanity check, we also show in the lower panel of Figure 3 the ratio of peak to integrated flux density, where we can observe a good clustering of values around unity, suggesting that our ionospheric corrections are satisfactory.

In Figure 4, we present a zoom of field 10, showing both the restored and residual images. The brightest source in this field is $34.6 \text{ Jy beam}^{-1}$. In the residual map, the estimated noise is just $7.5 \text{ mJy beam}^{-1}$, with a maximum value of 41 mJy beam^{-1} . The central residual map noise in the other fields is listed in Table 2.

Prior to stacking, we convert the residual maps from flux density (in units Jy beam^{-1}) to temperature (units K), taking into account the spatially varying restoring beam dimensions. In this

way, the stacked images are brought to have consistent units despite variable beam sizes, and this is consistent with the method employed in V2021.

3.3. Exclusion zones

We introduce a number of exclusion zones to our fields to improve the quality of our stacked images. In the first instance, during stacking we truncate around the edges of all fields where the beam power reaches less than 10% of its peak value. This excludes regions of high noise from being included in our stacks. Then, we visually inspect each field and identify areas to exclude based on two criteria. First, we check for extremely bright sources and draw exclusion zones around them, since their residuals tend to be areas of high noise. In the case of Virgo A, this exclusion zone is sizable in some fields as a result of small calibration errors throwing flux some distance away from the source. Secondly, we search for extended sources that remain in the residuals. Many of these are extended AGN sources that have been cleaned to the level of the noise in individual snapshots but which reappear above the noise once we mosaic, and appear as extended islands of emission typically a few beams in width. These visually inspected regions are collated and nulled in the image prior to stacking.^d

4. Stacking and model subtraction

Having created deep, well-calibrated images of our 14 fields with point sources subtracted, we can now turn to stacking the LRG pairs. We stack LRG pairs in an effort to drive down the uncorrelated noise in our images, and meanwhile reveal any correlated mean emission that might bridge the LRG pairs. In this section we detail the construction both of these stacked images as well as the process used to construct the LRG models that we ultimately subtract in an effort to detect any excess cosmic web emission.

4.1. Stacking

We have implemented our stacking methodology similarly to V2021. We first identify a maximum scaling size, which is at least the maximum pixel distance of any single LRG pair across all fields. All halo pairs are subsequently strictly up-scaled to this size. We iterate through each LRG pair, once for each field. If the LRG pair is located within the field and does not overlap with an exclusion zone, we proceed to stack this pair. To do this, we identify the pixel coordinates of the pair within the field projection, and calculate both the pixel distance between these coordinates, as well as the angle between their connecting line and horizontal. We rotate and scale the pixel coordinates of the entire field such that pixel distance becomes the maximum pixel distance, and that their connecting line is rotated to horizontal. Finally, we linearly interpolate these values onto a rectangular grid whose centre is the point equidistant the LRG pair. This final map is now ready to be stacked alongside all other LRG pairs.

LRG pairs are weighted by a function of the estimated noise of the field. This estimated noise map is scaled and rotated identically to the field itself. When it comes time to stack, we weight each LRG pair by the inverse square of this map. Note that this noise map is spatially varying and, especially near the edges of the field

^dFor the sake of reproducibility, these exclusion regions are included in the associated data release as DS9 region files.

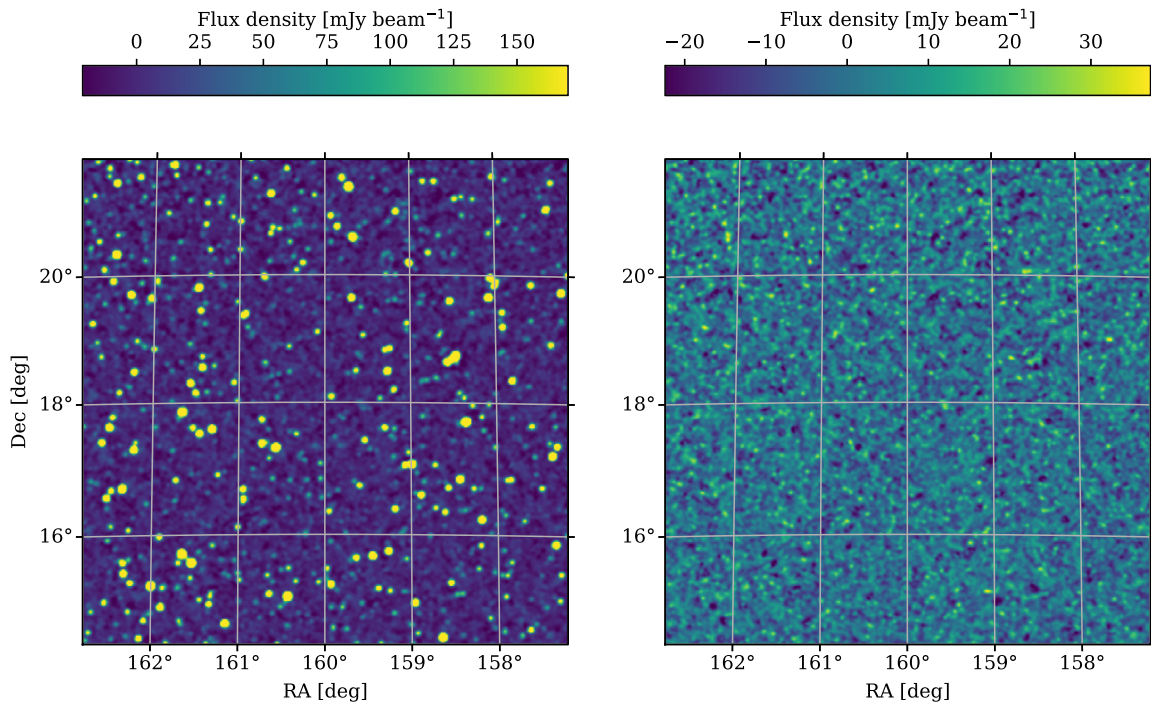


Figure 4. The central region of field 10, centred at RA 160° , Dec 18° , with $3'$ resolution. *Left:* The full mosaic, with all clean components restored into the image. The peak flux density in this image is 3.8 Jy beam^{-1} , whilst elsewhere in the field it is as high as $34.6 \text{ Jy beam}^{-1}$. *Right:* The residual image, with all clean components subtracted out. This inset has a mean noise of $7.5 \text{ mJy beam}^{-1}$, whilst the peak value is 41 mJy beam^{-1} .

where the underlying noise is rapidly changing, it is possible for the weighting used for a single LRG pair to vary across the length of the pair. We also track the sum of these weights, and in the final step divide the LRG pair stack by the weight stack to arrive at the weighted mean stack. See [Appendix B](#) for more detail on the stack weighting.

We construct a coordinate system on the final stacked images that places one LRG at $x = -1$, the other at $x = +1$, and the midpoint at the origin. The y direction is scaled identically, and we will herein refer to this as the normalised coordinate system.

At no point during stacking do we reproject the maps: they are rotated and scaled in pixel coordinates only. An alternative would have been to reproject each pair onto a common projection, but as we have noted earlier, our experience is that such reprojection creates scaling of the flux density values. Using pixel coordinates on an underlying SIN projection, however, has its own downsides whereby: geodesics on the sky are not, in general, straight lines in pixel coordinates; and the angular distance per pixel is not constant. In a SIN projection, these effects are most pronounced at the highest declinations where the field deviates most significantly from a Cartesian grid. They are, however, much smaller than the resolution element of the MWA. For example, in [Figure 5](#), we consider the worst case scenario of an LRG pair at the maximum separation of $180'$, and at the most northern declination of $+32^\circ$. The upper panel shows the transverse error that results from geodesics not being straight lines in pixel space which peaks at 0.003, whilst the lower panel shows the longitudinal error due to non-uniform pixel sizes which peaks at 0.01. The majority of

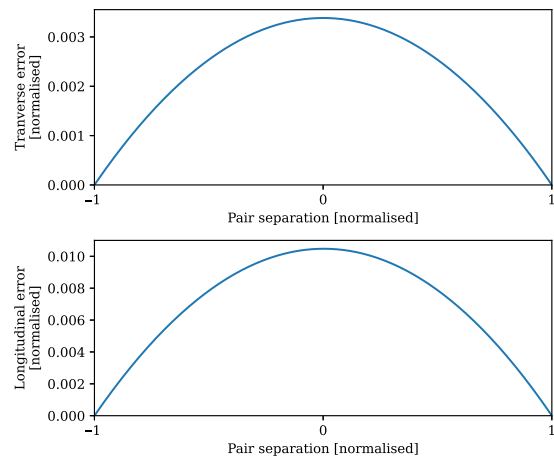


Figure 5. The maximum error associated with treating a SIN projection as a simple Cartesian grid, obtained at the maximum declination $+32^\circ$. *Top:* The maximum transverse error along a constant-declination $180'$ line as a result of geodesics being curved in pixel space. *Bottom:* The maximum longitudinal error along a constant-hour-angle $180'$ line, as a result of non-uniform pixel sizes.

our LRG pairs have a significantly smaller angular separation, and these errors are markedly smaller in these cases. These errors are small enough that we deem the simplicity and flux correctness of stacking in pixel space to be preferable.

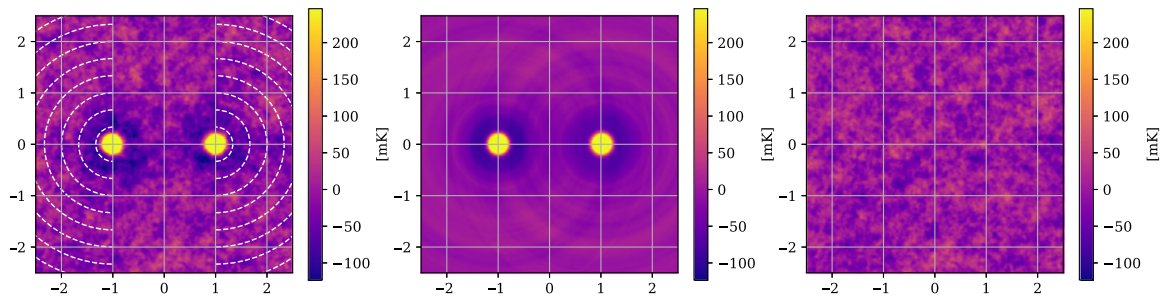


Figure 6. An example showing the LRG model construction and subtraction from the stacked image, with all coordinates in the normalised coordinate system such that the LRG peaks are at $x = [-1, 1]$ and the y direction scales identically. *Left:* The original mean stacked image, with the dashed arcs indicating the exterior sweep over which each radially averaged one-dimensional model is constructed. The LRG peaks rise to just over 4 K; we have set the colour scale limits on these images to make the noise, at 24.6 mK, visible. *Centre:* The model sum map, produced by interpolating the one-dimensional model for each LRG peak onto the two-dimensional map. *Right:* The residual image, after subtracting the model from the original mean stack.

4.2. Model subtraction

Model construction is implemented identically to V2021. It is assumed that emission about each LRG peak, either due to radio emission from the LRG itself or nearby cluster emission, should be radially symmetric. Any cosmic web emission spanning the LRG pair will appear as an excess against this model. Thus, we construct our model based on the 180° sweep *exterior* to the LRG pair and we radially average this to form a one-dimensional profile as a function of radial distance. The implementation of this involves binning pixels based on their radial distance, with the bin width set as 1 pixel, before each bin is then averaged. We can then create a function that linearly interpolates over these bins, allowing us to produce a full two-dimensional model independently for each LRG as a function of radial distance. Note by creating a model for each LRG peak independently, we are assuming the contribution from each peak is negligible for radial distances $r > 2$. Finally, we sum the LRG model contribution for each peak to produce the final model.

We show an example of this process in Figure 6. In the left panel we show the original mean stacked image. The LRG peaks rise to just over 4 K, however we have set the colour scale limits on these images to make the noise, at 24.6 mK, visible. The dashed arcs indicate the exterior sweep over which each radially averaged one-dimensional model is constructed. These models are then linearly interpolated onto the two-dimensional map and summed, so as to produce the model, shown in the central panel. Finally, we produce the residual stack by subtracting out the model from the mean stack, shown in the rightmost panel. Note the absence of all large-scale structures in the residual, including the LRG peaks themselves as well as the surrounding depressions caused by the MWA dirty beam.

We additionally provide the results of a synthetic test of our stacking and modelling processes in Appendix A.

4.3. Noise characteristics

To determine the significance of any excess signal in the residual stack, it is necessary to characterise the noise of our images. The original fourteen fields consist of real radio emission on top of a background of Gaussian noise. During stacking, the noise in these fields goes down proportionally to the inverse square root of the number of stacks. The presence of real emission peaks in

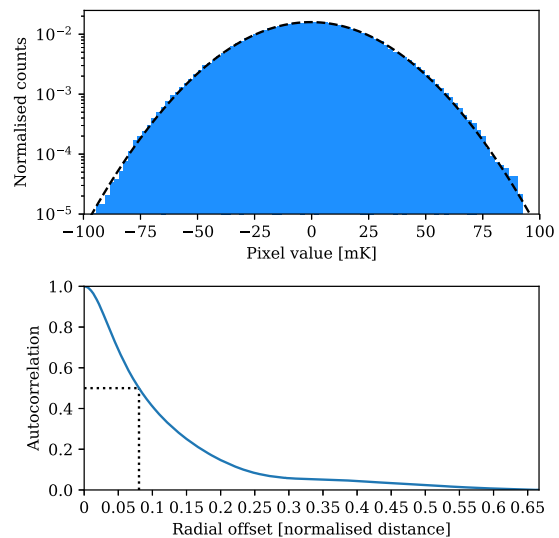


Figure 7. An example of the noise characteristics of the residual stack, in this case from the Max 15 Mpc stack. *Top:* The pixel distribution of the residual map, showing an approximately normal distribution. The dashed black line shows the Gaussian fit to the distribution, parameterised as $\sigma = 24.6$ mK. *Bottom:* The radially average autocorrelation of the residual stack, showing the autocorrelation as having a half width at maximum (dotted black line) of 0.074.

the residual field maps does not affect this, since these peaks are uncorrelated from stack to stack. In the upper panel of Figure 7, we show an example of the pixel distribution of one of our residual stacks, showing that it very nearly approximates a normal distribution, as indicated by the dashed black line, with $\sigma = 24.6$ mK. All our stacks exhibit this kind of normal distribution of pixel values, and so we will characterise them by reference to the standard deviation of their residual maps.

The noise, however, is spatially correlated. In the original fields prior to stacking, this spatial correlation is on the scale of dirty beam. In the stacked images, however, this is not the case, since during stacking we rescale each LRG pair. To characterise the effective resolution of the stacked image we perform a radially averaged two-dimensional autocorrelation of the residual stack,

and we present an example of this in the lower panel of Figure 7. We observe in this plot both an extended peak in this function, showing the spatial correlation of pixels persists in the stacked images, and also a slight depression showing the cumulative sidelobes of the stacked, dirty beams. We characterise the effective resolution by measuring the full width at half maximum (FWHM). In this case, the half width at half maximum of the autocorrelation is 0.074, corresponding to a FWHM value of the residual map of 0.105.

These two metrics—the standard deviation and the effective resolution—allow us to understand the significance of any potential signal in our stacks. Specifically, peaks of excess emission that deviate significantly from the measured map noise, or extended emission on scales greater than the effective resolution, are tell-tale markers that we are encountering signal that deviates from otherwise stochastic noise.

5. Results and discussion

5.1. Stacking results

In Figure 8, we present the stacked results for the Max 15 Mpc catalogue. This catalogue consists of 601 435 LRG pairs, allowing our stack to reach a noise of 25 mK, more than twice as deep as the 118.5 MHz stack in V2021. As can be seen in the upper left panel of Figure 8a, the peaks at $x = \pm 1$ are the dominant features, and have a mean value of 4 292 mK. The upper right panel in Figure 8a shows the same stacked image, only with the colour scale adjusted down so as to emphasise the noise. We now note the shallow depressions around each of the peaks, which are attributable to the dirty beam's negative sidelobes. The LRG model is shown in the bottom left panel, and the bottom right panel in Figure 8a shows the residual stack, after model subtraction. The model construction methodology is surprisingly effective, leaving no trace either of the sharp peaks at $x = \pm 1$, as well as removing the sidelobe depressions. There is no readily apparent excess emission in the residual image. In the top panel of Figure 8b, we compare the one-dimensional slice through $y = 0$ of both the mean stacked image (blue) and model (red). The stacked image and model are so similar that we scarcely observe any of the stacked plot. Note that the widths of the peaks are narrower than observed in V2021: the peaks here have a FWHM value of 0.11, and whilst this value is not given in V2021, their peaks appear visually much wider. These peaks will be in part a function of the instrumental dirty beam, however this is not sufficient to explain this discrepancy; we discuss this more in Subsection 5.3. In the second panel of Figure 8b, we show the one-dimensional $y = 0$ slice through the residual image, where we have renormalised the scale to the estimated map noise. There are no peaks in this residual exceeding 3σ . In the third panel, we display the mean value in the range $y = \pm 0.2$ as a function of x , and renormalise based on the estimated map noise. The aim of this transverse mean is to bring out faint, wide signals that might be present along the intercluster stacks. For this LRG catalogue, we observe no peaks exceeding 3σ . Finally, in the lower panel we display the longitudinal mean in the range $-0.95 < x < 0.95$, as a function of y . For a faint signal that spans the length of the intercluster stack, we would expect this plot to show a peak at $y = 0$, however we observe no statistically significant signal. We conclude there is no statistically significant excess emission along the bridge for the Max 15 Mpc stack.

The stacked results for the Max 10 Mpc catalogue are shown in Figure 9. With just a quarter of the LRG pairs as the larger Max 15 Mpc catalogue, the estimated noise of this stack is higher at 51 mK, just a slight improvement on the stated noise in the 118.5 MHz stack in V2021. The peaks at $x = \pm 1$ are higher than the previous stacks, at 4 699 mK, which is a result of the catalogue sampling from a more local redshift space, whilst their widths have a similar FWHM of 0.12. Once again, however, the residual image and one-dimensional slices show no indication of statistically significant excess emission along the bridge.

Likewise, the stacked results for the Max 60' and LRG-V2021 catalogues, in Figures 10 and 11 respectively, also show no evidence of excess emission. The Max 60' stack has a noise of 30 mK and a large effective resolution of 0.26 that is a result of reduced lower angular threshold and corresponding variation in scaling during stacking. Similarly, the peak width has increased to 0.23. This LRG catalogue also samples significantly deeper in redshift space than the others, with the result that the LRG peaks are diminished in comparison, with a mean value of 3 769 mK. One small $\sim 2.85\sigma$ peak is visible in the one-dimensional profile at $x = -0.73$, however its width matches the effective resolution, and similar peaks throughout the residual image suggest it is consistent with the noise. Meanwhile, the LRG-V2021 stack has a noise of 41 mK, approximately 30% lower than the equivalent 118.5 MHz stack in V2021. It has a peak in the longitudinal profile at $y = 0.14$ that reaches a significance of 3.04σ , but otherwise shows no evidence of intercluster signal and certainly not the kind of large-scale, clearly evident excess emission as shown in V2021.

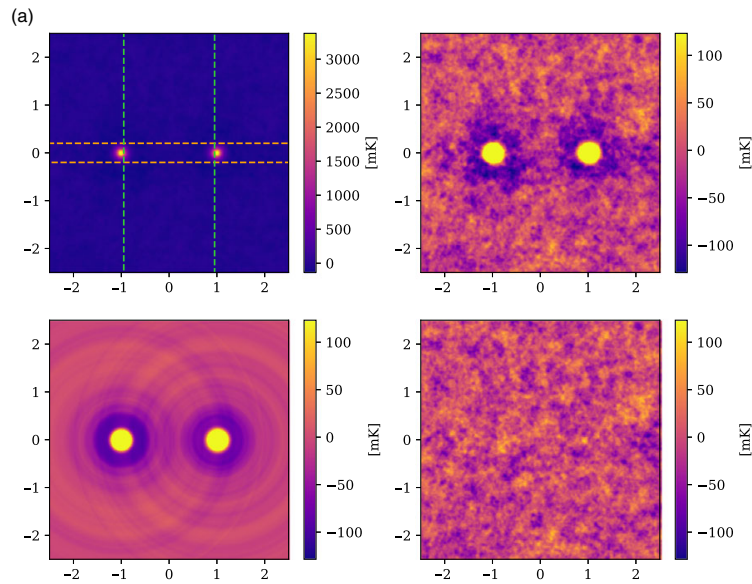
The analysis of each of our LRG catalogue stacks leaves us unable to corroborate the detection of V2021.

5.2. Sensitivity to extended emission

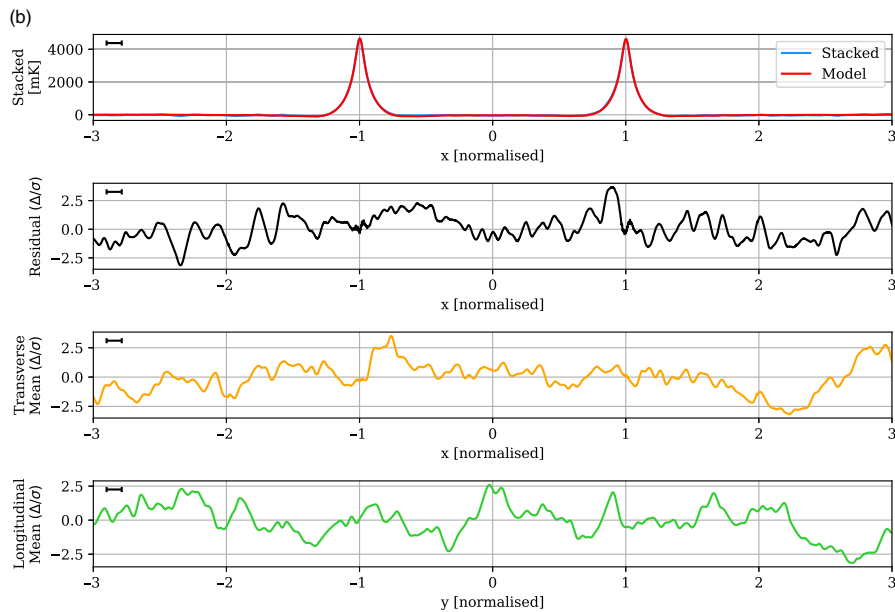
The chief distinction between the MWA Phase I and Phase II instruments is the location of the antennas, and in turn, each instrument's respective dirty beam. As noted previously, the point-source sensitivity is unchanged. However, these modified baselines may make the instrument less sensitive to extended emission, potentially even resolving out large-scale emission such as the cosmic web, and this may be a factor in our non-detection.

In Figure 12 we show the dirty beams of the Phase I and Phase II instrument, as well as the effective dirty beam of the Phase II instrument after our convolution to 3' (at zenith) resolution. These dirty beams have been generated from archival 118.5 MHz MWA observations at the centre of field 11 ($\alpha = 180^\circ$, $\delta = 18^\circ$) to best model the effect of the low-elevation pointings on the dirty beam. The Phase I dirty beam is produced with a Briggs -1 baseline weighting scheme such that it matches the original GLEAM imaging parameters, and has a resolution of approximately $3.74' \times 2.56'$. Note the sizeable negative sidelobes around the beam, owing to a dense core of short baselines. The Phase II dirty beam is produced with the same baseline weighting as used in the present work, Briggs $+1$, as well as its lower baseline length threshold of 15λ , and has a resolution of approximately $3.2' \times 1.9'$. After convolution, this grows to a resolution of $4.2' \times 3.1'$ at the centre of the field.

Hodgson et al. (2020) developed an empirical method to measure an instrument's sensitivity to large-scale emission, which we draw on here. Often angular sensitivity is estimated solely based on the angular size of the fringe patterns of the shortest baselines in an array, however, this does not take into account the imaging

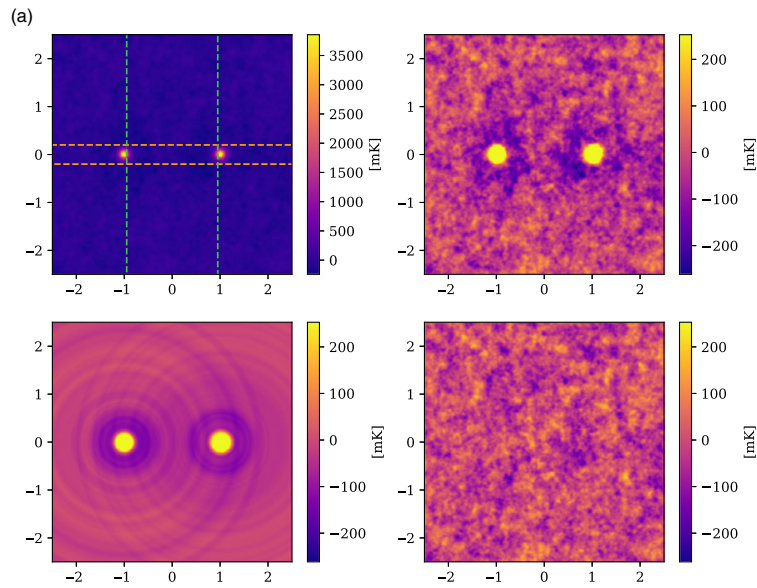


Top left: The original mean stack image, with overlays indicating the region over which the transverse mean (dashed orange horizontal lines) and longitudinal mean (dashed green vertical lines) are calculated. *Top right:* The mean stacked image with the colour scale reduced to $\pm 5\sigma$ to emphasise the noise. *Bottom left:* The model image, on the same colour scale. *Bottom right:* The residual stack after model subtraction, with the colour scale set to $\pm 5\sigma$.

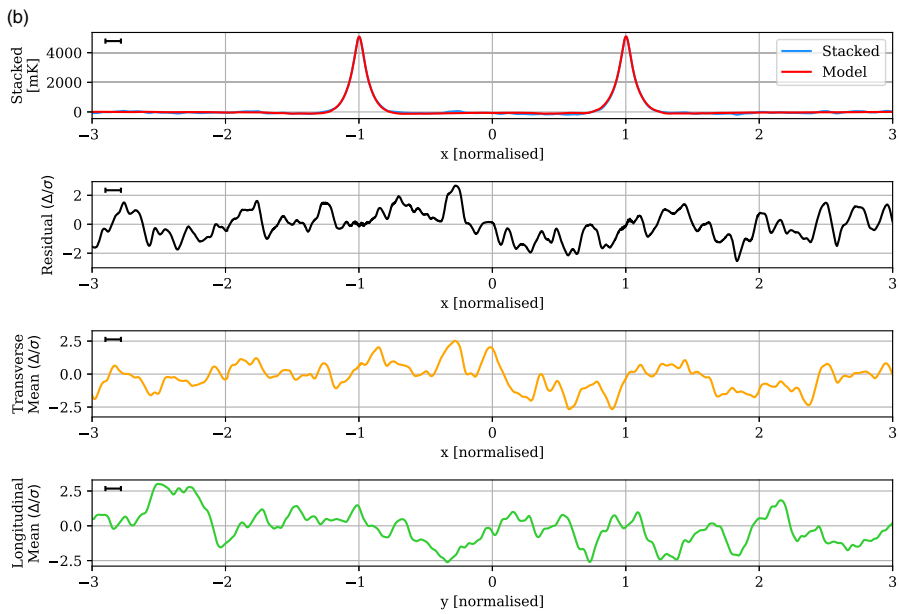


One: The one-dimensional profile along $y = 0$ for both the stacked image (blue) and the model (red). *Two:* The one-dimensional profile along $y = 0$ of the residual stack, renormalised to the estimated map noise. *Three:* The transverse mean along the region $-0.2 < y < 0.2$ of the residual stack, renormalised to the estimated map noise. *Four:* The longitudinal mean along the region $-0.95 < x < 0.95$ of the residual stack, renormalised to the estimated map noise. The black rule in the top left shows the FWHM of the effective resolution.

Figure 8. The Max 15 Mpc stack, with mean LRG peaks of 4 292 mK, residual noise of 25 mK, and effective resolution of 0.11.

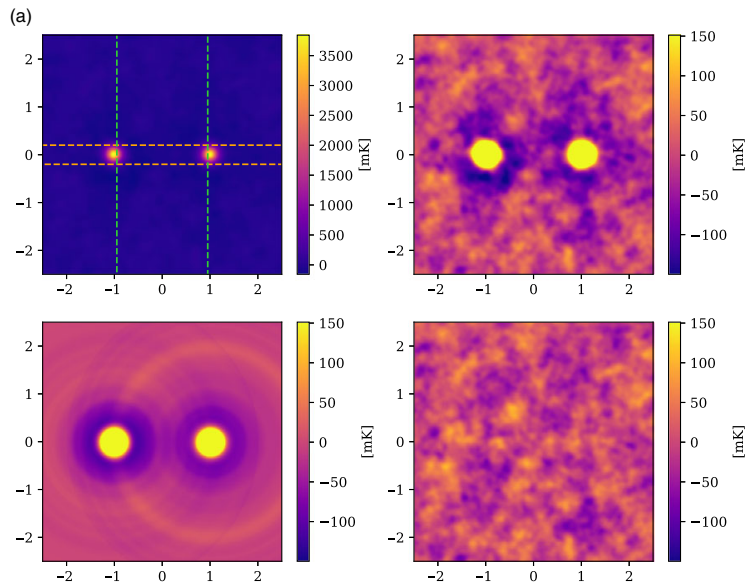


Top left: The original mean stack image, with overlays indicating the region over which the transverse mean (dashed orange horizontal lines) and longitudinal mean (dashed green vertical lines) are calculated. *Top right:* The mean stacked image with the colour scale reduced to $\pm 5\sigma$ to emphasise the noise. *Bottom left:* The model image, on the same colour scale. *Bottom right:* The residual stack after model subtraction, with the colour scale set to $\pm 5\sigma$.

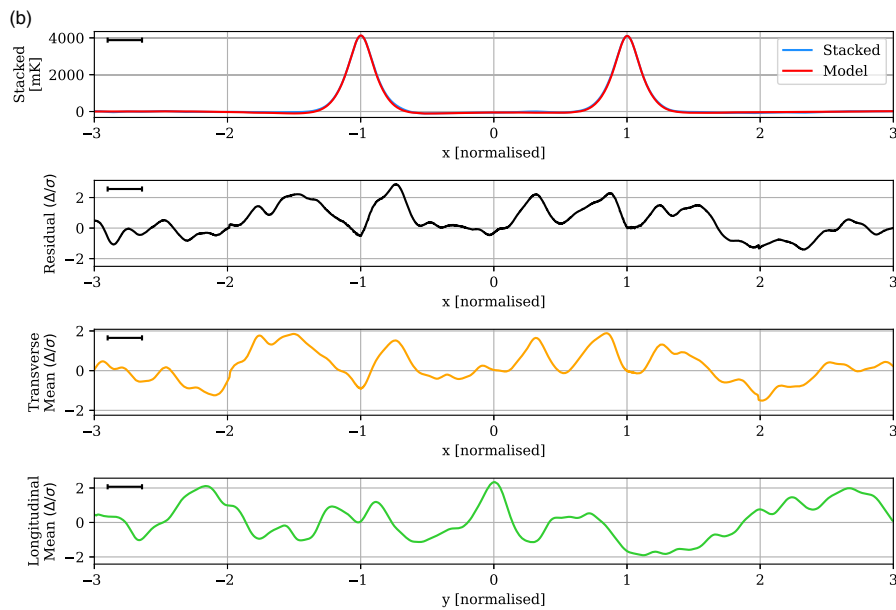


One: The one-dimensional profile along $y = 0$ for both the stacked image (blue) and the model (red). *Two:* The one-dimensional profile along $y = 0$ of the residual stack, renormalised to the estimated map noise. *Three:* The transverse mean along the region $-0.2 < y < 0.2$ of the residual stack, renormalised to the estimated map noise. *Four:* The longitudinal mean along the region $-0.95 < x < 0.95$ of the residual stack, renormalised to the estimated map noise. The black rule in the top left shows the FWHM of the effective resolution.

Figure 9. The Max 10 Mpc stack, with mean LRG peaks of 4 699 mK, residual noise of 51 mK, and effective resolution of 0.12.

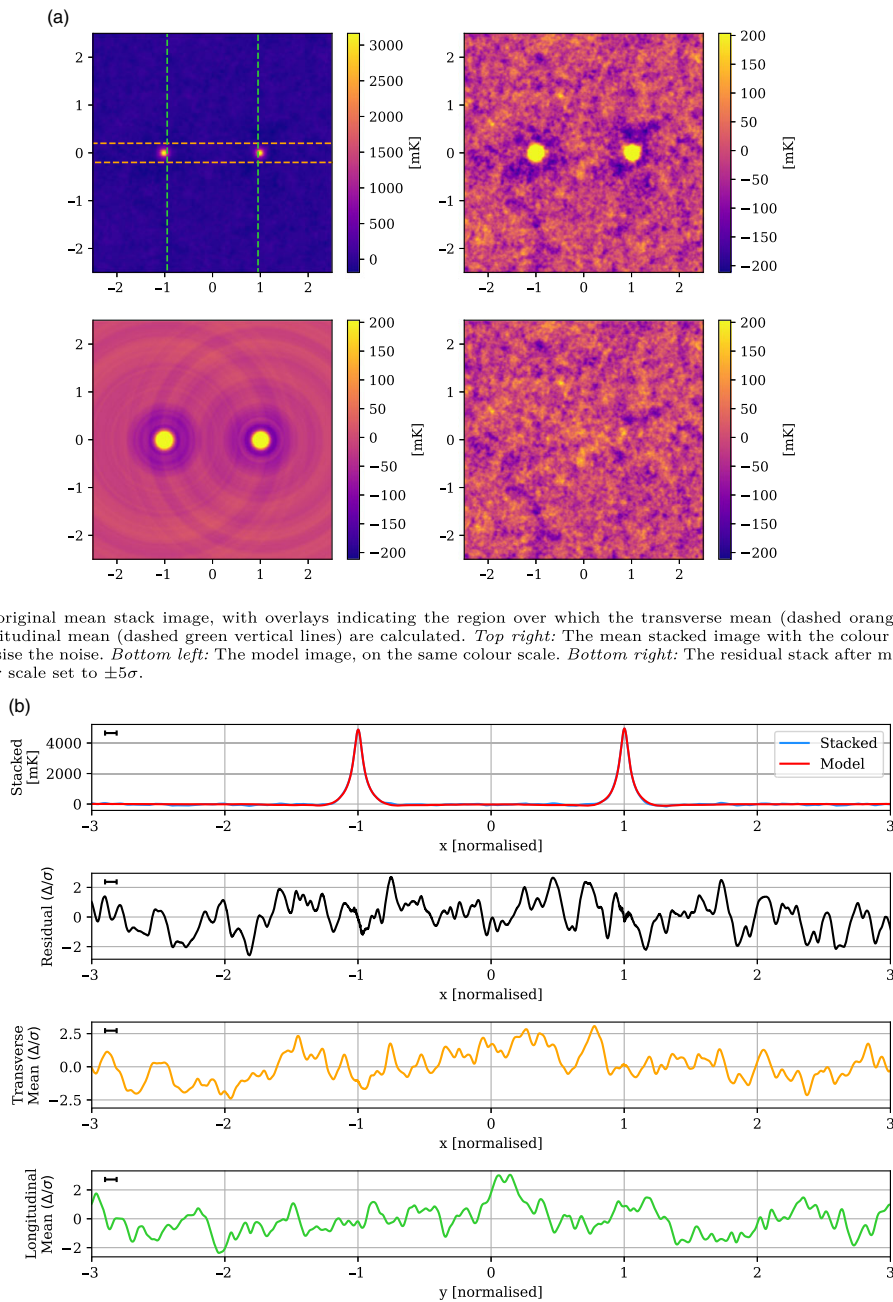


Top left: The original mean stack image, with overlays indicating the region over which the transverse mean (dashed orange horizontal lines) and longitudinal mean (dashed green vertical lines) are calculated. *Top right:* The mean stacked image with the colour scale reduced to $\pm 5\sigma$ to emphasise the noise. *Bottom left:* The model image, on the same colour scale. *Bottom right:* The residual stack after model subtraction, with the colour scale set to $\pm 5\sigma$.



One: The one-dimensional profile along $y = 0$ for both the stacked image (blue) and the model (red). *Two:* The one-dimensional profile along $y = 0$ of the residual stack, renormalised to the estimated map noise. *Three:* The transverse mean along the region $-0.2 < y < 0.2$ of the residual stack, renormalised to the estimated map noise. *Four:* The longitudinal mean along the region $-0.95 < x < 0.95$ of the residual stack, renormalised to the estimated map noise. The black rule in the top left shows the FWHM of the effective resolution.

Figure 10. The Max 60' stack, with mean LRG peaks of 3 769 mK, residual noise of 30 mK, and effective resolution of 0.26.



Top left: The original mean stack image, with overlays indicating the region over which the transverse mean (dashed orange horizontal lines) and longitudinal mean (dashed green vertical lines) are calculated. Top right: The mean stacked image with the colour scale reduced to $\pm 5\sigma$ to emphasise the noise. Bottom left: The model image, on the same colour scale. Bottom right: The residual stack after model subtraction, with the colour set to $\pm 5\sigma$.

One: The one-dimensional profile along $y = 0$ for both the stacked image (blue) and the model (red). Two: The one-dimensional profile along $y = 0$ of the residual stack, renormalised to the estimated map noise. Three: The transverse mean along the region $-0.2 < y < 0.2$ of the residual stack, renormalised to the estimated map noise. Four: The longitudinal mean along the region $-0.95 < x < 0.95$ of the residual stack, renormalised to the estimated map noise. The black rule in the top left shows the FWHM of the effective resolution.

Figure 11. The LRG-V2021 stack, with mean LRG peaks of 4 540 mK, residual noise of 42 mK, and effective resolution of 0.09.

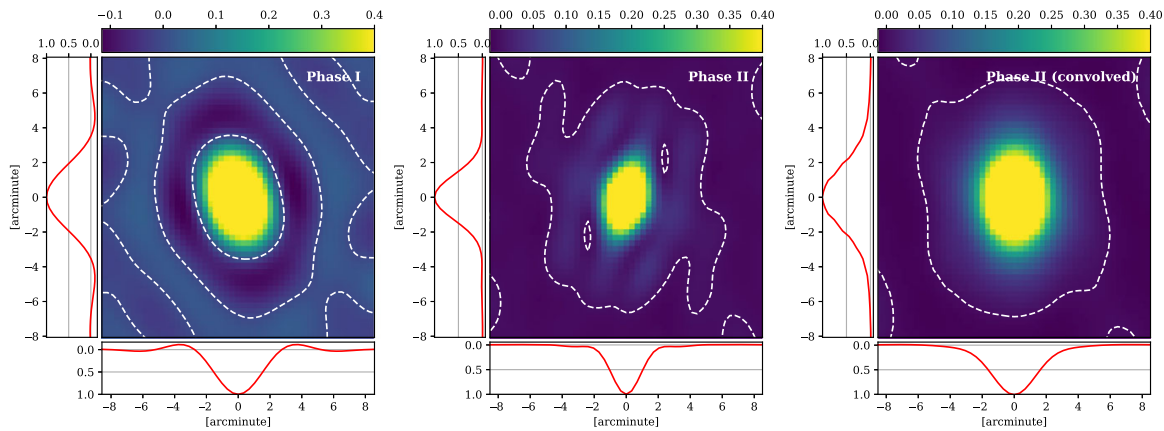


Figure 12. A comparison of dirty beams used in V2021 and the present study, measured at 118.5 MHz and pointing $\alpha = 180^\circ \delta = 18^\circ$. White dashed contours trace a response of zero, so as to better show the negative sidelobe regions. *Left:* The Phase I dirty beam with baseline weighting Briggs -1 , as used in GLEAM, having a resolution of $3.74' \times 2.56'$. *Centre:* The Phase II dirty beam with baseline weighting Briggs $+1$, as used in the current study, and having a resolution of $3.2' \times 1.9'$. *Right:* The Phase II dirty beam, after convolution, having a resolution of $4.2' \times 3.1'$.

parameters, baseline weightings, and most importantly, the cumulative effect of the instrument's baselines in determining angular sensitivity. Instead, the method we use here proceeds by simulating a range of extended emission sources—in our present case circular Gaussian sources—directly into the visibilities of an observation, and then producing a dirty image of the source. Given a surface flux density of 1 Jy deg^{-2} at the Gaussian peak, we can understand the instrument's response by measuring the flux density at the centre of the Gaussian in the dirty image. If we iterate through many such circular Gaussian sources of increasing size, we will identify a threshold angular scale at which point the central response will begin to reduce, above which scales the dirty image of the Gaussian will start to 'hollow out' in the centre and become increasingly dark. In this way we can identify the relative sensitivity of the instrument over a range of angular scales as well as the angular scale at which emission begins to resolve out.

In Figure 13 we show the results of this exercise, where we have measured the central response to circular Gaussians having a FWHM up to $180'$ in extent. It is immediately apparent that the larger beam size of the Phase I instrument makes it more sensitive than Phase II to large-scale emission features, as we'd expect. Moreover, the Phase I instrument does not begin to resolve out structure on these spatial scales; in fact, it continues to gain sensitivity over this range. The sensitivity of the Phase II instrument, on the other hand, begins to slowly decline on angular scales larger than $30'$, and then more rapidly decline on scales larger than approximately $50'$. The effect of convolving the Phase II dirty beam is dramatic, amplifying its sensitivity to extended sources more than a factor of two. Crucially, it also makes the instrument more sensitive than Phase I. It does not forestall the angular scales on which the instrument begins to resolve out structure, however it remains more sensitive than Phase I to extended emission out to approximately $130'$.

When considering whether these differences in sensitivity to extended emission can account for our non-detection of the synchrotron cosmic web we need to understand the typical angular scales we would expect. In the first instance, the majority of LRG pairs in each catalogue are separated by less than $60'$, with

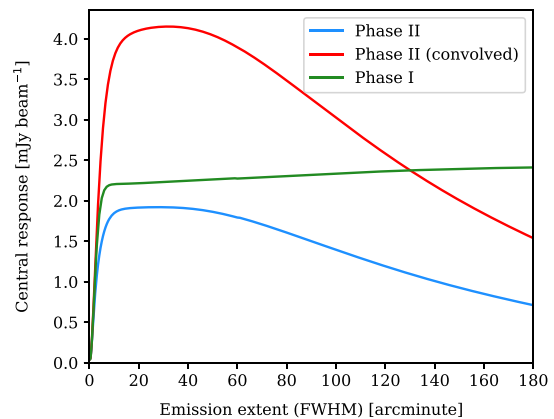


Figure 13. The sensitivity of Phase I, II, and Phase II (convolved) to extended emission. The plot shows the response at the centre of simulated circular Gaussians of varying sizes, with the simulated sources having a constant peak surface brightness of 1 Jy deg^{-2} . For large, extended emission sources, there exists a threshold angular scale above which the central response begins to drop, as these sources become increasingly 'resolved out'. On the other hand, for very small angular sizes, the simulated source becomes smaller than the dirty beam (i.e. is unresolved) whilst maintaining the same peak surface brightness; the total flux of the source thus rapidly drops to zero as does the instrumental response.

the exception of the LRG-V2021 catalogue which has a median separation of $79'$. We should expect our observations to be at least as sensitive as V2021 for those LRG pairs with separations less than $60'$, and specifically with regards to the Max $60'$ stack, there is no risk of resolving out structure across the entirety of its LRG pair catalogue. Secondly, we do not expect the emission spanning the intercluster region to be as wide as it is long: whilst our selection criteria allows for these bridges to span up to $180'$, we should expect the width of the bridge to be significantly more narrow. Any MWA baseline fringes aligned approximately along the narrower width will not be at risk of resolving out the

emission, and this will reduce the overall effect. Finally, as simulations by Vazza et al. (2019) and further showcased in Hodgson et al. (2021b) have shown, the morphology of the cosmic web is expected to consist of radio-relic-like accretion shocks. These typically appear as long extended arcs of emission, usually with a well-defined edge along the shock itself, with many such shocks spanning the length of the intercluster region. Crucially, these kinds of emission mechanisms do not form a broad, continuous bridge of emission that we might risk resolving out, rather they are punctuated and individually consist of sharply defined edges that interferometers are well-suited to detect.

For these reasons, we do not believe we are adversely affected by the higher resolution MWA Phase II instrument.

5.3. The expected peak widths

As noted, a key difference between our results and those of V2021 is that the width of the peaks at $x = \{-1, 1\}$ of our stacks are much narrower. In this section, we want to understand the expected minimum size of these peaks. This condition of minimum peak width occurs when the angular scale of the LRG emission (or other spatially correlated emission) is much smaller than the instrumental dirty beam, that is, when the LRG emission is unresolved and approximately ‘point-like’. In this case, the instrumental response is simply the dirty beam itself. We can then model the expected minimum-width LRG peak profile by stacking the dirty beam in the following way: for each LRG pair, we calculate the angular distance between the pair and find a scaling factor to upscale onto the maximum angular separation, being 3° ; we use this scaling factor to stretch the one-dimensional profile of the dirty beam; and then sum this alongside other similarly scaled profiles. We build in two additional assumptions in this simple model: first, for each pair we create a one-dimensional profile of the dirty beam at a uniformly random angle through the two-dimensional peak response, which assumes that the orientation of LRG pairs on the sky are approximately uniform; second, that each LRG has an equal contribution to the sum. A key limitation of this exercise is the use of a single dirty beam, as shown previously in Figure 12; these dirty beams have been generated for a fixed position on the sky, and at these low elevations the dirty beam is especially sensitive to the foreshortening effects of declination changes. Nonetheless, this exercise will give us a good approximation of the minimum peak sizes.

We show the results of this exercise in Figure 14 for both the Phase I (green) and Phase II (convolved; blue) dirty beams calculated across the Max 15 Mpc catalogue, as well as the model profile of the left peak of the Max 15 Mpc stack (red), shown previously in Figure 8. The FWHM of the Phase II (convolved) peak is 0.12, which compares to the actual model peak width of 0.11. The similarity in both the peak shape and width between this exercise and the actual model suggests the peaks in our stacks are dominated principally by unresolved sources.

In comparison, the peak widths of the stacks in V2021 appear significantly wider. In Figure 14, we also show the results of the same exercise for the Phase I dirty beam, showing a remarkably similar peak width to our own. That the peaks of V2021 are markedly wider would suggest that a significant proportion of sources in their stacks appear as resolved at Phase I resolution. Moreover, the lack of a ‘stepped peak’, caused by the addition of a dominant unresolved population and a fainter resolved population, would suggest that the resolved population actually dominates in the V2021 stacks. This is a fundamental discrepancy

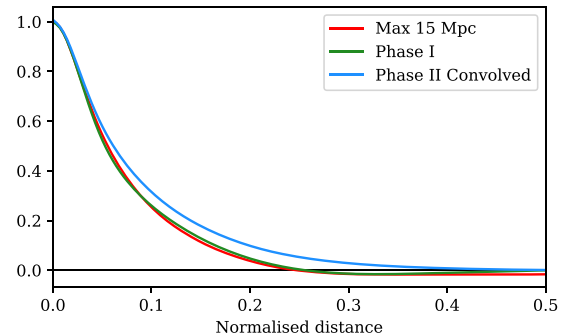


Figure 14. One-dimensional profiles of stacked dirty beams for Phase I (green) and Phase II (convolved; blue), in comparison to the Max 15 Mpc stacked model profile (red). The stacked dirty beams approximate a minimum peak profile for purely unresolved LRG sources, and the similarity to the Max 15 Mpc stacked model profile suggests this profile is dominated principally by unresolved sources.

with our own results, for which we do not currently have an explanation.

5.4. The effect of CLEANing

One point of difference between V2021 and the present study is the technique used to subtract bright point sources. V2021 used a wavelet decomposition technique, whereby image features on small angular scales were identified by imaging a limited range of wavelet scales. These small-scale image maps were searched for all pixels having values greater than 5σ of the map noise, which were then subtracted from the original maps. This technique subtracted out the brightest pixels of point sources but left a residual ring around the sources at values lower than 5σ . Only compact, point-like sources were subtracted from the images, thus leaving extended sources; it’s unclear what kind of additional filtering was applied to extended sources such as AGN lobes as this is not documented.

This differs with the present technique of using residuals after cleaning. Our cleaning process uses `wsclean` and its `automask` and `autothreshold` functionality. This worked by cleaning peaks of emission that are brighter than 3σ , and when this was exhausted, cleaning was allowed to continue within a mask defined by the existing clean components down to a level of 1σ . Recall that multiscale cleaning was disabled, and so this process removed *peak* emission that was greater than 3σ ; large, diffuse extended emission that did not peak above this threshold remained in the image. In practice, typical snapshot noise was approximately 20 mJy beam^{-1} , meaning that peak emission fainter than approximately 60 mJy beam^{-1} was left in the images. Compare this to the 5σ threshold used in V2021, which corresponds to approximately $175 \text{ mJy beam}^{-1}$. Thus there is significantly more emission remaining in the images of V2021.

For these point-source subtraction differences to contribute to the detection in V2021, this would imply that the excess emission arises from a population of especially bright sources that are visible in our own mosaics at levels of greater than 60 mJy beam^{-1} and which have been partially cleaned. Hodgson et al. (2020) showed that the luminosity of accretion shocks around the periphery of dark matter halos throughout their simulated cosmic web approximated a power law as a function of dark matter halo mass; in their $15 \times 15^\circ$ simulated field, there existed a few bright points of cosmic web emission, with the brightest at 64 mJy beam^{-1} (using

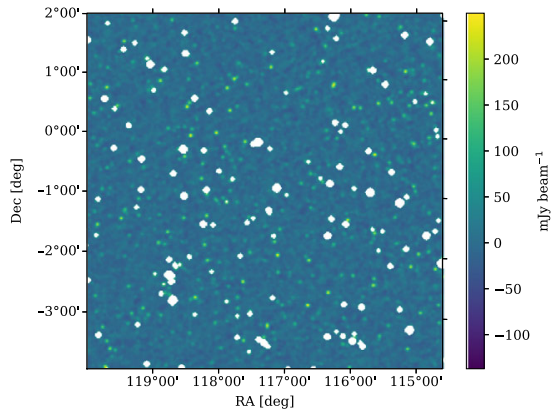


Figure 15. An example of masking the restored fields using a threshold of $250 \text{ mJy beam}^{-1}$, with masked sources depicted here as white. Note the presence of a low to medium brightness population of radio sources still clearly visible.

a Phase I MWA beam). Note, however, that these sources were located around the periphery of bright clusters, not in the true intercluster region, that they were morphologically akin to radio relics, and were likely stationary accretion shocks around massive clusters. Only a handful of such bright, outlier emission sources were predicted as part of the simulation.

To investigate this further, as an exercise we have re-run the stacking process using the restored field images, rather than the residuals. To mitigate the effects of bright point-source emission, we have masked bright sources, but note that we have extended the threshold for this masking out to $250 \text{ mJy beam}^{-1}$. The motivation for this much higher threshold is to capture emission that is present in the original V2021 images, but which we have removed by our deeper cleaning. Figure 15 shows an example of one of these masked fields, where we can clearly see a large population of sub- 250 mJy sources still present.

We show the stacked results of this exercise in Figure 16. Firstly, note that the mean residual value is much greater than zero. This results from the significant number emission sources present in the image when masking to only a threshold of $250 \text{ mJy beam}^{-1}$, and this non-zero background represents a kind of mean, stacked background temperature. Despite this, the peaks at $x = \{-1, 1\}$ have almost doubled against this background temperature, when compared with the Max 15 Mpc stack in Figure 8, showing that there is a considerable number of LRG sources (or sources otherwise correlated with the LRG population) with a peak brightness greater than approximately 60 mJy beam^{-1} . As a side-effect of the number of sources remaining in the image, however, the noise has also increased compared to the Max 15 Mpc stack, by a factor of just over 2.5 times at 62 mK . Note also the absence of the negative sidelobes about the LRG peaks. The extra emission of the LRG peaks compared to the original Max 15 Mpc stacks is the result of restored emission that has been convolved with an elliptical Gaussian fitted to the dirty beam, and this additional component will not have sidelobes; these brighter Gaussian sources in the stacks, combined with the overall higher noise, have washed out the subtle sidelobes of the fainter, uncleaned sources.

Turning now to the detection of excess emission, we can observe in Figure 16 that there is a peak of emission in the residual image centred at $(x, y) = (-0.57, 0.035)$, slightly off the y -axis, and

peaking at 4.58σ significance. This peak corresponds to the peak in the one-dimensional profile also at $x = -0.57$. The width of the peak is slightly extended beyond the FWHM typical of the rest of the residual image. A second, smaller peak is also evident in the residuals at $(x, y) = (-0.07, 0.13)$ with 4.2σ significance, and is also visible in the transverse mean. Combined, these two peaks contribute to a peak in the longitudinal mean, at $y = 0.04$ with 3.2σ significance. Note also the presence of a 4.1σ peak outside and to the left of the stacked intercluster region, at $(x, y) = (-1.85, 0.17)$.

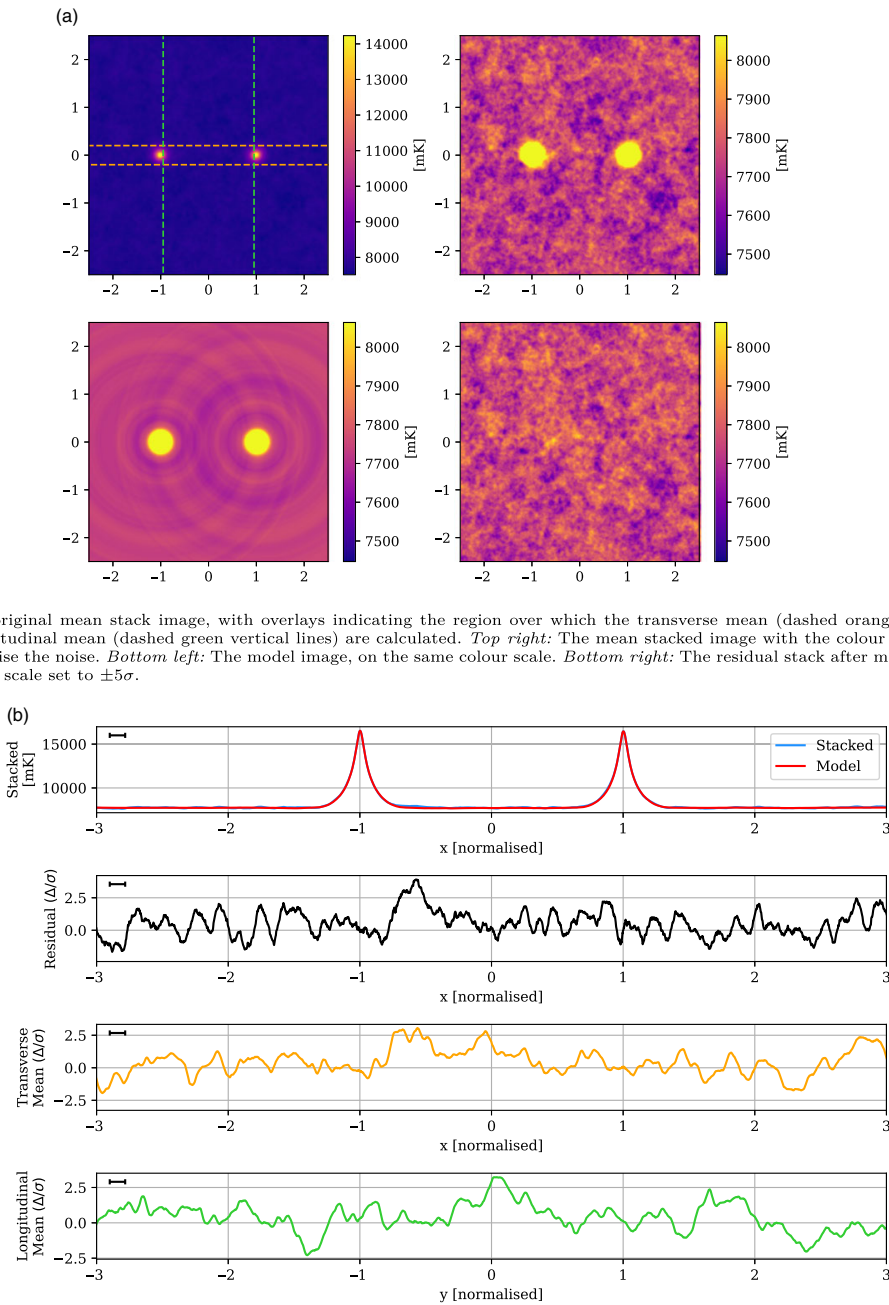
Are these emission peaks in the stacked residuals of Figure 16 evidence of the cosmic web? We can immediately note that these emission peaks have not reproduced the broad, excess emission of the kind in V2021 that filled the intercluster bridge; instead these are much more localised peaks. We can also note the asymmetry of the left peak at $x = -0.57$, which is not reproduced on the right: this would suggest that this is not a generalised feature of the intercluster region. Additionally, the 4.1σ peak to the left of the intercluster region cannot, by its location, be attributable to intercluster cosmic web emission. To investigate further, we have jackknife sampled the Max 15 Mpc catalogue, excluding a randomly selected 10% of the catalogue, and stacked each of the ten sub-catalogues. With 90% of the original catalogue in each stack, the noise is very similar, varying between $63\text{--}65 \text{ mK}$. We find that the peak at $x = -0.6 \pm 0.1$ is present in each stack, with at least a significance of 3.1σ , with the exception of one of the sub-catalogues, where it is entirely consistent with the noise, and peaking at most at 2.4σ . Similarly, the peaks at $x = -0.07$ and $x = -1.85$ are also each absent in one of the sub-catalogues. This exercise suggests that these peaks are not generalised features shared across the sample, but the effect of bright outlier emission left in the original fields.

This exercise suggests the absence of the broad excess emission feature found in V2021 in our own stacks is not a side-effect of cleaning.

5.5. Stacking the original GLEAM survey

We have every expectation that we should be able to detect the excess emission in our Phase II observations, given the low noise characteristics of our fields, our sensitivity to large-scale angular structures, and the additional LRG pairs that we have used in our stacks. It is still possible, however, that there is some aspect of these new observations or our image processing pipelines that has obscured or removed the synchrotron cosmic web. And so these concerns have led us to return to the original GLEAM survey data, and attempt to reproduce the results of V2021 by stacking an identical data set at 118.5 MHz .

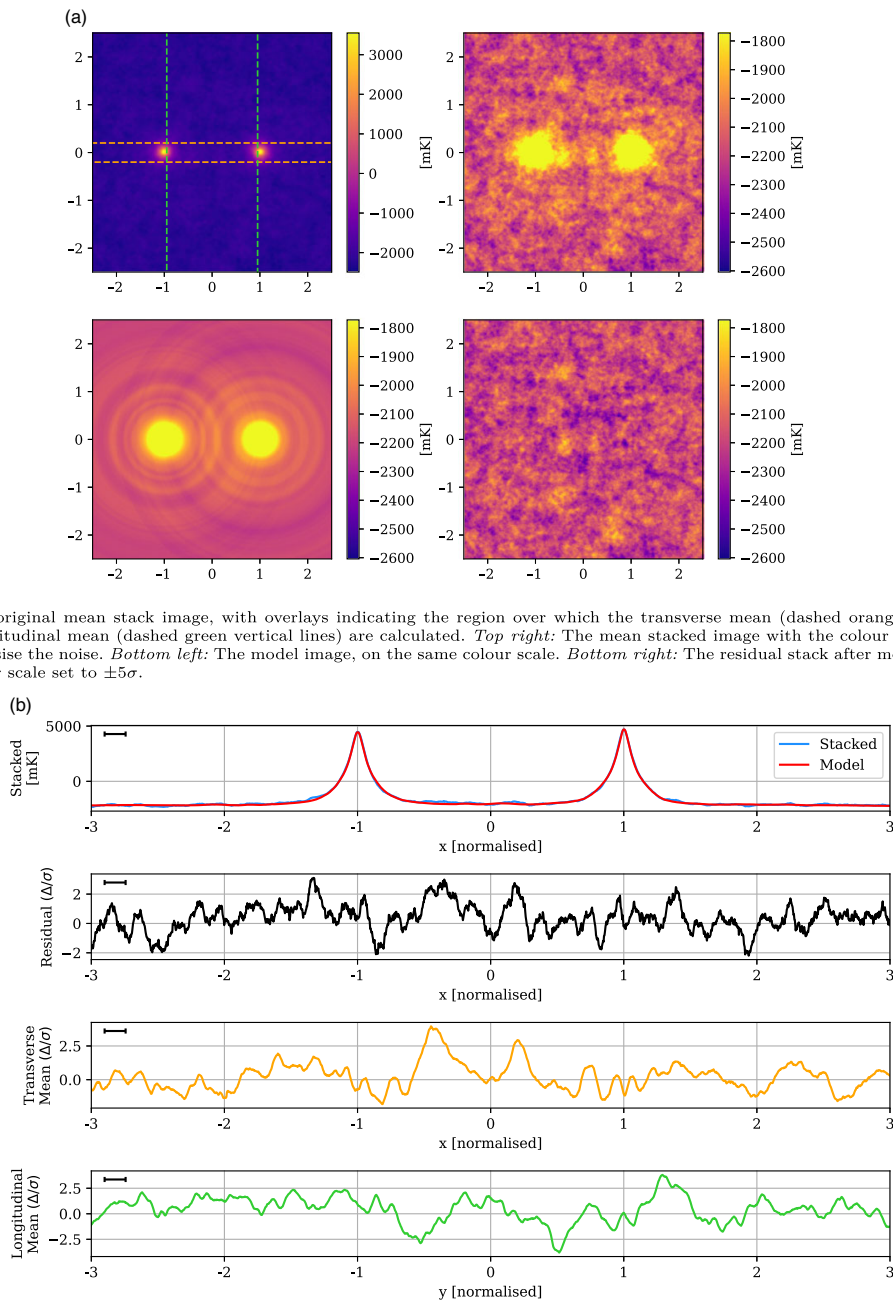
To stack the GLEAM survey data, we first start with the full zenith equal area (ZEA) projection images at 118.5 MHz , which cover the right ascension regions spanned by our LRG pairs. Unlike V2021, we leave these images in their original projection. We mask bright points by selecting all emission regions with values greater than 5σ of the local noise. To do this, we measure the spatially variable background—which is primarily the result of Galactic emission—as well as the noise using the Background and Noise Estimation tool (BANE; Hancock *et al.* 2018). The mask is then created by subtracting out the background emission from the full projection, dividing by the noise image, and then masking all regions that exceed 5σ of the local noise value. This process is substantially simpler than the wavelet subtraction method used in



Top left: The original mean stack image, with overlays indicating the region over which the transverse mean (dashed orange horizontal lines) and longitudinal mean (dashed green vertical lines) are calculated. *Top right:* The mean stacked image with the colour scale reduced to $\pm 5\sigma$ to emphasise the noise. *Bottom left:* The model image, on the same colour scale. *Bottom right:* The residual stack after model subtraction, with the colour scale set to $\pm 5\sigma$.

One: The one-dimensional profile along $y = 0$ for both the stacked image (blue) and the model (red). *Two:* The one-dimensional profile along $y = 0$ of the residual stack, renormalised to the estimated map noise. *Three:* The transverse mean along the region $-0.2 < y < 0.2$ of the residual stack, renormalised to the estimated map noise. *Four:* The longitudinal mean along the region $-0.95 < x < 0.95$ of the residual stack, renormalised to the estimated map noise. The black rule in the top left shows the FWHM of the effective resolution.

Figure 16. The Max 15 Mpc stack after masking fields at a threshold of $250 \text{ mJy beam}^{-1}$, with mean LRG peaks of 8 776 mK above the background, residual noise of 64 mK, and effective resolution of 0.12.



Top left: The original mean stack image, with overlays indicating the region over which the transverse mean (dashed orange horizontal lines) and longitudinal mean (dashed green vertical lines) are calculated. *Top right:* The mean stacked image with the colour scale reduced to $\pm 5\sigma$ to emphasise the noise. *Bottom left:* The model image, on the same colour scale. *Bottom right:* The residual stack after model subtraction, with the colour scale set to $\pm 5\sigma$.

One: The one-dimensional profile along $y = 0$ for both the stacked image (blue) and the model (red). *Two:* The one-dimensional profile along $y = 0$ of the residual stack, renormalised to the estimated map noise. *Three:* The transverse mean along the region $-0.2 < y < 0.2$ of the residual stack, renormalised to the estimated map noise. *Four:* The longitudinal mean along the region $-0.95 < x < 0.95$ of the residual stack, renormalised to the estimated map noise. The black rule in the top left shows the FWHM of the effective resolution.

Figure 17. Original GLEAM survey images at 118.5 MHz, stacked using the Max 15 Mpc LRG catalogue, displaying mean LRG peaks of 4 600 mK, residual noise of 87 mK, and effective resolution of 0.16.

V2021, and the inclusion of the background subtraction step mitigates their stated concerns about masking. We additionally ‘grow’ all masked regions by 2 pixels, which we have found to be sufficient to avoid visually obvious rings of faint emission around the masks. Note that even after growing the masks slightly, this process leaves surrounding negative sidelobes about the masked regions, and this results in the remaining non-masked region having an overall negative mean. As with the previous masked stacks in [Subsection 5.4](#), this will affect the ‘zero point’ of the final stacks. As previously, exclusion zones are identified around exceptionally bright sources, along sidelobe artefacts, and in one additional region where the background estimation had not been adequate due to a sharp change in the background brightness. Finally, the map is converted to temperature using the associated dirty beam map that described the major and minor axis variation of the beam. We then proceed to stack all LRG pairs from the Max 15 Mpc catalogue that overlap with the images, of which there are 645,950 unique pairs. All stacks are weighted by the inverse square of the local noise.

In [Figure 17](#), we show the results of the GLEAM stacking with the Max 15 Mpc catalogue. This residual image is noticeably different from the one presented in V2021. In the first instance, there is no obvious, large-scale region of excess emission. In V2021, this excess region spanned the length of the intercluster region, and surprisingly was wider than it was long. The residual image is also highly uniform, again differing from V2021 where all the residual images, including the null tests, displayed a distinctive large-scale pattern. Curiously, the noise in this image is at 87 mK, which is higher than reported in V2021 even though we stack a much larger number of LRG pairs.^e The one-dimensional profiles similarly display little evidence of excess emission in the residual, with the exception of a peak that reaches 3σ in the integrated profile, at $x \approx -0.5$, and which has a width very slightly wider than the effective resolution. There are at least 3 other peaks of similar magnitude and size throughout the residual image that cannot be attributed to intercluster cosmic web emission by reason of their location in the map, and so we must conclude that this peak is unexceptional.

Ultimately, we are unable to reproduce the broad and extended excess emission signal found in V2021, even when using the same data set, raising questions that these differences in results are due to the stacking procedure. In [Appendix C](#), we perform a similar stacking procedure on the ROSAT broad X-ray data, as was performed in V2021. In this case, however, we detect a strong 12σ signal for the Max 15 Mpc catalogue. This confirms the detection of V2021 for this data set, and provides us with confidence that our stacking and model subtraction processes will detect excess emission when it is present, and suggests that the discrepancy in results arises elsewhere in the analysis.

6. Conclusion

We have attempted to reproduce the detection of excess emission spanning LRG pairs in low-frequency radio data, as reported by V2021, and which they attributed to synchrotron emission along filaments spanning pairs of close-proximity clusters and galaxy groups. To reproduce their work, we have adhered very closely to their methodology: using the same LRG catalogue and selection criteria for pairs, stacking radio images at 118.5 MHz,

and modelling the LRG and cluster contribution in the same way as V2021. We differ from V2021 primarily in that we use the upgraded MWA Phase II array, which has almost twice the resolution as the Phase I instrument used in V2021, and that our calibration, imaging and point-source subtraction pipelines utilised improved workflows that have been developed since the original GLEAM survey.

We have not been able to reproduce their result. Indeed, we have not been able to reproduce their result across a number of LRG pair catalogues, including the original abridged catalogue used in V2021, as well as a much larger catalogue that uses the full range of LRG pairs that meet the original selection criteria of V2021. We reach noise levels in our final stacks consistently lower than those of V2021, and more than twice as deep when using the full range of available LRG pairs. At these noise levels, their reported filamentary temperature should appear as approximately an 8σ detection. Our residual stacks, however, are consistent with noise.

Our biggest concern with using MWA Phase II is the potential that we resolve out large, extended structures. However, we have shown that we are at least as sensitive to extended sources as Phase I out to $\sim 125'$ thanks to our extra convolution step, and that even for extended emission up to the maximum separation of $180'$, the likely shape and structure of this emission will reduce the effects of resolving out structure. Moreover, we have provided results of an additional LRG pair catalogue, with sources separated by $15 - 60'$, that mitigates these concerns; the stacking results of this catalogue reach noises lower than those of V2021 and yet still do not reproduce their observed excess emission.

In addition, we have returned to the original GLEAM survey data where we have performed stacking using the expanded Max 15 Mpc LRG pair catalogue. Whilst we do find an isolated peak at just above 3σ significance, we find this to be an unremarkable feature of the residuals and certainly not the broad, extended excess emission as found in V2021. This non-detection is in spite of clearly reproducing the excess emission after stacking the ROSAT broad X-ray data, giving us good confidence in our stacking and modelling processes.

If our results hold true, we have provided in this work the strongest limits on synchrotron emission from intercluster filaments. However, the discrepancy with the work of V2021 is concerning and begs explanation. Whilst our Phase II results alone left open the possibility that this discrepancy arose due to a real, intrinsic property of the emission, our inability to reproduce the results additionally with GLEAM points to a much more likely possibility: that an error has been made in these detection attempts either by V2021 or ourselves. To this end, we are making publicly available the images of our fields, our stacking and modelling code, and the stacked images themselves, in the hope that if we have indeed erred, it can be quickly identified. Given the significance of the V2021 result, and the surprising implications on our understanding of cosmic magnetism, there is a pressing need reproduce their detection.

Acknowledgements. This scientific work makes use of the Murchison Radio-astronomy Observatory, operated by CSIRO. We acknowledge the Wajarri Yamatji people as the traditional owners of the Observatory site. Support for the operation of the MWA is provided by the Australian Government (NCRIS), under a contract to Curtin University administered by Astronomy Australia Limited. We acknowledge the Pawsey Supercomputing Centre which is supported by the Western Australian and Australian Governments. This work was supported by resources provided by the Pawsey

^eNote that the stated value in V2021 was calculated assuming the average noise in the original images reduced from stacking N LRG pairs as a factor of $1/\sqrt{N}$, rather than being measured directly.

Supercomputing Centre with funding from the Australian Government and the Government of Western Australia. We acknowledge the use of NASA's SkyView facility (<http://skyview.gsfc.nasa.gov>) located at NASA Goddard Space Flight Center.

References

- Baugh, C. M., et al. 2004, *MNRAS*, **351**, L44
 Brown, S. D. 2011, *JApA*, **32**, 577
 Brown, S., et al. 2017, *MNRAS*, **468**, 4246
 Cen, R., & Ostriker, J. P. 1999, *ApJ*, **514**, 1
 Davé, R., et al. 2001, *ApJ*, **552**, 473
 Eastwood, M. W., et al. 2018, *AJ*, **156**, 32
 Eckert, D., et al. 2015, *Natur*, **528**, 105
 Govoni, F., et al. 2019, *Sci*, **364**, 981
 Hancock, P. J., Trott, C. M., & Hurley-Walker, N. 2018, *PASA*, **35**, e011
 Hodgson, T., Johnston-Hollitt, M., McKinley, B., Vernstrom, T., & Vacca, V. 2020, *PASA*, **37**, e032
 Hodgson, T., Vazza, F., Johnston-Hollitt, M., Duchesne, S. W., & McKinley, B. 2021a, arXiv e-prints, p. arXiv:2108.13682
 Hodgson, T., Vazza, F., Johnston-Hollitt, M., & McKinley, B., 2021b, *PASA*, **38**, e047
 Hoessel, J. G., Gunn, J. E., & Thuan, T. X. 1980, *ApJ*, **241**, 486
 Hoshino, H., et al. 2015, *MNRAS*, **452**, 998
 Hurley-Walker, N., & Hancock, P. J. 2018, *A&C*, **25**, 94
 Hurley-Walker, N., Seymour, N., Staveley-Smith, L., Johnston-Hollitt, M., Kapinska, A., & McKinley, B. 2017a, GaLactic and Extragalactic All-Sky MWA-eXtended (GLEAM-X) survey: Pilot observations, MWA Proposal id.2017A-11
 Hurley-Walker, N., et al. 2017b, *MNRAS*, **464**, 1146
 Lopes, P. A. A. 2007, *MNRAS*, **380**, 1608
 Macquart, J. P., et al. 2020, *Natur*, **581**, 391
 Nicastrò, F., et al. 2018, *Natur*, **558**, 406
 O'Sullivan, S. P., et al. 2019, *A&A*, **622**, A16
 Offringa, A. R., et al. 2014, *MNRAS*, **444**, 606
 Piffaretti, R., Arnaud, M., Pratt, G. W., Pointecouteau, E., & Melin, J. B. 2011, *A&A*, **534**, A109
 Planck Collaboration, et al. 2016, *A&A*, **594**, A27
 Postman M., & Lauer T. R. 1995, *ApJ*, **440**, 28
 Pshirkov, M. S., Tinyakov, P. G., & Urban, F. R. 2016, *PhRvL*, **116**, 191302
 Sault, R. J., Teuben, P. J., & Wright, M. C. H. 1995, in *Astronomical Society of the Pacific Conference Series*, Vol. 77, *Astronomical Data Analysis Software and Systems IV*, ed. R. A. Shaw, H. E. Payne, & J. J. E. Hayes, 433 (arXiv:astro-ph/0612759)
 Schneider, D. P., Gunn, J. E., & Hoessel, J. G. 1983, *ApJ*, **264**, 337
 Schuecker, P. 2005, *RvMA*, **18**, 76
 Sokolowski, M., et al. 2017, *PASA*, **34**, e062
 Tanimura, H., Aghanim, N., Douspis, M., Beelen, A., & Bonjean, V. 2019, *A&A*, **625**, A67
 Tanimura, H., et al. 2020, *MNRAS*, **491**, 2318
 Tingay, S. J., et al. 2013, *PASA*, **30**, e007
 Vacca, V., et al. 2018, *MNRAS*, **479**, 776
 Vazza, F., Etori, S., Roncarelli, M., Angelinelli, M., Brüggén, M., & Gheller, C. 2019, *A&A*, **627**, A5
 Vazza, F., Ferrari, C., Brüggén, M., Bonafede, A., Gheller, C., & Wang, P. 2015, *A&A*, **580**, A119
 Vernstrom, T., Gaensler, B. M., Brown, S., Lenc, E., & Norris, R. P. 2017, *MNRAS*, **467**, 4914
 Vernstrom, T., Gaensler, B. M., Rudnick, L., & Andernach, H. 2019, *ApJ*, **878**, 92
 Vernstrom, T., Heald, G., Vazza, F., Galvin, T. J., West, J. L., Locatelli, N., Fornengo, N., & Pinetti, E. 2021, *MNRAS*,
 Voges, W., et al. 1999, *A&A*, **349**, 389
 Wayth, R. B., et al. 2015, *PASA*, **32**, e025
 Wayth, R. B., et al. 2018, *PASA*, **35**, e033
 Wen, Z. L., Han, J. L., & Yang, F. 2018, *MNRAS*, **475**, 343
 York, D. G., et al. 2000, *AJ*, **120**, 1579

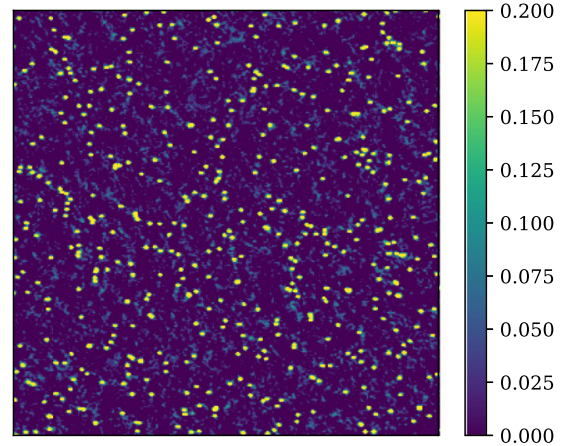


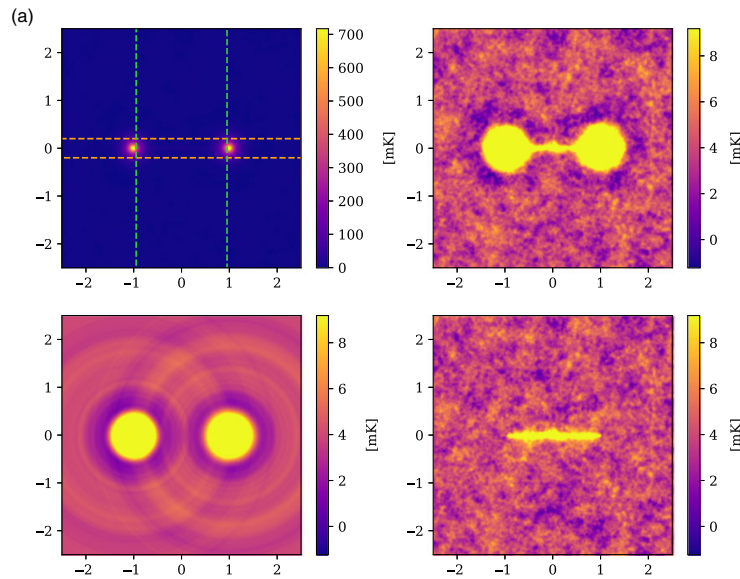
Figure A1. A zoom of the synthetic cosmic web image, showing randomly positioned 1 K point sources with a subset of pairs connected by faint ‘filaments’. After convolution with the Phase II (convolved) beam, the filaments become hidden beneath the 25 mK sidelobe confusion noise.

A. Synthetic stacks

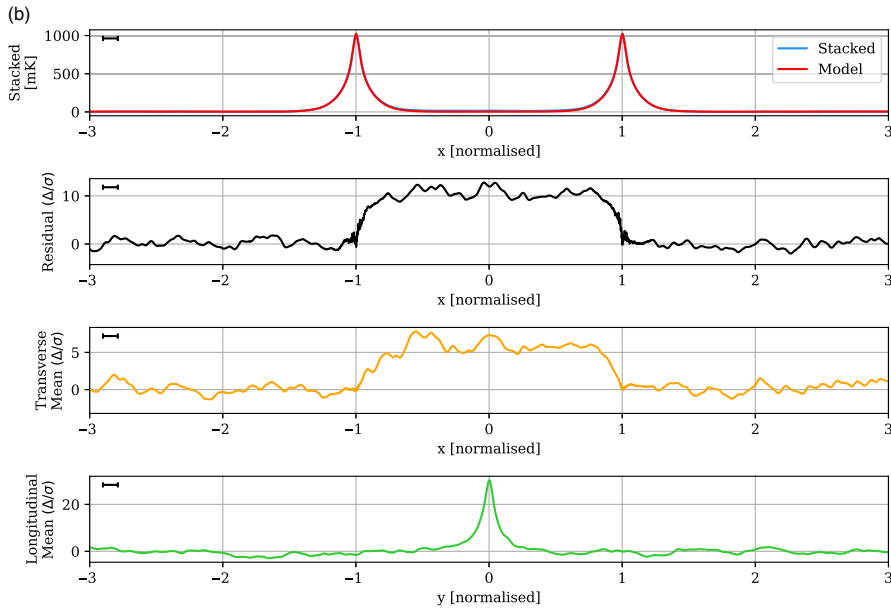
To validate our stacking and modelling process, we have created a synthetic ‘cosmic web’ map and associated catalogue. We created a $14\,000 \times 14\,000$ pixel map, randomly positioned 26 000 point sources with peak temperature of 1 K and then selected pairs of peaks that were separated in the range $20 - 180'$. Pairs were randomly selected to produce a pair separation distribution that strongly favoured shorter separations, so as to approximate the distributions as seen in Figure 2; 5 539 pairs were chosen in this way. For each chosen pair, we drew a ‘filament’ as a straight, single pixel line, with each pixel having a value of 0.005 K. Finally, we convolved the image with the Phase II (convolved) beam, as shown in Figure 12. The resulting map is shown in Figure A1 where the point sources can be readily observed whilst the cosmic web filaments are not visually detectable above the sidelobe confusion, which is approximately 25 mK.

In Figure A2 we show the results after stacking and model subtraction. The stacked point sources peak at approximately 1 K, in agreement with their injected values. Note also the presence of the faint, negative lobes about the exterior sweep of each peak, resulting from the negative lobes of the dirty beam. In practice, both the width of the peaks and positioning of the sidelobes are highly dependent on the distribution of the angular separation of pairs, which in turn affects the mix of rescaling that is required during stacking; for catalogues with more distant pairs, the peaks became narrower and the sidelobes less prominent. As can be seen in the residual image, after model subtraction we clearly recover the ‘cosmic web’ bridge. The model subtraction process does well to compensate for the negative sidelobes, resulting in a bridge that is fairly constant as can be seen in the one-dimensional profile, at approximately 11σ in the residual along $y = 0$. This is reduced in the transverse mean profile as a result of the narrowness of the filament, however the signal exceeds 30σ in the longitudinal profile.

We believe these results validate our stacking and modelling processes.



Top left: The original mean stack image, with overlays indicating the region over which the transverse mean (dashed orange horizontal lines) and longitudinal mean (dashed green vertical lines) are calculated. *Top right:* The mean stacked image with the colour scale reduced to $\pm 5\sigma$ to emphasise the noise. *Bottom left:* The model image, on the same colour scale. *Bottom right:* The residual stack after model subtraction, with the colour scale set to $\pm 5\sigma$.



One: The one-dimensional profile along $y = 0$ for both the stacked image (blue) and the model (red). *Two:* The one-dimensional profile along $y = 0$ of the residual stack, renormalised to the estimated map noise. *Three:* The transverse mean along the region $-0.2 < y < 0.2$ of the residual stack, renormalised to the estimated map noise. *Four:* The longitudinal mean along the region $-0.95 < x < 0.95$ of the residual stack, renormalised to the estimated map noise. The black rule in the top left shows the FWHM of the effective resolution.

Figure A2. The synthetic stacks, with mean peaks of 1.02 K, residual noise of 1 mK, and effective resolution of 0.11.

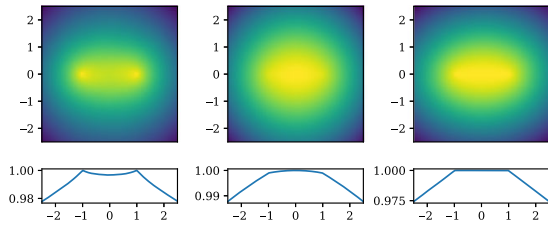


Figure B1. Stacked weight maps for the Max 15 Mpc catalogue, using a variety of weighting configurations. The weights are ultimately derived from the estimated noise maps of each field, which are spatially varying across the fields. The dominant effect seen here is the result of LRG pairs near the edge of the fields that produces the tapering effect towards the edges, with secondary effects caused by the ad-hoc exclusion zones and the convex geometry of the field perimeter. *Left:* The stacked weight map resulting from the default, noise-weighted stacking, also showing a one-dimensional profile through $y = 0$ in the lower panel. *Centre:* The stacked weight map using noise-weighted stacking but ad-hoc exclusion zones ignored during stacking and left unmasked. *Right:* The stacked weight maps using constant weight during stacking, and with ad-hoc exclusion zones ignored.

B. The weighting of the stacks

When stacking the LRG pairs from each field, we have weighted each pair by an estimate of the field noise. We have previously noted that these noise maps are spatially varying across a field, as a function of the primary beam attenuation, and that even across a single LRG pair the noise may be varying. What effect does this have on the final weighting of each stack?

In [Figure B1](#) we show the associated stacked weight maps constructed as part of the Max 15 Mpc stack for different weighting configurations. From left to right: the default $\frac{1}{\sigma^2}$ noise-weighted maps with ad-hoc exclusion zones as detailed in [Subsection 3.3](#), the same but with the ad-hoc exclusion zones ignored during stacking and left unmasked, and finally with a constant weighting and no ad-hoc exclusion zones. We also provide a one-dimensional profile for each map through $y = 0$, where we observe that each weighted map differs primarily by the weighting directly between the LRG pair.

Each stacked weight map shares a bright central component that tapers off towards the edge. This is not an effect of local variation of noise in each field, but rather is a result of the convex perimeter of each field. During stacking, any LRG pairs near the edge of this field window have significant areas of their rescaled and rotated images ‘outside’ the field, and are therefore both set to zero and weighted as zero. The combined effect of this has resulted in the dominant tapering effect as observed. The secondary effect that we can observe in the stacked weight maps is the intercluster weighting, which varies from left to right as a shallow depression, shallow rise and a constant weight. There are two separate effects at work in creating these intercluster weightings. The first effect is the presence of the ad-hoc exclusion zones. Recall that the only requirement during stacking was that each LRG pair occupied a non-masked pixel, that is, that each LRG was interior to a field, and was not masked by an exclusion zone. This requirement did not, however, exclude cases where an ad-hoc exclusion zone existed between an LRG pair. This is the effect that dominates in the default example, causing the shallow depression in weighting between the LRG pair. If we ignore the ad-hoc exclusion zones during stacking, however, we instead obtain a stacked weight map

with a slight rise in the intercluster region. This effect is caused by variations in local map noise caused by one special case: when stacking LRG pairs along the convex perimeter of the field. When stacking such pairs, the direct line between the LRG pair passes from the field perimeter towards the field interior, going from the maximum noise at the field edge towards a slightly reduced noise environment towards the interior. The effect of this is to slightly upweight the intercluster region. Finally, both of these effects are removed by considering the case of a constant weighted stack with no ad-hoc exclusion zones: we observe a constant weight between the LRG pair.

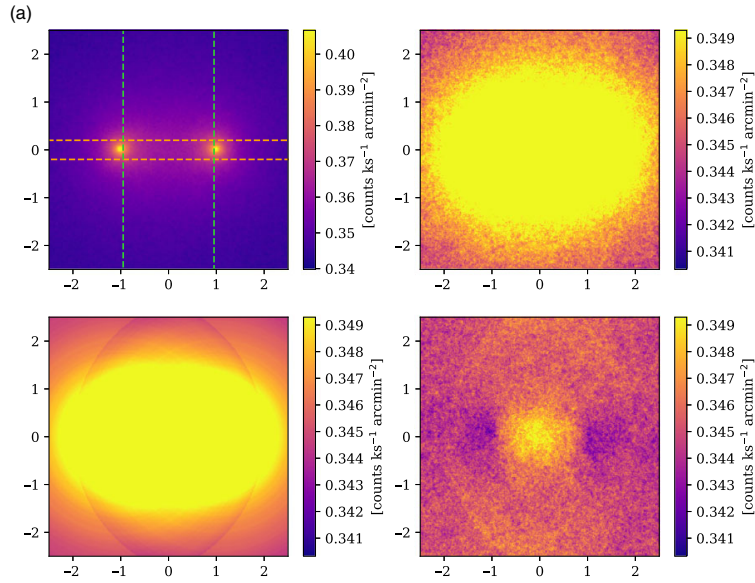
In practice, the weighting scheme has very little effect on the final stack. The constant weighted stack, which ignores both the local noise estimation and ad-hoc exclusion zones, has an estimated residual noise of 27 mK in comparison to the 25 mK of the noise-weighted stacks shown previously. Moreover, each of the three differently weighted stacks have visually identical residual maps.

C. ROSAT stacks

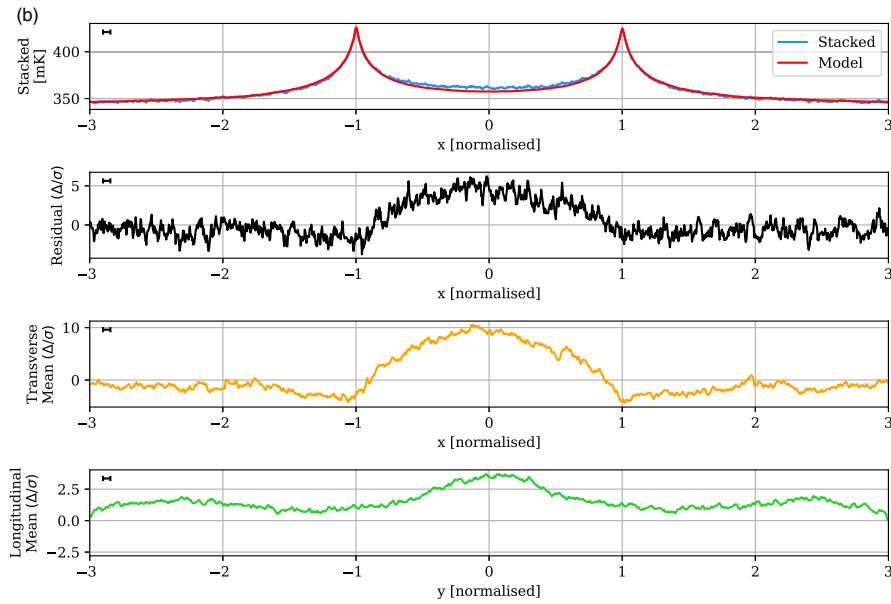
V2021 performed stacking on X-ray data from ROSAT All-sky Survey (Voges *et al.* 1999), and we reproduce this here using the ROSAT broad images (0.1–2.4 keV). These images span further North than is possible with the MWA pointings, and so we are able to stack 757 731 LRG pairs as part of the Max 15 Mpc catalogue. The ROSAT broad data were downloaded as a series of $20 \times 20^\circ$ images in a gnomonic (TAN) projection, spanning the field of LRG pairs at intervals of 10° on the sky. Bright pixels having a count greater than 20 counts $\text{ks}^{-1} \text{arcmin}^{-2}$ were blanked, but otherwise the images were not further processed.

The results of this stacking are shown in [Figure C1](#). The residual image shows a large, excess region centred at $x = 0$, but spanning the length of the intercluster region, and having a width approximately $-0.5 < y < 0.5$. The excess signal is very well detected, having a one-dimensional profile that peaks just above 7σ , corresponding to an excess value of $(6.6 \pm 0.9) \times 103 \text{ counts ks}^{-1} \text{arcmin}^{-2}$, and an integrated profile (between $-0.2 < y < 0.2$) that peaks above 12σ . A null test using unrelated LRG pairs ($\Delta r > 150 \text{ Mpc}$) but otherwise conforming to the angular separation distribution of the Max 15 Mpc catalogue returned no excess signal. These excess values compare to the value found by V2021 of $(11.5 \pm 1.4) \times 10^{-3} \text{ counts ks}^{-1} \text{arcmin}^{-2}$, although this value was found when stacking the abridged LRG-V2021 catalogue and was a mean across an unspecified ‘filamentary region’.

Note that the width of X-ray emission around each LRG peak is extremely broad. In fact, in the one-dimensional profile we can see the exterior sides do not become flat even out to $x = \{-3, +3\}$. Indeed, this extreme width of each peak causes our model subtraction process to handle poorly. As we noted in [Subsection 4.2](#), we independently model each LRG peak before simply adding each of their contributions. This works well when the contribution from each peak drops to zero for radial distances $r > 2$. However, since in this case each peak still includes a non-negligible component present from the opposing peak, we therefore over-subtract, causing both the negative bowls of emission that can be seen in the residual image, as well as to underestimate the central excess emission.



Top left: The original mean stack image, with overlays indicating the region over which the transverse mean (dashed orange horizontal lines) and longitudinal mean (dashed green vertical lines) are calculated. *Top right:* The mean stacked image with the colour scale reduced to $\pm 5\sigma$ to emphasise the noise. *Bottom left:* The model image, on the same colour scale. *Bottom right:* The residual stack after model subtraction, with the colour scale set to $\pm 5\sigma$.



One: The one-dimensional profile along $y = 0$ for both the stacked image (blue) and the model (red). *Two:* The one-dimensional profile along $y = 0$ of the residual stack, renormalised to the estimated map noise. *Three:* The transverse mean along the region $-0.2 < y < 0.2$ of the residual stack, renormalised to the estimated map noise. *Four:* The longitudinal mean along the region $-0.95 < x < 0.95$ of the residual stack, renormalised to the estimated map noise. The black rule in the top left shows the FWHM of the effective resolution.

Figure C1. The Max 15 Mpc stack of ROSAT broad images, with mean LRG peaks of $0.4238 \text{ counts ks}^{-1} \text{ arcmin}^{-2}$, residual noise of $0.9 \times 10^{-3} \text{ counts ks}^{-1} \text{ arcmin}^{-2}$, and effective resolution of 0.05.

Despite detecting a signal, we would hesitate to attribute this emission to true intercluster X-ray emission. The width of each peak implies that most of the emission in the centre of the residual images originates from cluster emission, and that a significant number of these pairs must overlap along our line of sight due to

projection effects. It is therefore equally plausible that the excess emission in the centre originates due to asymmetric cluster emission, rather than hot intercluster filamentary gas. This is especially plausible given the number of clusters known to host substructures away from their core (Schuecker 2005).

B.5 Hodgson et al. (2022a)


Stacking the synchrotron cosmic web with FIGARO

[Hodgson, Vazza, Johnston-Hollitt & McKinley \(2022b\)](#)

© The authors 2022. Reproduced with permission.

Research Paper

Stacking the synchrotron cosmic web with FIGARO

Torrance Hodgson^{1,2} , Franco Vazza^{3,4,5}, Melanie Johnston-Hollitt^{1,2} and Benjamin McKinley^{1,6}

¹International Centre for Radio Astronomy Research (ICRAR), Curtin University, 1 Turner Ave, Bentley, WA 6102, Australia, ²Curtin Institute for Computation, Curtin University, GPO Box U1987, Perth, WA 6845, Australia, ³Dipartimento di Fisica e Astronomia, Università di Bologna, Via Gobetti 92/3, Bologna 40121, Italy, ⁴Hamburger Sternwarte, Gojenbergsweg 112, Hamburg 21029, Germany, ⁵INAF, Istituto di Radio Astronomia di Bologna, Via Gobetti 101, Bologna 40129, Italy and ⁶ARC Centre of Excellence for All Sky Astrophysics in 3 Dimensions (ASTRO3D), Bentley, Australia

Abstract

Recently Vernstrom et al. (2021, MNRAS) claimed the first definitive detection of the synchrotron cosmic web, obtained by ‘stacking’ hundreds of thousands of pairs of close-proximity clusters in low-frequency radio observations and looking for a residual excess signal spanning the intracluster bridge. A reproduction study by Hodgson et al. (2022, PASA, 39, e013), using both the original radio data as well as new observations with the Murchison Widefield Array, failed to confirm these findings. Whilst the detection remains unsure, we here turn to stacking a *simulated* radio sky to understand what kind of excess radio signal is predicted by our current best cosmological models of the synchrotron cosmic web. We use the Filaments & GALactic RadiO (FIGARO; Hodgson et al. 2021a, PASA, 38, e047) simulation, which models both the synchrotron cosmic web as well as various subtypes of active galactic nuclei and star-forming galaxies. Being a simulation, we have perfect knowledge of the location of clusters and galaxy groups which we use in our own stacking experiment. Whilst we do find an excess radio signature in our stacks that is attributable to the synchrotron cosmic web, its distribution is very different to that found by Vernstrom et al. (2021, MNRAS). Instead, we observe the appearance of excess emission on the immediate interiors of cluster pairs as a result of asymmetric, ‘radio relic’-like shocks surrounding cluster cores, whilst the excess emission spanning the intracluster region—attributable to filaments proper—is two orders of magnitude lower and undetectable in our experiment even under ideal conditions.

Keywords: Cosmic web (330) – Warm-hot intergalactic medium (1786) – Radio astronomy (1338)

(Received 31 August 2021; revised 25 May 2022; accepted 26 May 2022)

1. Introduction

The imagery of the ‘cosmic web’ has been used to describe the Universe on the very largest of scales. It describes the ongoing process of structure formation, starting with primordial perturbations in the mass distribution of the early Universe, and since growing into an ontology of structures: large-scale voids, emptying onto surrounding sheets, collapsing down into filaments, and feeding into galaxy groups and clusters. Empirical evidence of this structure has come from galaxy surveys (e.g. Baugh et al. 2004), but cosmological simulations also suggest that these structures are much more massive than the galaxies that trace them out (e.g. Cen & Ostriker 1999; Davé et al. 2001), with up to 40% of the baryon population of the Universe—the so-called ‘missing baryon’ population (e.g. Nicastro et al. 2017)—located along the filaments and around the periphery of clusters. Empirical corroboration has proved difficult since the majority of the matter that traces this structure is predicted to exist in a low density, warm-hot ($10^5 - 10^7$ K), and highly ionised state, rendering it extremely difficult to detect in practice.

Nonetheless, numerous reports have claimed tentative detection of this ‘warm-hot intergalactic medium’ (WHIM), backing up the simulation predictions. Eckert et al. (2015), Nicastro et al. (2018), de Graaff et al. (2019), and Tanimura et al. (2019, 2020),

for example, used a range of techniques such as molecular absorption lines and statistical (stacking) detections of the Sunyaev–Zeldovich effect to claim detections of this large-scale structure. Perhaps the most definitive accounting for the missing baryon population was recently made by Macquart et al. (2020) using fast radio bursts to trace the intervening density of the Universe, and finding it to be overdense consistent with the missing baryons residing, hidden, along the line of sight.

Simulations have also pointed to the existence of a radio synchrotron component that traces out the cosmic web (e.g. Brown 2011; Araya-Melo et al. 2012; Vazza et al. 2015, 2019). This hypothesised emission is driven by accretion processes occurring within the WHIM—as part of the ongoing large-scale structure formation of the Universe—that are expected to produce strong shocks, with Mach numbers in the range $\mathcal{M} \sim 10 - 100$. These shocks occur in the low density peripheries of clusters and around filaments, and they are capable of accelerating a small fraction of the ambient electron population to relativistic energies by way of diffusive shock acceleration processes (e.g. Keshet et al. 2009). In the presence of intracluster magnetic fields, which we expect to be on the order of a few nG (e.g. Pshirkov, Tinyakov, & Urban 2016; O’Sullivan et al. 2019; Vernstrom et al. 2019; Carretti et al. 2022), these energetic electron populations should radiate their energy as synchrotron emission. But their emission is extremely faint. Simulations by Vazza et al. (2015), for example, predict only the very brightest peaks of emission from the synchrotron cosmic web to be detectable with the current generation of radio telescopes, and detection is made more difficult still due to much more

Corresponding author: Torrance Hodgson, email: torrance@pravic.xyz

Cite this article: Hodgson T, Vazza F, Johnston-Hollitt M and McKinley B. Stacking the synchrotron cosmic web with FIGARO. *Publications of the Astronomical Society of Australia* <https://doi.org/10.1017/pasa.2022.26>

luminous radio populations such as active galactic nuclei (AGNs) or star-forming galaxies (SFGs).

The difficulty of direct detection has driven statistical detection techniques, and foremost among these has been the cross-correlation method. This method seeks to overcome both the problem of the faint signal of the synchrotron cosmic web and the obscuring effect of the more luminous radio source populations by essentially integrating across a large area of sky. It does this by identifying a ‘best guess’ distribution of the synchrotron cosmic web in a region of the sky and performing a radial cross-correlation of this kernel with the observed radio emission. In theory, a peak at or near 0° offset would indicate a detection of the cosmic web. In practice, however, lots of other emission sources cluster similarly and pollute the signal (Hodgson *et al.* 2021a). And so while the cross-correlation analysis of Vernstrom *et al.* (2017) did indeed detect a peak at 0° , they were unable for this reason to make any kind of definitive claim of detection. Meanwhile, a similar cross-correlation analysis by Brown *et al.* (2017) found no detection at all.

Recently, however, there was a notable development in this field with the announcement of the radio detection of filaments by Vernstrom *et al.* (2021), herein V2021. This was also a statistical detection, but instead the authors employed a stacking technique. Their method used luminous red galaxies (LRGs) derived from the Sloan Digital Sky Survey Data Release 5 (Lopes 2007) as tracers for overdense regions such as clusters and galaxy groups. These LRGs had photometric redshift data, and so it was possible to create a catalogue of LRG pairs separated by no more than 15 Mpc, with the assumption that close-proximity clusters will, on average, be connected by filaments. V2021 proceeded by stacking continuum images from two low-frequency radio surveys, the GaLactic and Extragalactic All-sky MWA^a survey (GLEAM; Wayth *et al.* 2015; Hurley-Walker *et al.* 2017) and the Owens Valley Radio Observatory Long Wavelength Array (OVRO-LWA; Eastwood *et al.* 2018). Pairs of LRGs were extracted from these sky surveys, rotated, rescaled, and stacked along a normalised coordinate frame such that each pair was positioned at $x = -1$ and 1 , respectively. After many such pairs were stacked, the expectation was that the image noise would be sufficiently reduced so that excess filamentary emission would become detectable along the bridge between -1 and 1 . Indeed, V2021 reported excess filamentary emission along this bridge at 118 MHz with a temperature of 0.22 K and having a spectral index of $\alpha = -1.0$. Moreover, a null test with spatially distant pairs of LRGs produced no excess emission. The result of V2021 is surprising for a number of reasons, not least in that it implies intracluster magnetic field strengths that are stronger than previous upper limits, in the range of 30 – 60 nG for a significant fraction of filaments. In fact, we should note this is strictly a lower limit, as not all LRG pairs are centrally aligned with a host cluster or galaxy group, and further only a fraction of these will in fact be connected by filament.

Given this surprising result, Hodgson *et al.* (2022), herein H2022, attempted to reproduce this result by stacking both the original GLEAM survey data as well as stacking new observations made with Phase II of the MWA (Wayth *et al.* 2018). Their stacking methodology closely followed that described in V2021 and stacked the same catalogue of LRG pairs as well as additional, differently parameterised catalogues of LRG pairs. In each case,

no excess emission was detected that resembled the broad excess intracluster emission as detected in V2021.

Whilst it remains unclear the cause for this discrepancy in results, we can meanwhile turn to cosmological simulations to ask what kind stacking profile we should expect. In this paper, we make use of the Filaments and GALactic RadiO simulation (FIGARO; Hodgson *et al.* 2021a) to perform our own simulated stacking experiment. FIGARO simulates the low to mid frequency radio sky including AGN and SFG populations, against a backdrop of large-scale diffuse cosmic web synchrotron emission produced by Vazza *et al.* (2019), the largest magneto-hydrodynamic (MHD) cosmological simulation to date. Crucially, these different radio populations coherently cluster together with respect to an underlying mass distribution drawn from the same cosmological volume. FIGARO is able to produce light cones of each of these populations for both configurable fields of view and variable redshift depths.

We use FIGARO to create ten, $15^\circ \times 15^\circ$ fields at 150 MHz using an observing configuration designed to match the MWA Phase I instrument (Tingay *et al.* 2013). We aim to reproduce the stacking methodology of V2021 and H2022 applied to these simulated radio fields and thus construct simulated stacked profiles of both the synchrotron cosmic web as well as the much brighter embedded radio populations of AGN and SFG. The primary deviation from their methodology, however, is that we do not need to use LRGs as a proxy for cluster locations, since we have perfect knowledge of the location of dark matter (DM) halos throughout our fields, and we can thus stack clusters and galaxy groups directly. We hope by doing this exercise to give a sense of the expected magnitude and distribution of excess emission signature expected from any future stacking experiments.

This paper begins by outlining the construction of the $15^\circ \times 15^\circ$ simulated fields in Section 2. We follow in Section 3 by outlining the stacking process, which includes our choice of DM halo pairs. Finally, in Section 4 we discuss the results of our stacks, our predictions for future, deeper stacking experiments as well as the challenges of the technique.

Throughout this paper we assume a Λ CDM cosmological model, with density parameters $\Omega_{\text{BM}} = 0.0478$ (baryonic matter), $\Omega_{\text{DM}} = 0.2602$ (DM), and $\Omega_{\Lambda} = 0.692$, and the Hubble constant $H_0 = 67.8 \text{ km s}^{-1} \text{ Mpc}^{-1}$. These values are consistent with those used in both FIGARO and, ultimately, the original simulation by Vazza *et al.* (2019).

2. Field construction

The first step in this exercise was to produce the simulated fields that we would ultimately use in our stacking experiment. To produce these fields, we made use of the FIGARO simulation, which allowed us to construct realistic maps of the radio sky incorporating not just the synchrotron cosmic web, but also AGN and SFG populations. FIGARO is built off an underlying 100^3 Mpc^3 MHD cosmological simulation from Vazza *et al.* (2019) which, for our purposes, allows us to track the evolution of mass density, accretion shocks, and the resulting radio synchrotron cosmic web emission. To this, AGN and SFG populations were added in accordance to the underlying mass distribution using the Tiered Radio Extragalactic Continuum Simulation (T-RECS; Bonaldi *et al.* 2019), ultimately allowing us to create a realistic radio sky where mass, extragalactic radio sources, and the synchrotron cosmic web are distributed and cluster accurately with regards to one

^aMurchison Widefield Array (Tingay *et al.* 2013).

another. The full details of FIGARO, including its calibration of cosmic web emission to the observed radio relic population, are provided in Hodgson et al. (2021a).

We have used FIGARO to construct ten $15^\circ \times 15^\circ$ fields—or ‘realisations’—out to a redshift depth of $z = 0.6$ and at an observing frequency of 150 MHz. As with the original FIGARO, each realisation differs by laterally offsetting and rotating the simulation volume by some random factor each time it is appended in redshift space. For low redshifts, each realisation can appear quite drastically different depending on whether, by chance, the lateral offset places a massive cluster in the near foreground, or perhaps instead a massive void. By using ten such realisations, we hope to give a good sense of near-field cosmic variance. With a field this large, however, it becomes necessary to laterally replicate the underlying cosmological volume for redshifts $z > 0.09$, since the field of view spans greater than the 100 Mpc width of the underlying cosmological volume. The result of this is that there will be increasing redundancy of any stacking procedure as we go deeper in redshift space, since the same cosmic web features will be repeated more than once across the field of view. In practice, however, this increasing redundancy at high redshifts is mitigated by our selection criteria for halo pairs (see below) as we make use of a much more local region of redshift space, with more than half of the DM halo pairs located within $z < 0.2$. Moreover, whilst a cosmic web feature may appear more than once across a redshift slice, each will be obscured by a unique foreground of AGN, SFG, and unrelated cosmic web emission. The higher redshift cosmic web emission, meanwhile, serves primarily as a potentially obfuscating background to this foreground emission, just as we’d expect in practical observations of the radio sky.

For each of these realisations, FIGARO produces a catalogue of AGNs, SFGs, and DM halos, as well as a map incorporating the flux sum of cosmic web emission along the line of sight (in units Jy pixel^{-1}).

The next step is to transform the FIGARO catalogue into a map of the sky. In an effort to approximate the results of V2021 and H2022, we produce this map at the resolution of the MWA Phase I instrument. We do this by first constructing a map of the sky, in units Jy pixel^{-1} , where the pixel scale is sufficiently smaller than the MWA Phase I point spread function (PSF). FIGARO already provides us with such a map for the cosmic web, which we have set to a pixel scale of $4'' \times 4''$. And in the case of the AGN and SFG populations, we model these as simple point sources—that is, single pixel values—which is a good approximation given the low resolution of the MWA Phase I instrument. The final step is to convolve this map with the MWA Phase I PSF, transforming the units from Jy pixel^{-1} to Jy beam^{-1} . At no point do we add simulated thermal or sky noise to our images.

To do this final step, we need to model the MWA Phase I PSF. We have used a sample of archival Phase I observations from the original GLEAM survey to accurately reconstruct the shape of the PSF based on the geometry of the array, elevation of the pointings, and weighting of the baselines. Note that these archival observations are centred with a declination of $\delta = 18.6^\circ$, corresponding to the necessary low elevation pointings used in both V2021 and H2022 to observe the LRG population. These low elevation pointings result in a fairly significant lengthening of the PSF, and it is important in this simulated stacking that we replicate this elongated elliptical beam. Using the same process described in H2022, we find a PSF as shown in shown in Figure 1. When fitted with

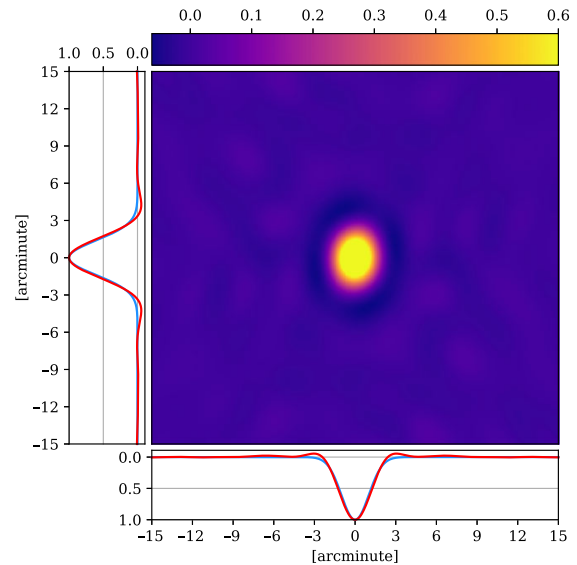


Figure 1. The dirty beam used in this modelling, which closely approximates the Phase I 154 MHz MWA dirty beam at $\sim 19^\circ$ declination and 30 min integration time. The red lines indicate the 2D profile of the dirty beam and the blue lines indicate the elliptical Gaussian fit with parameters $196.4'' \times 141.6''$ and position angle -14.5° .

an elliptical Gaussian, this PSF has dimensions $196.4'' \times 141.6''$, with position angle -14.5° . For simplicity, we use this fitted Gaussian beam when constructing our fields.

With these steps complete, we produce sky maps for each realisation. As an example, in Figure 2 we show the inner region of realisation 1. On the left of the figure, we show the AGN and SFG population after having been convolved with the fitted Gaussian beam, and on the right the synchrotron cosmic web having been convolved to the resolution of the same beam. For each realisation we produce maps of: the AGN and SFG populations; the cosmic web emission; and a third combined map.

2.1. Point source subtraction

Both V2021 and H2022 perform a point source subtraction step, with the aim to avoid contamination from comparatively bright AGN and SFG sources during stacking. In V2021, wavelet-based point source subtraction was performed upon GLEAM images, down to a threshold of 5 times the image noise, corresponding to about $175 \text{ mJy beam}^{-1}$ at 154 MHz. H2022 instead used the residuals after cleaning, removing all emission brighter than approximately 60 mJy beam^{-1} , with the assumption that bright emission—point-like or not—was unlikely to be attributable to filamentary emission.

We employ this latter cleaning technique to simply and effectively remove bright AGN and SFG emission. The cleaning of our dirty images was performed using a simple image-based algorithm, the equivalent of the Hogbom clean algorithm (Högbom 1974) or the purely ‘minor’ cycles of the Clark algorithm (Clark 1980). The gain parameter was set at 0.1, and the process was continued for each image until no peaks remained above a lower flux threshold, which we set as 10 mJy beam^{-1} .

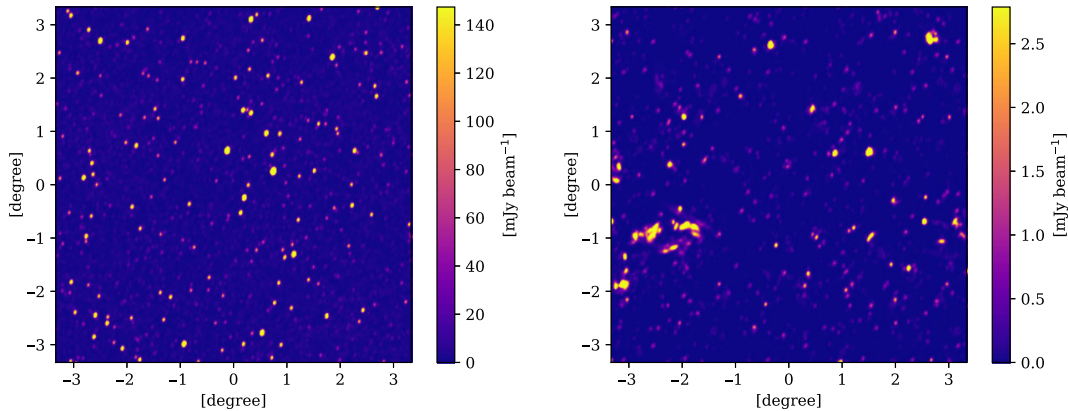


Figure 2. A $\sim 6^\circ \times 6^\circ$ subregion of the field 1, having been convolved with a Gaussian beam approximating the MWA Phase I beam. The colour scale for each map has been capped at the 99.5th percentile pixel value. *Left:* The AGN and SFG map, with a bright 30 Jy source located near the centre. Prior to stacking, this is cleaned down to 10 mJy beam $^{-1}$. *Right:* The cosmic web map, showing some nearby, extended emission structures in the bottom left.

3. Stacking

3.1. Selection of halo pairs

Before we can perform stacking, we must first create a catalogue of DM halo pairs. In V2021 and H2022, LRG pairs were drawn from the LRG catalogue constructed by Lopes (2007) if they met the following criteria: where the angular separation of a pair θ satisfied $20' < \theta < 180'$; and the physical separation satisfied $1 \text{ Mpc} < R < 15 \text{ Mpc}$ (comoving).^b

In contrast to V2021 and H2022, where cluster locations were inferred only by using LRGs as proxy, we have perfect knowledge of the DM halos within the simulation. It is therefore possible for us to exhaustively extract all such DM halo pairs that meet this criteria. Doing so, however, would result in a population of DM pairs with notably different distribution of spatial and angular separation, as well as skewed towards significantly deeper redshifts than used in these prior experiments. In fact, the stacking procedure is relatively sensitive to the distribution of pairs used in the stack, and in particular their angular separation (as this determines the required rescaling of the image during stacking) as well as their redshift (as this will on average determine the flux).

Thus we have chosen to select DM halo pairs that approximate the angular, spatial, and redshift distribution LRG pairs found in the ‘Max 15 Mpc’ catalogue from H2022. To do this, we have simply binned this reference catalogue in all three dimensions so as to roughly generate a probability distribution. From our exhaustive list of DM halo pairs, mass limited to $M_\odot > 10^{12.5}$, we have extracted, without replacement, 70 000 DM halo pairs across the ten realisations based on this probability distribution. In Figure 3, we plot the redshift, angular separation and spatial separation of our 70 000 DM halo pairs in (blue) in comparison to those found in the Max 15 Mpc catalogue (red). This process does a reasonably good job at replicating the LRG pair distribution, including the twin peaks found in the redshift distribution that is artifact found in the original LRG catalogue of Lopes (2007). There is, however, some small deviation between the two distributions, and

^bThe lower threshold on R is not documented in V2021, but was provided in personal communication, as was the use of a comoving distance metric.

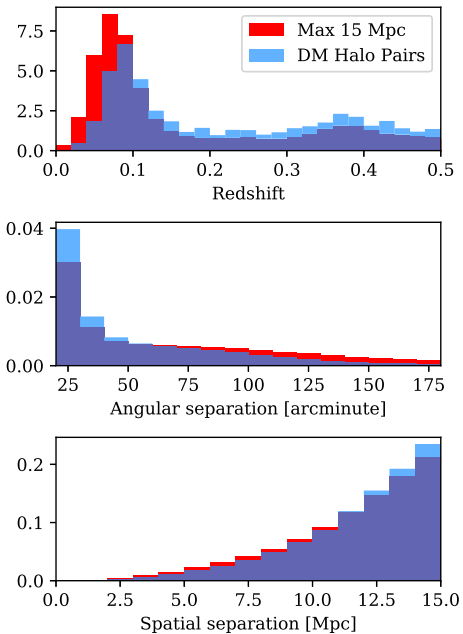


Figure 3. The redshift, angular separation and spatial separation distributions of our catalogue of halo pairs (blue) compared to the ‘Max 15 Mpc’ catalogue of LRG pairs from H2022 (red). Histograms are normalised so as to integrate to unity.

this has arisen where our own DM halo catalogue was exhausted for certain combinations of parameters.

3.2. Stacking and modelling methodology

Stacking proceeds nearly identically as described in V2021, and using the same code as used in H2022. We briefly summarise the process here. For a given catalogue, we first identify a maximum scaling factor and associated maximum pixel length. Then for each DM halo pair, we rescale the image, strictly larger, such that the

pixel distance between the DM halo pair exactly matches the maximum pixel length. This rescaled image is then rotated so that the line spanning the DM halo pair is rotated to horizontal and such that each DM halo is aligned to normalised coordinates at $(-1, 0)$ and $(+1, 0)$, before the image is then cropped and stacked onto previously processed cutouts. A respective weight map is also created, set to one for valid cutout pixels or to zero for invalid or out of bounds pixels, and this is similarly stacked. Finally, when all halos have been processed and stacked, the stacked DM halo pairs are divided by the stacked weight maps.

Once stacking is completed, as with both V2021 and H2022, we observe clearly discernible peaks of emission at the stacked DM halo centres, at $(-1, 0)$ and $(+1, 0)$. V2021 made the assumption that the majority of this emission is attributable to cluster emission such as AGN and SFG populations, radio halos, and other radio emission processes typically found in cluster environments. Crucially, they also made the assumption that this cluster emission should be, on average, radially symmetric, as opposed to the weaker filamentary emission which should only be present between the pair of clusters. Thus V2021 constructed a radio profile model for this core emission based on the exterior radial profile around each peak, and which they could later subtract so as to reveal excess intracluster emission. To do this, the profile was calculated by finding the radial average of emission around each of the central peaks, but calculated only across a 180° sweep strictly ‘behind’ the intracluster region (i.e. for $x < -1$ or $x > 1$, for each peak, respectively).

H2022 implemented an identical modelling procedure and verified this process on synthetic cosmic web images. We have used their modelling code without modification.

3.3. Noise estimation

In V2021 and H2022, the final stacked images were shown to be approximately normally distributed. This arises quite naturally as the original images are themselves dominated by noise arising from system noise, sky temperature and sidelobe confusion. In this case, we do not start off with noisy images: our simulated fields do not have any injected noise. Nonetheless, we find that after stacking, our stacked images have the appearance of noise that arises from variably sized cutouts of real emission features being scaled and rotated many thousands of times. To measure the typical distribution of pixels within our stacks, we construct an area within our model-subtracted stacks sufficiently far from either peak as well as the intracluster region: this excluded region is therefore the union of the region bounded by $-1 < x < 1$ and $-1 < y < 1$, as well as the regions with radius $r < 0.2$ of either peak at $(-1, 0)$ or $(1, 0)$. In Figure 4, we show in the upper panel the distribution of these pixels from the combined (AGN, SFG, cosmic web) stack. In fact, this distribution of pixels is still well approximated by a Gaussian distribution, as illustrated by the close fit of the Gaussian envelope parameterised by $\sigma = 7.34$, and we shall proceed to quantify the noise herein simply by the standard deviation.

Additionally, we note that this noise is spatially correlated across the stacked images. The size of this spatial correlation is a function both of the original resolution of the fields prior to stacking combined with magnitude of rescaling operations during stacking. Following H2022, we measure the resulting ‘effective resolution’ of the stacked image by way of autocorrelating the image. For example, in the lower panel of Figure 4 we show the

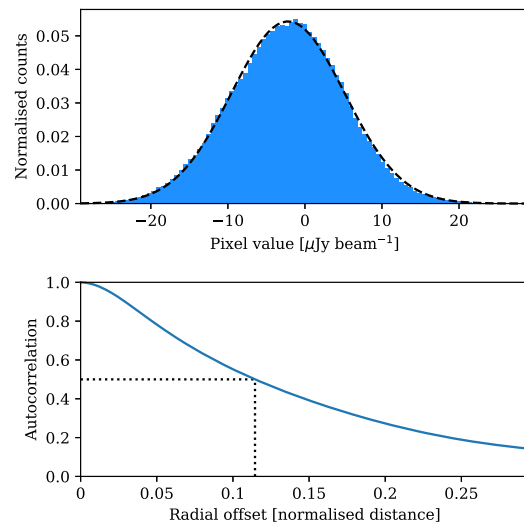


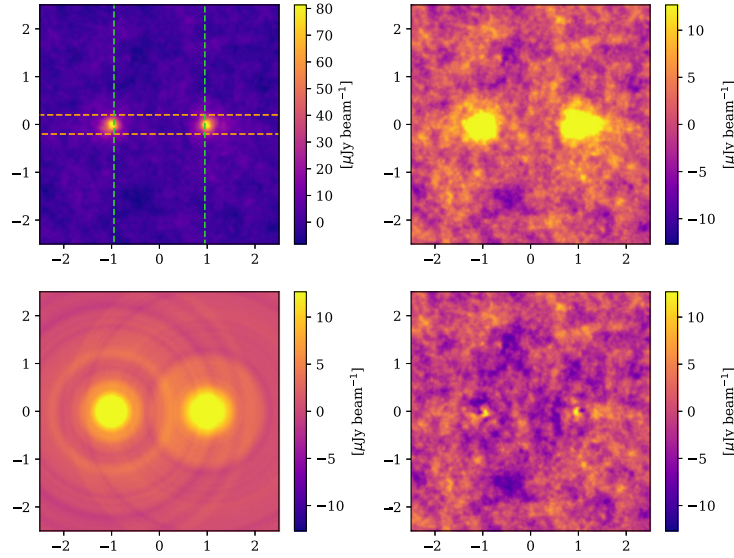
Figure 4. The noise properties of the stacked image for all combined observables with Gaussian beam, calculated across the model-subtracted image, excluding circular regions around the peaks of radius $r = 0.2$ and the inner region bounded by $-1 < x < 1$ and $-1 < y < 1$. *Upper panel:* The distribution of the pixel values (blue) and a fitted Gaussian (dashed black line) showing the stacked noise is approximately normal in distribution. *Lower panel:* The radial autocorrelation of this region, showing the pixel to pixel correlation. The dotted black line indicates the half width, half maximum of this autocorrelation.

autocorrelation of the combined image, using the same area over which we made the earlier noise calculation. From this plot we can read off a half width at half maximum value of 0.11 for the autocorrelation, which corresponds to an effective resolution of the original stacked image having a full width at half maximum (FWHM) of 0.16.^c Emission structures on scales larger than this effective resolution are likely therefore to be extended.

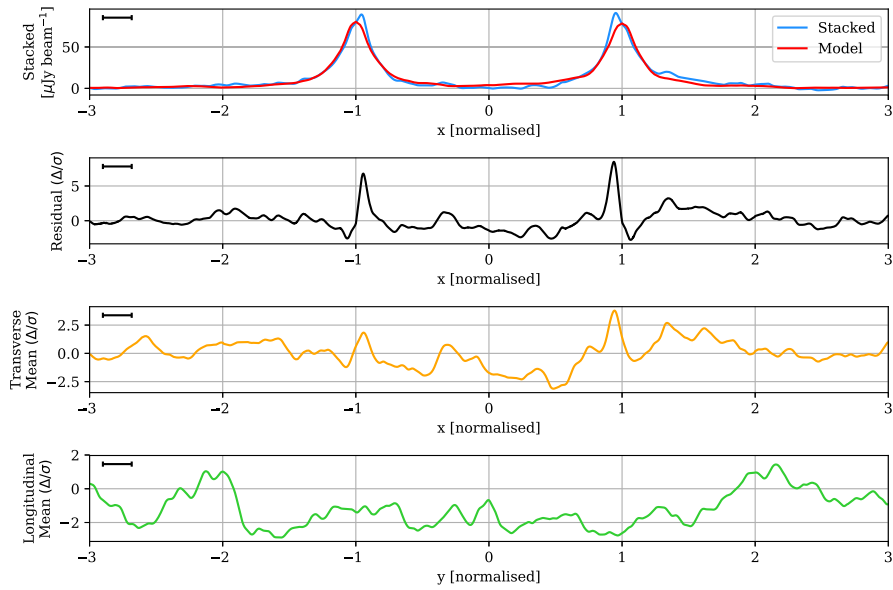
4. Results and discussion

We begin by presenting the stacked results for the synchrotron cosmic web alone, which we isolate here to focus on its unique signature. These results stack 70 000 DM halo pairs across all ten realisations, and in this case we have not undertaken any point source subtraction. In Figure 5a, the upper plots show the stacked image on two different colour scales, in which the upper right is scaled to emphasise the noise at $2.5 \mu\text{Jy beam}^{-1}$. We observe peaks centred approximately at $(-1, 0)$ and $(1, 0)$, and having maximum values of approximately $90 \mu\text{Jy beam}^{-1}$ and FWHM widths of about 0.28. In the lower left plot, we show the model constructed as per Subsection 3.2, and in the lower right panel we show the stack after model subtraction. In Figure 5b, we show one-dimensional profiles showing: at the top, the profile along $y = 0$ of the original stacked image compared to the model; in the second row, the profile along $y = 0$ of the residual image; in the third row, the transverse mean in the region $-0.2 < y < 0.2$ as a function of x ; and finally at the bottom, the longitudinal mean in the region

^cThe effective resolution of the original image is related to the HWHM of the autocorrelation by the relation $\theta_{\text{FWHM}} = \sqrt{2} \cdot \theta_{\text{HWHM}}$. This derives from the fact that the autocorrelation of a Gaussian function produces another Gaussian, with its width increased by a factor of $\sqrt{2}$.



(a) *Top left*: The original mean stack image, with overlays indicating the region over which the transverse mean (dashed orange horizontal lines) and longitudinal mean (dashed green vertical lines) are calculated. *Top right*: The mean stacked image with the colour scale reduced to $\pm 5\sigma$ to emphasise the noise. *Bottom left*: The model image, on the same colour scale. *Bottom right*: The residual stack after model subtraction, with the colour scale set to $\pm 5\sigma$.



(b) *One*: The one-dimensional profile along $y = 0$ for both the stacked image (blue) and the model (red). *Two*: The one-dimensional profile along $y = 0$ of the residual stack, renormalised to the estimated map noise. *Three*: The transverse mean along the region $-0.2 < y < 0.2$ of the residual stack, renormalised to the estimated map noise. *Four*: The longitudinal mean along the region $-0.95 < x < 0.95$ of the residual stack, renormalised to the estimated map noise. The black rule in the top left shows the FWHM of the effective resolution.

Figure 5. The synchrotron cosmic web stack, with estimated noise $2.5 \mu\text{Jy beam}^{-1}$ and effective resolution 0.21 . The left peak has a maximum of $89.46 \mu\text{Jy beam}^{-1}$ and a FWHM of 0.27 ; the right peaks at $91.1 \mu\text{Jy beam}^{-1}$ and has a FWHM of 0.28 .

$-0.95 < x < 0.95$ as a function of y . We apply the transverse mean in an attempt to draw out any faint but wide signals along the intracluster region; whilst the longitudinal mean attempts to bring out any faint signals the might span the length of the intracluster region.

The peaks that we observe are primarily the result of radio relic-like shocks surrounding the clusters and galaxy groups of the FIGARO simulation. As noted in Hodgson et al. (2021a), some 96% of the radio power of cosmic web emission in FIGARO was located about the 100 most massive DM halos, within the spherical regions $r < 1.5r_{200}$ (where r_{200} is the $M_{\odot} = 200\rho_c$ virial radius of the cluster). This radio power is generated by stationary accretion shocks that are morphologically akin to radio relics, often appearing as thin, elongated arcs that trace the shock front.

Outside of cluster peripheries, as noted in Hodgson et al. (2021a), the emission that traces the filaments proper is orders of magnitude fainter. Indeed, examining Figure 5 closely, we make no detection of faint filament emission along the intracluster region in our stack, nor in the one-dimensional profile, or the transverse and longitudinal means. Our modelling suggests that in a stacking experiment like this, the intracluster region will be devoid of any detectable emission attributable to the cosmic web.

We do, however, note a curious detail about the peaks: they are asymmetric about their respective centres. Both the left and right peaks are actually shifted slightly inward, and this is made especially clear when we construct the model, which assumes radial symmetry, as seen in the top panel of Figure 5b. As a result, the residual image in the lower right of Figure 5b shows peaks of emission left behind, and this is illustrated further in the one-dimensional profile of the residual image in panel two of Figure 5b, where we see peaks slightly interior to the halo pair reaching more than 5σ . We expand upon this feature shortly.

Next, we turn to the results in Figure 6 of stacking the combined fields, which incorporate all of the AGN, SFG, and cosmic web emission in one. This combined field has had bright sources subtracted, primarily AGN and SFG sources, by cleaning down to 10 mJy beam^{-1} . These additional sources increase the stacked noise which is about three times higher at $7.3 \text{ } \mu\text{Jy beam}^{-1}$. As previously, we note in these stacks bright peaks of emission at $x = \{-1, +1\}$, however in this case they are much brighter, at approximately $373 \text{ } \mu\text{Jy beam}^{-1}$, as well as much narrower, having a FWHM width of about 0.15. The effective resolution of the map is 0.16, meaning these peaks are essentially point-like, and are dominated by the compact emission of the AGN and SFG population. Note that the peak width is much narrower than observed in V2021, however it is similar to that found in H2022 and consistent with what would be expected after stacking a principally unresolved population of sources. Also note that the maximum peak values are primarily simply a function of the cleaning threshold.

Any cosmic web emission present in the stacked map is dominated by these AGN and SFG populations. In the top panel of Figure 6b, we show the one-dimensional profile of the combined stack in blue, and in dashed blue the cosmic web contribution (after cleaning) towards this peak. Whilst the cosmic web contribution is extended, having a FWHM of 0.28, this is lost in the combined peaks, which as we noted appear point-like. Moreover, the slight asymmetry of the cosmic web contribution is lost amongst the added noise of the AGN and SFG populations. The one-dimensional profile of the residual stack after model subtraction now shows no evidence of the peaks slightly interior to the halo pair that we observed earlier, and in fact there is a negative

peak at $x = -0.92$; since this depression is not mirrored on both sides of the stack about the centre at $x = 0$, we attribute this to stack noise.

The stated temperature of the filaments detected in V2021 was $100 \pm (40) \text{ mK}$ at 150 MHz. This value is equivalent to a flux density in our stacks of $51 \text{ } \mu\text{Jy beam}^{-1}$, which would amount to an approximately 7σ signal in the noisier, combined stack. It is clear that these simulated stacks do not support either the magnitude or location of the excess emission as detected in V2021.

4.1. The ubiquity of ‘relic’-like shocks

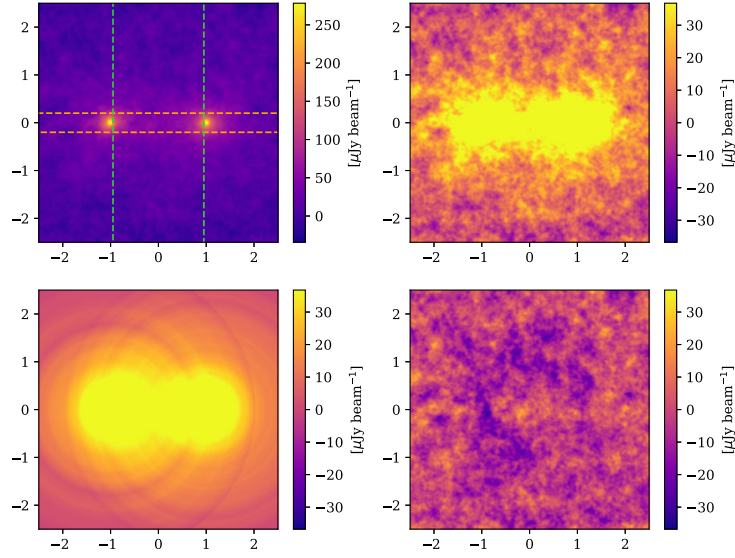
One of the key observations made about FIGARO in Hodgson et al. (2021a) was the degree to which the distribution of emission sources within the synchrotron cosmic web differed from prior expectations. It had been expected that emission structures traced the underlying mass of the filaments. Indeed, the Vazza et al. (2019) MHD simulation showed that the X-ray emission does trace this mass distribution. However, for the synchrotron component of the cosmic web, Hodgson et al. (2021a) noted a large population of emission structures in the spherical shell of DM halos, in the range $0.75 \cdot r_{200} < r < 1.5 \cdot r_{200}$ where r_{200} is the virial radius of the DM halo. These emission structures were morphologically similar to radio relics, most often tracing parenthetical arcs on opposing sides of the DM halo core. Outside of these regions, the filaments hosted emission orders of magnitude fainter. However, the mechanism for these shocks differs from radio relics: whilst relics are predominantly driven by cluster-scale merger events, the majority of these shocks are driven by strong accretion shocks at the virial boundary of overdense regions, forming stationary emission structures.

As we have noted, the cosmic web stacks display a unique asymmetry about the stacking centres, and instead peak slightly interior to halo pairs, at around $x = \pm 0.95$. In Figure 7 we show zoomed plots of the peaks of the stacked cosmic web, showing the one-dimensional profile along $y = 0$ around each peak. In addition to the peaks positioned interior to the intracluster region, we also note in these zoomed plots the presence of a second smaller peak at around $x = \pm 1.05$, and point of inflection in the vicinity of $x = \pm 1$.

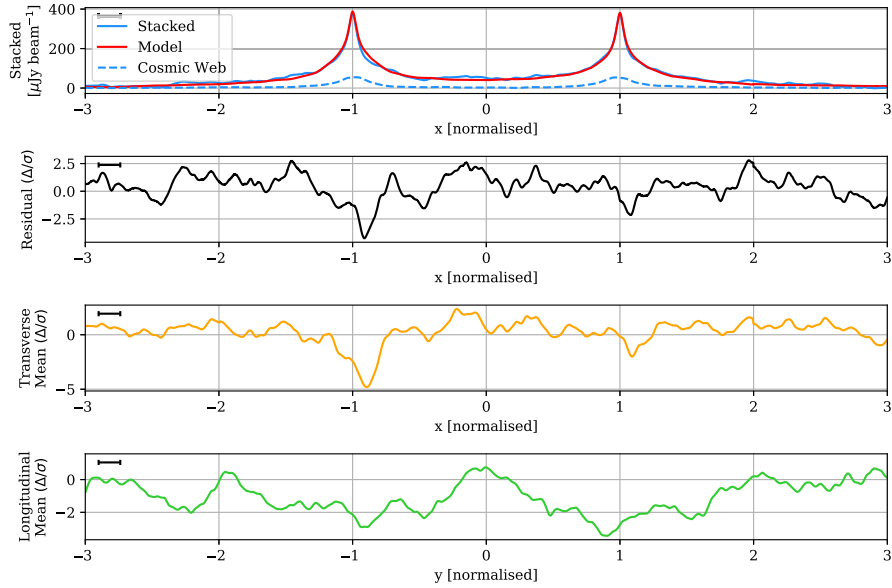
These features can be attributed to asymmetric accretion shocks about cluster peripheries, combined with projection effects. If we consider a double ‘relic’ cluster—two arcs of emission about an otherwise radio-quiet cluster core—then depending on the angle of observation this system will either appear as two separate peaks of emission, a single peak of emission where both the relic pair and the DM halo core are aligned along the line of sight, or some intermediary combination. When integrated over many such systems in the stacked image, these projection effects will contribute both to an emission peak at $x = \{-1, 1\}$ as well as additional emission immediately surrounding. Moreover, the asymmetry of the double-peak structure indicates that on average that the interior relic is more emissive (see Figure 8 for one such example). We can infer that the interior shock is subject to some combination of stronger shocks, a denser or hotter electron environment, or stronger magnetic fields; these are reasonable effects where the interior environment is slightly more compressed than the exterior.

4.2. Filamentary emission

We have not been able to detect excess filamentary emission in our stacks that is detectable above the stacking noise. However,



(a) *Top left*: The original mean stack image, with overlays indicating the region over which the transverse mean (dashed orange horizontal lines) and longitudinal mean (dashed green vertical lines) are calculated. *Top right*: The mean stacked image with the colour scale reduced to $\pm 5\sigma$ to emphasise the noise. *Bottom left*: The model image, on the same colour scale. *Bottom right*: The residual stack after model subtraction, with the colour scale set to $\pm 5\sigma$.



(b) *One*: The one-dimensional profile along $y = 0$ for the stacked image (blue), the model (red) and the synchrotron cosmic web component (dashed blue). *Two*: The one-dimensional profile along $y = 0$ of the residual stack, renormalised to the estimated map noise. *Three*: The transverse mean along the region $-0.2 < y < 0.2$ of the residual stack, renormalised to the estimated map noise. *Four*: The longitudinal mean along the region $-0.95 < x < 0.95$ of the residual stack, renormalised to the estimated map noise. The black rule in the top left shows the FWHM of the effective resolution.

Figure 6. The combined (AGN, SFG, cosmic web) stack, with estimated noise $7.3 \mu\text{Jy beam}^{-1}$ and effective resolution 0.16. The left peak has a maximum of $374.9 \mu\text{Jy beam}^{-1}$ and a FWHM of 0.16; the right peaks at $371.7 \mu\text{Jy beam}^{-1}$ and has a FWHM of 0.14.

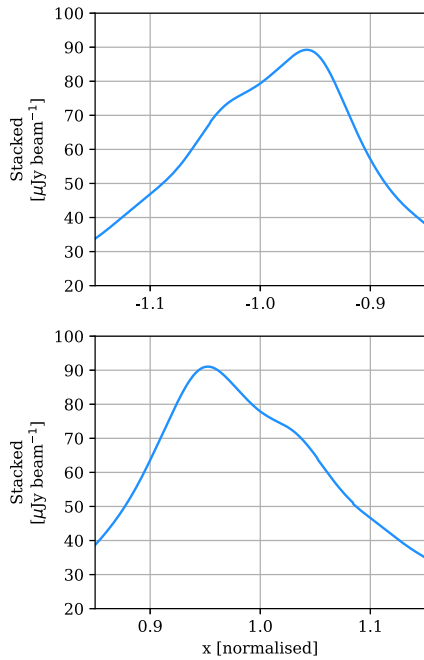


Figure 7. Zoomed plots of the peaks at $x = \{-1, 1\}$ in the one-dimensional profile of the stacked synchrotron cosmic web along $y = 0$ from Figure 6b. Note the profile peaks are interior to the intracluster region, at approximately $x = \pm 0.95$, as well as the inflection point at around $x = \pm 1$.

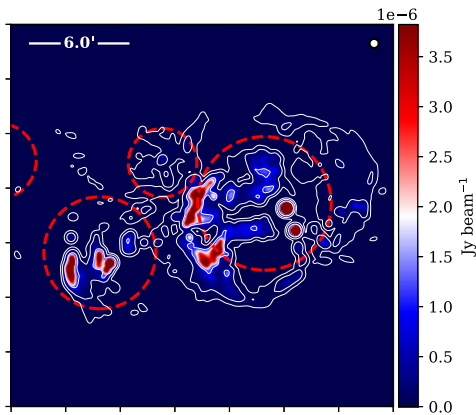


Figure 8. An example from FIGARO of asymmetric accretion-driven shocks about the periphery of interacting clusters. We observe three close-proximity clusters in the redshift range $0.15 < z < 0.2$, with approximate virial radii (r_{200}) indicated by dashed red lines. The contours show the integrated radio emission along the line of sight observed at 150 MHz and at a FWHM beam resolution of $20'$. The rightmost cluster displays a pair of parenteral arcs of emission about its centre, however with the interior arc significantly brighter. Whilst the projection makes some emission appear centrally located within cluster interiors, all emission is located at a radius from cluster centres of at least $r > 0.8 \cdot r_{200}$.

we could suppress this stacking noise if we could exclude all foreground and background emission sources, and stack the DM halo pairs in isolation. V2021 attempted a similar calculation on the same simulation data from Vazza et al. (2019) and we reproduce

this exercise here, however differing in a few key respects: we extract, isolate, and rotate the halo pair from within the three-dimensional volume, whereas they used only a flattened map; we use the simulation emission calibrated as per Hodgson et al. (2021a), resulting in an approximately sixfold increase in total emission across the volume; and in our analysis we also calculate the ‘background’ emission against which any excess would be measured. The latter difference is important, as the model construction method used here and in V2021 measures the *excess* emission with respect to the background, not the true strength of the filamentary emission itself.

Our method proceeded by extracting all halos with $M > 10^{12.5} M_{\odot}$ from the two nearest snapshots of the original MHD simulation, of which there are 931, and finding all halo pairs with comoving distance in the range $1 \text{ Mpc} < r < 15 \text{ Mpc}$ and angular separation $20' < \theta < 180'$ when placed at a redshift of $z = 0.14$, of which there are 4 919 pairs. For each pair, we have rotated and scaled the volume to align the pair at normalised coordinates $x = \{-1, 1\}$ and removed all emission in the foreground or background where $|z| > 0.5$. To match the method used in V2021, all emission was placed at a redshift of $z = 0.14$, however our method differs in that we use the PSF used throughout this paper and that we set the observing frequency to 150 MHz.

In Figure 9 we present the results of this isolated stack, showing the mean flux density of the full stack in the upper panel, and in the centre we show both the one-dimensional strip of values of this stack (blue) as well as the mean value across the region $-0.25 < y < 0.25$ (red). The peaks near $x = \{-1, 1\}$ have a mean value of $162 \mu\text{Jy beam}^{-1}$, with both peaks offset towards the interior.^d The mean value in the intracluster region spanning $-0.5 < x < 0.5$ and $-0.25 < y < 0.25$ is $4.4 \mu\text{Jy beam}^{-1}$ or equivalently 8.7 mK. This value is in comparison to the mean background emission of $3.0 \mu\text{Jy beam}^{-1}$, which we have calculated as the mean value across the full exterior 180° sweep about each peak, in the radial range $0.5 < r < 1.5$. The excess filamentary emission with respect to this background is therefore $1.4 \mu\text{Jy beam}^{-1}$ or equivalently 2.7 mK.

In the lower panel of Figure 9, we also present the distribution of individual halo pair contributions to the mean intracluster excess. Clearly, a small fraction of halo pairs are responsible for the bulk of the measured excess emission along the bridge, with the majority providing negligible signal. Note also that the turnover at lower excess fluxes is an artificial result of the minimum mass threshold; modification of this lower threshold moves the location of the peak in this distribution.

This is an artificial exercise, however it does tell us a couple of things. Firstly, that there is indeed a small intracluster excess present in the underlying simulation; secondly, that this emission is some two orders of magnitude lower than the cosmic web emission around the periphery of clusters and groups; and thirdly, that a small handful of intracuster pairs are responsible for the bulk of the emission. Detecting this excess with stacking, however, would require vastly more pairs of DM halos and observed sky area to sufficiently suppress the stacking noise. For example, we would

^dThe cosmic web peaks here are brighter than those stated previously in our stacked cosmic web. This discrepancy arises as the model construction process used in stacking subtracts away the mean background emission (produced from unrelated foreground and background emission sources) and so the peak values given there are actually only the excess peak emission above this background. In the case of the cosmic web stack, this background emission was $65.5 \mu\text{Jy beam}^{-1}$.

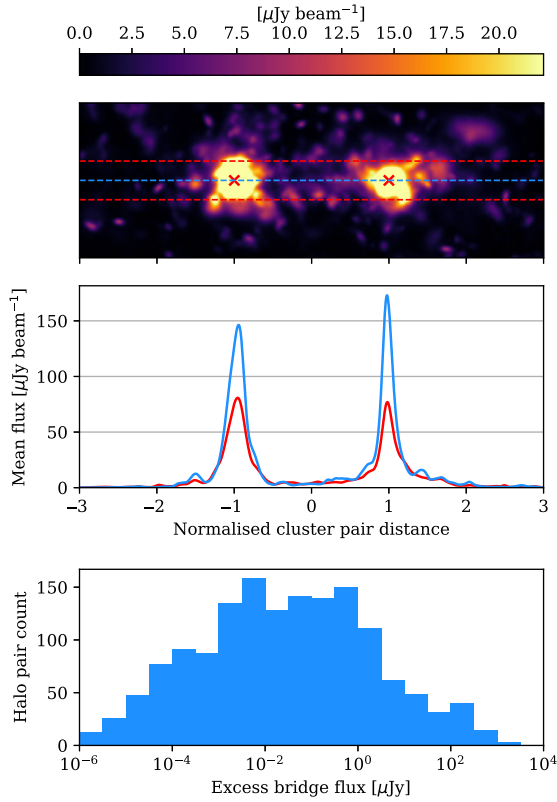


Figure 9. Stacked cosmic web emission between DM halo pairs (with $M > 10^{12.5} M_{\odot}$, $1 \text{ Mpc} < r < 15 \text{ Mpc}$) within the original simulation volume (snapshots 166 & 188) from Vazza *et al.* (2019), set at a redshift $z = 0.14$ and an observing frequency of 118 MHz. Crucially, this stack isolates the halo pair from all foreground and background emission. *Upper panel:* The stacked image of halo pairs, scaled such that the colour saturates at the 99th percentile pixel. *Centre panel:* The values measured between the two halo peaks (blue) along the line indicated in dashed blue; and the mean values (red) calculated in the region between the dashed red lines. *Lower panel:* The distribution of excess intracluster emission for individual halo pairs, showing that the majority of the bridge excess is the result of just a small handful of pairs.

need to increase the number of stacked DM halo pairs in our simulated stacks from 70 000 to approximately 17 million to allow a 3σ detection of this excess filamentary emission.

4.3. Limitations on the current study

The conflicting findings between V2021 and H2022 remain unresolved. Whilst this simulated stacking exercise does not support the findings of V2021, it's important to note some key limitations. In this section, we discuss some of the salient limitations of the underlying MHD simulation as well as explore possibilities where the simulated synchrotron emission along filaments might be amplified.

The first important caveat of note is that in the densest, most massive parts of the MHD simulation volume, there is good reason to believe synchrotron emission is underestimated. This underestimation arises from the simulation ignoring the role of fossil electrons—electrons that have been previously accelerated either by AGN or historic large-scale accretion shocks—in increasing

the acceleration efficiency of shocks. AGN were not modelled as part of the original MHD simulation upon which FIGARO is based, nor were the accumulated effects of earlier epoch shocks; instead, the electron population was always assumed to be at thermal equilibrium. The result of this is to underestimate synchrotron emission in dense environments, especially cluster interiors where fossil electrons can reasonably be expected to survive hundreds of millions of years (e.g. Hodgson *et al.* 2021b). In the development of FIGARO, we attempted to mitigate this by calibrating the simulated relics to match the known radio relic population (Nuza *et al.* 2012): dense regions subject to weak shocks had their electron acceleration efficiency artificially increased to 10^{-2} . Beyond these dense cluster environments, however, the origin, prevalence, and lifetimes of fossil electrons in cluster peripheries and in intracluster environments is poorly understood. For example, in their discovery of a ridge of radio emission between merging clusters Abell 399 and 401, Govoni *et al.* (2019) noted that the observed radio emission was three orders of magnitude brighter than from similar ENZO-based simulations. If, however, the ridge was filled with a population of electrons at energies $\gamma \gtrsim 1000$, it was possible to boost their simulation emission to match the observation. They did not attempt to explain the origin of this hypothetical fossil electron population, or whether it was especially plausible.⁶ Whilst Abell 399 and 401 were separated by 3 Mpc, in general a high density of energetic fossil electrons ($\gamma \gtrsim 1000$) is implausible across the kind of large ($r = 10 \text{ Mpc}$), low density intracluster environments that are typical of the LRG pairs used in V2021. At best, therefore, a large and energetic fossil electron population could be used to boost nearby pairs of clusters, but cannot be used to boost the filament strength in general.

We must also consider the limited volume of our original MHD simulation, at just 100^3 Mpc^3 . This volume reproduces only a handful of massive $\sim 10^{14} M_{\odot}$ clusters, whilst the full region over which V2021 and H2022 performed their stack includes numerous clusters on the order of $10^{15} M_{\odot}$. Whilst few in number, these most massive clusters are likely to be outliers in terms of their contribution to cosmic web emission. It is not clear, however, how such clusters would affect the stacked signal, and whether they would contribute substantially to the intracluster region, or instead simply increase the signal at $x = \{-1, 1\}$. The answer to this question must await larger volume MHD simulations.

Another key input to the MHD simulation is the value that was set for the primordial magnetic field. This was set as 0.1 nG, about a factor of 10 lower than the upper limits derived from cosmic microwave background observations (Planck Collaboration *et al.* 2016). In low density environments, dynamo amplification processes are believed to be negligible and observational data has placed tight limits on such effects (O'Sullivan *et al.* 2020). The resulting magnetic field strengths in these sparse environments are instead primarily the result of adiabatic gas compression, and the field strengths along filaments are therefore closely related to the primordial field strength. For values of $B \ll B_{\text{CMB}}$, where B_{CMB} is the equivalent magnetic field strength of the cosmic microwave background and is approximately $3.25(1+z)^2 \text{ mG}$, the synchrotron emission, S , along filaments scales as $S \propto B^2$ (Hoeft & Brüggen 2007). Thus, for small increases in the magnetic seeding scenario, we can significantly amplify the cosmic web emission. This 'lever', however, operates globally on both the filaments

⁶Brunetti & Vazza (2020) suggest instead that turbulent Fermi II processes could account for the emission.

proper as well as the relics and quickly becomes unphysically bright. As noted, in the construction of FIGARO, we have already calibrated the cosmic web emission using the radio relic population; further amplification would render a large population of previously hidden radio relics now plainly visible, in contradiction to their observed population statistics. In a sense, then, the brightest outliers of the cosmic web provide a relatively tight constraint on any amplification of the primordial magnetic field.

Finally, we can also consider the effect of a non-uniform primordial magnetic field. Whilst the MHD simulation of Vazza et al. (2019) initialised a uniform magnetic field at redshift $z = 45$, it is possible that these primordial fields already had more complex spatial configurations. Such a change could result in the radio signal of the cosmic web becoming increasingly different outside of DM halo interiors. Dedicated simulations, however, are the only way to accurately predict their effects (e.g. Vazza et al. 2021).

5. Conclusion

We have reproduced the stacking and modelling methodology used V2021, and more recently in H2022, using the recently published FIGARO simulation. Using FIGARO, we have constructed ten $15^\circ \times 15^\circ$ fields of the radio sky at 150 MHz and for redshifts $z < 0.6$, as observed by the MWA Phase I instrument. We have identified 70 000 DM halo pairs, forming a similar sample to that used in H2022, and have stacked these pairs for each of the combined radio sky (AGNs, SFGs, and synchrotron cosmic web) as well as the synchrotron cosmic web in isolation.

Ultimately, we have been unable to reproduce the specific location of excess intracluster emission observed by V2021. Instead, we observe an excess of emission in the stacks as a result of the cosmic web on the immediate interiors of the stacked peaks at $x = \{-1, 1\}$. These peaks are the result of stationary accretion shocks about the periphery of clusters and galaxy groups, and the asymmetry we observe is likely the result of more emissive interior shocks due to compression effects. These cosmic web peaks, however, are dominated by the AGN and SFG populations when we construct the combined stack, and the small asymmetric peak is obscured by the additional stacking noise.

The true intracluster excess emission in the region $-0.5 < x < 0.5$ is consistent with the noise in our stacked images. In a follow up stack, where we have isolated pairs of DM halos from all foreground and background emission to reduce the stacking noise further, we do find that the intracluster bridge has a small excess of emission compared to the background, but that this excess is two orders of magnitude fainter than the cosmic web peaks.

Our stacking experiment here represents a best case scenario: we know the DM halo population perfectly, and there is no noise or errors associated with our observations. Real-world observations and stacking experiments instead stack noisy, imperfectly calibrated images, and currently only have LRGs as an heuristic proxy for the location of clusters. Unless some of the noted limitations to the underlying MHD simulation prove to significantly change the results shown here, it would seem stacking LRG pairs is an especially difficult technique for the detection of the synchrotron cosmic web and future detection attempts will need to stack significantly larger areas of the sky.

Acknowledgements. The authors thank Tessa Vernstrom for providing additional details regarding the methodology used in V2021. F.V.

acknowledges financial support from the ERC Starting Grant ‘MAGCOW’, no. 714196. The cosmological simulations on which this work is based have been produced using the ENZO code (<http://enzo-project.org>), running on Piz Daint supercomputer at CSCS-ETHZ (Lugano, Switzerland) under project s805 (with F.V. as PI, and the collaboration of C. Gheller and M. Brüggen). We also acknowledge the usage of online storage tools kindly provided by the INAF Astronomical Archive (IA2) initiative (<http://www.ia2.inaf.it>).

References

- Araya-Melo, P. A., Aragón-Calvo, M. A., Brüggen, M., & Hoeft, M. 2012, *MNRAS*, **423**, 2325
- Baugh, C. M., et al. 2004, *MNRAS*, **351**, L44
- Bonaldi, A., Bonato, M., Galluzzi, V., Harrison, I., Massardi, M., Kay, S., De Zotti, G., & Brown, M. L. 2019, *MNRAS*, **482**, 2
- Brown, S. D. 2011, *JApA*, **32**, 577
- Brown, S., et al. 2017, *MNRAS*, **468**, 4246
- Brunetti, G., & Vazza, F. 2020, *PhRvL*, **124**, 051101
- Carretti, E., et al. 2022, *MNRAS*, **512**, 945
- Cen, R., & Ostriker, J. P. 1999, *ApJ*, **514**, 1
- Clark, B. G. 1980, *A&A*, **89**, 377
- Davé, R., et al. 2001, *ApJ*, **552**, 473
- de Graaff, A., Cai, Y.-C., Heymans, C., & Peacock, J. A. 2019, *A&A*, **624**, A48
- Eastwood, M. W., et al. 2018, *AJ*, **156**, 32
- Eckert, D., et al. 2015, *Natur*, **528**, 105
- Govoni, F., et al. 2019, *Sci*, **364**, 981
- Hodgson, T., Bartalucci, I., Johnston-Hollitt, M., McKinley, B., Vazza, F., & Wittor, D. 2021b, *ApJ*, **909**, 198
- Hodgson, T., Johnston-Hollitt, M., McKinley, B., & Hurley-Walker, N. 2022, *PASA*, **39**, e013
- Hodgson, T., Vazza, F., Johnston-Hollitt, M., & McKinley, B. 2021a, *PASA*, **38**, e047
- Hoeft, M., & Brüggen, M. 2007, *MNRAS*, **375**, 77
- Högbom, J. A. 1974, *A&AS*, **15**, 417
- Hurley-Walker, N., et al. 2017, *MNRAS*, **464**, 1146
- Keshet, U., Katz, B., Spitkovsky, A., & Waxman, E. 2009, *ApJ*, **693**, L127
- Lopes, P. A. A. 2007, *MNRAS*, **380**, 1608
- Macquart, J. P., et al. 2020, *Nature*, **581**, 391
- Nicastro, F., Krongold, Y., Mathur, S., & Elvis, M. 2017, *AN*, **338**, 281
- Nicastro, F., et al. 2018, *Natur*, **558**, 406
- Nuza, S. E., Hoeft, M., van Weeren, R. J., Gottlöber, S., & Yepes, G. 2012, *MNRAS*, **420**, 2006
- O’Sullivan, S. P., et al. 2019, *A&A*, **622**, A16
- O’Sullivan, S. P., et al. 2020, *MNRAS*, **495**, 2607
- Planck Collaboration, et al. 2016, *A&A*, **594**, A19
- Pshirkov, M. S., Tinyakov P. G., & Urban F. R., 2016, *PhRvL*, **116**, 191302
- Tanimura, H., Aghanim, N., Douspis, M., Beelen, A., & Bonjean, V. 2019, *A&A*, **625**, A67
- Tanimura, H., Aghanim, N., Kolodzig, A., Douspis, M., & Malavasi, N. 2020, *A&A*, **643**, L2
- Tingay, S. J., et al. 2013, *PASA*, **30**, e007
- Vazza, F., Ettori, S., Roncarelli, M., Angelinelli, M., Brüggen, M., & Gheller, C. 2019, *A&A*, **627**, A5
- Vazza, F., Ferrari, C., Brüggen, M., Bonafede, A., Gheller, C., & Wang, P. 2015, *A&A*, **580**, A119
- Vazza, F., Paoletti, D., Banfi, S., Finelli, F., Gheller, C., O’Sullivan, S. P., & Brüggen, M. 2021, *MNRAS*, **500**, 5350
- Vernstrom, T., Gaensler, B. M., Brown, S., Lenc, E., & Norris, R. P., 2017, *MNRAS*, **467**, 4914
- Vernstrom, T., Gaensler, B. M., Rudnick, L., & Andernach, H. 2019, *ApJ*, **878**, 92
- Vernstrom, T., Heald, G., Vazza, F., Galvin, T. J., West, J. L., Locatelli, N., Fornengo, N., & Pinetti, E. 2021, *MNRAS*,
- Wayth, R. B., et al. 2015, *PASA*, **32**, e025
- Wayth, R. B., et al. 2018, *PASA*, **35**, e033

Bibliography

- Bonaldi A., Bonato M., Galluzzi V., Harrison I., Massardi M., Kay S., De Zotti G., Brown M. L., 2019, [MNRAS](#), **482**, 2
- Botteon A., Brunetti G., Ryu D., Roh S., 2020, [A&A](#), **634**, A64
- Brown S. D., 2011, [Journal of Astrophysics and Astronomy](#), **32**, 577
- Brown S., et al., 2017, [MNRAS](#), **468**, 4246
- Brunetti G., Vazza F., 2020, [Phys. Rev. Lett.](#), **124**, 051101
- Cen R., Ostriker J. P., 1999, [ApJ](#), **514**, 1
- Colless M., et al., 2003, arXiv e-prints, [pp astro-ph/0306581](#)
- Condon J. J., Cotton W. D., Greisen E. W., Yin Q. F., Perley R. A., Taylor G. B., Broderick J. J., 1998, [AJ](#), **115**, 1693
- Davé R., et al., 2001, [ApJ](#), **552**, 473
- Davis M., Efstathiou G., Frenk C. S., White S. D. M., 1985, [ApJ](#), **292**, 371
- Eastwood M. W., et al., 2018, [AJ](#), **156**, 32
- Eckert D., et al., 2015, [Nature](#), **528**, 105
- Ensslin T. A., Biermann P. L., Klein U., Kohle S., 1998, [A&A](#), **332**, 395
- Frater R. H., Brooks J. W., Whiteoak J. B., 1992, [Journal of Electrical and Electronics Engineering Australia](#), **12**, 103
- Giovannini G., Feretti L., 2000, [New Astronomy](#), **5**, 335
- Govoni F., et al., 2019, [Science](#), **364**, 981

- Hodgson T., Johnston-Hollitt M., McKinley B., Vernstrom T., Vacca V., 2020, [PASA](#), *37*, e032
- Hodgson T., Vazza F., Johnston-Hollitt M., McKinley B., 2021a, [PASA](#), *38*, e047
- Hodgson T., Bartalucci I., Johnston-Hollitt M., McKinley B., Vazza F., Wittor D., 2021b, [ApJ](#), *909*, 198
- Hodgson T., Johnston-Hollitt M., McKinley B., Hurley-Walker N., 2022a, [PASA](#), *39*, e013
- Hodgson T., Vazza F., Johnston-Hollitt M., McKinley B., 2022b, [PASA](#), *39*, e033
- Hoefl M., Brüggem M., 2007, [MNRAS](#), *375*, 77
- Hopkins A., Georgakakis A., Cram L., Afonso J., Mobasher B., 2000, [ApJS](#), *128*, 469
- Hotan A. W., et al., 2014, [PASA](#), *31*, e041
- Huchra J., et al., 2005, in Fairall A. P., Woudt P. A., eds, *Astronomical Society of the Pacific Conference Series Vol. 329, Nearby Large-Scale Structures and the Zone of Avoidance*. p. 135
- Hurley-Walker N., et al., 2017, [MNRAS](#), *464*, 1146
- Hurley-Walker N., et al., 2022, [PASA](#), *39*, e035
- Kang H., Ryu D., Cen R., Ostriker J. P., 2007, [ApJ](#), *669*, 729
- Keshet U., Waxman E., Loeb A., 2004, [ApJ](#), *617*, 281
- Lane W. M., Cotton W. D., van Velzen S., Clarke T. E., Kassim N. E., Helmboldt J. F., Lazio T. J. W., Cohen A. S., 2014, [MNRAS](#), *440*, 327
- Lopes P. A. A., 2007, [MNRAS](#), *380*, 1608
- Macquart J. P., et al., 2020, [Nature](#), *581*, 391

Mauch T., Murphy T., Buttery H. J., Curran J., Hunstead R. W., Piestrzynski B., Robertson J. G., Sadler E. M., 2003, [MNRAS](#), **342**, 1117

McConnell D., et al., 2020, [PASA](#), **37**, e048

Miniati F., Ryu D., Kang H., Jones T. W., Cen R., Ostriker J. P., 2000, [ApJ](#), **542**, 608

Nicastro F., et al., 2018, [Nature](#), **558**, 406

O'Sullivan S. P., et al., 2019, [A&A](#), **622**, A16

Pfrommer C., Springel V., Enßlin T. A., Jubelgas M., 2006, [MNRAS](#), **367**, 113

Prandoni I., et al., 2017, [A&A](#), **608**, A40

Pshirkov M. S., Tinyakov P. G., Urban F. R., 2016, [Phys. Rev. Lett.](#), **116**, 191302

Ryu D., Kang H., Hallman E., Jones T. W., 2003, [ApJ](#), **593**, 599

Ryu D., Kang H., Cho J., Das S., 2008, [Science](#), **320**, 909

Skillman S. W., Hallman E. J., O'Shea B. W., Burns J. O., Smith B. D., Turk M. J., 2011, [ApJ](#), **735**, 96

Tanimura H., Aghanim N., Douspis M., Beelen A., Bonjean V., 2019, [A&A](#), **625**, A67

Tanimura H., Aghanim N., Kolodzig A., Douspis M., Malavasi N., 2020, [A&A](#), **643**, L2

Tegmark M., et al., 2004, [ApJ](#), **606**, 702

Tingay S. J., et al., 2013, [PASA](#), **30**, e007

Vacca V., et al., 2018, [MNRAS](#), **479**, 776

Vazza F., Ferrari C., Brüggén M., Bonafede A., Gheller C., Wang P., 2015, [A&A](#), **580**, A119

- Vazza F., Etori S., Roncarelli M., Angelinelli M., Brügger M., Gheller C., 2019, [A&A](#), **627**, A5
- Vernstrom T., Gaensler B. M., Brown S., Lenc E., Norris R. P., 2017, [MNRAS](#), **467**, 4914
- Vernstrom T., Gaensler B. M., Rudnick L., Andernach H., 2019, [ApJ](#), **878**, 92
- Vernstrom T., Heald G., Vazza F., Galvin T. J., West J. L., Locatelli N., Fornengo N., Pinetti E., 2021, [MNRAS](#), **505**, 4178
- Voges W., et al., 1999, [A&A](#), **349**, 389
- Wayth R. B., et al., 2015, [PASA](#), **32**, e025
- Wayth R. B., et al., 2018, [PASA](#), **35**, e033
- White S. D. M., Frenk C. S., Davis M., Efstathiou G., 1987, [ApJ](#), **313**, 505
- Zel'dovich Y. B., 1970, [A&A](#), **500**, 13
- de Graaff A., Cai Y.-C., Heymans C., Peacock J. A., 2019, [A&A](#), **624**, A48

Every reasonable effort has been made to acknowledge the owners of copyright material. I would be pleased to hear from any copyright owner who has been omitted or incorrectly acknowledged.